2008

An experimental assessment of the size effects on the strength and ductility of freestanding Cu films under macroscopically homogenous deformation

Shakti Singh Chauhan
Iowa State University

An experimental assessment of the size effects on the strength and ductility of freestanding Cu films under macroscopically homogenous deformation

by

Shakti Singh Chauhan

A dissertation submitted to the graduate faculty

in partial fulfillment of the requirements for the degree of

DOCTOR OF PHILOSOPHY

Major: Engineering Mechanics

Program of Study Committee:
Ashraf F. Bastawros, Major Professor
Thomas J. Rudolphi
Wei Hong
Pranav Shrotriya
Ersan Ustundag

Iowa State University

Ames, Iowa

2008

To my family, especially my mother.

TABLE OF CONTENTS

LIST OF FIGURES

LIST OF TABLES

..

LIST OF SYMBOLS

t	=	Thickness of specimen
d_g	=	Average grain size
λ	=	Thickness to grain size ratio i.e. average number of grains across the thickness
Φ	=	Volume fraction of surface grains
σ_y	=	Yield Stress
σ_f	=	Flow stress
σ^S	=	Surface grain response i.e. contribution to the overall yield/flow stress from surface grains
σ^B	=	Bulk grain response i.e. contribution to the overall yield/flow stress from bulk grains
σ_t	=	Contribution from GB source starvation strengthening to the overall yield/ flow stress
ε	=	Strain
ε_u	=	Maximum uniform strain, found using Considere criterion
ρ	=	Resistivity
ρ_0	=	Resistivity of undeformed specimen
$\rho_{0.5\%}$	=	Resistivity of deformed specimen at 0.5% total strain
Ω	=	Grain boundary area per unit specimen volume
Ω_N	=	Normalized grain boundary area per unit specimen volume

ACKNOWLEDGEMENTS

I would like to acknowledge the support from National Science Foundation as well as Department of Aerospace Engineering throughout my studies at Iowa State.

I have learnt a great deal at Iowa State, both inside the classroom and outside. My advisor, Dr. Ashraf Bastawros, played a big role in my life during my graduate studies. He was a great source of encouragement and guidance throughout the course of my research. I have also learnt a great deal from Dr. Rudolphi. He introduced me to the wonderful world of mechanics. I also greatly enjoyed our random discussions on a lot of topics in the coffee room and in his office. I would like to acknowledge everyone on my committee, Dr. Pranav Shrotriya, Dr. Abhijit Chandra and Dr. Ersan Ustundag.

I would also like to acknowledge a lot of friends and colleagues at Iowa State. Many thanks are due especially to Hui, who was not only a great office mate but also a dependable friend. The camaraderie of all my friends at Iowa State was also a great source of joy to me throughout my years in Ames.

Finally, I would like to express my deepest gratitude to my family, especially my mother and my grandmother. None of this would be possible without their sacrifices. This work, and all that follows, is humbly dedicated to them.

ABSTRACT

Metallic interconnects and circuitry has been experiencing excessive deformation beyond their elastic limits in many applications, ranging from micro-electro-mechanical systems (MEMS) to flexible electronics. These broad applications are creating needs to understand the extent of strength and ductility of freestanding metallic films at scales approaching the micron and sub micron range.

This work aims to elucidate the effects of microstructural constraint as well as geometric dimensional constraint on the strength and ductility of freestanding Cu films under uniaxial tension. Two types of films are tested (i) high purity rolled films of 12.5-100μm thickness and average grain sizes of 11-47μm and (ii) electroplated films of 2-50 μm thickness and average grain sizes of 1.8-5μm. Several experimental tools including residual electrical resistivity measurements, surface strain measurements and surface roughness measurements are employed to highlight the underlying deformation mechanisms leading to the observed size effects.

With respect to the strength of the specimens, we find that the nature and magnitude of thickness effects is very sensitive to the average grain size. In all cases, coupled thickness and grain size effects were observed. This study shows that this observed coupling, unique to the case of freestanding specimen, arises because the observed size effects are an outcome of the size dependence of two fundamental

microstructural parameters i.e. volume fraction of surface grains and grain boundary area per unit specimen volume.

For films having thickness and grain sizes greater than 5μm, thickness dependent weakening is observed for a constant grain size. Reducing thickness results in an increase in the volume fraction of grains exposed to the free surface as well as a reduction in the grain boundary area per unit specimen volume. The former effect leads to a reduction in the effective microstructural constraint on the intragranular dislocation activity in individual grains. This free surface related effect is the origin of a weakening contribution to the overall specimen strength with reducing thickness. For specimens with grain sizes ~ O (10-50μm), this effect was found to be dominating i.e. reducing thickness resulted in reducing strength. A phenomenological model employing the flow strength of surface and bulk grains is proposed to model the observed trends.

For films having thickness and grain sizes smaller than 5μm, size dependent strengthening is observed for a constant grain size. At this scale, grain boundary dislocations dominate. As a consequence, thickness effects arise because grain boundary dislocation source density per unit specimen volume reduces with reducing specimen thickness. This statistical reduction in dislocation source density leads to increasing specimen strength via source starvation strengthening. Our results show that such increasing specimen strength with reducing thickness, which has only been observed previously for nanocrystalline thin films, first appears at average grain size of ~5μm or

smaller. The measurements showed a characteristic length scale of about 5μm, which defines the size dependent strengthening or weakening of the film.

With respect to the thickness effects on ductility, it was found that both thickness and average grain size affect ductility. While prominent thickness effects persist at larger grain sizes, for specimens with grain size approaching 1μm, the loss of strain hardening ability at such fine microstructures dominates and a limiting ductility of ~2% is seen irrespective of the thickness. The observed thickness effects on ductility were investigated via surface roughness measurements that allow the characterization of initiation and evolution of deformation heterogeneities. It was found that thickness has a strong influence on the characteristic heterogeneity of deformation. At small specimen thicknesses, the deformation was found to be highly localized i.e. widely spaced regions showing substantial thickness reduction, hence increasing the vulnerability to the onset of plastic instabilities. At larger thicknesses, however, the increasing microstructural constraint delocalizes the strain and thereby precludes the early onset of instability, leading to enhanced ductility.

CHAPTER 1: INTRODUCTION

This thesis is primarily focused on the study of mechanical properties, such as strength and ductility, of metallic films at small length scales. The study not only provides an experimental measurement of such properties for a specific material system, but also addresses the underlying physical mechanisms to explain the observed mechanical behavior. In this chapter, the motivation behind this work is discussed. Electronics miniaturization, which enables a whole host of other technologies, is identified as the driving force behind the study of material properties at small length scales.

1.1 BACKGROUND: ELECTRONICS MINIATURIZATION AND MATERIALS RELIABILITY

The idea of electronics miniaturization can best be illustrated by a discussion of Integrated Circuits, or ICs. ICs are at the very heart of the ongoing digital revolution that enables various other technologies such as modern computers, telecommunications (including the internet), financial services and banking, transportation, manufacturing systems, aerospace applications (avionics in aircrafts, guidance and navigation systems in satellites etc.). Modern day ICs are essentially a large number of tiny transistors on a Silicon substrate. The most sophisticated applications for ICs today, microprocessors, employ almost 1 Billion transistors, each reaching the 45nm or less in size. As compared to the first ICs in 1971, these devices have roughly a million times more transistors per

cm^2 of chip area, each of which is about a millionth of its original size.

However, one may contemplate about the reason to put such a large number of tiny transistors on one integrated circuit. There are two primary reasons for this: firstly, increasing the number of transistors not only increases the capability of the ICs, but also makes their operation faster i.e. faster switching speeds. The second reason is sheer economics of scale: current microfabrication techniques employ ~300mm Silicon wafers, thus, increasing the density of transistors allows the chip sizes, for the same capability, to shrink. As a result, more ICs can now be fabricated on a single Si wafer at the same time. Consequently, the fabrication cost, per unit IC, reduces. Besides these developments related to microelectronics, the last decade has also seen rapid growth in the development and application of Micro/Nano-electromechanical systems (MEMS/NEMS) as well as opto-electronic systems. The basic premise behind the concept of MEMS/NEMS is that the efficiencies of low unit cost and high volume production achieved by the microelectronics industry can be translated to devices in which mechanical and electrical devices are integrated into a single chip. In addition to the potential economic benefits, unique capabilities can be achieved by such integration to realize very small and efficient devices such as sensors, actuators, power producing devices, chemical reactors and biomedical devices, to name a few (Spencer at al, 2000). Such trends illustrate the economic driving force behind the ongoing miniaturization in electronics devices. Figure 1.1 shows the transistor density (per unit chip area) in the microelectronics industry along with the currents trends in MEMS devices (Peterson et

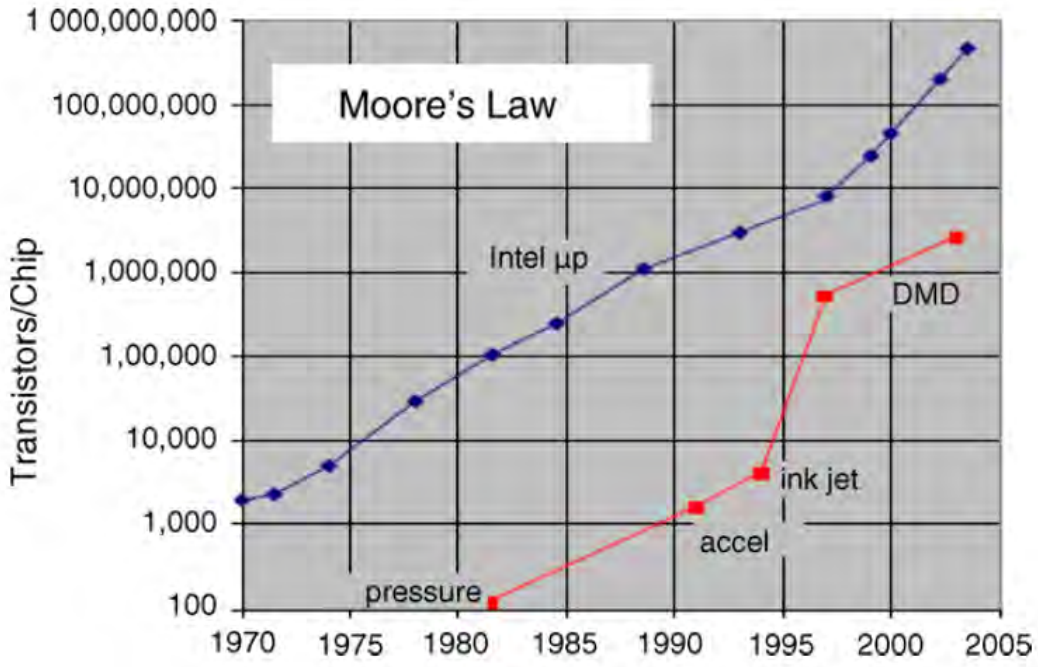

Figure 1.1 The evolution of transistor density in microelectronics and MEMS. The established trend for microelectronics is commonly referred to as Moore's Law (blue line). The emerging trends for MEMS devices (red line) suggest similar scaling. (Peterson et al, 2005).

al, 2005). It becomes apparent that the trends for MEMS devices are very much along the lines of the Moore's law for microelectronics miniaturization.

The success of microelectronics and MEMS/NEMS, as well as further development of key technologies involving miniaturized structures, depends primarily on the solution of key materials issues associated with the design, fabrication as well as reliability of the various components in these devices. In the case of microelectronics, large mechanical stresses, either 'intrinsic' i.e. due to growth/processing conditions, or 'extrinsic' due to external loading, are often present. Even in cases where such stresses do not degrade the functionality of the constituent material, they may result in premature failure due to the formation of voids or cracks. The effects of such large mechanical stresses are further exacerbated by the fact that thin films are often employed in a complex environment featuring interfaces with mechanically (or thermally) dissimilar materials. In applications involving either large mechanical loads or large deflection levels, the choice of a specific material is primarily dictated by its mechanical properties. Structural and moving parts in MEMS devices such as hinges for micro-mirrors and optical switches, as well as coatings on cutting tools, are examples of such applications. In many other applications, material selection for thin films is often dictated by their unique electrical, magnetic, optical or thermal properties. However, even in such applications, mechanical behavior of the constituent materials is not unimportant because of the high power densities often employed in end-user applications or due to the large mechanical stresses that arise from fabrication processes. Such large mechanical stresses

in thin films often affect their ability to perform their expected functions (electrical/thermal/optical/magnetic) due to the coupling between mechanical and functional properties. For example, abnormally high stresses may adversely affect the phase transformation in a shape memory alloy thin film and, thus, result in a loss of their functionality.

Therefore, our ability to model and increase device reliability and lifetime is contingent upon our ability to understand, and control, the mechanical behavior of the constituent materials at such small length scales. These factors serve as the technological driving force for the study of mechanical behavior of materials in miniaturized specimen, as the microelectronics and MEMS/NEMS industry moves towards new material systems and dimensions continue to shrink.

1.2 MOTIVATION: STUDY OF SIZE EFFECTS

A distinguishing characteristic of many such miniaturized components employed commonly in microelectronics, MEMS and NEMS is the use of materials with limiting dimensions far smaller than most bulk (or conventional) materials, as shown in Figure 1.2 (Prorok et al, 2006). While MEMS features foils/membranes with limiting dimensions in the range of a few *mm* to just a few μm, microelectronics, MEMS and NEMS can feature device sizes from just a couple of μm down to few nanometer range. In addition to the aforementioned technological benefits, the study of small-scale mechanical behavior also

serves an important scientific function. It has long been recognized that material response at such small length scales, common to most miniaturized structures, is quite different from bulk response. Such deviations from bulk mechanical properties are often, collectively, termed as '*size effects*'. While, in some instances, size effects can be explained through scaling of bulk properties to small length scales (Spearing et al, 2000), in most cases small-scale mechanical behavior has been shown to be sensitive to mechanisms that remain elusive (Arzt et al, 1998). For example, from the point of view of mechanical strength, most experimental studies have shown that thin films can sustain much higher stresses (sometime an order of magnitude higher) than similar bulk materials (Nix et al, 1989; Vinci et al, 1996; Espinosa et al, 2003; Xiang et al, 2005; Haque et al, 2003).

From a scientific point of view, our understanding of mechanical properties i.e. material response to deformation and the associated fundamental unit processes, taken together, is essentially couched in terms of different physical length scales and their interactions. In this context, the underlying physical mechanisms behind the observed size effects in miniaturized specimen have generally been attributed to the overlap between the microstructural and structural length scales of the constituent materials. The microstructural length scale is understood to encompass the relevant size parameters of the microstructure of the material, e.g. grain size, d_g, twin spacing etc., while the structural length scale is usually the limiting specimen dimension of miniaturized components, commonly thickness, t.

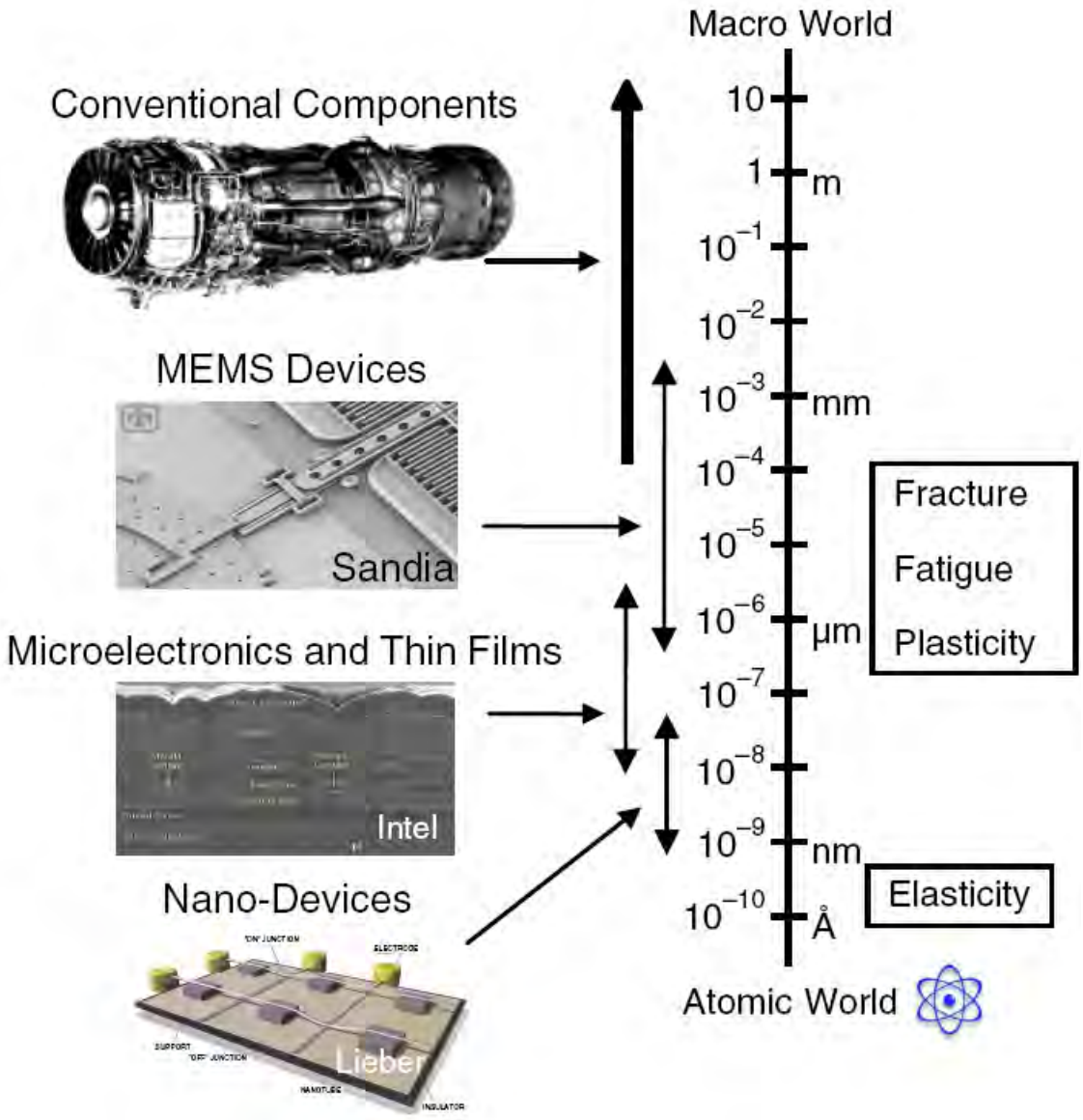

Figure 1.2 An illustration of length scale effects on the mechanical properties of materials. The characteristic length scales associated with specific deformation regimes i.e. plasticity, elasticity etc. are also shown alongside the typical structural and microstructural length scales (described in Sec. 1.2) in conventional components, MEMS, NEMS etc. (Prorok et al, 2006)

In addition to these length scales, the physical mechanisms responsible for a materials' response to deformation, whether elastic or plastic, involve certain characteristic length scales. For example, dislocation-mediated plastic deformation in metals, would feature the Burger's vector, dislocation mean free path, equilibrium dislocation loop diameter etc., as the characteristic length scale (Arzt et al, 1998). When the characteristic length scale of deformation process zone overlaps the geometric microstructure length scale (t, d_g, twin spacing etc.) very different macroscopic response arises due to the added microstructural constraints. As shown in Figure 1.2, most miniaturized structures feature dimensions, both structural and microstructural, of the same order as many of the characteristic length scales of plastic deformation. As a result, in addition to the microstructural constraint (also experienced in conventional structures), the physical mechanisms related to plastic deformation in miniaturized specimen start to 'feel' a dimensional constraint i.e. the presence of a free surface or an interface. To this effect, as a general experimental observation for miniaturized specimen, mechanical properties related to plastic deformation i.e. yield/flow stress, ductility etc., are often found to be related to, both, microstructural characteristic length scales (commonly d_g) as well as the specimen thickness (Arzt et al, 1998; Fleck et al, 1992; Evans et al, 1998; Nix et al, 1989; Espinosa et al, 2003; Espinosa et al, 2004; Xiang et al, 2006; Haque et al, 2003).

In essence, understanding and exploring the size effects landscape, especially with regards to plastic deformation, is important not just for the technological benefits of attaining better device reliability in microelectronics and MEMS/NEMS, but also to

expand our knowledge of the structure-property relationships in materials, a basic aim of materials science as well as engineering mechanics. This idea serves as the motivation for this study.

1.3 MATERIAL SYSTEM: COPPER

In the current study, Copper (Cu) was chosen as the model material system due to its increasing technological significance. Cu is slated to replace Aluminum as the new interconnect material in microelectronics industry due to its superior electrical as well as thermal properties. In the past, most interconnects in the microelectronics industry were made out of Al thin films. With continued miniaturization, and the need for high device current densities in interconnect lines, electro-migration was recognized to be a major failure mechanism. In this context, various studies predicted that the reliability and performance of Al, and its alloys, would soon reach practical limits (Clement et al, 1995; Havemann et al, 2001; Thompson et al, 1986).

In addition to these reliability/performance issues with Al, Figure 1.3 (NTRS, 1997) shows that with shrinking device sizes, resistance-capacitance (RC) delay in interconnects becomes the dominant factor, as compared to gate delay. Figure 1.3 also suggests that the total delay (gate + RC) – a measure of the attainable switching speed - can be minimized by reducing interconnect resistivity (from Al to Cu) and dielectric

permittivity (SiO_2 to low-κ). The combination of higher electrical/thermal conductivity of Cu and higher melting temperature (as compared to Al) – all of which increase the

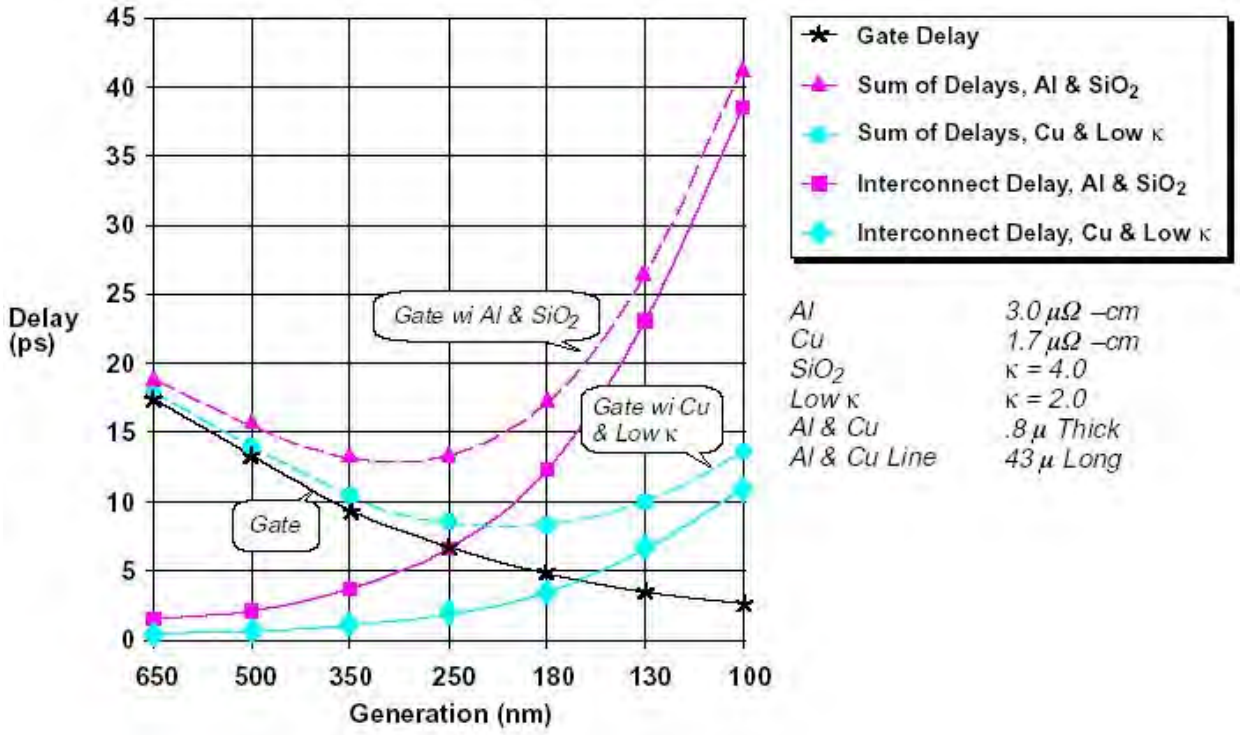

Figure 1.3 The effect of interconnect material on the RC delay. Reduction of thickness dominates gate delay. Transition from aluminum to copper based interconnects would significantly reduce the gate delay in ICs. (NTRS, 1997)

resistance to electromigration - make Cu a more attractive interconnect material, and therefore technologically more attractive, than Al (Thompson et al, 1986; NTRS, 1997; Clement et al, 1995; Havemann et al, 2001).

With regards to mechanical behavior, Cu also poses some significant challenges regarding device integration and reliability. For example, Young's Modulus of Cu is about 50% higher than that in Al. This implies that Cu interconnect lines, as well as the surrounding dielectric, would develop much higher stresses as a result of thermal mismatch and thermal cycling, compared to Al. Furthermore, Cu also has higher strength than Al. While on the one hand, high mechanical strength is beneficial from the performance/reliability point of view, on the other hand it can lead to far higher intrinsic residual stresses or promote cracking of the surrounding dielectrics (Tsui et al, 2005). Therefore, in order to utilize the full potential of Cu as an interconnect material, and to further improve the reliability of devices based on Cu-metallization, it is necessary to characterize and understand its mechanical behavior i.e. plastic deformation, fracture and fatigue.

1.4 OUTLINE OF THESIS

The goal of the current work is to extend our current understanding of size-dependent plastic deformation, as related to strength and ductility, of freestanding Cu films over a wide range of thicknesses and grain sizes. The films are produced with a

controlled microstructure such that the observed size effects, on the strength as well as ductility, can be attributed to the variation of the thickness and grain size alone. Particular emphasis is placed on the quantitative characterization of thickness and grain size effects on such properties independently of each other. Phenomenological relationships are also formulated, wherever possible, to address the thickness and grain size dependence of the observed strength. The underlying deformation mechanisms, and their sensitivity to the structural as well as microstructural length scales, are also explored through microscopic post-mortem structural investigations at the microstructural level. Specifically, the observed size effects on the strength are related to the measurements of total defect (e.g. dislocation) accumulation and storage, as a result of deformation, through residual electrical resistivity measurements (RERM). Also, the size effects on the observed ductility are understood through the quantitative characterization of the nucleation and evolution of deformation heterogeneities at the microstructural level.

This thesis is organized in six chapters as follows. Chapter 2 presents a review of literature on the mechanical properties of miniaturized specimen. Review of relevant experimental techniques and processes, as well as the current understanding of size effects on the mechanical properties are highlighted. The significance of studying size effects in freestanding films, as in this study, is discussed.

Chapter 3 presents the experimental measurements of the size effects on the observed strength (yield stress and flow stress) of freestanding Cu foil specimen with d_g

=10-45μm and t/d_g ratio of 0.5-5 across the thickness. The role of the free surface on the effective microstructural constraint is highlighted in this chapter. This chapter is based in part on a manuscript to be submitted to *Acta Materialia.*

Chapter 4 presents the measurement of thickness effects on the strength of free-standing electrodeposited films with grain sizes approaching the ultrafine grained regime i.e. ~O(1μm). Residual electrical resistivity measurements are employed to highlight the effect of grain size dependent deformation mechanisms on the nature and magnitude of the observed thickness effects. This chapter reveals the role of source starvation strengthening with reducing thickness at these length scales. This chapter is based on an *Applied Physics Letters* (Chauhan et al, 2008) manuscript as well as *Journal of Applied Physics* paper currently under preparation.

Chapter 5 is devoted to the observed thickness effects on the ductility of the freestanding specimen tested in this study. Surface roughness measurements are used as a novel tool to study the evolution and distribution of deformation heterogeneities (strain distribution) at the microstructural level. In addition to the effects of thickness, the role of average grain sizes is also discussed. This chapter is based in part on a manuscript to be submitted to *Acta Materialia.*

Chapter 6 summarizes the findings in this study and provides some ideas for future work.

1.5 REFERENCES

1. Petersen, K.E. (2005) "A new age in MEMS" *Dig. 13th Int. Conf. Solid-State Sens., Act. Microsys. (Transducers '05),* 1, 1
2. Ko, W.H. (2007) "Trends and frontiers of MEMS" *Sensors and Actuators*136, 62
3. Spearing, S.M. (2000) "Materials issues in micro-electromechanical systems (MEMS)" *Acta Mater.*, 48, 179
4. Prorok, B.C., Zhu, Y., Espinosa, H.D., Guo, Z., Bazant, Z., Zhao, Y. and Yakobson, B.I. (2006) "Micro and nano-mechanics", *Encyclopedia of Nanoscience and Nanotechnology,* Ed. By H.S. Nalwa
5. Nix, W.D. (1989) "Mechanical properties of thin films", *Metall.Trans.* A 20, 2217
6. Vinci, R.P. and Vlassak, J.J. (1996) "Mechanical behavior of thin films" *Ann. Rev. Mater. Sci.*, 26, 431
7. Espinosa, H.D., Prorok, B.C. and Peng, B. (2004) "Plasticity size effects in free-standing sub-micron polycrystalline FCC thin films subjected to pure tension", *J. Mech. Phys. Sol.*, 52, 667
8. Espinosa, H.D., Prorok, B.C. and Fisher, M. (2003) "A methodology for determining mechanical properties of free-standing thin films and MEMS materials", *J. Mech. Phys. Sol.*, 51
9. Xiang, Y. and Vlassak, J.J. (2006) "Bauschinger and size effects in thin film plasticity", *Acta Mater.* 54, 5449
9. Haque, M.A. and Saif, M.T.A (2003), "Strain gradient effects in nano-scale thin films", *Acta Mater.*, 51, 3053, 2003
10. Arzt, E. (1998) "Size effects in materials due to microstructural and dimensional constraints: A comparative review", *Acta Mater.*, 46, 16, 5611-5626

11. Fleck, N.A., Mueller, G.M., Ashby, A.F. and Hutchinson, J.W. (1994) “Strain gradient plasticity - theory and experiment” *Acta Metall.*, 42, 475

12. Stolken, J.S. and Evans, A.G (1998) “A Microbend test method for measuring the plasticity length scale” *Acta Mater.*, 46, No. 14, 5109

13. Clement, J.J. and Thompson, C.V. (1995) “Modeling electromigration-induced stress evolution confined metal lines”, *J. Appl. Phys.*, 78, 900

14. Havemann, R.H. and Hutchby, J.A. (2001) “High performance interconnects: An integration overview”, *Proc. IEEE* 89, 586

15. Thompson, C.V. and Cho, J. (1986) “A new electromigration testing technique for rapid statistical evaluation of interconnect technology” *IEEE Elec. Dev. Lett.* 7, 667

16. National Semiconductor Technology Roadmap (1997)

17. Tsui, T.Y., McKerrow, A.J. and Vlassak, J.J. (2005) “Constraint effects on thin film channel cracking behavior” *J. Mater. Res.*, 20, 9, 2266

18. Chauhan, S. and Bastawros, A.F. (2008) “Probing thickness-dependent dislocation storage in freestanding Cu films using residual electrical resistivity” *Appl. Phys. Lett.*, 93, 041901

CHAPTER 2. REVIEW OF LITERATURE

This chapter presents a brief literature review of the relevant experimental methods for mechanical characterization of miniaturized specimen as well as current understanding of the size effects on the mechanical properties of metallic films.

2.1 EXPERIMENTAL METHODS AND PROCESSES

2.1.1 Material preparation and processing

Miniaturized specimens typically have geometric dimensions of the same order as the microstructure material length scale. As a result of this overlap, the overall mechanical properties are influenced by both the microstructural features as well as the macroscopic geometric constraint. Given this inherent coupling between the microstructural and geometrical size parameters in miniaturized specimen, it is important to address the effect of each of these length scales independently as well their interdependence.

The most convenient way to achieve this goal is to use fabrication techniques that allow precise control of both dimensions; the microstructural size parameters (as defined by d_g, in the absence of other sub-structural features), and the specimen thickness. Since the mechanical properties of most metals are known to be very sensitive to their processing history, careful consideration to the choice of the fabrication process in such studies is important. In order to be able to extend the results from any experimental study on a given material system to similar components used in the industry, it is preferred to

utilize similar fabrication processes as those used for commercial purposes.

The choice of fabrication methods for producing miniaturized specimen is essentially dictated by the desired structural as well as microstructural size parameters. In case of thin foil specimen, with thickness ~O (*10-100μm*) and grain size ~O (*5-100μm*), bulk manufacturing processes, such as rolling, are commonly employed. However, for thin films, with thickness typically less than ~10μm or so, specialized deposition processes, such as vapor deposition, spin coating (for non metallic films) and electrodeposition need to be employed. While a detailed review of all of these fabrication/deposition processes is beyond the scope of this review, we briefly introduce several most commonly used techniques, relevant to this work, used to fabricate both foil type as well as thin film type specimen.

2.1.1.1 Foil and plate type specimen: Rolling

Rolling (Hosford et al, 2004) is a fabrication process in which metal, plastic, paper, glass, etc. is successively passed through a pair (or pairs) of rolls. With each such pass, the thickness of the deformed material is reduced. There are two types of rolling process, flat and profile rolling. In *flat rolling* the final shape of the product is either classed as *foil* (typically thickness less than 3 mm, also called "sheet") or plate (typically thickness more than 3 mm). In *profile rolling*, the final product may be a round rod or other shaped bar such as a structural section (beam, channel, joist etc). Rolling is also classified according to the temperature of the metal rolled. If the temperature of the metal

is above its recrystallization temperature then the process is termed as hot rolling, If the temperature of metal is below its recrystallization temperature the process is termed as cold rolling. Cold rolling typically leads to a highly textured microstructure with elongated grains. Furthermore, the large deformation that typically accompanies such a process leads to the creation of sub-structural features (like dislocation cells) of dimensions much smaller than the grain size itself. In order to reduce the influence of prior deformation history on the observed response and relieve the residual stresses, cold rolled specimens are often annealed prior to testing. Annealing typically leads to much weaker texture distribution (Janssen et al, 2006) and a stored defect content closer to virgin material (Hosford et al, 2004).

2.1.1.2 Thin film specimen: Sputtering and Electrodeposition

Sputtering (Madou et al, 2002) is a process in which the vapor of the source materials is formed through ionic impingement of a target. In sputter deposition, an evacuated chamber is filled with a sputtering gas, typically Ar. The gas is ionized by imposing a direct-current (DC) or radio-frequency (RF) voltage, which forms a plasma in the chamber. An imposed electrical field accelerates the Ar^{+} ions toward the target at high speed. The target atoms are dislodged when the energetic ions bombard the target surface. These atoms then travel through the gas phase and condense onto the substrate, leading to film growth. Sputtering is a versatile technique that can be applied to many crystalline and amorphous materials. Alloy thin films with highly precise compositions can be fabricated through co-sputtering. There are also some disadvantages. For example,

because the target atoms usually have a high kinetic energy when they arrive at the growth surface, the probability of defect nucleation and damage in sputtered films is generally higher than in evaporated films. The condensation of high energy atoms also causes the substrate temperature to increase; as a result, sputtered films can feature substantial residual stresses. The sputtering gas may also cause contamination by introducing impurity atoms in the films. Metal films sputtered at room temperature are typically polycrystalline, consisting of very fine grains. The microstructure is of course affected by many parameters such as substrate temperature, deposition rate, power, and working gas pressure, as a result precise control of the microstructure can be difficult. Sputtering is commonly employed in cases where uniform film thickness is the priority.

Electrodeposition (Dini et al, 1993), also called electroplating, is a process in which a metal is coated on a conductive surface through electrochemical reactions that are facilitated by an applied electrical potential. In this process, the surface to be coated is immersed into a solution of one or more metal salts. This surface needs to be conductive and forms the *cathode* of the electrical circuit. With an electrical current passing through the solution, the positive ions of the source metal are attracted to the cathode surface, where they are reduced, resulting in a coating of the source metal on that surface. Precise control over the microstructure of the deposited metal coating can be exercised either via controlling the current (galvanostatic electrodeposition), controlling the voltage (potentiostatic electrodeposition) (Dini et al, 1993). In addition to these electrical parameters, bath composition plays a major role in controlling the deposited film topology. Electroplating is a simple and economical process to deposit uniform coatings.

It has been used in many applications across a wide range of industries for more than a century. For example, copper conductor lines in printed circuit boards, chromium coatings on steel parts in automobiles, zinc coatings on galvanized steel, and decorative gold and silver coatings on jewelry and various consumer products are all realized by means of electroplating. Electrodeposition is also the method of choice for growing Cu coatings in advanced integrated circuits by the microelectronics industry, given its advantages of simplicity, safety, low cost, low deposition temperature, low resistivity, and high gap filling capacity in a dual-damascene process as compared to other metallization techniques.

Recently, pulsed electrodeposition (PED), in addition to conventional galvanostatic or potentiostatic electrodeposition has been employed as a fabrication route to prepare laboratory specimen to study size dependent mechanical properties (Lu et al, 2004; Natter et al, 1996). PED has proved to be a versatile and powerful technique for producing nano-structured materials with precisely controlled microstructural size parameters such as avg. grain size or twin spacing (Natter et al, Ebrahimi et al,). PED also yields specimen with very high purity, low porosity as well as high electrical conductivity at a wide range of thicknesses i.e. thin films samples with thickness ~ few μm to 3mm. As compared to potentiostatic or galvanostatic deposition techniques, PED features the application of either constant voltage (V_{peak}) or constant current (I_{peak}) square wave pulses with a certain duty cycle (τ) and time period (T). The use of these four

electrical parameters, in addition to the bath chemistry/composition, allows precise control of the microstructural size parameters.

2.1.2 Microstructural Characterization

For most metals, microstructure is usually understood to encompass the arrangement of individual crystallites (of equal or different phase constitution) and the associated crystalline defects such as dislocations, vacancies, impurities as well as surface and interfacial features (Arzt et al, 1998). Therefore the nature of the phases present, their topology (geometric distribution and interconnection) as well as their dispersion (described by relevant size parameters) constitutes the microstructure. Such microstructural characteristics can be affected by many factors, including materials class, deposition technique and deposition conditions, heat treatment, and deformation history. All other parameters of the microstructure being equal, its size parameters exert a strong influence on the observed mechanical properties at the macroscopic level (Arzt et al, 1998). Therefore, accurate mechanical characterization of metallic structures must include precise characterization of microstructural size parameters such as avg. grain size, avg. twin spacing etc.

2.1.3 Experimental Techniques

Mechanical testing of miniaturized specimen has long been recognized to be a challenging task (Sharpe et al, 2003). While a small, and often fragile, specimen is

difficult to handle and mount on testing frame, the amplitude of force/displacement to be measured is also quite small. Therefore, mechanical testing at such small length scales often requires the development of specialized experimental techniques. As a result of such difficulties, many specialized experimental techniques have been developed over the years for reliable mechanical characterization of miniaturized specimen.

Current experimental techniques can be classified according to the film configuration as layered configuration or freestanding configuration. Layered configuration essentially allows mechanical testing of specimen in a configuration, or mechanical environment, similar to that they are often employed in i.e. film-on-substrate systems. Since thin films are often employed on substrates, there is certainly merit in performing experiments on such systems. However, layered configuration suffers from an important drawback i.e. the mechanical properties of the test material are often coupled with many other extrinsic effects that arise due to the specific mechanical environment of the test specimen. For example, film on substrate systems often feature strain gradients in the thin films, and as a result, the clear interpretation of other size effects (e.g. microstructural of thickness effects) is not possible until the strain gradient effect is accounted for (Keller et al, 1997; Xiang et al, 2004, 2006). Indentation (Ma et al, 1995) and thermal cycling experiments (Keller et al, 1997; Venkataraman et al, 1994) are two examples of such techniques. Free standing configuration on the other hand allows clear identification of material properties without having to account for any other extrinsic effects (Espinosa et al, 2003; Haque et al, 2003). However, such a technique is quite

difficult to realize given the fragility of the specimen and, therefore, the obvious challenges in handling/testing them. Uniaxial tensile testing (Yu et al, 2000; Saif et al, 2003), micro-bend tests (Evans et al, 1998), bulge test (Xiang et al, 2005, 2006), torsion experiments (Fleck et al, 1994), membrane deflection experiments (Espinosa et al, 2003), pillar micro-compression (Greer et al, 2005, Uchic et al, 2004) etc. are all example of techniques where freestanding, or unconstrained specimen configurations are tested.

Experimental techniques can be also classified according to the nature of the imposed deformation field as those featuring homogenous deformation and those featuring non-homogeneous deformation (or strain gradients). In the homogenous deformation category, only those techniques that allow deformation either under homogenous tension or compression are included. These include uniaxial tensile testing (Yu et al, 2000; Haque et al, 2003), pillar micro-compression testing (Greer et al, 2005; Uchic et al, 2004) as well as the membrane deflection experiment (a modified form of tension test) (Espinosa et al, 2003, 2004). Besides these three testing methodologies, all the other loading techniques impose strain gradients.

2.2 SIZE EFFECTS ON PLASTIC DEFORMATION

One of the defining characteristics of miniaturized specimen i.e. thin film, foil or plate type specimen, is the length scale similarity of the thickness and grain size to many of the characteristic length scales of plasticity. As a result of this overlap between microstructural and structural length scales, prominent size effects are seen in such

specimen. Based on previous literature on the topic, this section presents a brief description of the different types of size effects. A more detailed discussion can be found in Arzt et al (1998).

2.2.1 Microstructural Size Effects

The dependence of yield/flow strength of a material on d_g has been the subject of various studies in literature. Generally, the observed grain size strengthening has been reported in terms of a Hall-Petch type relationship (Hall et al, 1951; Petch et al, 1953). The classical Hall-Petch relationship predicts the yield/flow stress as a linear function of the inverse of the square root of a specific microstructural size parameter. For pure polycrystalline metals, in case of yield stress i.e. stress at the initiation of macroscopic plasticity, d_g has been used in such a relationship. Similarly, for a highly twinned material, d_g is often replaced with avg. twin spacing. On the other hand, in case of flow stress, the microstructural size parameter is usually taken to be the avg. dislocation cell size (Hansen et al, 1983; Tabata et al, 1975).

The physical mechanisms responsible for such microstructure dependent strengthening were explained on the basis of dislocation pile-ups at the grain boundaries (Hall et al, 1951; Petch et al, 1953). Macroscopic initiation of plastic deformation (characterized by yield stress) or continued plastic flow (characterized by flow stress) requires initiation and transmission of slip across grain boundaries. The external stress causing plastic deformation must therefore not only account for the required resolved

shear stress on specific slip systems within each grain, but also account for the additional requirement for such transmission of slip across the grain boundaries. These grain boundaries require internal stress concentrations proportional to the grain diameters - a consequence of piled up dislocations near the grain boundary - from within the grain volume (Petch et al, 1953; Hall et al, 1951). Alternatively, Li et al (1963) showed that a relation similar to the Hall-Petch relation can be derived based on the assumption of forest hardening by the activation of grain boundary ledge dislocations.

While the Hall-Petch relation has been confirmed for a wide range of metals, there is clear experimental evidence that grain size strengthening breaks down for smaller grain sizes. To this effect, grain size softening according to an inverse Hall-Petch law was reported (Chokshi et al, 1989; Masumara et al, 1998; Arzt et al, 1998). For example, such deviation from Hall-Petch strengthening in Cu appears at a grain size in the range of 20-50 nm (Masumara et al, 1998; Cheng et al, 2003). However, for grain sizes much larger than this limiting value, the validity, and the exact form, for Hall-Petch relation is not clear for miniaturized specimens. To this effect, Janssen et al (2006) showed that for Al foil specimen, with grain sizes around ~ 100μm and just one grain across the thickness, the observed yield as well as flow stress was virtually grain size independent. On the other hand, for thin film specimen, in both film-on-substrate (Keller et al, 1997) as well as free-standing film systems (Xiang et al, 2005, 2006), the strength of the observed Hall-Petch strengthening (characterized by the slope on a Hall-Petch plot) was found to be larger than that observed in bulk specimen with similar grain sizes.

2.2.2 Grain Statistics Effects

Plastic flow of crystalline metals follows the maximum resolved shear stress and becomes highly dependent on the loading direction. The plastic response of a polycrystalline aggregate is thus affected by the number of grains involved as well as the size and texture distribution. As the number of grains within the specimen volume reduce with shrinking dimensions, such size and texture distributions can cause substantial experimental scatter (Armstrong et al, 1961; Kals et al, 2000; Janssen et al, 2006). The stronger and sharper the crystallographic texture, the lesser these variations will be (Janssen et al, 2006). On the other hand, for a bulk specimen, given the relatively large number of grains within the specimen volume, each material cross-section yields a good measure of the average properties that only scale with the average size as well as texture of the constituent crystallites.

2.2.3 Strain Gradient Effects

Structural elements subjected to non-uniform macroscopic deformation have shown the so-called *strain gradient effects*, especially at smaller length scales (Fleck et al, 1994; Evans et al, 1998, among many others). Considering the observed material response with macroscopic strain gradients in loading configurations such as bending (Evans et al, 1998), torsion (Fleck et al, 1994), indentation (Ma et al, 1995) or crack tip field (Bastawros, 2006), it has been proven that at such small length scales, non-homogenous deformation implies “smaller is stronger”. These strain gradient effects

essentially arise due to the imposed lattice curvature, which has to be accommodated by geometrically necessary dislocations (GND), in addition to the statistically stored dislocations (SSD). This dependence of the total dislocation density (GND + SSD) on the macroscopic strain gradients, which, in turn, are a function of the dimension of the specimen, yields size dependent mechanical response. Such higher order effects are, however, excluded in this study by applying homogeneous deformation to the specimen by means of uniaxial tension.

2.2.4 Thickness effects under macroscopically homogenous deformation

Under macroscopically homogeneous deformation, thickness dependent strength has been reported. For foil or plate-like specimen, with grain size and thickness an order of magnitude larger than those in thin film materials, various experimental studies (Pell-Walpole et al, 1953; Feltham et al, 1957; Miyazaki et al, 1979; Kals et al, 2000; Janssen et al, 2006) have clearly shown that with reducing thickness for a constant grain size i.e. with reducing number of grains across the thickness, yield/flow stress and the observed strain hardening reduce. Armstrong et al (1961) attributed this thickness dependent weakening to an orientation effect i.e. with reducing the number of grains across the thickness, the Taylor-type (Taylor et al, 1934, 1938, 1956; Kocks et al, 1958) orientation constraint is greatly diminished as a result of the reduced microstructural constraint. Furthermore, with reducing number of grains across the thickness, the number of grain boundaries within an average specimen cross-section also reduces. As a result, the external loading has to satisfy less stringent Taylor type orientation conditions (compared

to bulk grains) and lesser number of grain boundary related stress concentrations. It was hypothesized in this work that a multicrystalline specimen, a specimen with just one grain across the thickness, would yield grain size independent behavior. The experimental results of Janssen et al (2006), however, show that Hall-Petch type grain size strengthening, albeit much weaker than the bulk case, may still exist for the multicrystalline case. However, due to lack of data in Janssen et al (2006), no quantitative conclusions were drawn as to the exact form of this grain size dependence.

In case of thin films, with thickness and grain size in the range of few microns, thickness effects in the absence of strain gradients have only been observed unambiguously by Espinosa et al (2003, 2004) in Au, Cu as well as Al thin films. These experiments utilized uniaxial tensile tests on freestanding films with varying thickness for a constant grain size of ~ 200nm. For all three materials, it was shown that smaller thickness yielded a higher yield stress as well as strain hardening. These origin of these thickness effects was interpreted based on the hypothesis that at such small length scales plasticity is source controlled i.e. with reducing thickness, the available dislocation sources reduce and as a result thickness dependent strengthening commences.

Various other studies on freestanding thin films featured films in the submicron to micron range. For example, Xiang et al (2005, 2006) tested Cu films with thickness of 0.3-4.5μm and grain size of 0.3-1.5 μm. Bravman et al (2004) tested Al films with thickness of 2-12μm and grain size of 1-4μm. These studies attributed the observed size

effects on yield stress to the microstructural length scale alone. A common feature of all these studies, in contrast with the thin films tested by Espinosa et al (2003, 2004), was that the grain size was changed along with the film thickness. As a result, in these cases, similar to film-on-substrate systems after accounting for the imposed gradient by the substrate, the strength of the observed grain size strengthening was higher than that observed for bulk material with the same grain sizes. This anomaly could possibly imply that there are thickness effects, in addition to the microstructural effects, even at these larger length scales.

Therefore, while previous literature suggests fairly consistent trends for thickness effects in constrained film systems i.e. reducing thickness leads to increasing strength, the ambiguous trends for thickness effects in freestanding films merits further study. It is this specific scenario i.e. freestanding polycrystalline films under macroscopically homogenous deformation, which is the focus of this study.

2.3 REFERENCES

1. Hosford, W.F. (2004) “Mechanical behavior of materials”, *Cambridge University Press*
2. Madou, M. J. (2002) “Fundamentals of microfabrication: the science of miniaturization” *CRC Press Ltd.*
3. Dini, J.W. (1993) “Electrodeposition”, *Noyes Publications*, NJ, USA

4. Lu, L., Shen, Y., Chen, X., Qian, L. and Lu, K. (2004) “Ultrahigh strength and high electrical conductivity in Cu”, *Science,* 304, 422
5. Natter, H. and Hempelmann, R. (1996) “Nanocrystalline Copper by pulsed-electrodeposition: influence of organic additives, bath temperature and pH” *J. Phys. Chem.*, 100, 19525
6. Sharpe, W. N. (2003) “Tensile testing at the micrometer scale” opportunities in experimental mechanics”, William M. Murray lecture, *Exp. Mech.,* 43, 3, 228
7. Keller, R.R., Phelps, J.M. and Read, D.T. (1996) “Tensile and fracture behavior of free-standing copper films” *Mater. Sci. Eng. A*, 214, 42
8. Arzt, E. (1998) “Size effects in materials due to microstructural and dimensional constraints: A comparative review”, *Acta Mater.* , 46(16), 5611-5626
9. Xiang, Y., Tsui, T. and Vlassak, J.J. (2006) “Mechanical properties of free-standing electroplated Cu thin films”, *J. Mater. Res.*, 21, 6
10. Xiang, Y., Vlassak, J.J., Perez-Prado, M.T., Tsui, T.Y. and McKerrow, A. (2004) “The effects of passivation layer and film thickness on the mechanical behavior of freestanding electroplated Cu thin films with constant microstructure” Mat. Res. Soc. Symp. Proc., 795, U11.37.1
11. Xiang, Y. and Vlassak, J. J. (2006) “Bauschinger and size effects in thin film plasticity” *Acta Mater.,* 54, 5449-5460
12. Ma, Q. and Clarke, D.R. (1995) “Size dependent hardness of silver single crystals” *J. Mater. Res.* 10, 853
13. Venkataraman, R. and Bravman, J. C. (1994) “Separation of film thickness and grain-boundary strengthening effects in freestanding Al thin films on Si” *J. Mater. Res.*, 7, 2040

14. Yu, D.Y.W and Spaepen, F. (2004) “The yield strength of thin copper films on Kapton”, *J. App. Phys.* , 95(6), 2991
15. Espinosa, H.D., Prorok, B.C. and Fisher, M. (2003) “A methodology for determining mechanical properties of free-standing thin films and MEMS materials”, *J. Mech. Phys. Solids.*, 51
16. Espinosa, H.D., Prorok, B.C. and Peng, B. (2004) “Plasticity size effects in free-standing sub-micron polycrystalline FCC thin films subjected to pure tension”, *J. Mech. Phys. Solids*, 52, 667
17. Haque, M.A. and Saif, M.T.A (2003) “Strain gradient effects in nano-scale thin films”, *Acta Mater.*, 51, 3053
18. Stolken, J.S. and Evans, A.G (1998) “A Microbend test method for measuring the plasticity length scale” *Acta Mater.* 46(14), 5109
19. Fleck, N.A., Mueller, G.M., Ashby, A.F. and Hutchinson, J.W. (1994) “Strain gradient plasticity theory and experiment” *Acta Metall.*, 42, 475
20. Greer, J. R., Oliver, W. C. and Nix, W. D. (2005) “Size dependence of mechanical properties of gold at the micron scale in the absence of strain gradients” *Acta Mater.* 53(6), 1821
21. Uchic, M. D., Dimiduk, D. M., Florando, J. N. and Nix, W. D. “Sample dimensions influence strength and plasticity” *Science* 305, 986
22. Hall, E.O (1951) “The deformation and aging of mild steel”, *Proc. R. Soc. Lond.* B 64, 474
23. Petch, N.J. (1953) “The cleavage strength of polycrystals”, *J. Iron Steel Inst.* 174, 25
24. Armstrong, R., Codd, I., Douthwaite, R.M. and Petch, N.J. (1961) “Plastic deformation of polycrystalline aggregates” *Phil. Mag.* 7, 45

25. Masumara, R.A., Hazzledine, P.M. and Pande, C.S. (1998) “Yield stress of fine grained materials” *Acta Mater.* 46(13), 4527
26. Chokshi, A.H., Rosen, A., Karch, J. and Gleiter, H. (1989) “On the validity of Hall-Petch relationship in nanocrystalline materials” *Scripta Metall.* 23, 1679-1684
27. Li, J.C. (1963) *Trans. Soc. Petro. Eng. Am. Inst. Min. Metall. Pet. Eng. ,* 227, 239
28. Tabata, T., Takagi, K., and Fujita, H. (1975) “The effect of grain size and deformation sub-structure on mechanical properties of polycrystalline Copper and Cu-Al alloys” *Trans. J I M,* 16, 569
29. Cheng, S., Spencer, J.A., Milligan, W.W. (2003) “Strength and tension/compression asymmetry in nano-structured and ultrafine-grain materials” *Acta Mater., 51,* 4505
30. Janssen, P.J.M, Keijser, Th. H., and Geers, M.G.D (2006) “An experimental assessment of grain size effects in uniaxial straining of thin Al sheets with a few grains across the thickness” *Mat. Sci. Eng. A* 419, 238
31. Miyazaki, S., Fujita, H. and Hiraoka, H. (1979) “Effects of specimen size on the flow stress of rod specimen of polycrystalline Cu-Al alloy” *Scripta Metall.* 13, 447
32. Armstrong, R. W. (1961) “On size effects in polycrystalline plasticity”, *J. Mech. Phys. Solids,* 9, 196
33. Kals, R.T.A and Eckstein, R. (2000) “Miniaturization in sheet metal working” *J. Mat. Proc. Tech.* 103, 95
34. Fleischer, R. L. and Hosford, W. F. Jr. (1961), *Trans. TMS-AIME,* 221, 244
35. Taylor, G. I. (1934) “The mechanism of plastic deformation of crystals” *Proc. Roy. Soc.* A 145, 362, 388
36. Taylor, G. I. (1938) “Plastic strain in metals” *J. Inst. Met.*, 62, 307
37. Taylor, G. I. (1956), “Deformation and Flow of Solids”, *Springer,* Berlin
38. Kocks, U.F. (1958), “Polyslip in Polycrystals”, *Acta Metall.,* 6, 85

39. Lee, H.J., Zhang, P. and Bravman, J.C., (2003) “Tensile failure by grain thinning in micromachined Aluminum thin films” *J Appl. Phys.*, 93(3), 1443

CHAPTER 3: THE EFECT OF MICROSTRUCTURAL CONSTRAINT ON THE FLOW STRESS OF FREE STANDING Cu FOIL SPECIMEN

3.1 ABSTRACT

This chapter presents an experimental assessment of the size effects on the yield stress as well as flow stress in thin Cu sheet metal with few grains across the thickness under uniaxial tensile deformation. The experiments reveal size effects in scenarios where the film thickness, t, representing the geometric length scale, is of the same order as the average grain size, d_g, representing the microstructural length. The resulting overlap is characterized by $\lambda=t/d_g$. The experiments reveal two distinct regimes of behavior based on λ. For $\lambda < 1$, a polycrystalline film with about one grain across the thickness, a weakening effect is observed. The grain exposure to free surfaces reduces its post hardening characteristics. As a result, the flow stresses in this regime show much weaker thickness and grain size dependence. A unique Hall-Petch type grain size effect is identified in this regime. For $\lambda > 1$, a polycrystalline film with many grains across the thickness, a strengthening effect is observed. The grain size reduction would reduce the volume of the film exposed to the free-surface. As a result, relatively stronger grain size effects reappear. There was a strong coupling between thickness and grain size effects. A modified Hall-Petch relation is proposed to account for the observed thickness dependence strengthening.

3.2 INTRODUCTION

Most size effects observed in bulk materials on mechanical properties related to plastic deformation e.g. yield strength or flow stress at a given plastic strain, are an outcome of the interaction between some intrinsic characteristic length scale of plasticity and a microstructural size parameter, commonly grain size (Arzt et al, 1998). In the case of miniaturized metallic structures, the physical mechanisms related to plasticity are also influenced by a dimensional or structural constraint (usually a limiting specimen dimension), in addition to the effects of the microstructure. A defining characteristic of many such components is the fact that the constituent materials often contain just a few grains across the limiting specimen dimension. As a result of this overlap between the structural and microstructural length scales, our understanding of many known bulk phenomenon often fails to explain the resulting mechanical behavior in miniaturized specimen.

One such example of a well characterized bulk phenomenon is the effect of grain refinement on the strengthening of bulk metals i.e. classical Hall-Petch (HP) relation (Hall et al, 1951; Petch et al, 1953; Armstrong et al, 1961; Chokshi et al, 1989; Sanders et al, 1997; Masumara et al, 1998). The HP relation predicts a linear relationship between the yield/flow stress (defined at a given macroscopic strain) with the inverse of the square root of the grain size. This effect of grain size on the yield stress or flow stress has generally been explained by a dislocation pile-up model wherein the dislocations, emitted

as a consequence of plastic deformation, are obstructed by the grain boundaries. The resulting stress concentration -a function of the grain size- would lead to the observed size effect (Hall et al, 1951; Petch et al, 1953; Armstrong et al, 1961). Alternatively, Li et al (1963) showed that HP-type dependence can also be derived based on the assumption of forest hardening by the activation of grain boundary ledge dislocations. Notwithstanding these alternative interpretations of the origin of microstructural strengthening, strong empirical evidence in literature confirms the existence of a HP-type relation for a wide range of polycrystalline materials (Masumara et al, 1998). There is clear experimental evidence that the bulk HP relation cannot be extended to very small grain sizes (~ 50 nm or less) (Chokshi et al, 1989; Arzt et al, 1998; Sanders et al, 1997; Masumara et al, 1998). This apparent physical limitation on the validity of conventional HP behavior was attributed to the relative scale of dislocation curvature and grain size. The 'conventional' grain size strengthening can be only expected for large enough grain size to encompass at least one dislocation loop (Arzt et al, 1998). However, the validity limit of the HP-relation is obscured when the geometric length scale of the structure approaches the grain size dimensions. The additional effect is experienced in many applications such as thin films on a substrate (Yu et al, 2004; Keller et al, 1998), or free-standing thin films (Lee et al, 2004; Nicola et al, 2006; Miyazaki et al, 1979; Janssen et al, 2006; Fleischer et al, 1961; Armstrong et al, 1961; Michel et al, 2003; Kals et al, 2000; Raulea et al, 2001; Weiss et al, 2002).

This work focuses on the role of free-standing film thickness on the macroscopic film strength for a range of d_g = 11-45 μm, t= 12.5-100 μm and range of λ=1-5. For foil like specimens, it is found that HP relation would hold *only* for λ>5-15 (Miyazaki et al, 1979; Armstrong et al, 1961). For λ<15, the observed yield/flow stress has been shown to be lower than that predicted for bulk material for similar d_g (Miyazaki et al, 1961; Kals et al, 2000; Michel et al, 2003; Raulea et al, 2001; Janssen et al, 2006) Furthermore, substantial weakening (reducing yield/flow stress) has been reported with reducing thickness (or no. of grains across the thickness) for a given d_g (Miyazaki et al, 1979; Kals et al, 2000).

While a number of experimental studies have confirmed this general trend i.e. reducing yield/flow stress with reducing thickness (Armstrong et al, 1961; Miyazaki et al, 1979; Kals et al, 2000; Janssen et al, 2006) some ambiguities still remain. With regards to the underlying mechanism itself, it was hypothesized that this weakening arises due to the reduction in microstructural constraint on individual grains within the specimen cross-section (Armstrong et al, 1961; Miyazaki et al, 1979). Thus λ is considered to dictate the observed size effects (Miyazaki et al, 1979; Janssen et al, 2006). It is understood that a specimen with just a few grains across the thickness, say λ ≤ 5-15 (Miyazaki et al, 1979), can be considered to be somewhere between a single crystal and a true polycrystal (Armstrong et al, 1961), in the Taylor sense (Taylor et al, 1934; Taylor et al, 1938; Taylor et al, 1958). In the limiting scenario of a multicrystalline specimen (Armstrong et al, 1961), a specimen with just one grain across the thickness, the overall behavior was

thus suggested to be representative of a single crystal undergoing single slip, notwithstanding the grain size (Armstrong et al, 1961). To this effect, the observed flow stress for a multicrystalline specimen would be related to the single crystal shear strength by an orientation factor, *m*, of 2 i.e. analogous to a 'bamboo' structure with at least one grain of appropriate orientation. It was also assumed that grain boundaries would contribute little of their own strength in this regime and as a result the yield/flow stress is expected to be independent of the grain size (Armstrong et al, 1961).

With increasing number of grains across the thickness, the requirements of internal stress concentrations at the grain boundaries for plastic flow must be satisfied, in addition to the orientation conditions as described by Taylor et al (1934, 1938, 1956) and modified by Kocks et al (1958). Therefore, the grains within the specimen interior take on a typical polycrystalline character and the flow properties of the intragranular regions in the polycrystal must now be compared with the flow properties of a single crystal under multi-slip conditions, as opposed to single slip for the multicrystalline case. A schematic representation of this hypothesis, from Armstrong et al (1961), is shown in Figure 3.1 (a). For small specimen cross-section, the flow stress is grain size independent and related to single crystal shear strength (τ_{CRSS}) by a factor of 2. With increasing number of grains across the thickness, the flow stress increases as more grains get involved and the orientation factor increases from 2 towards the Taylor value of 3.1. Also, additional contribution from grain boundaries ($k\, l^{-1/2}$) appears. '*l*' here represents the microstructural length scale (or average grain size) and τ_R is the critical stress

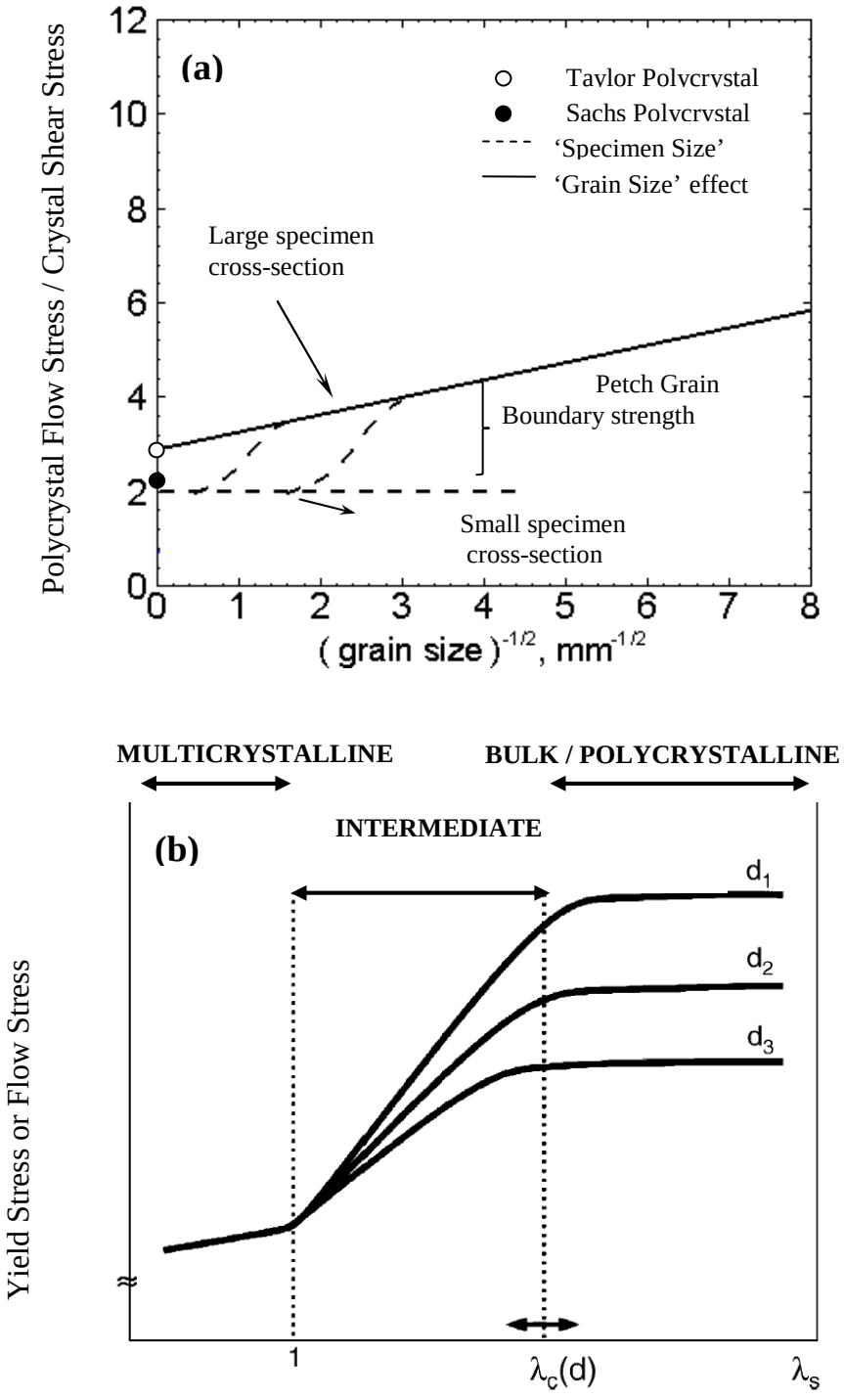

Figure 3.1 (a) Specimen size effects on the observed microstructural strengthening in polycrystalline FCC materials. (Armstrong et al, 1961). **(b)** Schematic representation of the variation of yield stress (or flow stress) with varying number of grains across the thickness (λ) (Janssen et al, 2006).

required for dislocation slip in the grain interior. The following equation shows these bounds

$$2\,\tau_{CRSS} \;\le\; \sigma_Y \;\le\; m\left(\tau_R + k\,l^{-1/2}\right) \qquad (3.1)$$

While the existence of the upper bound i.e. Bulk HP-type grain size strengthening has been confirmed and well characterized, there is still ambiguity with regards to the lower bound. Unfortunately, the measurement of yield/flow stresses to confirm the lower bound i.e. in a multicrystalline specimen with just one grain across the thickness, usually suffers from quite substantial experimental scatter due to uncontrolled grain orientation variation. Despite these difficulties, various experimental studies have been performed on specimen with $\lambda \leq 1$ (Stolken et al, 1998; Janssen et al, 2006; Weiss et al, 2002). While all of these studies showed deviation from bulk behavior, quantitative conclusions were not drawn due to limited data. Janssen et al (2006) however suggested that a separate HP-type grain size strengthening, albeit much weaker than the bulk case, might exist as opposed to the grain size independent behavior predicted by Eq. (3.1) from Armstrong et al (1961). The tensile test data presented in Stolken et al (1998) for Ni foils with d_g = 31-71 µm, t= 12.5-50 µm and $\lambda \sim$ 0.4-0.7 also indicates clear size effects for the multicrystalline case. However, tension test results for Cu foils with thickness between 50-250µm in Weiss et al (2002) imply nearly grain size independent behavior for $\lambda \sim$ 1-5. Therefore, the existence of a distinct lower bound behavior for multicrystalline specimen, and its exact form, merits further study and quantification.

At the other end of the spectrum, for large λ approaching true polycrystalline or bulk behavior, Miyazaki et al (1979) studied Cu, Cu-13% Al, Al and Fe specimens in uniaxial tension with λ=2-50 to explore the transition to full polycrystalline behavior. Their results showed that for a given d_g, bulk strength is attained for a λ_{cr} ~5-15. Larger grains approached bulk behavior with just about 5 grains across the thickness, while smaller grain sizes were found to be far more sensitive to thickness effects with λ_{cr} closer to 15. While Miyazaki et al (1979) showed the deviation from bulk response with reducing λ and formulated a phenomenological relationship - based on thickness effects on the effective microstructural constraint - to describe the observed deviation from the upper bound, due to lack of data for the lower bound regime ($\lambda \leq 1$) they simply extrapolated the stresses to $\lambda = 0$. Their conclusions therefore, and the proposed phenomenological model, are only applicable for $\lambda > 1$ and do not encompass the limiting multicrystalline behavior.

Janssen et al (2006) presented a schematic relationship (Figure 3.1(b)) based on their data for $\lambda < 1$ and the observed trends in Miyazaki et al (1979), describing the entire range of size effects incorporating multicrystalline behavior for $\lambda \leq 1$, a transitional regime ($1 \leq \lambda \leq \lambda_{cr}$) featuring prominent, and coupled, thickness and grain size effects and finally the attainment of thickness independent polycrystalline or bulk behavior for specimen with $\lambda \geq \lambda_{cr}$. In contrast to Figure 3.(a), Figure 3.1(b) describes multicrystalline behavior as featuring a certain size dependence, albeit much weaker than the intermediate and bulk case. The aim of the current study is to address, quantitatively, the lower bound

or multicrystalline behavior as well as the apparent coupling between the thickness and grain size effects in the transitional regime. Specifically, the possibility of a phenomenological relationship, encompassing the two limiting regimes of behavior as well as the transitional regime, will be explored.

Thin Cu foils with thickness, t=12.5-100μm, of the same order as the grain size d_g=11–45μm, giving rise to λ= 0.6-5, are tested under uniaxial tension. A carefully chosen range of annealing parameters (temperature and time) were employed in order to obtain the same average grain size for different thicknesses to assess the thickness effects and, at the same time, also obtain the same thickness for multiple grain sizes to ascertain the effect of grain refinement independently of the thickness effect. For all thickness-grain size combinations in the current study, the predominant texture was almost the same (verified by orientation imaging method, OIM). Therefore, any variation in the observed mechanical properties can be attributed to the appropriate length scales i.e. thickness and avg. grain size.

The details of the work are given in the following order. Section 3.3 presents the relevant details of the experimental methods and processes employed in this study. Section 3.4 presents the obtained experimental results from the microstructural characterization as well mechanical testing. Both thickness and grain size effects are studied separately and the inherent coupling between the two is elucidated. In Section 3.5, following a discussion of the underlying physical mechanisms, the rational for a

phenomenological relationship describing the entire range of size effects is presented and the results of the model are compared with the experimental results obtained in this study.

3.3 EXPERIMENTAL PROTOCOL

3.3.1 Material

A commercial high purity (4N5 – 99.995%) rolled copper foils from ESPI-materials are utilized in this work. The films showed prominent texture in the as-received state. Dog-bone tensile specimens were cut using a stamping technique from the as-received sheets. The gauge length was carefully aligned to be parallel to the rolling direction. The shaped specimens are heat treated to varying temperature to control the film grain size, as described in Sec. 3.4.1. The tensile specimen was designed with a gauge length of 5 mm and width of 1 mm.

3.3.2 Experimental Methodology

In order to exclude strain-gradient size effects from the current analysis, uniaxial tensile testing was employed as the experimental method. This methodology has the advantage of yielding a uniform stress and strain field in the test specimen and, therefore, simpler data analysis without recourse to any assumptions. The tensile tests were performed at room temperature using an Instron 8862 machine with a servo-controller

under displacement control. In order to facilitate tensile testing of sub-sized specimen, an auxiliary test fixture was employed. The text fixture, along with the tensile specimen is shown schematically in Figure 3.2. The design of the test fixture was motivated by the ease of specimen handling while loading for testing as well as alignment considerations.

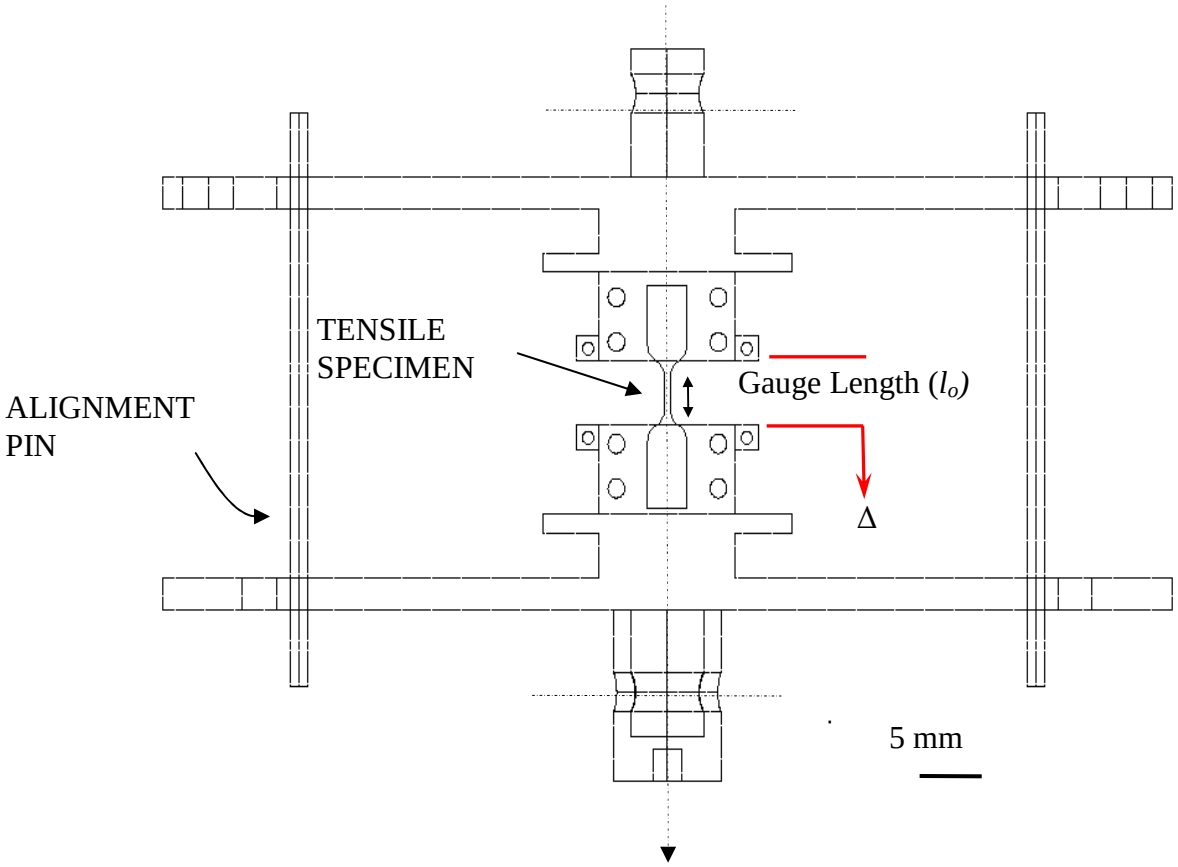

Figure 3.2 Auxiliary test fixture used in the tension testing set-up. Δ is the machine crosshead displacement.

Testing sub-sized specimen, given the fragility of the specimen as well as the vertical loading axis of most mid-sized tension testing frames, can be a challenging task with regards to specimen gripping, specimen handling during loading and unloading as well as specimen alignment within the testing frame. The tensile specimen, in this study, was first placed in its marked position in the grip section on the test fixture and held in place using frictional force. The specimen was aligned with the loading axis of the test fixture under a low magnification microscope. A special holding frame was designed to facilitate the mounting and dismounting of the fixture-specimen assembly in the tensile frame without causing any deformation in the specimen. The test fixture–tensile specimen assembly, held within the holding frame, using secure but easily detachable clips, was then moved to the Instron machine and held in place using pin-connections. The test fixture and its grip section were so designed that the tensile specimen would be accurately aligned with the loading axis of the machine. Two vertical pins were also incorporated in the test fixture to aid in alignment, as shown in Fig 3.2. The holding frame was removed prior to actual loading.

All experiments were performed at a nominal displacement rate of 0.2 µm/s and at ambient temperature. The load was measured using a 300 N load cell (AM Cells Inc.) and a non-contact capacitive displacement gauge (Lion Precision Inc.), with sub-micron resolution (~70nm) and full-scale range of 2mm, was used for displacement measurement. In order to preclude metrology errors, specimen thickness was measured using SEM and all other pertinent specimen dimensions i.e. gauge width and gauge

length, were measured using an optical microscope to within +5 µm. The true stresses were found from the measured force assuming volume conservation. The strains were calculated based on the initial gauge length and the imposed crosshead displacement. A finite element based calibration, based on the chosen specimen geometry, was used to determine the uniform average strain over the gauge length of the specimen from the crosshead displacement value and the initial gauge length (Appendix B). This average strain value was further confirmed with the strain distribution in the gauge section of the specimen obtained using digital image correlation. A detailed description of the methodology is presented in Appendix B.

3.4 EXPERIMENTAL RESULTS

3.4.1 Microstructural analysis

Table 3.1 summarizes the results of the microstructural analysis. Four thicknesses of the Cu foils were tested i.e. 12.5µm, 25µm, 50µm and 100µm. Each thickness was annealed at three temperatures (400 °C, 500 °C and 600 °C) for 2 hrs each to obtain three different average grain sizes. The post-annealing microstructure comprised of approximately equiaxed grains. The average grain size was calculated as per ASTM E112. The heat-treatment temperature and time was chosen so that the same set of material can be organized into two distinct groups. Group A, where for each thickness 3 different grain sizes are obtained, is referred to as the “grain size samples”. This group is

GROUP A – Grain Size Samples

t (μm)	d (μm)	λ	α	Φ
100	22 (3.4)	4.55	0.46	0.22
	27 (3.14)	3.70	0.56	0.27
	40 (5.6)	2.50	0.82	0.4
50	19 (2.2)	2.63	0.76912	0.38
	28 (4.26)	1.79	1.11328	0.56
	45 (7.7)	1.11	1.728	0.9
25	14 (1.3)	1.79	1.11664	0.56
	20 (2)	1.25	1.576	0.8
	26 (2.8)	0.96	2.02384	1.04
12.5	11 (1.4)	1.14	1.74328	0.88
	14 (2.1)	0.89	2.20528	1.12
	20 (2)	0.63	3.112	1.6

GROUP B – Thickness Samples

d (μm)	t (μm)
14	25
	12.5
20	100
	50
	25
	12.5
27	100
	50
	25
40	100
	50

Table 3.1 Results of microstructural analysis of the rolled Cu foils.

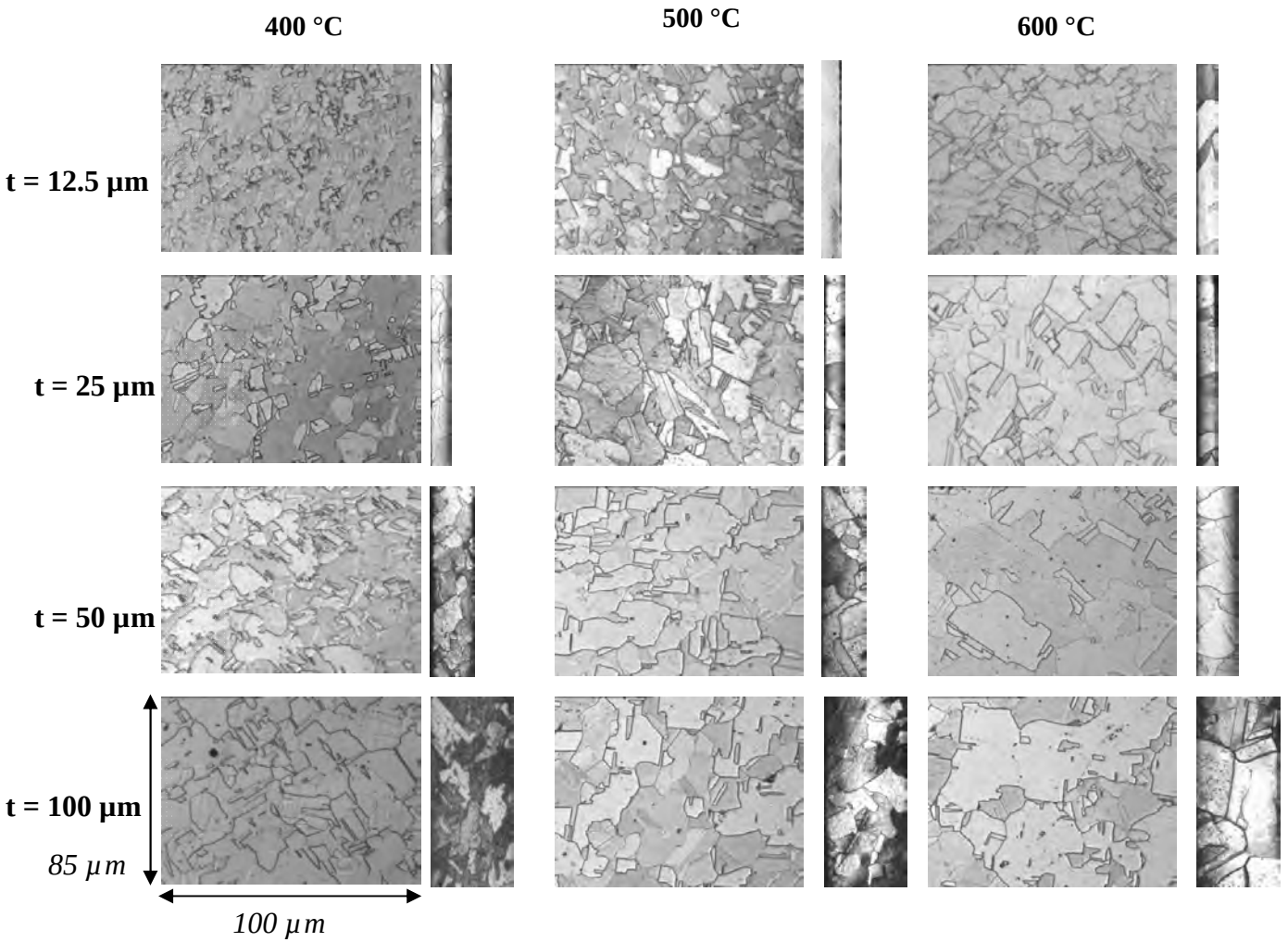

Figure 3.3 Optical images of the specimen surface as well as specimen cross-section (normal to tensile axis) showing the microstructure. The grains are approximately equiaxed and λ (Table 3.1) is a good measure of the avg. no. of grains across the thickness.

used to evaluate the effect of average grain size on the observed mechanical response for each thickness. Group B, the thickness samples, involves five distinct groups of grain sizes i.e. 11μm, 14μm, 20μm, 27μm, and 40μm. Only one thickness i.e. 12.5μm was available for the 11μm grain size. Two thicknesses are available for the 14μm and 40μm grain size while for the 20μm and 27μm grain sizes there are 4 and 3 thicknesses respectively. This group is used to study the effect of thickness on the mechanical properties for a given grain size. Therefore, the choice of heat-treatment allows for the separate analysis of both, grain size and thickness, effects as well as any interdependence or coupling that may exist between them. For equiaxed grains, the thickness to grain size ratio (λ) represents the average no. of grains across the thickness. Table 3.1 also shows the volume fraction of the grains at the free surface, α_{sg} (Kals et al, 2000), along with a phenomenological parameter, Φ, calculated as the inverse of λ. The significance of Φ is discussed in Sec. 3.5.2. Figure 3.3 shows the optical images of the microstructure for each thickness-grain size combination. In addition to the surface grain size window for each case, $85\ \mu m \times 100\ \mu m$, the optical image of the cross-sectional area normal to the tensile direction is also shown. Given the equiaxed grains, the observed number of grains across the thickness in the images validates the interpretation of the λ value as the average no. of grains across the thickness, as long as $\lambda \geq 1$. However, for cases with $\lambda < 1$, λ denotes the aspect ratio of the grains i.e. thickness of the grains relative to their in-plane expanse.

3.4.2 Mechanical response

Five samples for each case i.e. thickness-grain size combination, were tested in this work. For the purpose of quantitative comparison, the yield stress (0.2% strain offset) as well as the flow stress (10% strain) is averaged over five runs for each thickness-grain size combination. For the purpose of showing qualitative differences, representative stress-strain curves are compared for different thickness-grain size values.

3.4.2.1 Effect of Grain Size

Figure 3.4 shows the typical true stress-log strain curves obtained for the each film thickness and three different grain sizes each (Group A). Qualitatively, three salient observations can be made on the basis of these curves. Firstly, the stress at a particular strain level reduces with increasing grain size for a given thickness (or with reducing no. of grains across the thickness). Also, the observed strain hardening reduces with increasing grain size for a given thickness. Therefore, increasing grain size for a fixed thickness results in weakening. Finally, this weakening effect on the yield/flow stress as well as the strain hardening tends to saturate for the two larger grain sizes for the 12.5 µm thick specimen, both featuring just one grain across the thickness with avg. grain aspect ratios between 0.6 – 0.9.

These trends are further elucidated by a HP type analysis of the yield and flow stress (at 10% strain) as shown in Figure 3.5. Qualitatively similar trends are seen for both yield as well as flow stress. The corresponding fit (prediction) for bulk specimen is also shown (Hansen et al, 1983). For all the tested thicknesses, bulk Hall-Petch relation overestimates the yield/flow stress i.e. the obtained stresses for each thickness are lesser the thickness (λ), either with reducing thickness for a constant grain size or increasing grain size for a constant thickness, results in a strong weakening effect. These experimental trends further show that grain size effect and thickness effects are coupled i.e. unlike the bulk case, a unique relationship accounting for the microstructural contribution to the overall yield or flow stress for the entire set of data cannot be identified. These observations are largely in agreement with Janssen et al (2006). A unique HP type fit can be identified for the three cases with just one grain across the thickness i.e. $\lambda \leq 1$. This group features the two larger grain sizes for 12.5µm thickness i.e. d_g =14µm and 20µm and 25µm grain size for 25µm thickness. This specimengroup features multicrystalline specimen with varying avg. grain aspect ratios (λ) between 0.6-1. The observed weakening with reducing number of grains across the thickness tends to saturate as there is just one grain across the thickness. Beyond this point ($\lambda \leq 1$), there is negligible effect of further increase in grain size, although a much weaker Hall-Petch type trend can still be identified.

Based on these observations, three distinct regimes of behavior can be identified bounded by two Hall-Petch type relations. The bulk regime, with $t \geq d_g$ and $\lambda \geq$ 5-15

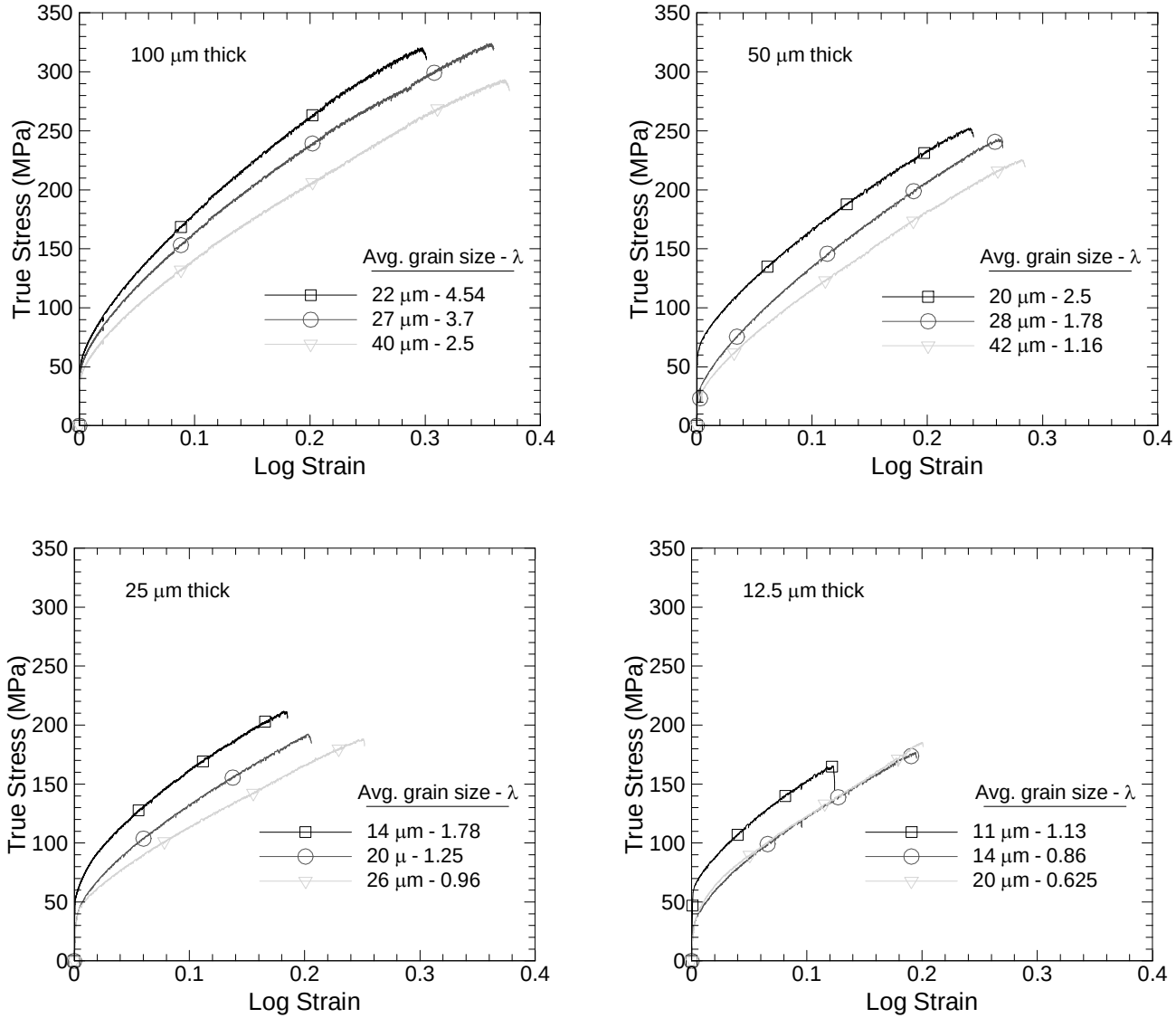

Figure 3.4 Typical stress–strain curves for each thickness for different grain sizes. The avg. grain size (d_g) along with the λ value is shown alongside each curve.

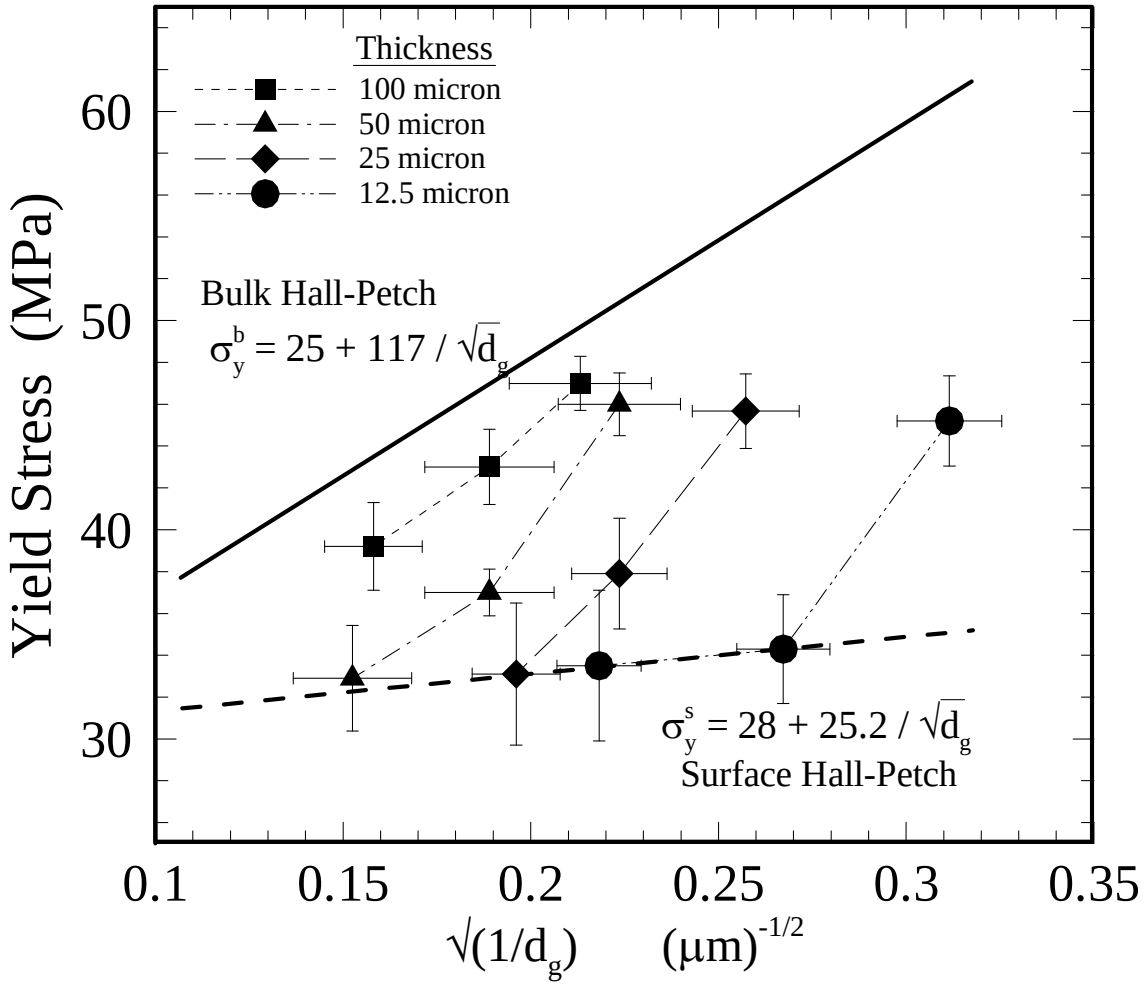

Figure 3.5 (a) Observed grain size effects on yield stress - @0.2% strain offset - on a Hall-Petch plot. The parameters for the Bulk Hall-Petch relation for yield stress were obtained from Hansen et al, 1983. The surface Hall-Petch relation for the multicrystalline specimen (i.e. specimens with $\lambda < 1$) is also shown.

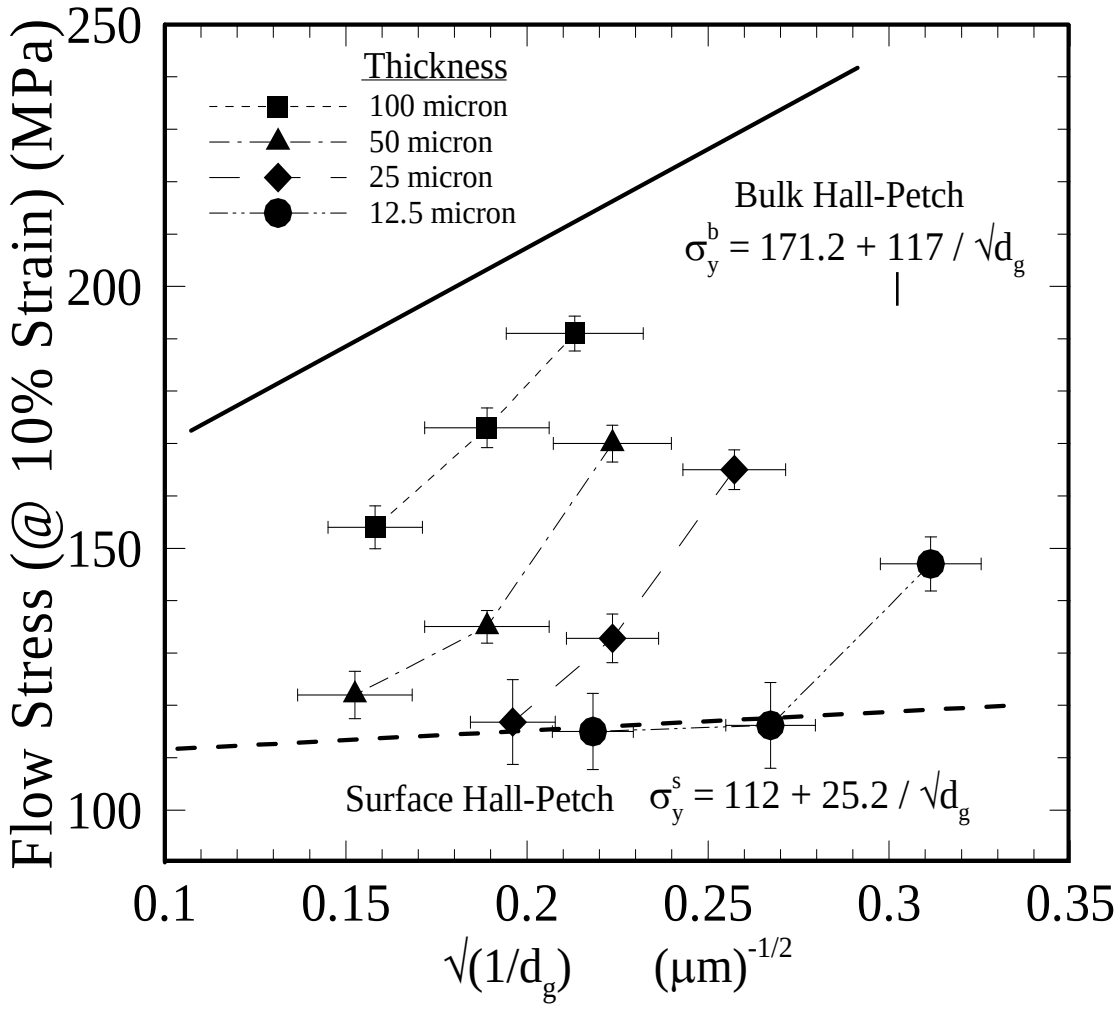

Figure 3.5 (b) Observed grain size effects on flow stress @10% strain on Hall-Petch plot. The parameters for the Bulk Hall-Petch relation for the flow stress were obtained from Hansen et al, 1983. The surface Hall-Petch relation for the multicrystalline specimen (i.e. specimens with $\lambda < 1$) is also shown.

(approximately), although not tested in this study, is otherwise well characterized [Armstrong et al, 1962; Hansen et al, 1983; Armstrong et al, 1983; Miyazaki et al, 1979). The flow stress in this regime is insensitive to any change in thickness and therefore, no thickness effects are seen in bulk specimen (Armstrong et al, 1961). The observed grain size strengthening in this regime conforms to the upper bound, bulk Hall-Petch relation. At the other end of the spectrum, for $t \leq d_g$ and $\lambda \leq 1$, the specimen can be approximated as a 2-D aggregate of crystallites, with each grain exposed to free surface on at least two sides. This regime is hereby referred to as the surface regime and the associated Hall-Petch type trend as the surface Hall-Petch relation. The surface grains regime is characterized by a very weak Hall-Petch type grain size effect as can be seen for the 25µm and 12.5µm thicknesses in Figure3.5. The representative average stress-strain curve for these cases in Figure 3.7 also reflects this trend.

An intermediate regime, bridging the bulk regime and the surface regime can also be identified. With increasing grain size, we observe a transition from the bulk regime to the surface regime. In the intermediate regime, a single Hall-Petch type fit cannot describe the trend in its entirety as the observed grain size dependence i.e. the flow stress at a given grain size, is different for different thicknesses, implying coupled thickness-grain size effects. Also, the yield/flow stress, for a given thickness, is not a linear function of $d_g^{-1/2}$ anymore, a consequence of the grain size effects being coupled with the thickness effect. These observations suggest that the bulk Hall-Petch relation is expected to breakdown at the onset of the intermediate regime, where the thickness effects first

appear. As per Miyazaki et al (1979), the onset of thickness effects and, therefore, the intermediate regime, occurs at a critical λ value ($\lambda_c \sim$ 5-15) that in turn depends on the avg. grain size.

3.4.2.2 Effect of Thickness

From the thickness-dependence perspective, Figure 3.6 shows the yield stress as a function of the thickness for each grain size i.e. Group B. Here, schematic lines are drawn to represent the thickness effects on yield stress for each grain size. The corresponding data points obtained in this study are also shown. For a given grain size, and with relatively larger thickness, the yield stress is expected to be dictated by the bulk Hall-Petch relation alone through the grain size. As a result, no thickness effects are expected in the bulk regime. With reducing thickness however, at a certain critical thickness for a given grain size, thickness effects appear. The yield stress reduces rapidly with reducing thickness for each grain size, eventually converging onto much weaker thickness dependence when $t = d_g$ is reached. This regime is again identified as the surface regime. Further reduction in thickness has a marginal effect on the yield stress. The experimental data reported here suggests ‘smaller is weaker’ trend for all tested grain sizes. Thus, similar conclusions as those drawn for observed the grain size dependence may be drawn for the thickness effects: there is a transition from bulk Hall-Petch stress to a unique, almost thickness independent, multicrystalline behavior. In the intermediate regime featuring this transition, thickness effects are clearly grain size dependent i.e. small grain

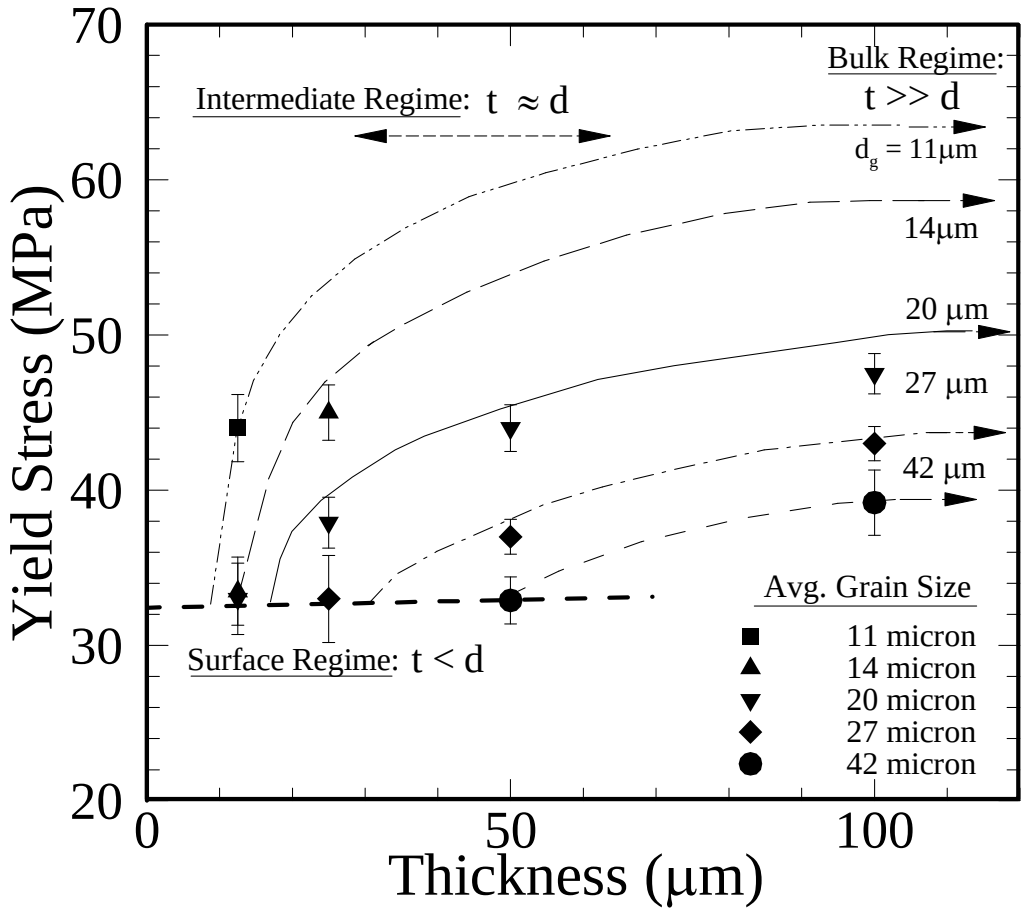

Figure 3.6 The effect of thickness on yield stress for specimens with different average grain sizes. The three different regimes of behavior i.e. Bulk regime, Intermediate regime and Surface regime are highlighted.

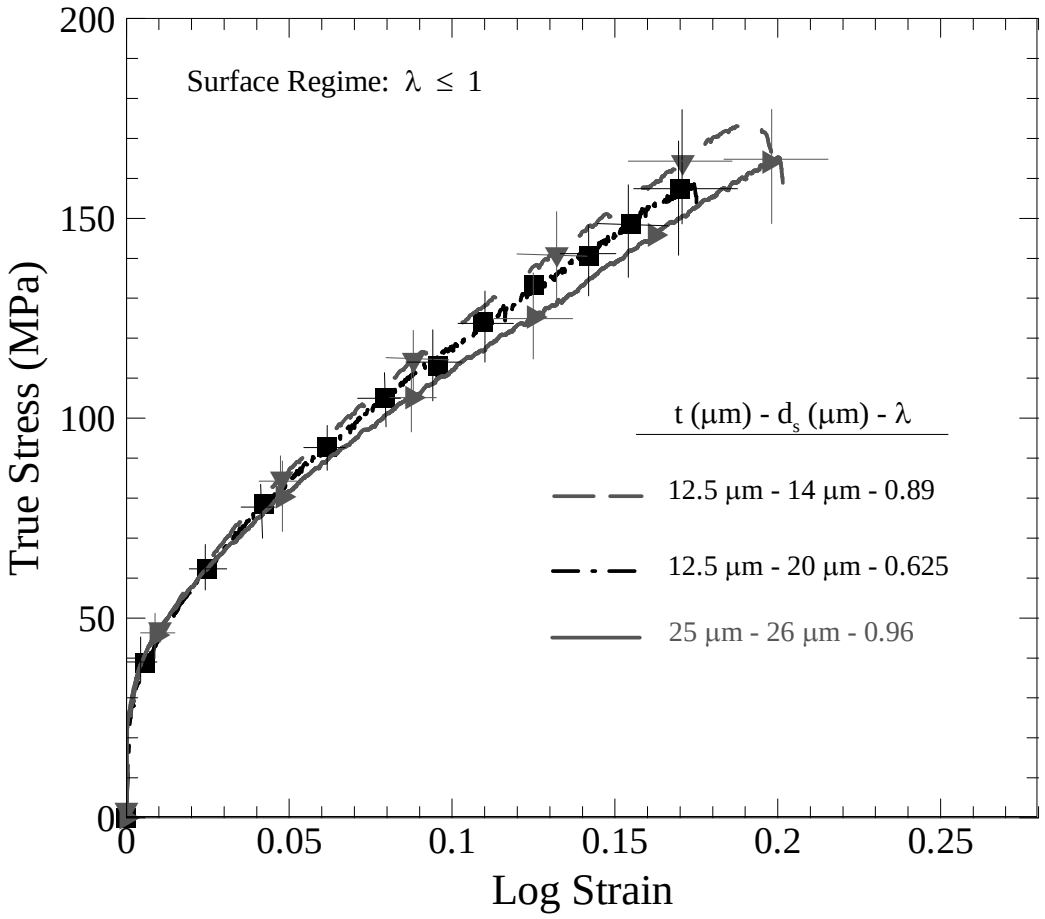

Figure 3.7 Typical true stress-log strain curves for the multicrystalline specimen ($\lambda < 1$) highlighting the negligible size effects observed in the surface regime as compared to the relatively wider statistical variations.

size results in higher yield stress for the same thickness. Thus, both perspectives reveal the inherent coupling between the thickness and grain size effects. Therefore, the formulation of any phenomenological relationship to describe the observed size effects is contingent upon the inclusion of both the thickness and avg. grain size in the analysis.

3.4.2.3 Statistical variations

The three distinct regimes identified previously i.e. bulk regime with $t \geq d$, surface grains regime with $t \leq d$ as well as the intermediate regime, can be characterized by the avg. no of grains across the thickness i.e. thickness to grain size ratio, λ; bulk regime with approximately $\lambda \geq \lambda_c$, intermediate regime with $1 \leq \lambda \leq \lambda_c$ and the surface grains regime with $\lambda \leq 1$. As the no. grains across the thickness reduce, it is expected that the individual orientations of the grains would play an increasingly important role in the overall mechanical response of the specimen. Therefore the resultant statistical variations in the observed mechanical response would increase with increasing grain size for a given thickness i.e. reducing avg. no of grains across the thickness. Furthermore, OIM analysis for the material in this study revealed very similar strength and sharpness of the texture distribution for the as-received material, however, the post-annealing microstructure was such that while the dominant texture (<110> for the present case) was the same for all thickness-grain size combinations, the strength and sharpness of the orientation distribution were reduced with decreasing no. of grains across the thickness, possibly an outcome of recrystallization. Thus, the scatter in orientation distribution was found to

increase with decreasing λ. This increased scatter in orientation and the resulting statistical variations with reducing λ is reflected in the observed increase in variance of the macroscopic mechanical response obtained experimentally as shown in Figure 3.6 for the multicrystalline specimen. Thus any meaningful quantitative conclusions in this regime can only be based on the average response of many specimens.

3.5 DISCUSSION

The experimental results presented in the previous section identified three distinct regimes of behavior. Two limiting cases i.e. bulk (true polycrystalline) case and surface (multicrystalline) case, constitute an upper and lower bound regime respectively. The yield/flow stress in both these regimes was shown to be amenable to a Hall-Petch type relation. On the other hand, the intermediate regime, bridging these two limiting cases, features coupled thickness and grain size effects and it was shown that a unique Hall-Petch type relation cannot encompass these combined effects. In this section we first address the underlying physical basis for these different regimes of behavior and, finally, present a rationale for a phenomenological relationship for the entire range of the observed size effects i.e. including the three identified regimes.

3.5.1 Physical Mechanisms

Macroscopic yielding or plastic flow requires initiation, and transmission, of plastic slip across all the grains within the specimen. Therefore, material response under plastic deformation can be understood as the outcome of the different unit processes that constitute the initiation and transmission of plastic slip at the microscopic (dislocation) level as well as macroscopic i.e. granular and aggregate level.

At the microscopic level, plasticity results from activation of intra-granular dislocation sources under applied loading. Therefore, for plastic flow to commence within the grains of the specimen, firstly the requirement of a critical resolved shear stress along specific slip systems within each grain must be met. In this context the interior regions of the grains, away from the grain boundaries, would behave in a way similar to a single crystal. However, unlike in a single crystal, polycrystalline plasticity is also subject to deformation compatibility requirements between neighboring grains. Primary slip in each of these neighboring crystallites would generally be incompatible and as a result there would be considerable internal stresses in regions adjoining the grain boundaries. While at small strains such incompatibility can be accommodated by an additional elastic strain field at the grain boundaries, at large strains compatibility would require the activation of additional slip systems (secondary slip) in the vicinity of the grain boundaries (Rey et al, 1988). As plasticity commences within the grain interiors, dislocations gradually get piled up at the grain boundaries. Activating plastic slip in the

adjoining grain ahead of the pile-up relieves the resulting internal stresses resulting from the strain field of these piled up dislocations. The grain size dependence of the required stress for initial yielding as well as continued plastic flow stems from the fact that these internal concentrations at the grain boundaries, required for slip transmission to the adjoining grains, depends on the grain size (Armstrong et al, 1962).

At the aggregate level, the external stress required for initiation or continuation of plastic deformation must therefore meet the following requirements (Armstrong et al, 1961):

1. The critical resolved shear stress required for activation of slip on a specific slip system within each of the grains making up the aggregate must be achieved.
2. In addition to achieving intragranular slip, the requirement of additional stress concentration at the grain boundary to initiate slip in the adjoining grains must be met.
3. Finally, slip in the adjoining grains must occur on suitable slip systems so as to maintain compatible deformation.

The first requirement is dictated by the crystallographic orientation of each grain with respect to the external load. The external load must therefore account for the appropriate orientation factors of the individual grains. Similarly, the third requirement is also orientation dependent however in this case, the relative orientations of neighboring grains would be important. The second requirement, achieving the required stress

concentration at the grain boundaries, is grain size dependent. These orientation constraints and the internal stress concentrations at the grain boundaries, taken together, constitute the overall microstructural constraint that dictates specimen behavior.

3.5.1.1 Bulk Regime

The bulk regime essentially encompasses specimen with a large no. of grains within its volume. Assuming the thickness to be the limiting specimen dimension, bulk behavior is expected to hold until there are about 5-15 grains across the thickness (Miyazaki et al, 1979). For bulk grains i.e. grains embedded within the bulk of the specimen and surrounded by other grains, compatibility requirements must be met at all surrounding grain boundaries. Such an interpretation, at its extreme i.e. imposing the entire strain tensor on each grain, yields a minimum of 5 required slip systems to maintain compatible plastic deformation. Under such so-called ‘polyslip’ conditions, orientation conditions as described by Taylor (Taylor et al, 1934, 1938, 1958; Kocks et al, 1958) can be used to relate the tensile yield/flow stress of the polycrystal to the critical resolved shear stress for a single crystal under multislip (Hansen et al, 1983). In addition to these orientation requirements, the additional stress concentrations would be required at all the surrounding intergranular interfaces.

Therefore, the experimentally measured overall yield stress and flow stress of the aggregate in the bulk regime is simply the cumulative effect of internal stress

concentrations at all the grain boundaries, shear stress required for intragranular slip as well as the effect of Taylor type orientation conditions for all specimen grains within an average cross-section of the specimen. When there are sufficiently large no. grains across the thickness of the specimen, every material cross-section yields a good measure of the combined effect of statistical orientation constraints on plastic flow (through an average measure of orientation factor) and the avg. grain boundary barrier to flow transmission between grains (related to avg. grain size). Therefore, any reduction in specimen thickness, as long as sufficiently large no. of grains still exist in an average specimen cross-section, would not have any effect on the overall yield/flow stress (Armstrong et al, 1961). Thus, bulk Hall-Petch relation adequately describes the effect of microstructural constraint, through the avg. grain size and avg. orientation factor, on the overall behavior and no thickness effects are expected in this regime.

3.5.1.2 Surface Regime

A remarkable feature of our data is the identification of a unique Hall-Petch type grain size effect for multicrystalline specimen. For such specimen with $t \leq d_g$ i.e. a specimen with just one grain across the thickness, only the vertical grain boundaries (those normal to the film surface and extending across the thickness) would present an effective obstruction to the dislocation motion. The two free surfaces, however, act as a dislocation sink wherein dislocations upon reaching the free surface are annihilated and leave behind a residual surface step and therefore do not contribute to hardening. In order

to relieve the image stresses imposed by the free surface, the grain interior in such grains is expected to feature enhanced dislocation mobility along slip systems that end at the free surface and permit dislocation annihilation. In this scenario, as validated by many TEM observations, the interior regions of the grain, away from the vertical grain boundaries, constitute a *soft* central region prone to *thinning* with deformation, while the outer region of the grain adjacent to the vertical grain boundaries constitutes a *hard* region with dislocation pile-up impeding plastic deformation (Lee et al, 2003).

In addition to this free-surface effect, surface grains also experience a greatly diminished microstructural constraint as compared to bulk grains. In this case, stress concentrations are only required to be met at the through-thickness grain boundaries. Since a multicrystalline specimen is essentially a 2-D aggregate of crystallites, only in-plane orientation constraints are to be met i.e. there are no orientation or compatibility requirements in the thickness direction. Generally, it can also be expected that enhanced lattice rotation, given the greatly reduced rotational constraint, would be admitted in such conditions and this would allow compatible deformation with lesser required slip systems as compared to the bulk case. Such an interpretation is in agreement with the experimental observations by Miyazaki et al (1979) i.e. substantial lattice rotation was noted for a specimen with $\lambda \sim 1$. In fact, assuming plane stress deformation in each grain, a maximum of three independent slip systems would yield deformation compatibility, unlike five systems required for the bulk case. To this effect, post-mortem investigations of the microstructural features in the multi-crystalline specimen revealed a maximum of

three distinct families of slip lines within each grain.

Therefore, these effects taken together imply that a much weaker response, as compared to bulk grains, is to be expected from the surface grains because an average cross-section of the specimen would feature far lesser grain boundaries as well as less stringent orientation requirements as compared to the bulk case. While Armstrong et al (1961) hypothesized grain size independent behavior in this regime, our results clearly indicate the existence of a distinct, albeit much weaker, Hall-Petch type grain size effect. Therefore, our results do not agree with the lower bound of 2 τ_{CRSS} as described by Armstrong et al (1961). On the other hand, scaling the bulk Hall-Petch parameters assuming a Sachs type orientation factor (Scahs et al, 1928), $m_s = 2.2$, instead of $m_T = 3.1$ (for a Taylor polycrystal), taking an order of magnitude $\sigma_o : m$ and $k : m^2$, after Armstrong et al (1962), we obtain a new HP relation as $\sigma_S = 18 + 58/\sqrt{d_g}$. Figure 3.10 compares this HP relation with the experimental best-fit Surface HP relation. While we find that given the experimental scatter, the agreement between the two is quite reasonable, it is quite likely that such close agreement is merely accidental because a Sachs polycrystal would only feature single slip i.e. only the slip system with the highest Schmid factor within each grain would be active. While at small strains single slip can be admitted, for large deformation single slip would yield incompatible deformation. Thus, while the average orientation factor in surface regime can certainly be expected to be lower than the Taylor value (5 slip systems), it will, however, be greater than the Sachs' assumed single slip system. Therefore, the observed grain size dependence of yield or

flow stress for multicrystalline specimen cannot be explained on the basis of an orientation effect alone as hypothesized by Armstrong et al (1961).

The much weaker Hall-Petch relation for the surface regime could, on the other hand, be an outcome of the fact that the intragranular ‘hard’ regions in the vicinity of the grain boundaries would occupy a larger volume fraction of the total grain volume in smaller grains as compared to much larger grains (Janssen et al, 2006). In this context, while larger grains may exhibit grain size independent behavior, much weaker grain size dependence can still be expected for smaller grains. This would imply that it is likely that the surface Hall-Petch parameters obtained in this study are grain size dependent i.e. specimen with even smaller grain sizes than those studied here would reveal a stronger grain size effect in the surface regime. Therefore, the formulation of a Hall-Petch type relation describing yield/flow stress as a function of grain size in this regime would likely be amenable to two-phase models (Ashby et al, 1970) where the grain interior and grain boundary regions are modeled independently, in addition to accounting for the reduced in-plane orientation constraints (somewhere between Taylor type and Sachs type formulations) as well as incorporating the free-surface effects acting on the intragranular volume.

3.5.1.3 Intermediate Regime

For a bulk specimen, the grains at the free surface would have a response similar to the grains in a multicrystalline material. However, since surface grains occupy a negligible volume fraction of the total specimen volume, bulk grains dictate the specimen's overall response to external loading. On the other hand, in the intermediate regime, with just a few grains across the thickness, the volume of the region affected by the aforementioned weakening due to proximity to the free surface is not negligible to the total specimen volume anymore. The limiting specimen dimension i.e. thickness, in this context, characterizes the proximity of the individual crystallites within the specimen to the free surface. Therefore, the overall behavior in this regime would be a combination of the two scenarios i.e. the grains within the bulk of the specimen that are not exposed to the free surface experience both enhanced resistance to dislocation motion due to pile ups at the grain boundaries and dislocation interactions within the grain as well as a greater microstructural/rotational constraint at all the grain boundaries while the grains exposed to the free surface have a softer overall response owing to dislocation annihilation at the free surface as well as reduced constraint. With reducing number of grains across the thickness, the volume fraction of the bulk grains within the specimen, α_b, reduces at the cost of the volume fraction of the outer surface region, α_s (obviously, $\alpha_s + \alpha_b = 1$). The resultant overall response, in the intermediate regime may thus be understood as a volume average of the two constituent contributions. Therefore, the observed coupling

between the thickness and grain size effects in the current scenario can be addressed through an appropriate definition of the bulk region/surface region volume fraction.

One candidate for such a definition is the volume fraction of surface grains, α_{sg}, as derived from a geometric relationship between the thickness and grain size by Kals et al (2000) as

$$\alpha_{sg} = 1 - \frac{(w-2d_g)(t-2d_g)}{wt} \quad . \qquad (3.2)$$

Assuming the width of the specimen, w, to be much larger than the avg. grain size, d_g, i.e. w >> d_g, the expression reduces to 2 t / d_g or 2/ λ.

The 'surface' grains in this definition are modeled as grains with any one surface exposed to the free surface i.e. $\lambda = 2$ yields $\alpha_{sg} = 1$. This definition cannot be extended to the $\lambda = 1$ case (each grain exposed to free-surface on both sides); $\lambda = 1$ yields a volume fraction of 2, which is physically meaningless. However, as discussed previously, if we define the limiting scenario of $\lambda \leq 1$ as the surface regime i.e. surface grains are defined as those grains which are exposed to the free surface on both sides i.e. a multicrystalline specimen, then the definition of the volume fraction of the surface region must have an alternative formulation such that $\lambda = 1$ yields $\alpha_s = 1$. To this end, we define a dimensionless parameter, ϕ as

$$\phi = 1 - \frac{(w-d)(t-d)}{wt},$$

such that, in the limiting case of w >> t,

$$\phi = \frac{t}{d} = \frac{1}{\lambda}. \qquad (3.3)$$

The parameter ϕ here, shown graphically as a function of λ in Figure 3.8, characterizes the multicrystalline character of a specimen with a given thickness and grain size. The overall 'effective microstructural constraint' in a specimen would be inversely related to ϕ. For λ = 1, ϕ = 1 implies a multicrystalline specimen with a greatly diminished microstructural constraint. On the other hand, for sufficiently large λ (t >> d_g) i.e. bulk regime, $\phi \approx 0$ implies true polycrystalline behavior under relatively substantial microstructural constraint. The intermediate regime would thus feature a specimen somewhere between a true polycrystalline and a multicrystalline type behavior.

The effect of this direct relationship between ϕ and λ on the overall yield stress of the specimen is shown in Figure 3.9. In this study, λ was varied in a range of ~0.6 – 5. For a multicrystalline specimen i.e. $\lambda \leq 1$, surface grains yield a very weak dependence of yield strength with λ with a small positive slope. As suggested by Janssen et al (2006), this weak dependence may arise from the fact that for a multicrystalline specimen, the volume fraction of the hard grain boundary regions, with respect to the total grain volume, will scale approximately linearly with λ. With increasing λ, a monotonic increase in yield stress is seen for all grain sizes. This increase, however, is expected because the effective be a function of grain size i.e. small grains are far more sensitive as compared to larger grains. These observations agree with those presented in Miyazaki et al (1979) and Janssen et al (2006).

3.5.2 Phenomenological Description

With this as background, a simple phenomenological relationship for the intermediate regime, addressing the observed coupling between the thickness and grain size effects on yield/flow stress, can be formulated. The yield/flow stress- avg. grain size relationship i.e. classical Hall-Petch relation, for the bulk regime is well defined and the parameters σ_o and k can be found in the literature for both the yield stress and the flow stress at a constant strain (Hansen et al, 1983; Armstrong et al, 1962). For the surface regime, we obtain a Hall-Petch type relationship based on a linear fit on the yield stress v/s $d^{-1/2}$ curve for all cases with $\lambda \leq 1$. For our experimental data, there are three data points in the surface regime i.e. 12.5 µm thickness with 14 µm and 20 µm grain size and the 25 µm thickness with 25 µm grain size. The bulk Hall-Petch parameters taken from the available literature along with the surface Hall-Petch parameters from this work are shown in Figure 3.5 for the flow stress (Figure 3.5(b)) as well as yield stress (Figure 3.5(a)). The combined overall response i.e. yield/flow stress in the intermediate regime can now be written as

$$\sigma = \sigma^s \phi + \sigma^b (1-\phi) \ , \qquad (3.4)$$

where σ_s and σ_b are the respective contributions from the outer surface region and the inner bulk region respectively. ϕ, as defined previously, is the volume fraction of the surface region within the specimen cross-section. The grain size effects on the respective

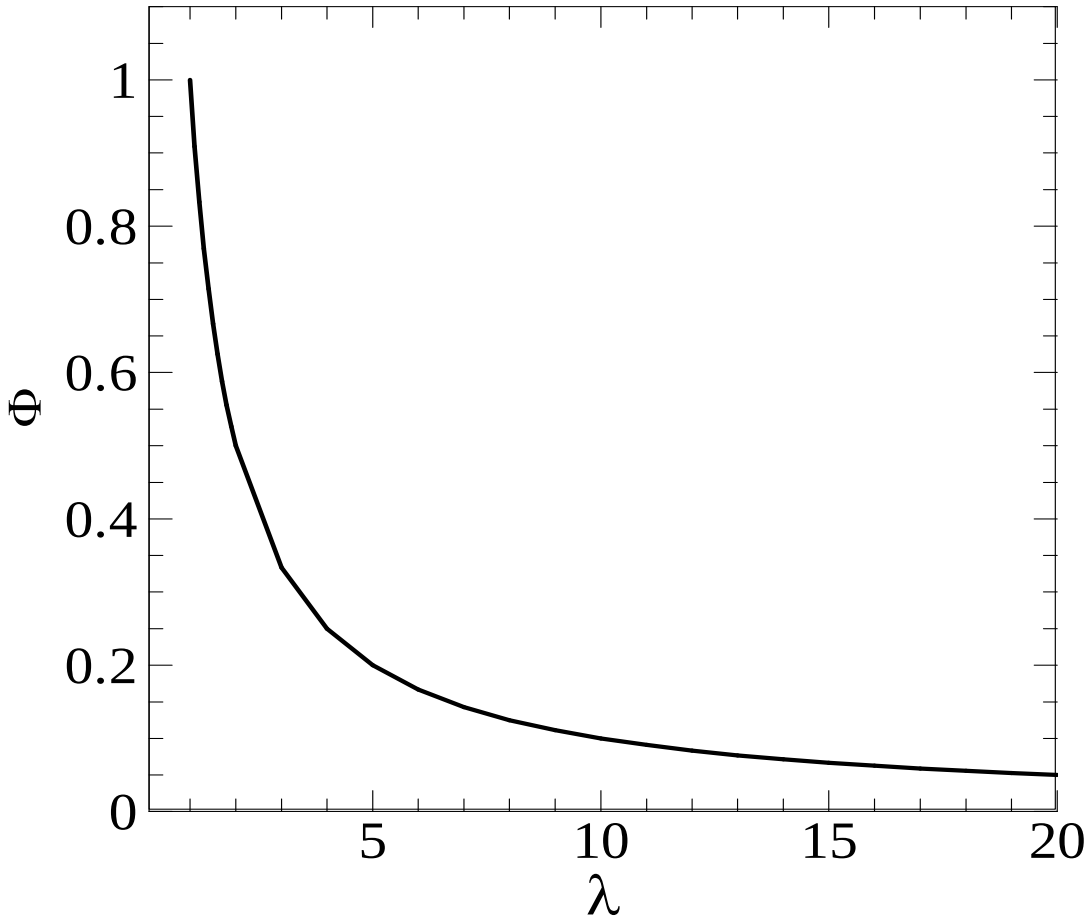

Figure 3.8 Variation of ϕ with λ. ϕ here represents the multicrystalline nature of a specimen with given λ, assuming equiaxed grains. It is directly proportional to the volume fraction of surface grains.

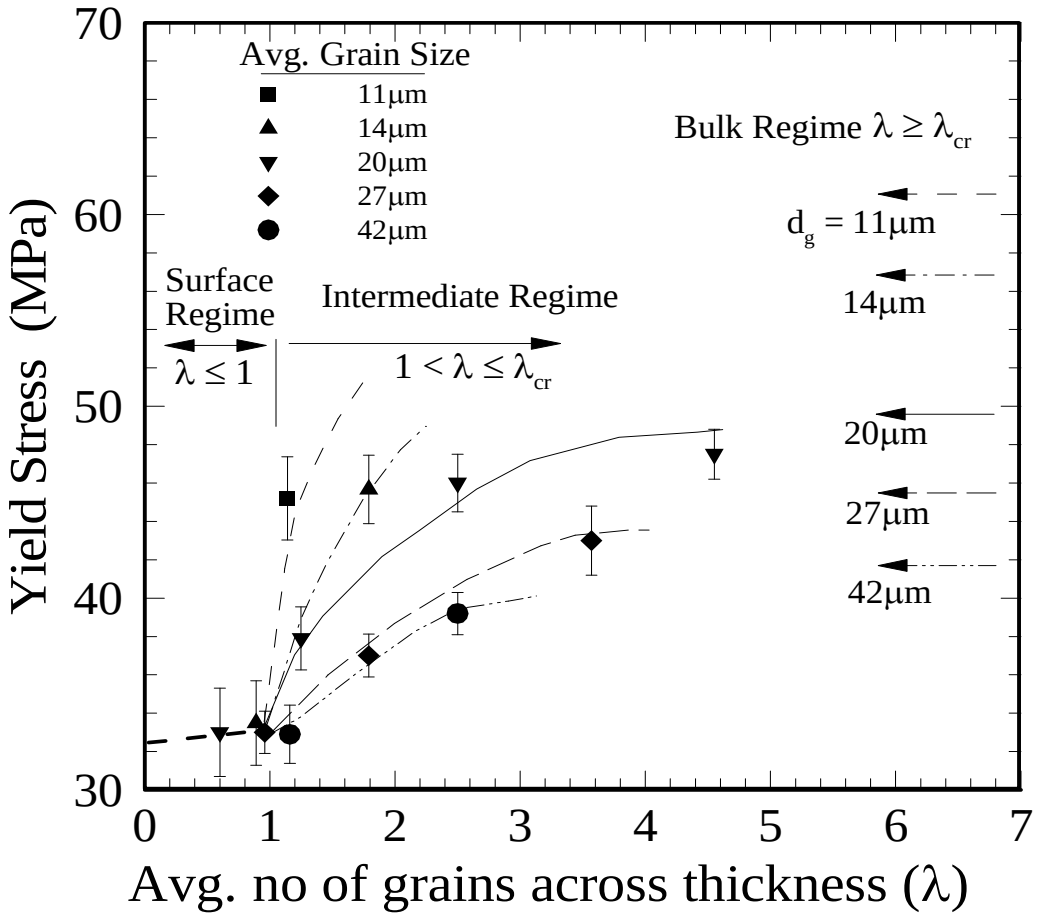

Figure 3.9 Experimentally obtained Yield stress as a function of λ. The expected trends for the bulk regime are shown schematically. There is no effect of λ on the yield stress until $\lambda = \lambda_{cr}$ (critical no. of grains across the thickness where thickness effects first appear). With reducing λ further, the yield stress reduces until λ = 1 (i.e. surface regime), beyond which the yield stress shows a near-linear variation with λ with a small slope.

contributions of the bulk and the surface regions can be substituted in terms of a Hall-Petch type relationship to yield,

$$\sigma = \left\{ \sigma_o^s + \frac{K^s}{\sqrt{d}} \right\} \phi + \left\{ \sigma_o^b + \frac{K^b}{\sqrt{d}} \right\} (1-\phi) \qquad (3.5)$$

Introducing two new dimensionless parameters, $\beta_o = \sigma_o^s / \sigma_o^b$ and $\beta_K = K^s / K^b$, Eq. (3.5) can be recast as

$$\sigma = \sigma_o^b \left\{ 1-\phi(1-\beta_o) \right\} + \frac{K^b}{\sqrt{d}} \left\{ 1-\phi(1-\beta_k) \right\}. \qquad (3.6)$$

Eq. (3.6) predicts the stress as a function of both, thickness and grain size, in thin Cu foils with just a few grains across the thickness, based on the two experimentally calibrated parameters β_o and β_k. Comparing the surface Hall-Petch relation obtained in this study with the bulk parameters for the yield stress, we obtain $\beta_o \approx 0.68$ and $\beta_k \approx 0.22$. The yield stress as a function of grain size for the tested thicknesses, obtained using Eq. (3.6), is compared with the experimentally obtained values in Figure 3.10. As can be seen, the agreement between the predicted values and the experimental results is reasonably good. Given the peculiar definition of the parameter ϕ, the resultant grain size dependence in the intermediate regime is asymptotic to the bulk Hall-Petch relation. Thus while this model adequately predicts the trend in the multicrystalline as well as the transitional regime, it does not capture the experimentally observed phenomenon of there being a grain size dependent λ_{cr} at which polycrystalline or bulk behavior is attained.

3.6 CONCLUSIONS

The flow stress of thin Cu foils with just a few grains across the thickness was obtained under homogeneous tensile deformation. Based on the experimental results in thus study, in conjunction with previous studies, three distinct regimes of behavior were identified; bulk regime ($t >> d$ and $\lambda > \lambda_{cr}$) where bulk Hall-Petch relation holds and no thickness effects are observed, intermediate regime ($t \approx d$ and $1 < \lambda < \lambda_{cr}$) where thickness and grain size effects are coupled and 'smaller is weaker' trend is observed and surface regime, where a much weaker grain size and thickness independence is seen. A separate Hall-Petch type behavior was associated with the surface regime for cases where there is just one grain across the thickness. The inherent coupling between the thickness and grain size effects in the intermediate regime was shown to be an outcome of the competition between the regional contributions of the inner bulk grains and the outer surface grains that constitute a softer region. A phenomenological relationship, in the form of a modified Hall-Petch type relation, was suggested which expresses the behavior in the intermediate regime as a volume average of the bulk Hall-Petch response and the surface Hall-Petch response.

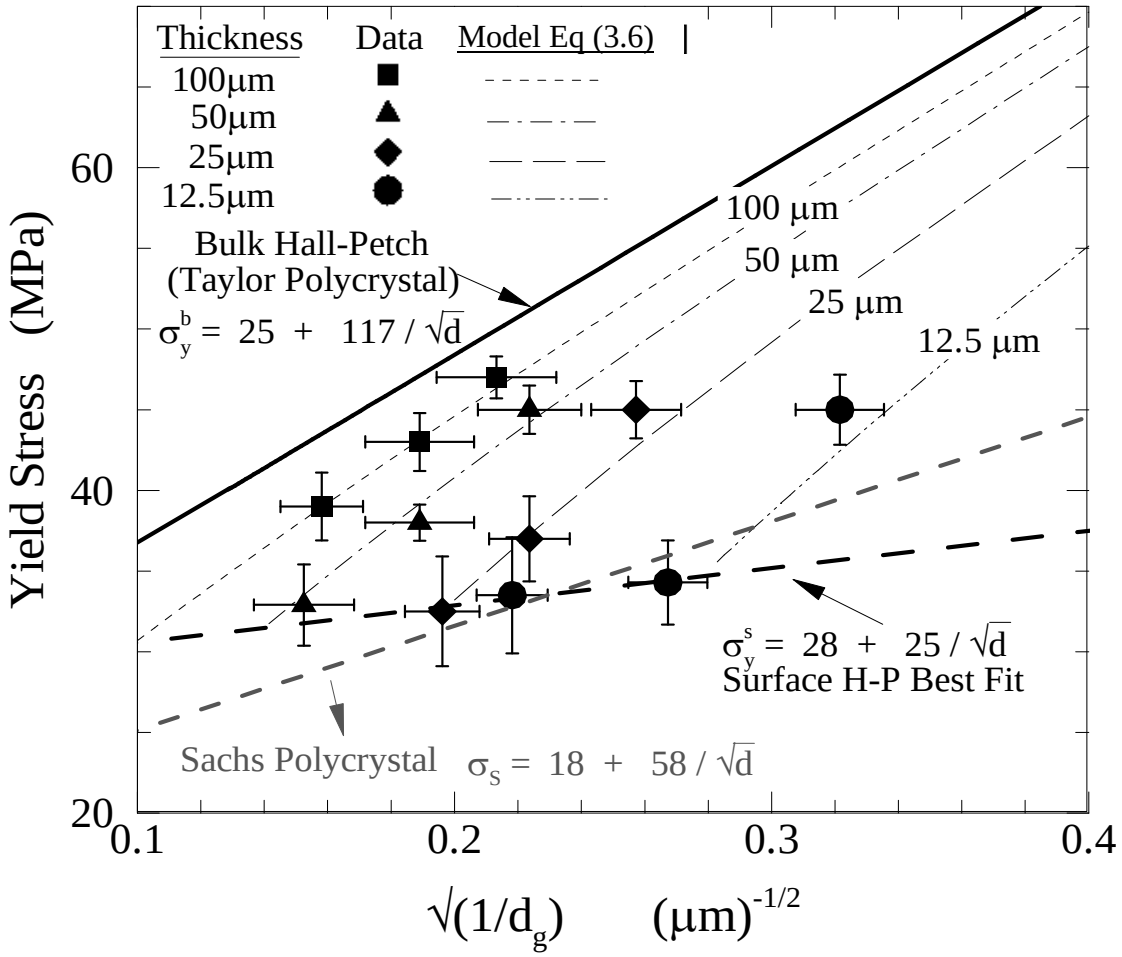

Figure 3.10 Comparison between the yield stress predicted by the phenomenological model and the obtained experimental values for the intermediate regime. H-P relation for a Sachs polycrystal (Armstrong et al, 1983) is also compared with the experimentally obtained Surface H-P relation. The bulk HP relation was obtained from Hansen et al, 1983

3.7 ACKNOWLEDGEMENTS

I would like to acknowledge the support of NSF under Contract No. CMMI-0134111. I am also grateful to Dr. Brian Gleeson and Takeshi Izumi at Ames Laboratory for help and assistance with annealing.

3.8 REFERENCES

1. Arzt, E. (1998) "Size effects in materials due to microstructural and dimensional constraints: A comparative review", *Acta Mater.* 46, No. 16, 5611-5626
2. Hall, E.O (1951) "The deformation and aging of mild steel", *Proc. R. Soc. Lond.* B 64, 474
3. Li, J.C. *Trans. Soc. Pet. Eng. Am. Inst. Min., Metall. Pet. Eng.* 227, 239
4. Petch, N.J. (1953) "The cleavage strength of polycrystals", *J. Iron Steel Inst.* 174, 25
5. Armstrong, R., Codd, I., Douthwaite, R.M. and Petch, N.J. (1962) "Plastic deformation of polycrystalline aggregates" *Phil. Mag.* 7, 45
6. Chokshi, A.H., Rosen, A., Karch, J. and Gleiter, H. (1989) "On the validity of Hall-Petch relationship in nanocrystalline materials" *Scrpita Metall.* 23, 1679-1684
7. D.G. Sanders, J.A. Eastman and J.R. Weertman. (1997) "Elastic and tensile behavior in nanocrystalline copper and palladium" *Acta Mater.* 45, 4019
8. Masumara, R.A., Hazzledine, P.M. and Pande, C.S. (1998) "Yield stress of fine grained materials" *Acta Mater.* 46, No. 13, 4527-4534
9. Yu, D.Y.W and Spaepen, F. (2004) "The yield strength of thin copper films on Kapton", *J. Appl. Phys.* 95, No. 6, 2991
10. Keller, R-M, Baker, S. P. and Arzt, E (1998) "Quantitative analysis of strengthening mechanisms in thin Cu films: Effect of film thickness, grain size and passivation" *J. Mater. Res.* 13, No. 5, 1998

11. Lee, H., Zhang, P. and Bravman, J.C. (2004) “Study on the strength and elongation of free-standing Al beams for microelectromechanical applications” *App. Phys. Lett.* 84, No. 6, 915
12. Nicola, L., Xiang, Y., Vlassak, J.J., E. Van der Giessen and Needleman, A. (2006) “Plastic deformation in freestanding thin films: Experiments and modeling” *J. Mech. Phys. Sol.* 54, No. 10, 2089
13. Miyazaki, S., Fujita, H. and Hiraoka, H. (1979) “Effects of specimen size on the flow stress of rod specimen of polycrystalline Cu-Al alloy” *Scripta Metall.* 13, 447
14. Stolken, J.S. and Evans, A.G (1998) “A Microbend test method for measuring the plasticity length scale” *Acta Mater.* 46, No. 14, 5109
15. Janssen, P.J.M, Keijser, Th. H., and Geers, M.G.D (2006) “An experimental assessment of grain size effects in uniaxial straining of thin Al sheets with a few grains across the thickness” *Mat. Sci. Eng. A* 419, 238
16. Fleischer, R. L. and Hosford, W. F. Jr. (1961), *Trans. TMS-AIME*, 221, 244
17. Armstrong, R. W. (1961) “On size effects in polycrystalline plasticity”, *J. Mech. Phys. Sol.*, 9, 196
18. Kals, R.T.A and Eckstein, R. (2000) “Miniaturization in sheet metal working” *J. Mater. Proc. Tech.* 103, 95
19. Michel, J.F. and Picart, P. (2003) “Size effects on the constitutive behavior for Brass in sheet metal forming” *J. Mater. Proc. Tech.* 141, 439
20. Raulea, L.V., Goijaerts, A.M., Govaert, A.V. and Baaijens, F.P.T. (2001) “Size effects in processing of thin metal sheets” *J. Mater. Proc. Tech.* 115, 44
21. Weiss, B., Groger, V., Khatibi, V., Kotas, A., Zimprich, P., Stickler, R. and Zagar, B. (2002) “Characterization of mechanical and thermal properties of thin Cu foils and wires”, *Sensors and Actuators* A, 99, 172
22. Cheng, S., Spencer, J. A. and Milligan, W. W. (2003) “Strength and tension/compression asymmetry in nano-structured and ultrafine-grain metals” *Acta Mater.* 51, 4505

23. Taylor, G. I. (1934), *Proc. Roy. Soc.* A 145, 362, 388

24. Taylor, G. I. (1938), *J. Inst. Met.*, 62, 307

25. Taylor, G. I. (1956), "Deformation and Flow of Solids", *Springer, Berlin*

26. Kocks, U.F. (1958), "Polyslip in Polycrystals", *Acta Metall.*, 6, 85

27. Sachs, G. (1928), *Z. Ver. Dtsch. Ing.*, 734, 72

28. Armstrong, R. W. (1983) "The yield and flow stress dependence on polycrystal grain size" *Yield, Flow and Fracture of Polycrystals,* Ed. By T.N. Baker, Applied Science Publishers, 1

29. Hansen, N. (1983) "Flow stress and grain size dependence of non-ferrous metals and alloys", *Yield, Flow and Fracture of Polycrystals,* Ed. By T.N. Baker, Applied Science Publishers, 311

30. Rey, C. (1988) "Effects of grain boundaries on the mechanical behavior of grains in polycrystals", *Revue Phys. Appl.* 23, 491

31. Lee, H., Zhang, P. and Bravman, J.C. (2003) "Tensile failure by grain thinning in micromachined Aluminum thin films", *J. App. Phys.* 93, No. 3, 1443

32. Ashby, M.F. (1970) "The deformation of plastically non-homogeneous materials" *Phil Mag.*, 21, 399

CHAPTER 4: SIZE DEPENDENT STRENGTH AND DISLOCATION STORAGE IN FREESTANDING ELECTRODEPOSITED Cu FILMS

4.1 ABSTRACT

This chapter presents an experimental assessment of the combined effects of average grain size, d_g, size as well as thickness, t, on the strength (yield as well as flow stress) of freestanding electrodeposited Cu films. The films were produced using pulsed electrodeposition and annealing to control d_g for different t. The film is tested in a micro-tensile fixture to the failure strain. Residual electrical resistivity measurements are employed to study the role of d_g and t on dislocation storage with deformation. The experimental measurements showed that for films with d_g<5μm, grain boundary (GB) dislocations dominate, while intragranular dislocations are greatly diminished as the average grain size approaches ~1μm. Intergranular dislocations are susceptible to dislocation annihilation at the free surface. Thus, they are responsible for strength deterioration with reduction of thickness. We speculate that the observed strengthening with reducing film thickness for a given d_g is attributed to the statistical reduction of GB dislocation density with reduction of film thickness. Such effect leads to increasing strength via GB dislocation source starvation. The experimental measurements identified a critical grain size of d_{cr} ~5μm, below which GB dislocation starvation dominates in freestanding thin films.

4.2 INTRODUCTION

The study of size effects on the strength of freestanding thin films has attracted considerable attention in recent years. This is primarily due to the fact that thin film reliability in common applications such as MEMS and NEMS is often a direct outcome of the underlying material behavior. The characterization of material behavior and deformation at small length scales (microstructural and structural) is particularly important because most concepts related to bulk material properties often fail to describe the observed mechanical properties at these length scales. Such deviations from bulk material properties are commonly termed as size effects. The two most common length scales in this context are the microstructural length scale i.e. average grain size (in the absence of any sub-grain structure) and the structural length scale, some limiting specimen dimension (commonly thickness).

4.2.1 Thickness effects on the strength of freestanding films under homogeneous deformation

While the role of average grain size has been investigated extensively in literature over the last 50 years or so (Hall et al, 1951; Petch et al, 1953; Armstrong et al, 1961; Chokshi et al, 1989; Sanders et al, 1997; Masumara et al, 1998), studies of thickness effects, or the influence of sample dimensions, on the strength as well as ductility are quiet recent. Such studies can typically be classified as either those that feature macroscopic strain gradients or studies that feature macroscopically homogeneous

deformation. The former group includes studies involving nano-indentation (Stelmashenko et al, 1993; Guzman et al, 1993; Ma et al, 1995), bending (Stolken et al, 1998) as well as torsion (Fleck et al, 1994). Recent analysis of the role of through-thickness strain gradients in multi-layered thin film systems under uniaxial tension (Xiang et al, 2006) suggest that multi-layered film systems i.e. bi-layers etc, under macroscopically homogeneous deformation, could also be included in this category.

A common feature of all such studies was the observed strengthening with reducing specimen dimensions i.e. reducing beam thickness in bending (Stolken et al, 1998), reducing rod diameter in torsion (Fleck et al, 1994) and reducing indentation depth in nano-indentation (Stelmashenko et al, 1993; Guzman et al, 1993; Ma et al, 1995) leads to increasing strength. As a result, the proposition that ‘smaller is stronger’, with respect to plasticity and the associated flow stress in miniaturized specimen was put forth. The observed trends in film-on-substrate configurations, either under bending in thermal cycling experiments (Keller et al, 1996; Venkataraman et al, 1992) or under uniaxial tension with either a polymeric substrate (Yu et al, 2004; Kraft et al, 2000) or in the presence of a passivation layer (Xiang et al, 2006; Nicola et al, 2005), also confirm the smaller is stronger hypothesis. However, in the absence of strain-gradients – under uniaxial tension and a freestanding configuration – the trends relating the observed strength to specimen thickness are not well understood and ambiguity still remains. It is this specific scenario that is the focus of this study i.e. freestanding polycrystalline films under macroscopically homogeneous deformation.

While the reported trends in this specific scenario for larger grain sizes are quite consistent i.e. reducing strength with reducing thickness for a given avg. grain size (Armstrong et al, 1961; Miyazki et al, 1979; Janssen et al, 2006), the trends for smaller grain sizes, typically in free-standing thin film specimen, are quite ambiguous. For example, most studies involving thin films with thickness and avg. grain sizes ~O(1μm) – O(100nm) (Lee et al, 2004; Nicola et al, 2005; Xiang et al, 2006) i.e. i.e. ultrafine grained regime, typically discount thickness effects altogether and associate the observed strength to the microstructural size parameters alone, through a Hall-Petch type correlation. It is important to note, however, that the validity of bulk HP parameters for d_g < 1μm is not clear (Gertsman et al, 1994), especially in specimen featuring thickness of the same order as the avg. grain size (Keller et al, 1996; Venkataraman et al, 1992; Lee et al, 2004; Yu et al, 2004; Nicola et al, 2005; Xiang et al, 2006). For example, for freestanding Cu thin films with d_g = 1.5μm–0.3μm (Xiang et al, 2006), it was found that $k_y \approx 0.19$ MPa $m^{1/2}$ i.e. 70% higher than the bulk slope (from Hansen et al, 1983). Similar results were found for Al thin films where the slope of HP relation was found to be approximately twice that of bulk Al (Lee et al, 2004). Similar estimates of microstructural contribution to the overall strength were also obtained from studies featuring thin film-on-substrate configurations after accounting for the effect of the constraint due to the substrate-film interface (Keller et al, 1998; Yu et al, 2004; Venkataraman et al, 1992) – the residual strength after such accounting was typically attributed to the microstructure alone. For Cu films on Kapton under uniaxial tension with $d_g \approx 1.3$μm and avg. twin size between 0.4μm - 1μm, $k_y \approx 0.233$ MPa $m^{1/2}$ was obtained (Yu et al, 2004) with twin

spacing as the HP parameter. In case of Cu films on Si substrate in thermal cycling experiments, Keller et al (1996) found the slope on a HP plot, after accounting for the additional thickness effect through Nix-type hardening mechanism, was approximately 3 times higher than the bulk HP slope for Cu i.e. $k_y \approx 0.344$ MPa $m^{1/2}$ (Keller et al, 1996).

On one hand it is reasonable to expect that bulk HP parameters, typically found for much larger grain sizes than these studies, will not be strictly applicable at these grain sizes given the possibility of different deformation mechanisms (Cheng et al, 2003). However, these results also raise the possibility of there being an additional thickness effect i.e. higher observed strength in miniaturized specimens, as compared to the bulk value for similar average grain sizes, is an outcome of not only the dissimilar deformation mechanisms (Cheng et al, 2003), but also an additional, as yet uncharacterized, thickness effect. This possibility clearly merits further study with a systematic variation of film thickness for a constant microstructure in this regime.

4.2.2 Probing internal defect content and evolution via Residual Electrical Resistivity Measurements

In order to address the issue of the influence of microstructural as well as structural length scales on the underlying deformation mechanisms responsible for plastic deformation and to establish the relationship of such effects with the observed size effects on the mechanical response, we employ residual electrical resistivity measurements (RERM) as a means to characterize the evolution of the internal defect density in the

tested films. While there are ways of qualitatively assessing the underlying defect density via x-ray diffraction or TEM analysis, such techniques are fairly cumbersome and inferring the total defect density (dislocations, voids or impurities) is not straightforward. Residual electrical resistivity measurements, on the other hand, present an effective and a relatively convenient way of addressing this challenge. The measurements are performed using a four-point probe method. Originally developed by Wenner (Wenner et al, 1915) and adopted for semiconductor wafer resistivity measurements (Valdes et al, 1954) and measurement of sheet resistivities of conducting materials (Smits et al, 1958), the four-point probe method presents an effective and reliable way of characterizing the resistivity of a conducting material.

Being an important electronic property, the relationship of resistivity and its relation to the underlying defects that contribute to it have been a focus of a number of studies. For Cu, the specific contribution from dislocations (Kaveh et al, 1986), grain boundaries (Qian et al, 2004) as well as vacancies (Wollenberger et al, 1983) is well characterized. With regards to the applications of resistivity measurements, RERM are usually employed to characterize the effect of processing (especially in electronic materials) on the electrical properties and the defect content (Gangulee et al, 1972; Chopra et al, 1977, Lu et al, 2003). Relatively few studies have employed RERM to study the evolution of defects (dislocations as well as vacancies) with deformation. For example, Ungar et al (2007) employed RERM to study vacancy production during severe plastic deformation (ECAP and cold rolling). They employed RERM to estimate the

correlation between vacancy content evolution with evolution of dislocation density. Schaefler et al (2005) assessed dislocation density evolution with shear strain in ECAP Cu. They compared the results from RERM with X-Ray line profile analysis as well as calorimetery to show that the observed trends were qualitatively similar. Keller et al (2005) have also used RERM measurements to study reliability issues in metallic interconnects under thermal fatigue loading. Therefore, the use of RERM to study internal defect content, while certainly not very prevalent, is not a novel idea either.

RERM are essentially based on Mattiessen's rule, an empirical rule that implies that the measured resistivity of a material is a collective response of thermal vibrations, impurities and lattice defects. Lattice defects encompass the bulk resistance due to line (dislocations) and point defects (vacancies), and the grain boundary resistance. In our study, all measurements are made at room temperature and as a result the contributions from thermal vibrations to the resistivity measurements is constant across all specimen sets. All the measured variations, in undeformed specimens at room temperature, can therefore be attributed to differences between the internal defect content (impurities, vacancies, dislocations, grain boundaries etc.). The measurement of this property in an undeformed specimen can, therefore, provide an effective estimation of the volume average density of all such defects taken together. Furthermore, the change in the measured resistivity with deformation is indicative of the evolution of such defects with deformation i.e. vacancies and dislocations (since impurity content does not change with deformation).

This work addresses the thickness-dependent strengthening effect for free standing films with small grains, d_g=1-5μm, and thickness between 2-50μm to provide thickness to grain size ratio (λ) in the range 0.5-30. Following a description of the experimental protocol in Sec. 4.2, the experimental results are presented in Sec. 4.3. Sec. 4.4 discusses the observed trends in the light of the underlying physical mechanisms. Residual electrical resistivity measurements (RERM) were conducted on the films before and after deformation to characterize their defect storage capability. The results of these measurements are used here to draw qualitative conclusions regarding the microstructural basis, as well as the underlying deformation mechanisms, behind the observed size effects on specimen strength.

4.3 EXPERIMENTAL PROTOCOL

The primary objective of this study was to quantify thickness effects on freestanding films. The material processing as well as experimental methodology was chosen so as to allow the clear identification of thickness and grain size effects independently of each other over a wide range of length scales.

4.3.1. Uniaxial tension testing

In order to exclude additional size effects due to strain gradients, a uniaxial tensile testing methodology was employed in this study. The tensile tests were performed at room temperature using an Instron 8862 machine with a servo-controller under

displacement control. In order to facilitate tensile testing of sub-sized specimen, an auxiliary test fixture was employed. The text fixture, along with the tensile specimen is shown schematically in Figure 4.1. The design of the test fixture was motivated by the ease of specimen handling while loading for testing as well as alignment considerations.

Testing sub-sized specimen, given the fragility of the specimen as well as the vertical loading axis of most mid-sized tension testing frames, can be a challenging task with regards to specimen gripping, specimen handling during loading and unloading as well as specimen alignment within the testing frame. The tensile specimen, in this study, was first placed in its marked position in the grip section on the test fixture and held in place using frictional force. The specimen was aligned with the loading axis of the test fixture under a low magnification microscope. A special holding frame was designed to facilitate the mounting and dismounting of the fixture-specimen assembly in the tensile frame without causing any deformation in the specimen. The test fixture–tensile specimen assembly, held within the holding frame, using secure but easily detachable clips, was then moved to the Instron machine and held in place using pin-connections. The test fixture and its grip section were so designed that the tensile specimen would be accurately aligned with the loading axis of the machine. Two vertical pins were also incorporated in the test fixture to aid in alignment, as shown in Fig 4.1. The holding frame was removed prior to actual loading.

All experiments were performed at a nominal loading rate of 2×10^{-4} per sec and at ambient temperature. The load was measured using a 30 Kg (~294 N) load cell and a non-contact capacitive displacement gauge, with sub-micron resolution (~ 70nm), was used for displacement measurement. In order to preclude metrology errors, specimen thickness was measured using SEM and all other pertinent specimen dimensions i.e. gauge width and gauge length, were measured using an optical microscope to within 5μm. The true stresses were found from the measured force assuming volume conservation. The strains were calculated based on the initial gauge length and the imposed crosshead displacement. A finite element based calibration based on the chosen specimen geometry was used to determine the uniform average strain over the gauge length of the specimen from the crosshead displacement value and the initial gauge length. This average strain value was further confirmed with the strain distribution in the gauge section of the specimen obtained using digital image correlation.

4.3.2 Material

The electrodeposited films, were prepared via galvanostatic pulsed electrodeposition (Natter et al, 1996) in a $CuSO_4$ and $(NH_4)_2SO_4$ solution. Peak current density of 250 mA/cm^2 with a 400ms pulse and 1% duty cycle were employed to yield Cu films with d_g ~200nm and average relative density of 99.83%. Figure 4.2 shows the fabrication methodology. The fabrication was carried out on microscopic glass slides. The glass slides had been pre-baked at 100°C for 20 minutes and a ~ 2μm AZ 5214

photoresist (PR) layer was deposited to facilitate lift-off of the deposited layer (Figure 4.2 (a)). The electrodeposited films were deposited on microscopic glass slide with the photoresist and a 50nm Cu seed layer, deposited via e-beam evaporation (Figure 4.2 (b) - (c)). The deposited film was then patterned using a photolithographic lift-off technique – additional ~ 2μm PR layer was used as a mask for wet etching with a 5% nitric acid and water solution (Figure 4.2 (d) - (f)). The deposited film, along with the 5 nm seed layer, was patterned into tensile dog-bone specimen with a 1mm wide and 5mm long gauge section (to retain an aspect ratio of 5). The patterned films were subsequently released to obtain freestanding specimens (Figure 4.2 (g)).

4.3.3. Residual electrical resistivity measurements

RERM are employed, using a standard 4-point probe system, shown schematically in Figure 4.3. The 4-point probe method is a standard way of characterizing the electrical resistivity of conductive (as well as semi-conducting) materials (Smits et al, 1958). This method essentially involves using 4 equi-spaced probes, as shown in Figure 4.3. A known current (I) is forced through the outer probes, 1 and 4, and the resulting voltage drop (V) is measured across probes 2 and 3. Generally, the voltage across probes 2 and 3 is measured through a very high Ohmic measurement device so as to minimize the current flowing through probes 2 and 3. In addition to this, the decoupling of the current source and the potential drop measurement ensures that the

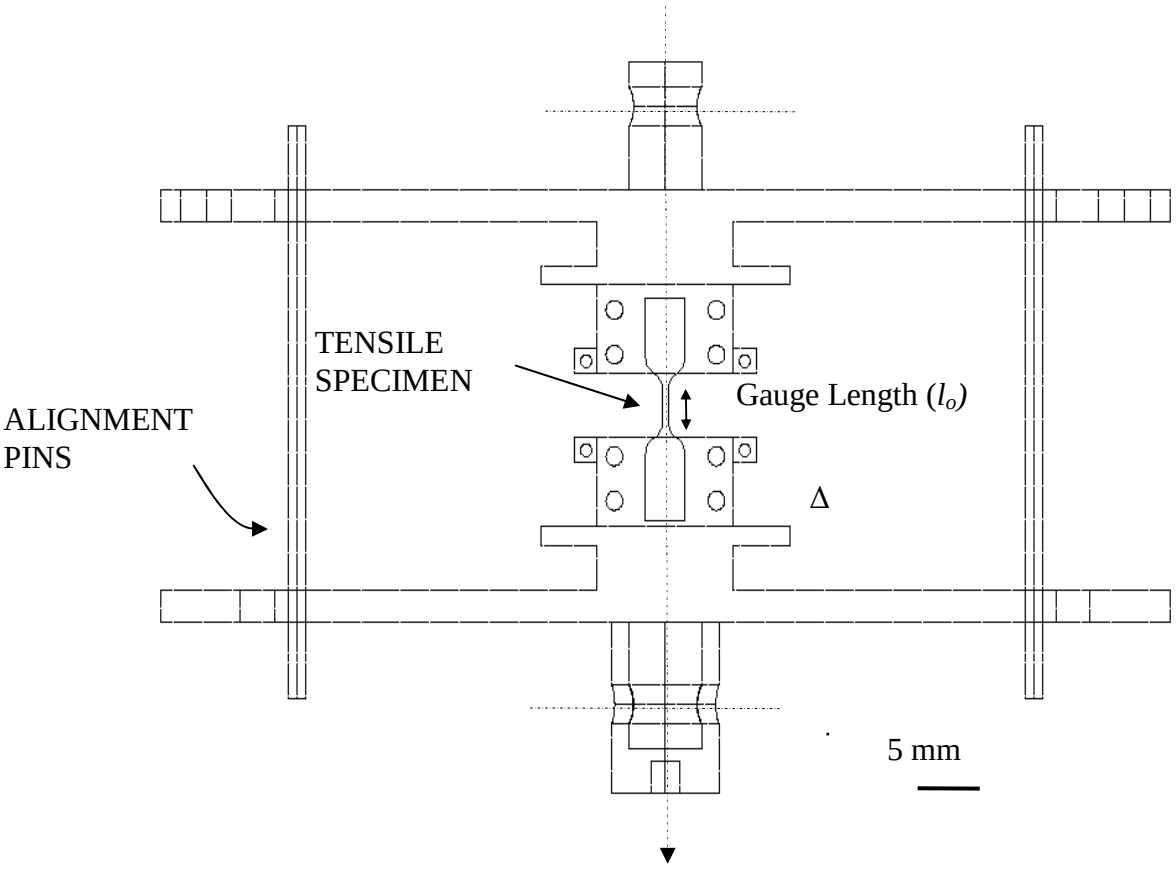

Figure 4.1 Auxiliary test fixture used in the tension test system. The tensile specimen had a gauge length (l_o) of 5 mm and a width of 1 mm. Ä is the machine crosshead displacement.

contact resistances between the probes and the material being measured do not play a role. Because the contact resistance can be much larger than the resistances being measured and can also depend on the condition and material of the electrode, 4-point probe technique yield more reliable results as compared to a 2-point probe measurement. Typically, a V v/s I curve is generated. This measurement of the *V* v/s *I* response is further used to calculate the sheet resistance, R_S, as follows:

$$\frac{\rho}{t} = R_S = C.F \times \left\{ \frac{V}{I} \right\} \qquad (4.1)$$

ρ here is the resistivity of the specimen being measured and *t* is its thickness. *C.F* is the correction factor that accounts for the probe size, the spacing as well as probe position in relation to the boundary of the specimen into account. For the set-up used in this study, the probe spacing (s) was 10 mils i.e. 2.5mm. For a semi-infinite thin sheet with thickness, $t << s$, *C.F.* of $\pi / \ln(2)$ i.e. 4.53, is obtained. Equation (4.1) can therefore be simplified as:

$$\frac{\rho}{t} = R_S = \frac{\pi}{\ln(2)} \times \left\{ \frac{V}{I} \right\} \qquad (4.2)$$

Thus, knowing the thickness of the specimen, the resistivity can be found from the *V* v/s *I* measurement.

4.4 RESULTS

The relevant mechanical properties related to plastic deformation i.e. yield as well

as flow stress are based on the true stress i.e. calculated from the measured force assuming volume conservation during plastic deformation. For the purpose of qualitative comparison, average true stress – log strain curves are used while quantitative comparisons are made on average measurements for 5 specimens for each thickness – grain size combination.

4.4.1 Microstructural analysis

The as-deposited films were annealed at 400˚C, 500˚C and 600˚C for 1 hr, in a Nitrogen environment, to yield three different avg. grain sizes, d_g = 1.8, 3.2 and 5µm respectively. The average grain size was calculated as per ASTM E112 from SEM images of the microstructure. Figure 4.4 shows typical SEM images of the grains and Table 4.1 summarizes the results of the microstructural analysis for this set. The thickness of the electrodeposited films was measured using a non-contact Profilometer (Zygo Corp.) and also confirmed via SEM investigations.

For a given thickness, increasing grain size results in reducing number of grains across the thickness. For approximately equiaxed grains, as in this study, the t/d_g ratio (λ) can be used to categorize the average number of grains across the thickness in the films. For specimens with $t < d_g$, λ represents the average aspect ratio of grains i.e. the grains would be pan-cake shaped with a greater in-plane expanse as compared to their thickness. Table 4.1 also shows the λ value for each case alongside the thickness and avg. grain size.

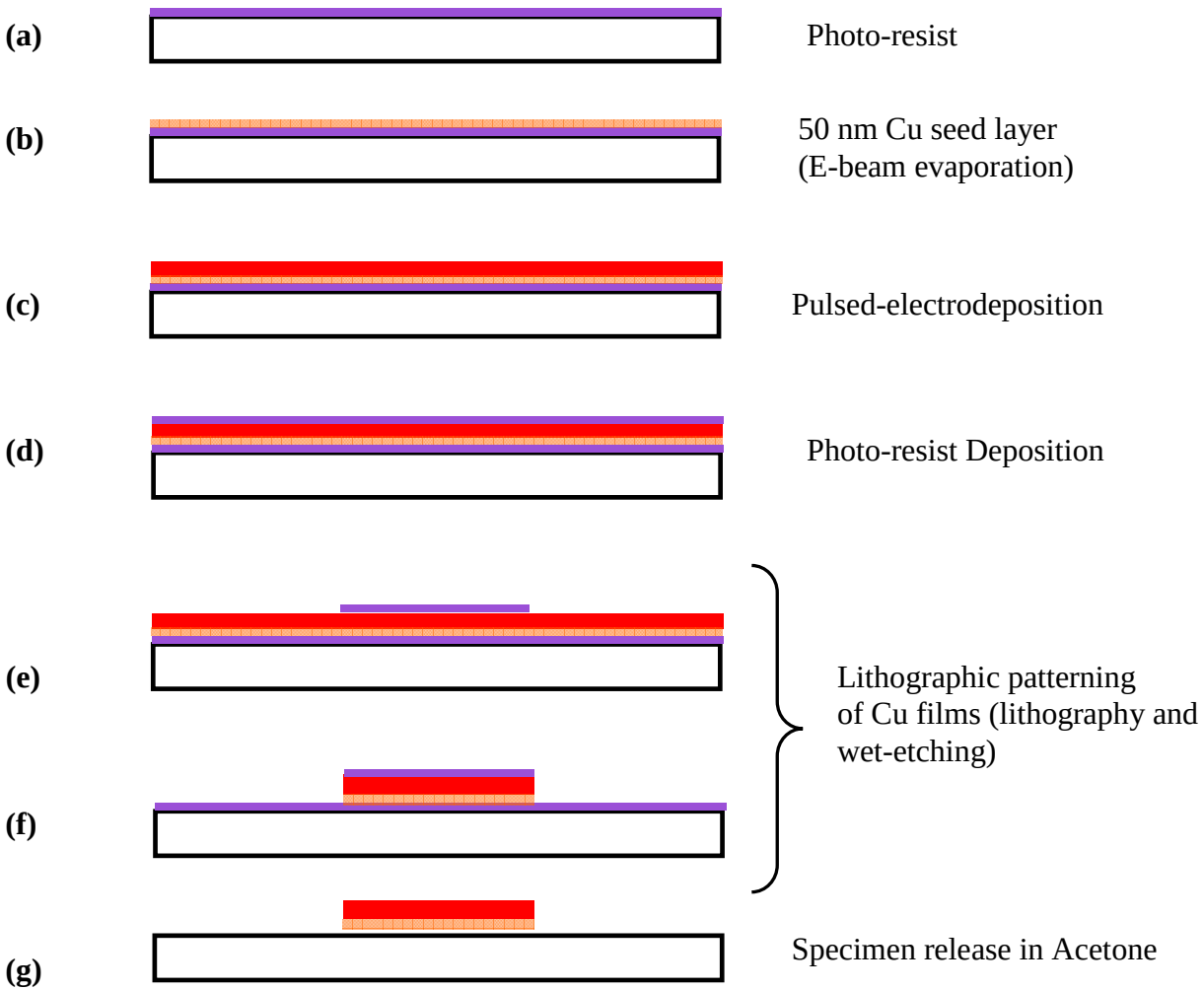

Figure 4.2 Specimen fabrication methodology. The tensile specimens were deposited using Pulsed-electrodeposition on a microscopic glass slide. Following lithographic patterning, they were released in an Acetone bath to obtained freestanding dog-bone tensile specimen.

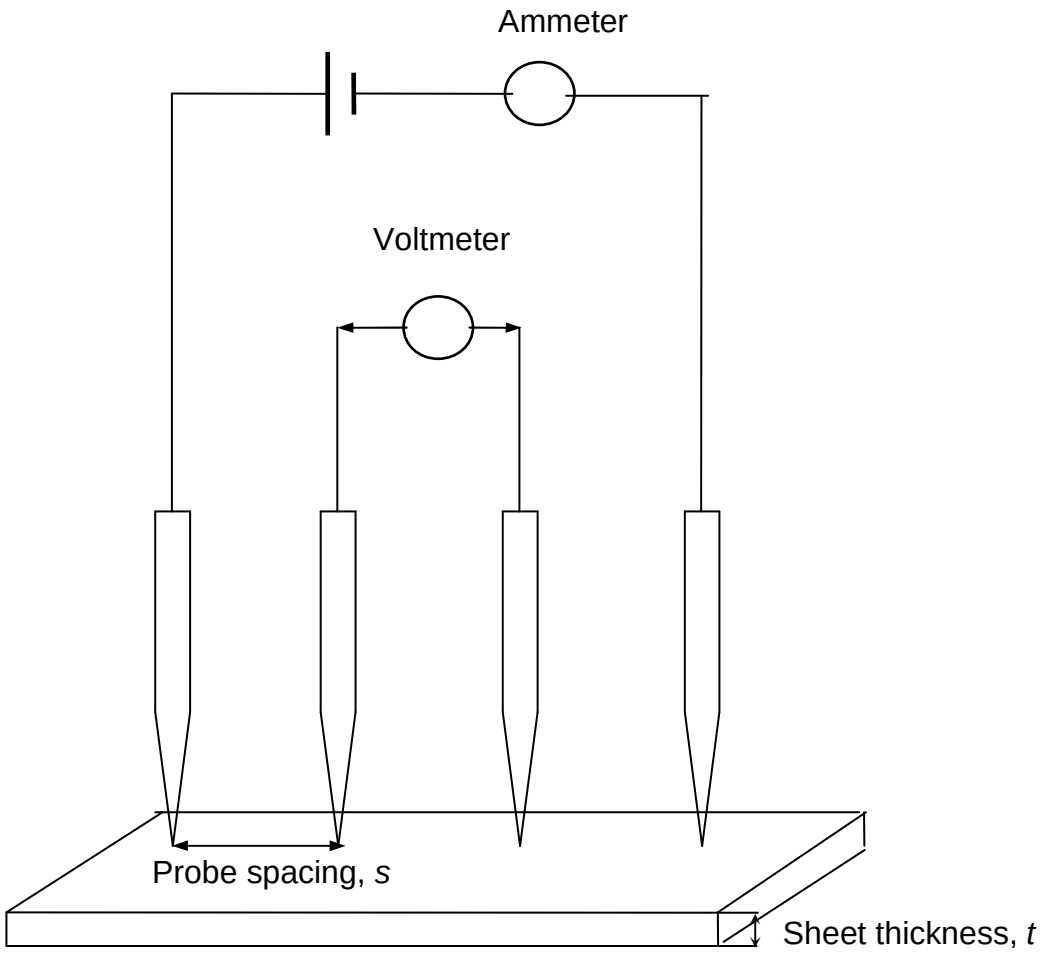

Figure 4.3 Schematic representation of a 4-point probe set-up to measure electrical resistivity of a conductive film.

The RERM of the undeformed films at 293K, shown in Figure 4.5, showed no thickness dependence of the film resistivity for the entire range of the grain sizes tested. By employing a typical grain boundary resistivity of 3.6×10^{-4} μΩ mm^2 for copper (Brandes et al, 1975) to account for the volume averaged grain boundary areas for each set of grain-size measurements, all the measurements yield consistent line/point defect resistivity of $0.92 \pm 0.05\ \mu\Omega.mm$. Such a trend is consistent with various studies on thickness effects due to surface scattering on electrical resistivity of Cu films, which showed that thickness effects appear only for thickness smaller than about 100nm (Ungar et al, 2007). The measurement of almost constant internal defect density for films with different average grain sizes and thickness is significant because any variation in the observed mechanical response (strength as well as ductility) can thus be attributed to the thickness and grain size variation.

4.4.2 Mechanical Response

Representative stress-strain curves for the tested specimens with three different average grain sizes i.e. d_g = 1.8μm, 3.2μm and 5μm, are shown in Figure 4.6. Generally, with reducing thickness for a given grain size, increasing yield/flow stress is observed. This trend is very apparent in the smaller grain size specimen i.e. d_g = 1.8μm and 3.2μm. For d_g = 5μm, however, largely no thickness effects are seen with reducing thickness until a much weaker response appears at a thickness of 4μm and 2μm i.e. for $\lambda \leq 1$. Such weakening is also observed for the 3.5μm average grain size specimens for

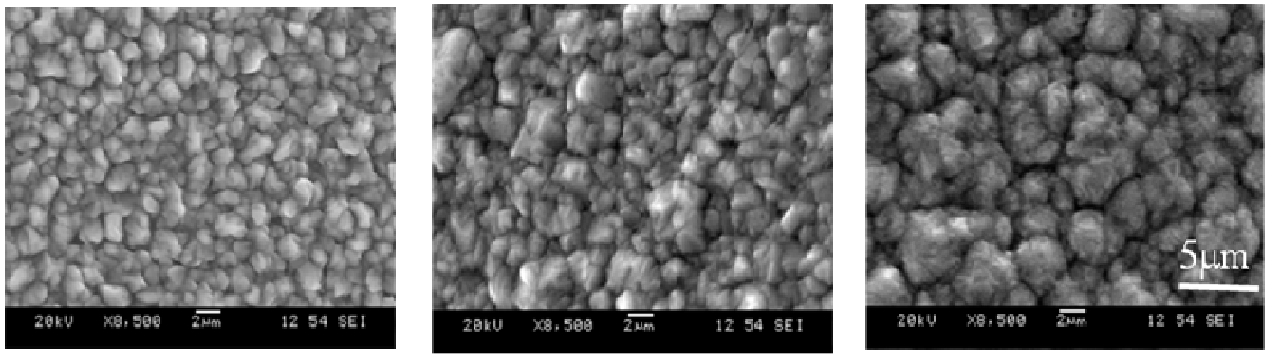

Figure 4.4 SEM micrographs showing the typical microstructure of the annealed specimen.

Avg. Grain Size d_g (μm)	**Thickness, *t* (μm)**					
1.8	**2.34** (0.23)	**4.23** (0.19)	**6.13** (0.21)	**8.51** (0.31)	**12.12** (0.18)	**49.86** (0.46)
t/d_g =	1.3	2.35	3.41	4.73	6.73	27.7
3.5	**2.56** (0.19)	**4.32** (0.21)	**6.59** (0.15)	**8.45** (0.26)	**12.36** (0.14)	**50.21** (0.33)
t/d_g =	0.73	1.23	1.88	2.41	3.53	14.35
5	**2.55** (0.31)	**4.44** (0.12)	**6.5** (0.11)	**8.36** (0.22)	**12.19** (0.24)	**50.36** (0.44)
t/d_g =	0.51	0.89	1.3	1.67	2.44	10.07

Table 4.1 Results of microstructural analysis. The average grain size (d_g), thickness (t) and average number of grains across the thickness (λ) for all the tested films are shown. The standard deviation in the thickness measurements for different specimen is shown in brackets.

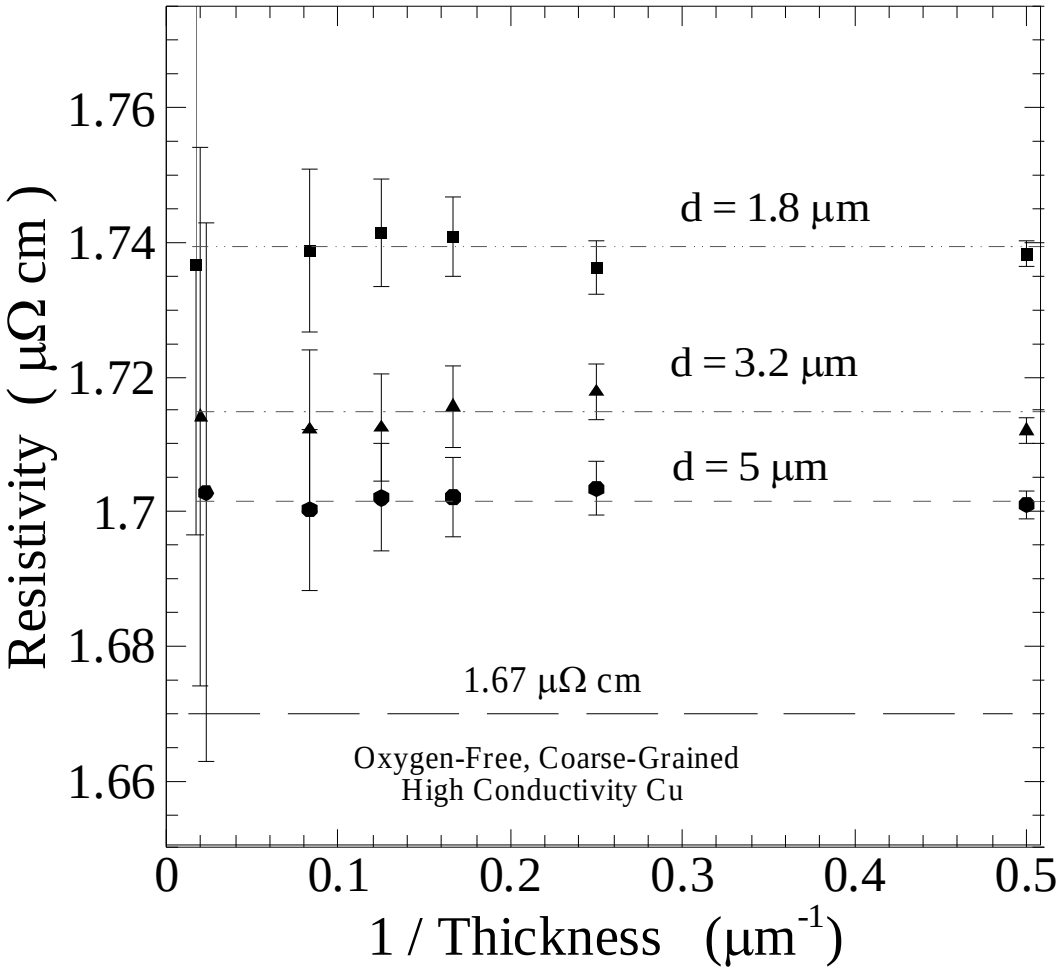

Figure 4.5 The resistivity of undeformed films measured via 4-point method. The reference resistivity value for coarse-grained high-conductivity Cu from Brandes et al is also shown for reference.

the smallest thickness of 2µm. With regards to ductility, both thickness and grain size effects are apparent. For d_g = 3.5µm and 5µm, reducing thickness yields reducing ductility. For example strain to failure varies from 10% to 4% as thickness is ductility reduces from 15% to 4%. However, d_g = 1.8µm specimen show largely thickness independent strain to failure of ~ 2%.

Such remarkably different behavior at these small grain sizes is also seen clearly in Figure 4.7, where the yield stress i.e. σ_y (Figure 4.7 (a)), as well as flow stress i.e. σf at 0.5% strain (Figure 4.7 (b)), for varying film thickness is plotted on a HP plot as a function of the avg. grain size. Qualitatively similar trends are seen for both, yield and flow stress. Therefore, in the discussion that follows, only the yield stress is discussed. However, the discussion can generally be applied to the flow stress of the films as well. Several near linear correlations between σ_y and $\sqrt{1/d_g}$ can be identified in Figure 4.7 for each film thickness. For the yield stress, the lowest of these, for t = 50µm, features a slope of 128 MPa $\mu m^{-0.5}$ i.e. just about 10% higher than the bulk slope of 112 MPa $\mu m^{-0.5}$ (Hansen et al, 1983). This observation indicates that at large thicknesses i.e. in specimens with about 10 or more grains across the thickness, there are no thickness effects and the observed specimen strength agrees with the bulk H-P estimate for the given average grain size. However, with reducing thickness, the observed slope for specimens with different average grain sizes is larger than the bulk H-P slope. In fact, as the data in Figure 4.7 (a) as well as (b) shows, higher slope is observed for smaller thicknesses. For the yield stress, the highest slope, obtained for t= 2µm, is 308 MPa $\mu m^{-0.5}$ (~3X bulk H-P slope).

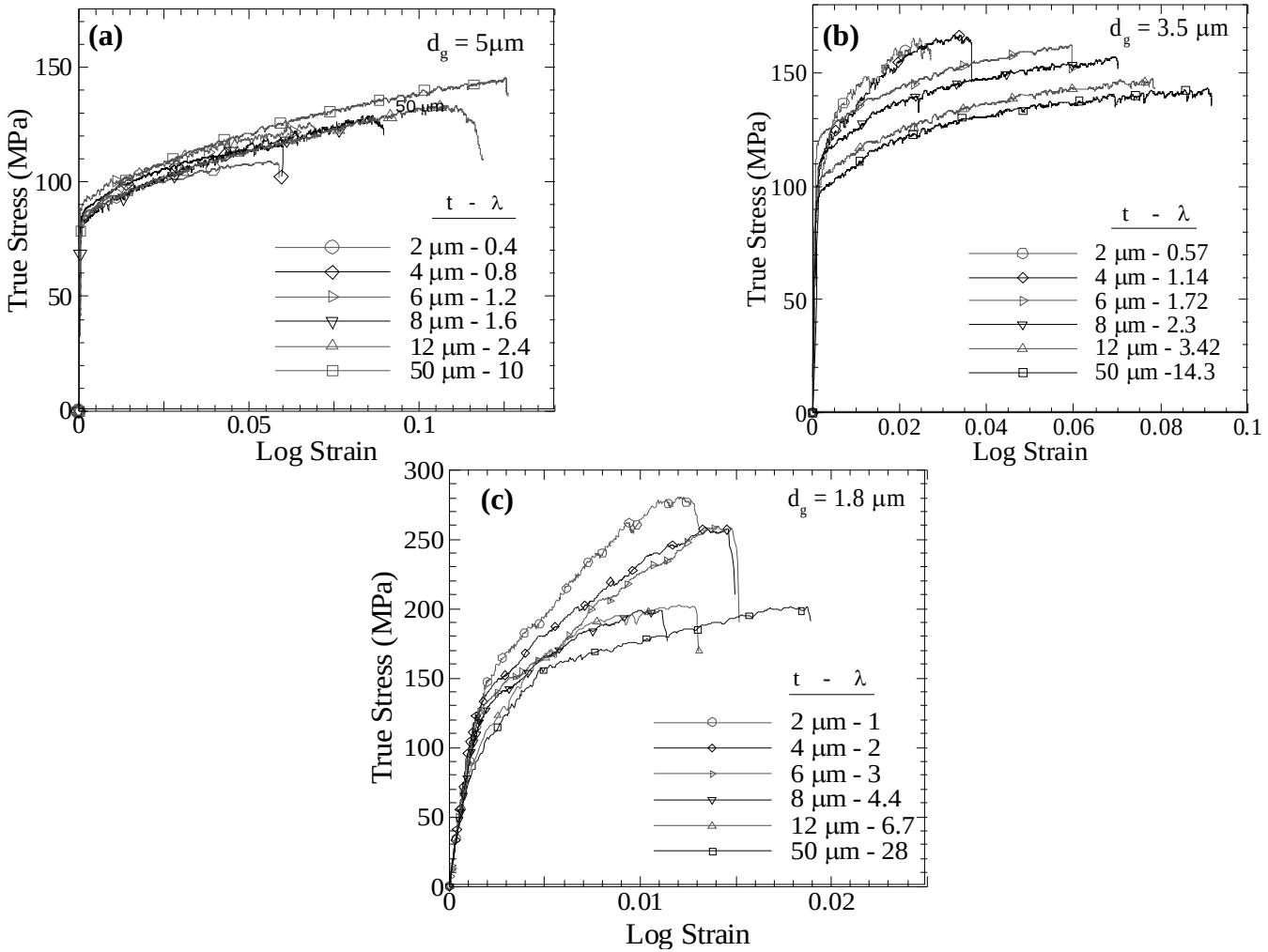

Figure 4.6 Typical true stress log strain curves for all the tested specimen.

(a) $d_g = 5\mu m$ **(b)** $d_g = 3.5\mu m$ **(c)** $d_g = 1.8\mu m$

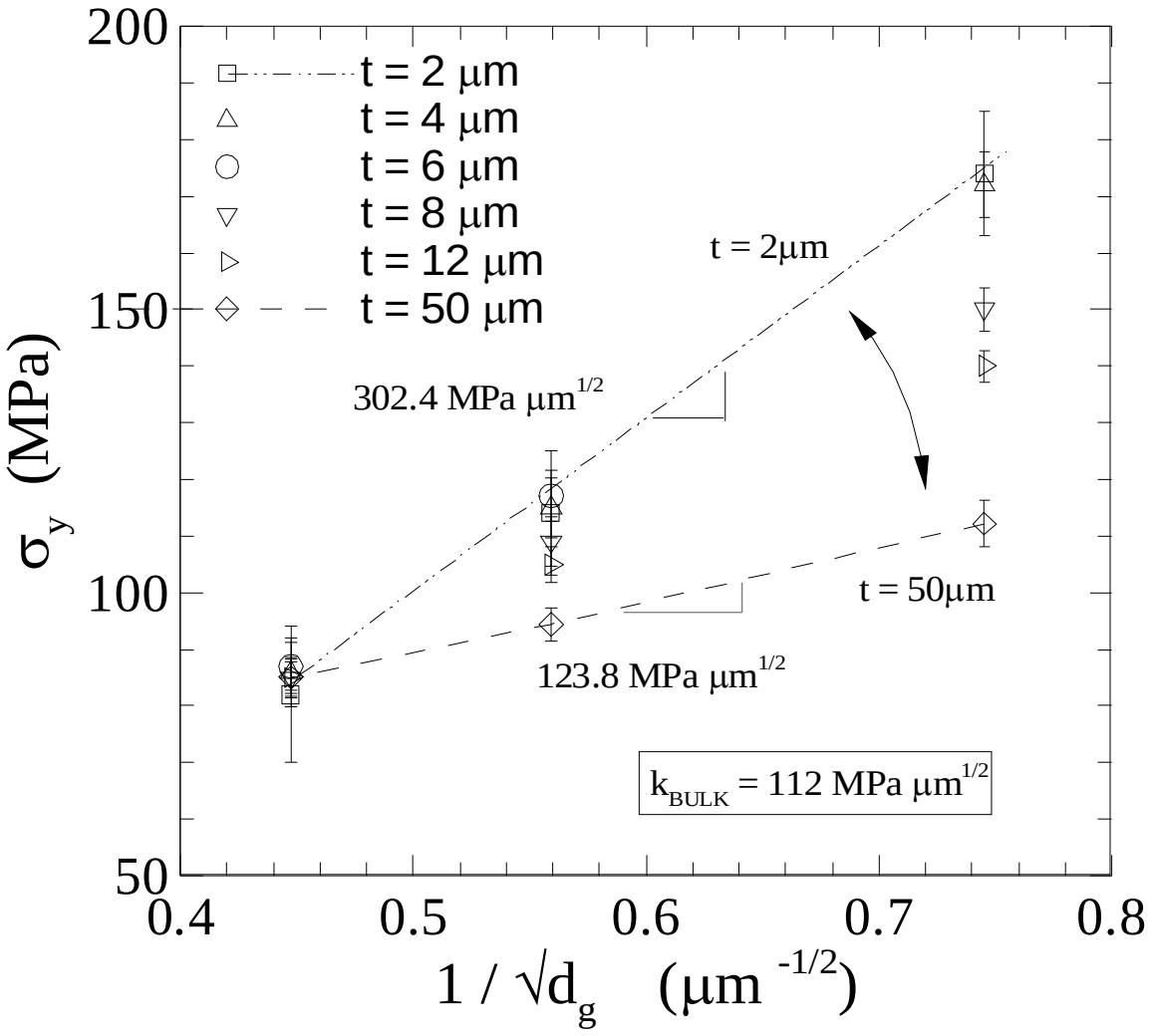

Figure 4.7 (a) The yield stress, σ_y, for all the tested films, for varying film thickness on a Hall-Petch plot. The slope for linear-fits for t = 2μm and t = 50μm specimens is shown. The bulk HP slope (from Hansen et al, 1983) is also shown for comparison.

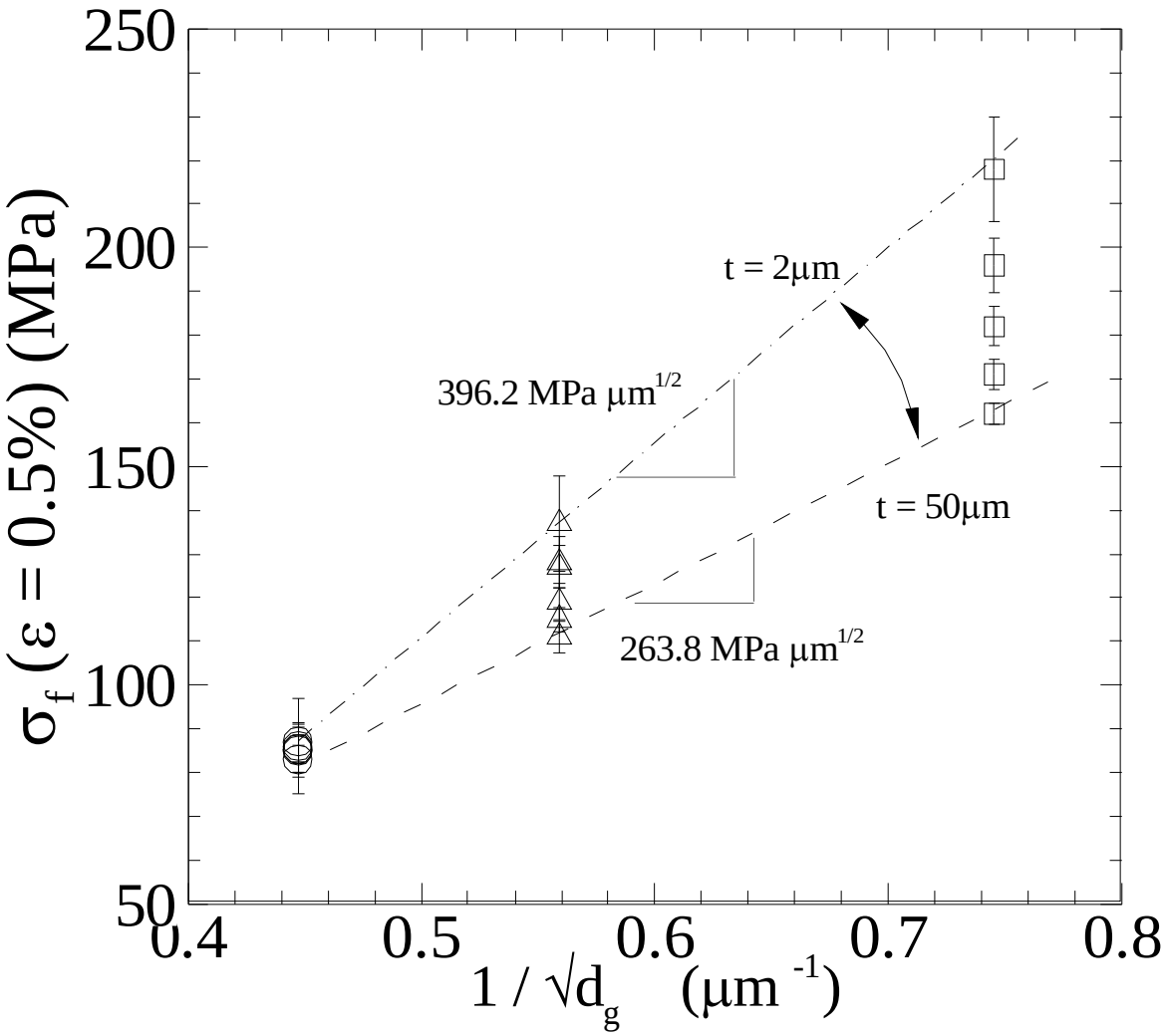

Figure 4.7 (b) The flow stress at 0.5% strain, σ_f (ε=0.5%), of all the tested films for varying film thickness on a Hall-Petch plot. The slope for linear-fit for *t* = 2μm and *t* = 50μm specimens is shown.

These results clearly imply that the observed strengthening with reducing grain size on a HP plot, reported previously in a number of studies for thin film specimen (Venkataraman et al, 1992; Lee et al, 2004; Xiang et al, 2006; Keller et al, 1996) also fe Furthermore, it is also apparent that smaller grain sizes are far more sensitive to thickness effects as compared to the larger grain sizes i.e. thickness and grain size effects are coupled. For example, d_g = 1.8µm specimens are seen to be far more sensitive to reducing thickness as compared to d_g = 5µm specimens.

These trends are further revealed in Figure 4.8, which shows the yield stress, Figure 4.8 (a), as well as the flow stress, Figure 4.8. (b), as a function of the inverse of the thickness for different avg. grain sizes. While reducing thickness, from 50µm to 2µm, has marginal effect on the yield stress of 5µm grain size specimen, prominent thickness related strengthening (w.r.t the bulk estimate) is seen for the 3.5µm and 1.8µm grain size specimens. For example, for d_g = 1.8µm, the yield stress for 2µm thickness is about 70% higher than the yield stress for 50µm specimen with the same avg. grain size (~ bulk estimate). However, for d_g = 3.5µm, the highest yield strength (for t = 6µm) is just about 30% higher than the bulk estimate (for t = 50µm). Therefore, the yield/flow stress on a Hall-Petch plot features an additional thickness effect.

Cumulatively, these trends suggest that thickness dependent strengthening in free-standing films, heretofore only observed unambiguously for much smaller grain sizes (Espinosa et al, 2004; Espinosa et al, 2006), first appears at grain size just smaller

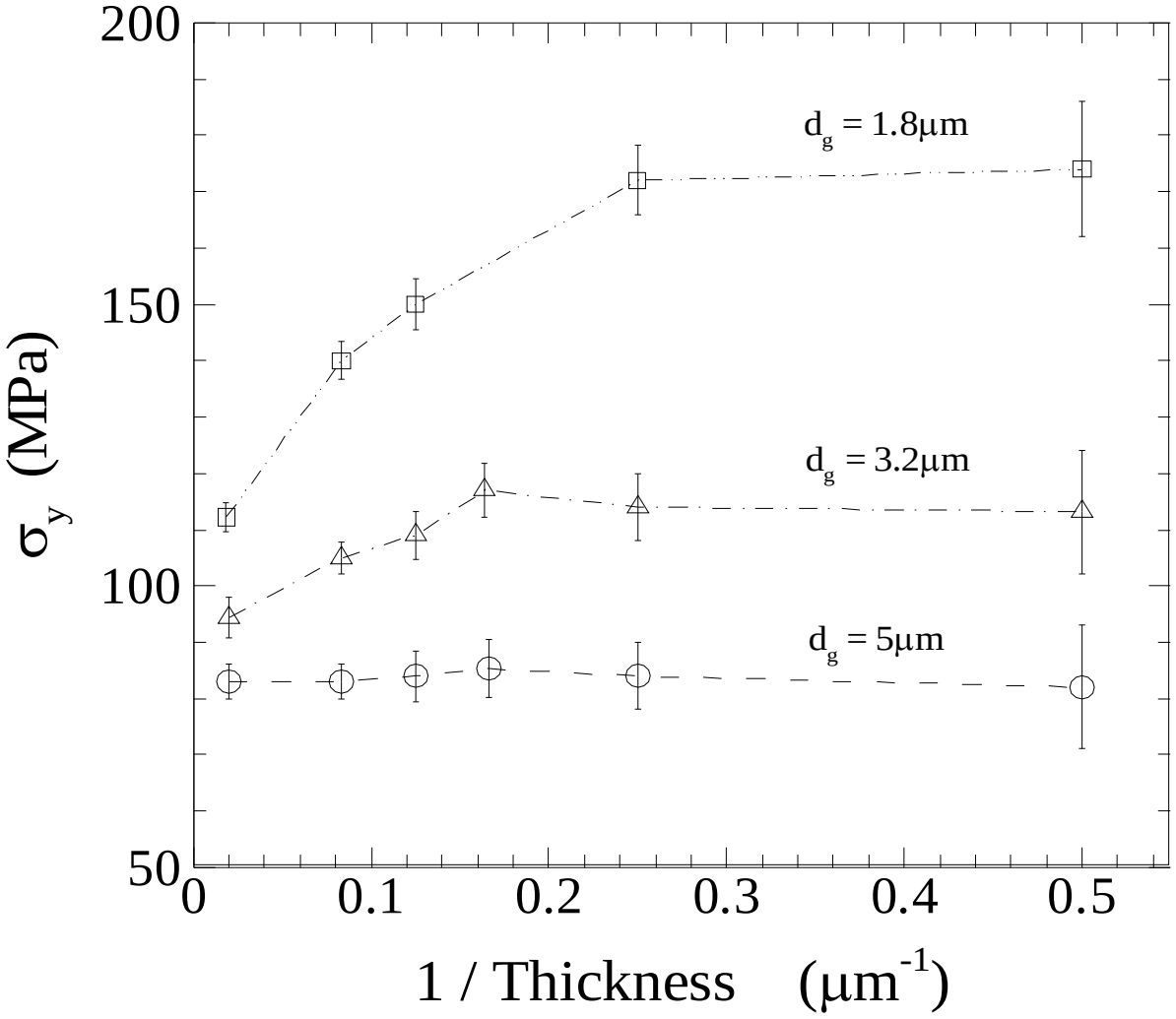

Figure 4.8 (a) The yield stress (σ_y) of films, for varying average grain sizes, as a function of the inverse of the film thickness. While negligible thickness effects are seen for the d_g = 5μm specimens, d_g = 1.8μm specimens show increasing yield strength with reducing film thickness. The trend also shows the apparent saturation in film strength as $t \rightarrow d_g$ i.e.$\lambda \rightarrow 1$.

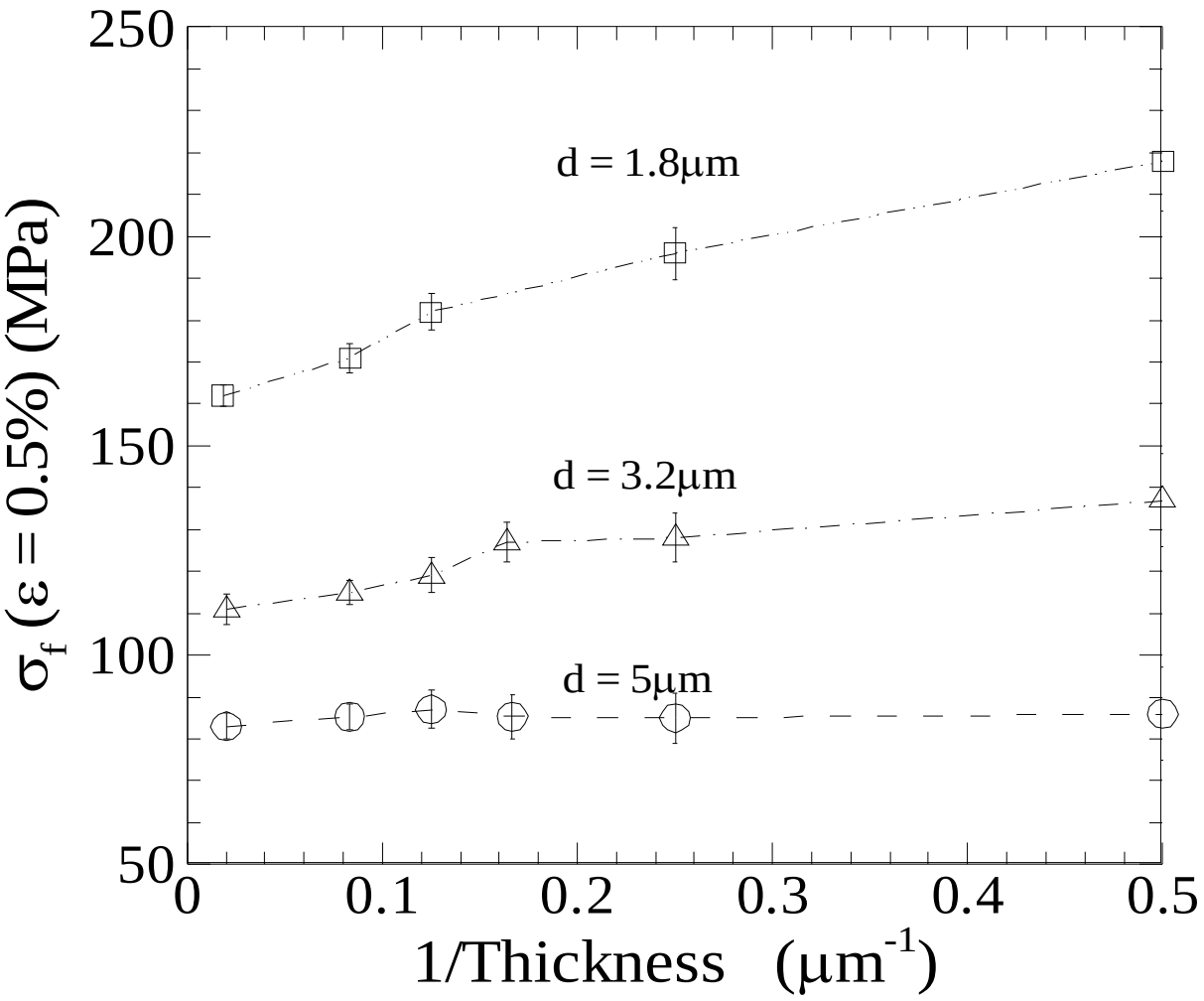

Figure 4.8 (b) The flow stress at 0.5% strain, σ_f (ε=0.5%), for varying average grain sizes as a function of the inverse of the film thickness. While negligible thickness effects are seen for the d_g = 5μm specimens, d_g = 1.8μm specimens show increasing flow stress with reducing film thickness. The saturation in film strength as $\lambda \rightarrow 1$, seen for the yield stress, is not so apparent in the flow stress.

than ~5μm. With reducing grain size, this strengthening becomes more apparent. On the other hand, for grain sizes larger than 5μm, as shown in Chap. 3 and previous studies (Armstrong et al, 1961; Miyazaki et al, 1979; Kals et al, 2000; Janssen et al, 2006; Chauhan et al, 2008), thickness dependent weakening can be expected. It is sensible to assume that d_g = 5μm represents a critical grain size, d_{cr}, wherein the deformation mechanism responsible for thickness dependent strengthening in freestanding films, is almost balanced by the weakening attributed to the increasing proximity to the free-surface with reducing thickness (Miyazaki et al, 1979; Lee et al, 2004; Janssen et al, 2006). In essence, for grain sizes ~5μm, two distinct deformation mechanisms, with competing contributions associated with strengthening as well as weakening, may operate concurrently.

4.4.3 Probing dislocation storage via RERM

The RERM of the deformed films, at 0.5% strain, was performed. Figure 4.9 shows the measured resistivity of the specimens as a function of the film thickness. Each data point here is a result of 4 different measurements. It should be noted that the measured resistivity, after deformation, is indicative of total defect density (per unit volume) in the films including the initially present defects as well as 'stored' defects, generated as a result of deformation. The relative change in residual electrical resistivity, $\overline{\rho}$ (w.r.t. the undeformed state) – defined here as $(\rho_{0.5\%} - \rho_0)/\rho_0$ –, is shown in Figure 4.10. Here, we choose *1/t* as the X-axis, as opposed to *t* as in Figure 4.8, so as to clearly show the effect

of thickness over a wide range of thickness values i.e. t = 2μm – 50μm. Since, bulk HP estimates for yield stress were attained for t = 50μm, this case is referred to as the 'bulk' case in the discussion below. It can be seen in Figure 4.10 that at bulk thicknesses, the relative change in residual resistivity with deformation is grain size dependent. Such a trend is expected since smaller grains, given the relatively larger GB area per unit volume, would accumulate more defects. For a constant avg. grain size, as the number of grains across thickness are reduced, the general trend in Figure 4.9 and Figure 4.10 suggests that ability to store defects generally reduces. Such a trend however is logical because with reducing thickness, the amount of GB area within the specimen volume also reduces. However, the trends in Figure 4.9 suggests that besides the expected reduction in residual resistivity due to reducing GB area, there is an additional mechanism that is related to the particularly sharp drop in the larger grain sizes as λ approaches 1. For example, with reducing thickness, $\bar{\rho}$ changes significantly for d_g = 5μm to about 14% of its bulk value. Similarly, d_g = 3.5μm specimens show a 35% drop as compared to the bulk value. At the same time, for 1.8μm, the sharp drop is not apparent and $\bar{\rho}$ reduces gradually by about 20% with a reduction in thickness from 50μm to 2μm. These observations suggest that the effect of thickness on defect storage, largely dislocations in the current context, is very different for the three tested avg. grain sizes. While the larger grains (5μm and 3.5μm) drastically lose their ability to store dislocations and show a sharp drop in $\bar{\rho}$ with reducing thickness, smaller grains (1.8μm) are more or less unaffected by reducing

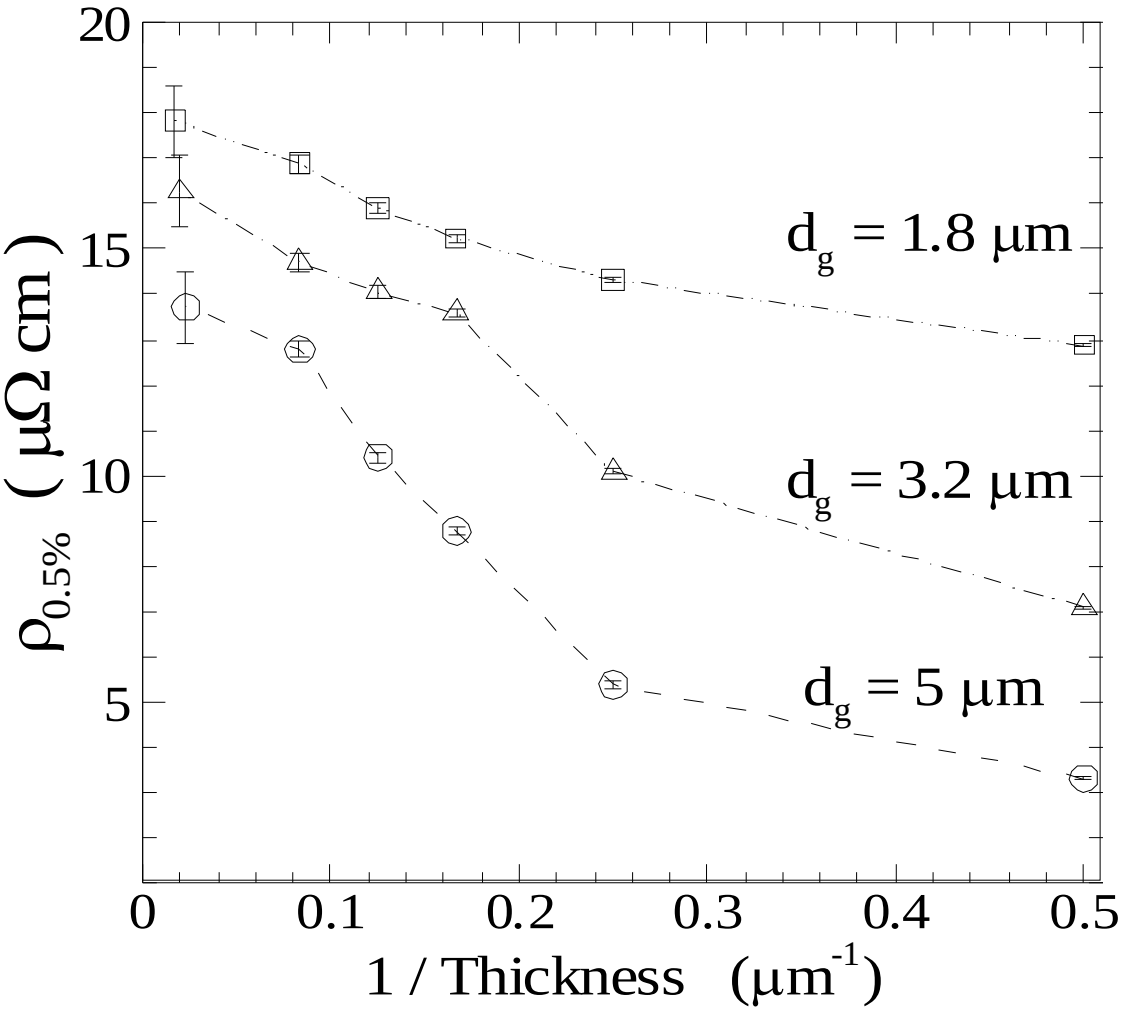

Figure 4.9 Electrical resistivity of deformed specimen (at 0.5% macroscopic strain), with different average grain sizes, as a function of the inverse of film thickness.

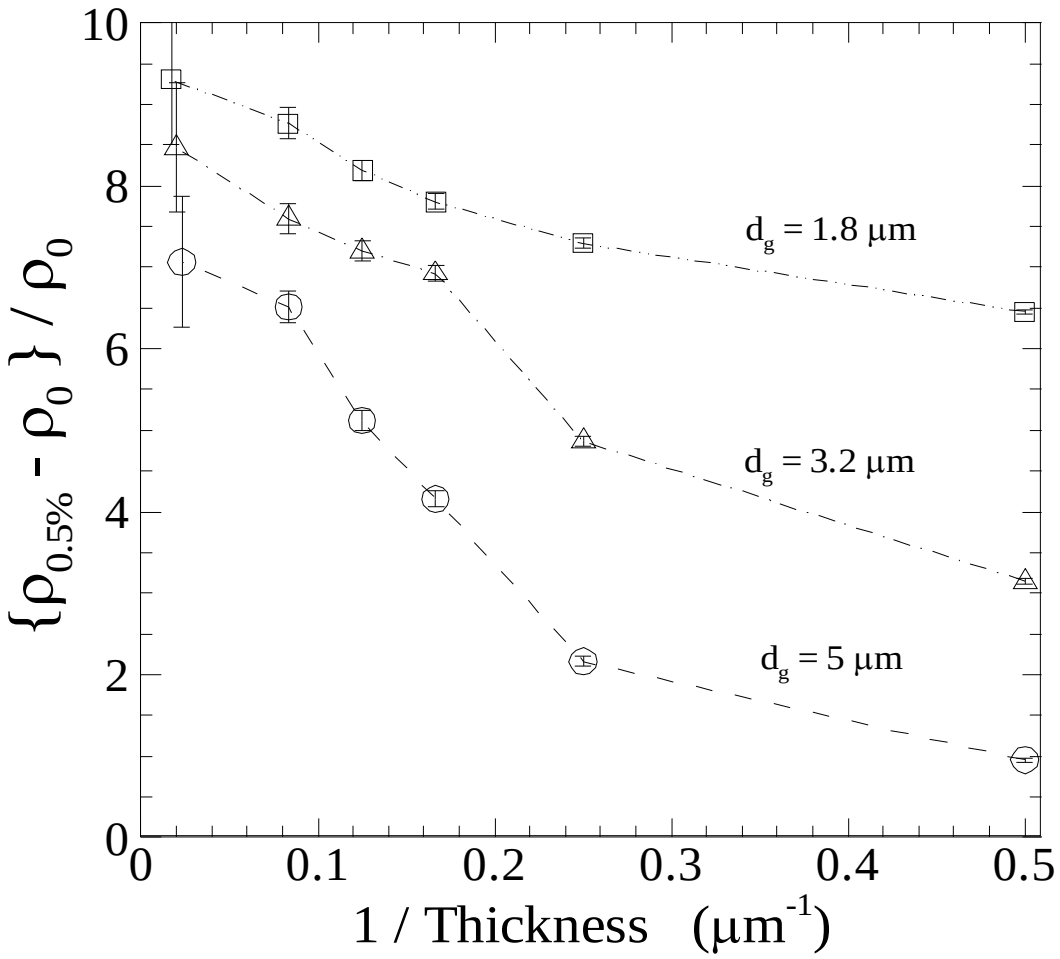

Figure 4.10 The relative change in resistivity with deformation (0.5% strain) as a function of the inverse of the film thickness. The relative change in the film resistivity w.r.t. undeformed films i.e. $\rho_{0.5\%} - \rho_0$, is normalized here with the resistivity of the undeformed films (ρ_0). The sharp drop in the residual resistivity with reducing thickness, seen here for d_g = 5μm and d_g = 3.5μm specimens, is attributed to the annihilation of intragranular dislocations at the free surface.

thickness and the observed gradual, and modest, reduction in $\overline{\rho}$ for this case can largely be attributed to reducing GB area per unit specimen volume alone.

In the discussion that follows, these RERM results, revealing the effect of thickness as well as average grain size on the generation and storage of dislocations with deformation, are analyzed to draw inferences regarding the underlying physical mechanisms. More importantly, these observations are reconciled with the observed size effects on the yield as well as flow strength, presented in Sec. 4.3.2.

4.5 DISCUSSION

4.5.1 Diminishing intra-granular dislocation activity

The observation of diminishing dislocation storage with reducing thickness, reported in Sec. 4.3.3, can be understood in the context of the discussion in Chap. 3 and previous studies (Chauhan et al, 2008; Kals et al, 2000; Janssen et al, 2006) i.e. reducing λ essentially implies increasing volume fraction of surface grains. As a result, with reducing λ, an increasingly larger fraction of the intragranular (IG) volume is in close proximity to the free surface. The effect of free-surface on the overall mechanical strength as well as dislocation storage can be understood in the context of diminishing compatibility constraints as well as increased dislocation mobility along slip systems that end at the free-surface owing to the net attractive configurational force acting on

dislocations due to the free surface. In order to relieve such free-surface induced image forces, intragranular (IG) dislocations essentially glide out to the free surface and annihilate, leaving behind surface steps. Therefore, the observed sharp drop in residual resistivity, $\overline{\rho}$, with reducing thickness is to be expected since with reducing λ the fraction of total specimen volume exposed to the free surface, which is susceptible to dislocation annihilation, increases in addition to the reducing GB area per unit specimen cross-section. Thus the onset of the sharp drop in the accumulated defect density is likely to be due to annihilation of IG Frank-Read type dislocations for d_g = 5μm & 3.2μm. Previous investigations of the texture of deformed specimen with similar grain sizes in Al thin films revealing prominent grain thinning as well as relatively dislocation free grain interiors (Lee et al, 2004) support such an interpretation. Therefore, such drastic loss of stored dislocation content within grains, seen with reducing thickness for d_g = 5μm & 3.2μm, is indicative of prominent IG dislocation activity in close proximity to the free surface.

With regards to the overall mechanical strength, this interpretation also suggests that the free surface related weakening on the mechanical strength with reducing thickness, presented in Chap. 3 here as well as in pervious studies (Armstrong et al, 1961; Miyazaki et al, 1979; Kals et al, 2000; Janssen et al, 2006), is quite likely also prevalent in specimens with d_g = 5μm & 3.2μm. However, with reducing grain size further to d_g = 1.8μm, the free-surface effect that contributes to the aforementioned weakening contribution, gets diminished. Our residual resistivity measurements validate this

interpretation since the observed annihilation of IG dislocations and the resulting loss in dislocation storage, is almost non-existent in d_g = 1.8μm specimens (only a gradual reduction in residual resistivity with reducing thickness), but quite prevalent in d_g = 5μm and 3.5μm (sharp drop, in addition to the gradual reduction in residual resistivity, with reducing thickness). Thus, taken together, the residual resistivity measurements in Sec. 4.3.3 suggest that with reducing average grain size from 5μm to 1.8μm, IG dislocation activity is progressively diminished. These observations may also suggest that d_g = 1.8μm or so is the minimum dislocation mean free-path required for activation of IG Frank-Read type dislocations.

4.5.2 Role of GB dislocation sources

An important feature of the reported trends in Figure 4.9 and Figure 4.10 is that the smaller grains i.e. d_g = 1.8μm, featuring only a gradual and modest reduction in residual resistivity with reducing thickness, do not show prominent IG dislocation activity. This observation is in agreement with the current understanding on the influence of grain size on the nucleation of IG dislocations. Various TEM observations (Keller et al, 1996; Espinosa et al, 2004) as well as studies employing molecular dynamics and discreet dislocation dynamics (Yamakov et al, 2002; Yamakov et al, 2003; Espinosa et al, 2006) based simulations to study the mechanisms pertaining to plasticity suggest that with reducing grain size, a gradual break-down of conventional IG Frank-Read type dislocation activity is seen. In fact, below a certain critical grain size in FCC metals <

200nm - 1μm, likely a function of the stacking fault energy (Cheng et al, 2003), lattice dislocations are nucleated only at the grain boundaries. This can be understood in the context of the influence of the microstructural constraint on dislocation nucleation. Espinosa et al (2006) argue that in geometrically confined systems, dislocation nucleation, characterized by an activation stress, is very sensitive to quantities such as dislocation source length, distance from grain boundaries, distance from the free-surface etc. In traditional materials i.e. d_g > 1μm or so, dislocations are nucleated at both the grain boundaries as well as grain interior. While IG dislocations are activated within the grain interior in regions away from the grain boundaries, regions adjoining the grain boundaries generally feature GB dislocations since the activation stress for IG dislocations near the grain boundary would be much higher (Espinosa et al, 2006). However, as the grain size reduces, the fraction of favorably located IG dislocations reduces and consequently GB dislocations dominate. To this effect, TEM observations by Keller et al (1996) as well as Espinosa et al (2004) in Cu thin films d_g ~ 200nm reveal that following deformation, no dislocations are observed in the grain interiors.

Therefore, in the current study, while d_g = 5μm features considerable FR type dislocation activity as well as GB type dislocations, however, with reducing grain size from d_g = 5μm to d_g = 1.8μm, the amount of IG type dislocations reduces and dislocations are primarily generated at the GBs. Such GB dislocations are highly entrapped (or piled up) by the grain boundaries and are less susceptible to annihilation at the free surfaces (Yamakov et al, 2002; Espinosa et al, 2006). As a result, while free

surface strongly influences the dislocation storage in the larger grain sizes, for d_g = 1.8μm case, the free-surface effect is less prominent. Thus the fact that prominent IG dislocation activity is absent in d_g = 1.8μm specimen indicates that plastic deformation in these specimens proceeds primarily via GB dislocations.

From the point of view of thickness effects on the strength as well as dislocation storage, such a transition in the underlying deformation mechanism from mixed dislocations (both IG and GB dislocations) to mostly GB dislocations with reducing grain size has two primary consequences. Firstly, the free surface related weakening seen for traditional materials with reducing thickness (discussed in Chap. 3) while still expected to be prevalent, would get diminished. Secondly, increasingly prominent GB dislocation activity would introduce an additional strengthening effect with reducing thickness as follows: with reducing thickness for a constant avg. grain size, the volume fraction of GB area per unit specimen volume reduces. As a result, the amount of GB dislocation sources available also reduces. Such a statistical effect i.e. reducing available GB dislocation sources with reducing thickness, would lead to a strengthening effect with reducing thickness. Thus, the thickness effects on the overall strength can be considered to be an outcome of two distinct mechanisms: weakening with reducing thickness due to increasing exposure to the free-surface and strengthening due to a reduction in the available GB dislocation sources with reducing thickness. The relative contribution of the two effects to the overall thickness effects is, obviously, a strong function of the average grain size.

The data for thickness effects on yield stress as well as flow stress, presented in Fig 4.8, in fact reveals that for d_g = 5μm, the two effects are balanced by each other. With reducing thickness from 50μm to ~ 2μm, the overall yield strength shows only a negligible thickness effect indicating that while both weakening and strength type effects are present, their magnitudes are comparable to each other and consequently cancel each other out. However, for d_g = 3.5μm, with reducing thickness a slight increase in strength is noted indicating that while the weakening effect is present, the increase in strength due to GB dislocation source starvation is slightly greater. d_g = 1.8μm specimens here show very prominent increase in strength with reducing thickness, indicating that GB dislocation source starvation dominates the free-surface effect. Therefore, the range of average grain sizes tested in this study i.e. 1.8μm ≤ d_g ≤ 5μm, represents a regime of transition where, while both free-surface related weakening as well as source starvation strengthening, with reducing thickness for a constant avg. grain size, are present. With reducing average grain size, the role of the former gets diminished while the latter becomes increasingly dominant. The significance of d_g = 5μm as a critical length scale where these two effects are equal, is not quite clear at this stage. It is quite likely related to the peculiar initial defect density in the films i.e. it could be an artifact of the processing. Therefore, while the trends observed here might be qualitatively universal, the exact length scales where this transition occurs is quiet likely processing dependent.

A simple geometric argument can be formulated to validate this interpretation. It is expected that the GB dislocation source content would scale with the GB area within

an average specimen cross-section. Therefore, the additional increase in strength (derived from experimental measurements in this study) attributed to source starvation strengthening, would yield a unique correlation with the GB area within an avg. specimen cross-section. The grains in a polycrystalline specimen can be approximated with a simple space filling geometry i.e. either a cube or a hexahedral prism (more realistic). Assuming individual grains to be cubic with each side being d_g or hexahedral prisms with each edge $d_g/2$ and height being d_g, the total GB area per unit volume, Ω, can be calculated for specimen with λ grains across the thickness i.e. thickness, $t = \lambda\, d_g$. Only surface area of the grains that is shared by surrounding grains is counted towards Ω i.e. the surface area exposed to the free surface is not accounted. These assumptions yield:

$$\begin{aligned} \Omega &= \frac{3.3077\lambda - 1}{\lambda\, d_g} \qquad (hexahedral) \\ &= \frac{5\lambda - 1}{\lambda\, d_g} \qquad (cubic) \end{aligned} \tag{4.3}$$

Figure 4.11 (a) shows Ω as a function of λ for both hexahedral as well as cubic grains, for d_g = 1.8µm, 3.5µm and 5µm. Clearly, Ω is very sensitive to the no. of grains across the thickness (or, for a constant avg. grain size, the thickness). In general, with reducing λ, Ω reduces until it becomes 0 for a certain λ – a peculiarity of the choice of the geometry. For very large λ however (around 10 or so), a limiting GB area per unit specimen volume is attained, Ω_{bulk}, such that smaller grains yield larger GB area per unit volume as compared to larger grains. Figure 4.11 (b) presents the Ω value from Eq. (4.3) for different grain sizes normalized by Ω_{bulk} (obtained for t = 50µm - largest thickness

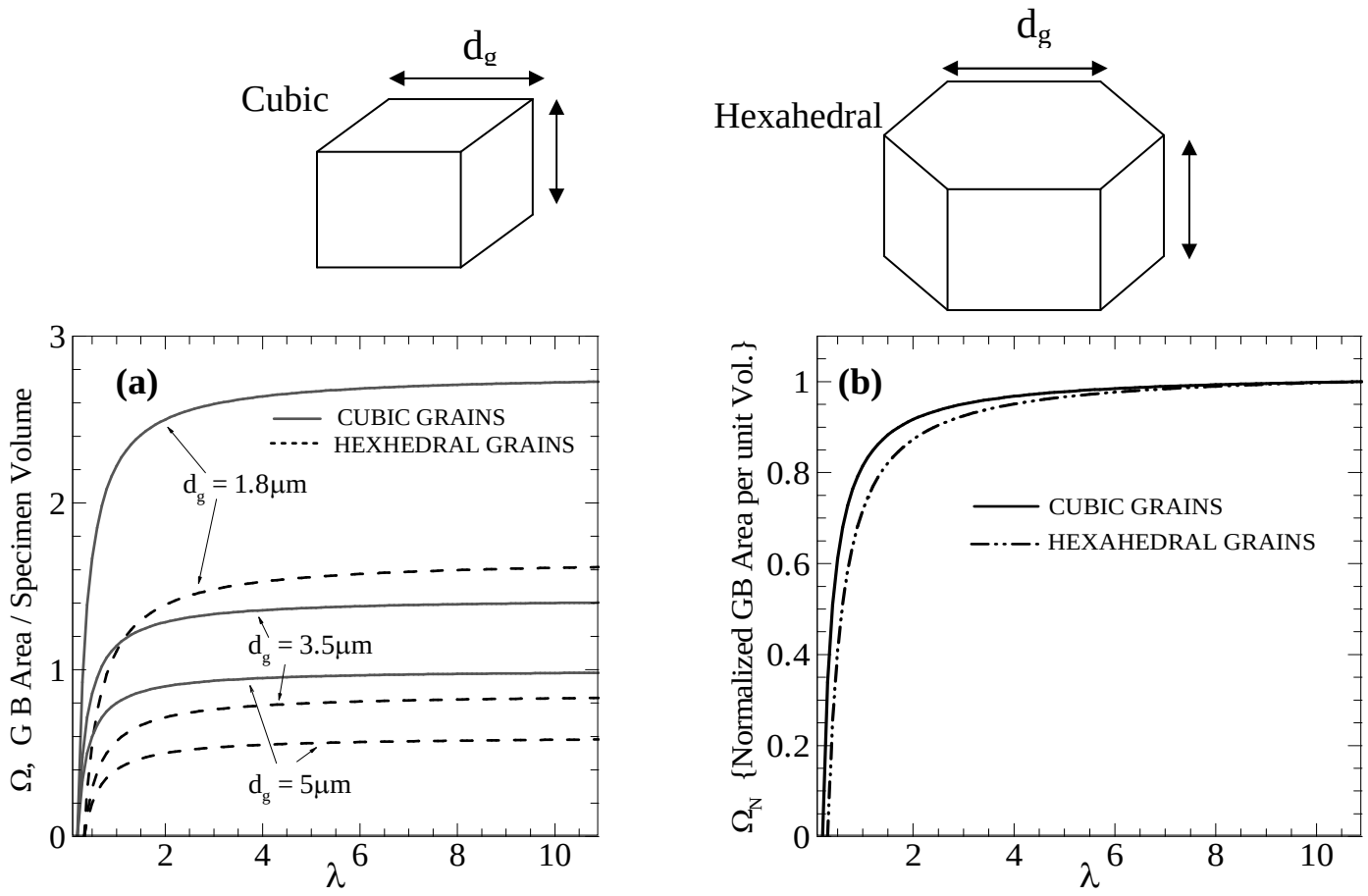

Figure 4.11 Effect of thickness, for a given grain size, on the total GB area per unit specimen volume. **(a)** GB area per unit volume as a function of λ for d_g = 1.8, 3.5 and 5μm **(b)** Normalized GB area per unit specimen volume for cubic as well as hexahedral grain assumptions.

tested in this study) for each grain size, represented as Ω_N. Ω_N here represents the relative reduction in the GB area per unit volume with reducing thickness, with respect to the 'bulk' thickness for a given avg. grain size. It can be seen in Figure 5.6 (b) that while the overall magnitude of Ω may scale with avg. grain size, the trend of reducing relative GB area per unit specimen volume with reducing λ is grain size independent. It is however sensitive to geometry i.e. cubic assumption yields a different trend as compared to the hexahedral assumption.

The additional contribution to the overall yield strength due to dislocation source starvation, σ_t , is identified with the difference between the overall yield strength, σ_{film}, and the prediction from the previously introduced model that accounts for the free surface effect observed in the foil specimen in Chap. 3 i.e. Eq. (3.4) and shown in Figure 3.9. Therefore,

$$\sigma_t = \sigma_{film} - \left\{ \sigma_Y^S(d) \times \frac{1}{\lambda} + \sigma_Y^B(d) \times (1 - \frac{1}{\lambda}) \right\} \qquad (4.4)$$

Figure 4.12 shows the overall yield stress obtained for the electrodeposited films, σ_{film} *in* Eq. (4.4), as function of λ. Phenomenological prediction along the lines of the trends obtained for the rolled foil specimen from Chap. 3 (Set A) is also shown for d_g = 1.8µm, 3,2µm and 5µm i.e. second term on the RHS of Eq. (4.4). The surface HP estimate, σ_Y^S ,

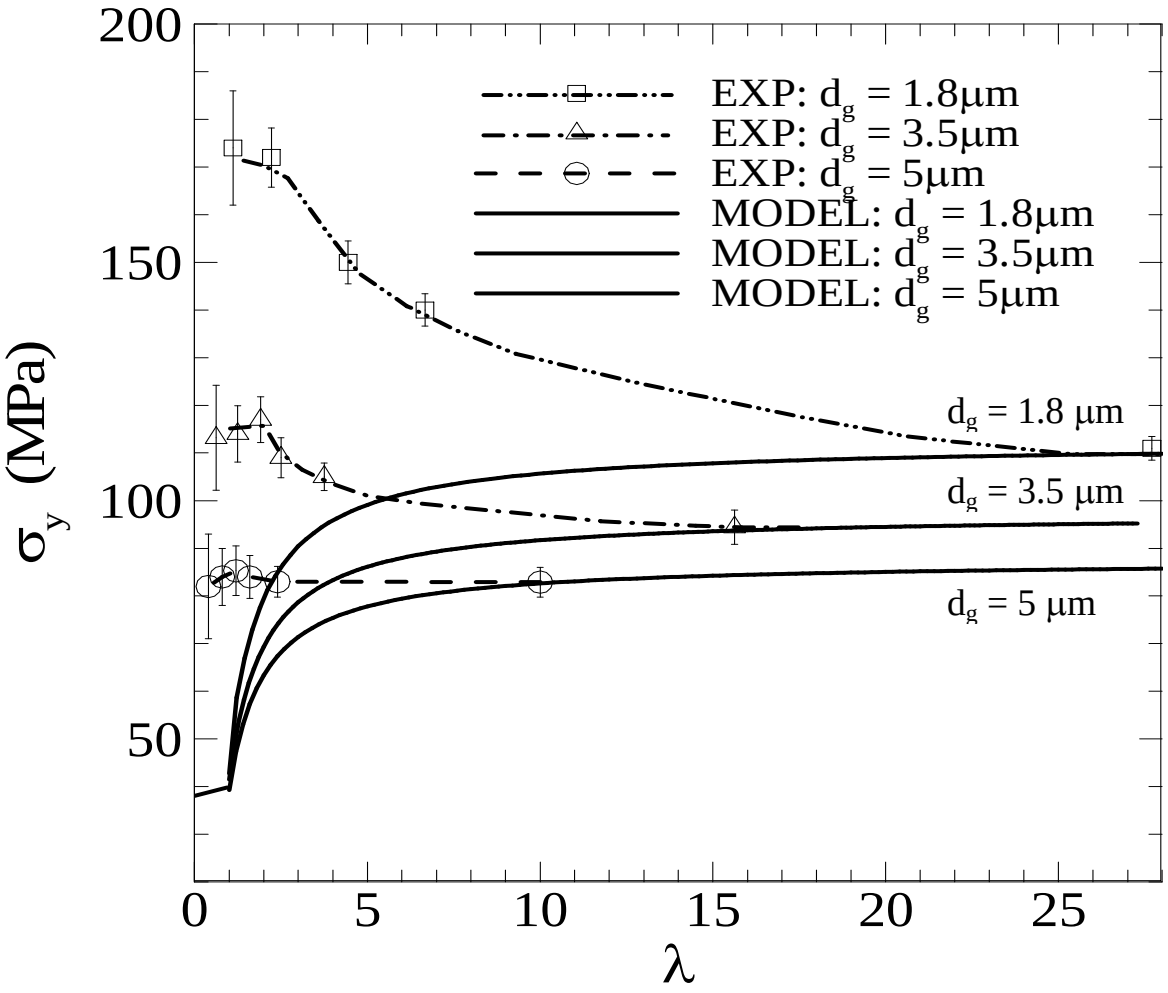

Figure 4.12 Comparison between model predictions, accounting for thickness effect on microstructural constraint based on the trends for Set A specimens, and experimental values for yield strength for Set B specimens. It can be seen that while the model predicts reducing yield stress with reducing λ, the experimental data shows increasing strength with reducing λ for d_g = 1.8μm, 3.5μm and 5μm specimens.

for d_g = 1.8μm, 3,2μm and 5μm, was calculated using the surface HP parameters found for Set A specimen with d_g = 11 - 50μm (Figure 3.9). The implications of this assumption i.e. that the surface HP parameters obtained for the foil specimens with much larger grain sizes also apply to these electrodeposited films (Set B) is discussed later in this section. It is quite clear that the expected weakening with reducing grains across the thickness on the overall yield stress, as observed for the Set A specimens with larger grain sizes (Figure 3.8), is absent for these specimens. In fact, Set B specimens show increasing overall yield stress with reducing no. of grains across the thickness for both d_g = 1.8μm and 3.2μm. For d_g = 5μm, almost no strengthening is observed until weakening appears with λ approaching 1 i.e. multicrystalline specimen. In Eq. (4.4), we associate the difference between the experimental yield stress and the predictions from the phenomenological model with the additional contribution from the source starvation strengthening.

The total GB dislocation source content, related to the total GB area within the specimen of a given thickness and avg. grain size, can be found from the GB area per unit volume in Eq. (4.5) after multiplication with the total specimen volume (of the gauge section). We normalize this quantity with the GB area in a bulk specimen, of the same avg. grain size but with a thickness of 50μm (identified with bulk in this study). A new dimensionless parameter, Ψ, is introduced as follows:

$$\Psi = \frac{\Omega \times t\, w l}{(\Omega \times t\, w l)_{bulk}} = \Omega_N \frac{t}{t_{bulk}} \qquad (4.5)$$

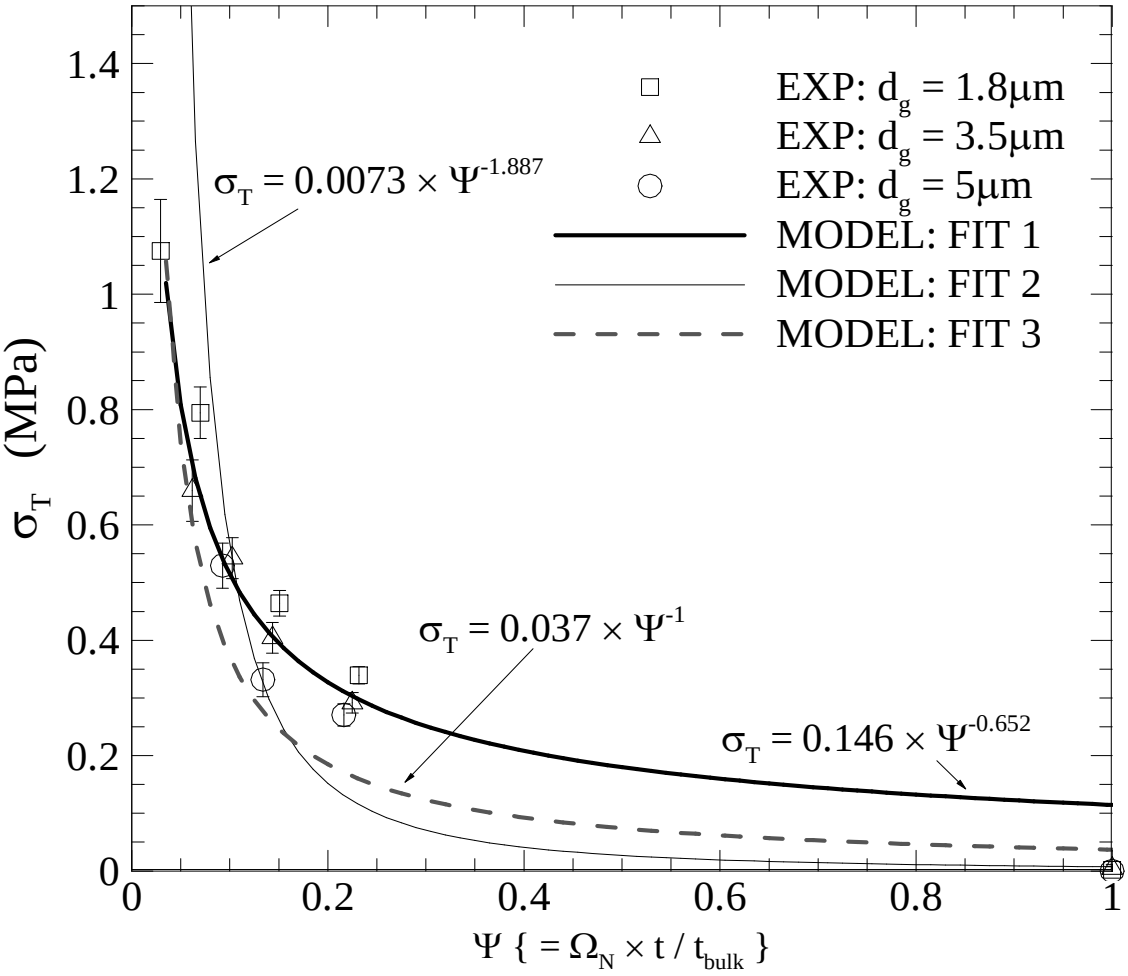

Figure 4.13 Contribution from GB dislocation starvation, σ_T (from Eq. (4.4, as a function of normalized GB area per unit specimen volume, Ψ (from Eq. (4.5)), for hexahedral grains). The experimental data is compared with the corresponding fits.

where, *w* and *l* are the gauge width and gauge length respectively and t_{bulk} is 50μm. Ψ, thus, represents the relative GB area within a specimen of given thickness and avg. grain size, with respect to a bulk specimen of the same avg. grain size.

Figure 4.13 plots σ_t from experiments obtained for d_g = 1.8, 3.5 and 5μm and varying thickness, normalized with the HP prediction of the yield strength for the bulk specimen with the same avg. grain size, as a function of Ψ assuming the grains to be hexahedral prisms. Power law equation i.e. $\sigma_t = C\,\Psi^m$, was found suitable to describe the overall trend in Figure 4.13. The fitting coefficients were obtained for the best fit for all data points except the bulk specimen with Ψ = 1 (Fit 1). Fit 1 yields an exponent of -0.65. The best fit including the bulk specimen, with an exponent of ~ -2, is also shown, Fit 2. It is seen that upon extrapolation of Fit 1 to Ψ = 1, the predicted contribution from starvation strengthening is not zero, as expected from experiments, but attains a value of around $0.1\,\sigma_{bulk}$. However, Fit 2, which does yield σ_t = 0 for $t = t_{bulk}$, does not agree very well with the overall trend of the data points, for thicknesses other than the bulk case. Much lower strengthening contribution is seen at smaller thicknesses as compared to the prediction from Fit 2. Fit 3 is obtained by fitting the entire data including the bulk specimen with an exponent of -1. For this case, residual strengthening at bulk thickness is found to be $0.03\,\sigma_{bulk}$.

The source of this discrepancy is not quite clear at this stage; however it appears to be related to our accounting of the weakening contribution from diminishing

microstructural constraint as shown in the second term on the right hand side Eq. (4.4). This term is plotted in Figure 4.12 for Set B specimen. Although it is to be expected that a weakening contribution due to the thickness effect on the microstructural constraint would persist even for these smaller grain sizes, it is quite likely that this contribution may not be amenable to the model obtained for the larger grain sizes (Set A). Specifically, the surface HP parameters used in Eq. (4.4), obtained for Set A specimen with much larger grain sizes (shown graphically in Figure 3.9), could be grain size dependent themselves. This is primarily because, unlike at larger grain sizes comparable to those in Set A where the contribution from the grain interiors dominates (Armstrong et al, 1961; Geers et al, 2006), grain sizes in set B (approaching ~1μm) would likely have a larger contribution from regions in the vicinity of the grain boundaries. This is partly expected because with reducing grain size, the volume fraction of grain interior region would reduce considerably. Also, given the transition from GB + IG dislocations to primarily GB dislocations, the role of intragranular regions would diminish at such small grain sizes. As a result, we expect Eq. (4.4) overestimates the weakening contribution due to the free-surface effect (second term on the RHS) for d_g = 1.8, 3.5 and 5μm specimens. Thus, it follows that the contribution from starvation related effects could be even larger than what we interpret here. One would expect that experimental characterization of such starvation related strengthening for grain sizes well within the ultrafine grained regime, where only GB dislocation sources are active, would be more amenable to the formulation of a phenomenological relationship.

4.5.3 Transition to source-limited plasticity and the onset of source starvation strengthening

Qualitatively, these trends can be extrapolated further. The observation of drastic increase in strength noted by Espinosa et al (2003; 2004; 2006) in Cu, Al and Au thin films with d_g ~ 200 - 300nm, as the thickness reduces from 1μm to 200nm, indicates that for grain sizes within the ultrafine grained regime, where only GB type dislocations are active, thickness-dependent strengthening is to be expected with reducing thickness. These observations suggest that the overall trend of thickness effects on the strength of free-standing metallic films can be rationalized as follows: at larger grain sizes i.e. d_g ~ O (10 - 100μm) common to most foil or plate type specimen, thickness effects primarily arise due to reducing microstructural constraint with reducing thickness – a result of the influence of the free-surface on intra-granular dislocation activity. In these cases, dislocations can propagate and multiply at lower resolved shear stresses with reducing thickness; consequently the observed strength (yield or flow stress) reduces with reducing thickness. On the other hand, for d_g < O (1μm-100nm), thickness effects arise primarily due to the statistical reduction of available dislocation sources with reducing thickness. Such small grain sizes typically do not feature prominent intra-granular dislocation activity and free-surface related weakening with reducing thickness is not observed. As a result, an increase in strength with reducing thickness is to be expected. Therefore, with reducing thickness in polycrystalline freestanding films, we note a transition from propagation-limited plasticity in traditional materials to source limited plasticity in ultra-fine grained materials. This transition in the underlying deformation mechanism

consequently leads to a transition from thickness-dependent weakening to thickness-dependent strengthening.

The results presented in this study are significant in that they tie together previous observations of ‘dislocation starvation’ related strengthening observed in freestanding specimens under homogenous deformation. The idea of dislocation starvation leading to thickness effects upon miniaturization is not new. G.F. Taylor in 1924 (Taylor et al, 1924) reported the tensile strength of 30μm diameter single crystal Antimony wires to be 180-220 MPa, while 4mm diameter wires, prepared via the same processing techniques, showed fracture strengths of just 5-8 MPa. Similar observations of much higher strengths in miniaturized specimens were also made for cadmium crystals i.e. 14X strength at ~25μm as compared to ~500μm. The earliest interpretations of such effects came as far back as 1947 in the context of extremely high size dependent strengths observed in single crystal Cu whiskers (Fisher et al, 1947; Brenner et al, 1956; Brenner et al, 1958). Brenner et al (1947) presented data for Cu, Fe and Ag whiskers with diameters ranging from ~2μm to ~10μm. Such whiskers initially contained a very small amount of defects (dislocations). Upon loading, elastic response is seen until a very high critical stress (~ 600 MPa). Beyond this point of criticality, the stress drops drastically and plasticity commences at a very low stress. The very high observed stresses are observed initially because of the high stresses required for the nucleation of the very first dislocations, in the absence of prominent dislocation sources. This is a direct consequence of dislocation source starvation leading to higher strength. Once dislocations are initially nucleated, subsequent plastic flow can occur at much lower stresses because dislocations sources

increase rapidly because of dislocation multiplication via double cross-slip and other processes (Greer et al, 2005).

Another example of dislocation starvation related effects are the recent studies involving compression of micro and nano sized pillars, which are often single crystals (Greer et al, 2005; Uchic et al, 2004). These studies typically employ Focused Ion Beam (FIB) to create pillars within grains of a bulk sample. The individual pillars are then compressed using a nano-indenter and force displacement response is obtained. Greer et al (2005) for example tested pillars with diameters varying from 200nm to ~10μm. The pillars typically had an aspect ratio of 5 i.e. pillar height was ~5 times the diameter. They found increasing strength with reducing pillar diameter. Similar results were obtained for single crystal Ni pillar, with pillar diameters varying between a few millimeters to just 0.5μm (Uchic et al, 2004). These experiments showed that while pillar response with reducing diameter up to ~20μm was within ~30% of the bulk response (the response of pillars which were a few millimeters in diameter), pillars with diameter less than 5μm showed strengths as much as 100% higher than the bulk case. Reducing the diameter below 5μm, lead to even higher strengths.

Their interpretation, again, was based on the idea of dislocation starvation. In this case, higher initial yield strength is obtained due to the scarcity of dislocations, similar to the whisker experiments. However, unlike the sudden softening observed in the whisker experiments, micro-pillars showed progressive increase in strength with continued deformation. The reason for this, as suggested in Greer et al (2005) is that once the initial

dislocations are nucleated in the pillars, these dislocations glide out along specific slip planes and are lost to the free surface, where they annihilate. This is because of the small dimensions of the pillars where due to their proximity to the free surface, the distance traveled by dislocations before annihilation is much smaller than that required for dislocation multiplication processes to occur (Greer et al, 2005; Gillman et al, 1953). As a result, small pillar dimensions combined with the proximity to the free surface, results in continued plastic deformation under dislocation-starved conditions. This effect of dislocation-starvation was observed to be particularly prevalent in pillars with a diameter of ~1μm or less. After Gillman et al (1953), there is a minimum required length scale of dislocation propagation required for dislocation multiplication to occur in a given material. For typical FCC materials, this length scale was calculated to be ~1μm. As a result, in cases where the dislocation mean free-path is smaller than ~1μm, dislocation multiplication with continued deformation is unlikely to occur.

The source starvation effects reported in this study (Chap. 4 and Sec. 5.3.2) show similarities to these cases. At smaller grain sizes, the activation of intragranular dislocations is quite limited. As a result, GB dislocations are the primary source of dislocations at these length scales. In these conditions, dislocation source starvation occurs with reducing GB area per unit specimen volume with reducing thickness for a constant average grain size. This leads to increasing specimen yield strength due to a reduction of the initial GB dislocation sources, similar to the case for whiskers as well as micro-compression of pillars. Furthermore, small crystallite sizes and thicknesses, result

in increased proximity to grain boundaries as well as the free surface. As a result, in addition to the initial scarcity of GB dislocations (related to the thickness and grain size through Ω), substantial dislocation multiplication is unlikely to occur. Therefore, with reducing microstructural as well as structural length scales in freestanding thin films, plastic deformation occurs in source-starved conditions.

4.6 CONCLUSIONS

Mechanical response of freestanding Cu films with varying thickness between 50μm to ~ 2μm and three different avg. grain sizes i.e. 1.8μm, 3.5μm and 5μm, was obtained via uniaxial tension testing. Residual electrical resistivity measurements were employed to highlight the effect of thickness as well as grain size on the storage of dislocations with deformation. These measurements reveal that with reducing average grain size from ~5μm to ~1.8μm, the role of intragranular dislocations gets diminished and GB dislocations start to play an increasingly important role. Such a transition in the underlying deformation mechanism is associated with the observed transition in the nature of thickness effects on the yield as well as flow stress of the films. With diminishing intragranular dislocation activity as average grain size is reduced from ~5μm to ~1.8μm, free surface related weakening with reducing thickness (for a constant average grain size) also gets diminished. Our measurements reveal that for d_g < 1.8μm, there is virtually no intragranular dislocation activity and the film strength increases strongly with reducing thickness. GB dislocation source starvation is suggested as the dominant mechanism behind the observed thickness effects for grain sizes approaching

the ultrafine-grained regime. The experimental results show that thickness-related strengthening i.e. increasing yield/flow stress with reducing thickness for a constant average grain size, first appears for grain sizes around ~5μm or smaller.

4.7 ACKNOWLEDGEMENTS

I would like to acknowledge the support of NSF under Contract No. CMMI-0134111. I am also grateful to Dr. Gary Tuttle at Microelectronics Research Center for help and assistance with the resistivity measurements.

4.8 REFERENCES

1. Hall, E.O (1951) “The deformation and aging of mild steel”, *Proc. R. Soc. Lond.* B, 64, 474
2. Petch, N.J. (1953) “The cleavage strength of polycrystals”, *J. Iron Steel Inst.*, 174, 25
3. Armstrong, R., Codd, I., Douthwaite, R.M. and Petch, N.J. (1961) “Plastic deformation of polycrystalline aggregates” *Phil. Mag.*, 7, 45
4. Masumara, R.A., Hazzledine, P.M. and Pande, C.S.(1998) “Yield stress of fine grained materials” *Acta Mater.*, 46, 13, 4527
5. Chokshi, A.H., Rosen, A., Karch, J. and Gleiter, H. (1989) “On the validity of Hall-Petch relationship in nanocrystalline materials” *Scripta Metall.* 23, 1679
6. D.G. Sanders, J.A. Eastman and J.R. Weertman. (1997) “Elastic and tensile behavior in nanocrystalline copper and palladium” *Acta Mater.*, 45, 4019

7. Stolken, J.S. and Evans, A.G (1998) “A Microbend test method for measuring the plasticity length scale” *Acta Mater.*, 46, 14, 5109
8. Fleck, N.A., Mueller, G.M., Ashby, A.F. and Hutchinson, J.W. (1994) “Strain gradient plasticity theory and experiment” *Acta Metall.*, 42, 475
9. Stelmashenko, N.A., Walls M.G., Brown, L.M. and Milman, Y.W. (1993) “Mechanical properties and mechanical behavior of materials with ultra-fine microstructures” Eds. Nastasi, M., Parkin, D. M. and Gleiter, H. *NATO ASI*, Series E 233, 602
10. De Guzman, M.S., Neubauer, G., Flinn, P. and Nix, W.D. (1993) *Mater. Res. Symp. Proc.*, 308, 613
11. Ma, Q. and Clarke, D.R. (1995) “Size dependent hardness of silver single crystals” *J. Mater. Res.*, 10, 853
12. Lee, H.J., Zhang, P. and Bravman, J.C., (2003) “Tensile failure by grain thinning in micromachined Aluminum thin films” *J Appl. Phys.*, 93 (3), 1443
13. Xiang, Y. and Vlassak, J. J. (2003) “Bauschinger and size effects in thin film plasticity” *Acta Mater.*, 54, 5449-5460
14. Xiang, Y., Tsui, T. and Vlassak, J.J. (2006) “Mechanical properties of free-standing electroplated Cu thin films”, *J. Mater. Res.*, 21, 6
15. Keller, R.R., Phelps, J.M. and Read, D.T. (1996) “Tensile and fracture behavior of free-standing copper films” *Mater. Sci. Eng. A*, 214, 42
16. Venkataraman, R. and Bravman, J. C. (1994) “Separation of film thickness and grain-boundary strengthening effects in freestanding Al thin films on Si” *J. Mater. Res.*, 7, 2040

17. Nicola, L., Xiang, Y., Vlassak, J.J., E. Van der Giessen and Needleman, A. (2006) "Plastic deformation in freestanding thin films: Experiments and modeling" *J. Mech. Phys. Sol.,* 54, No. 10, 2089
18. Yu, D.Y.W and Spaepen, F. (2004) "The yield strength of thin copper films on Kapton", *J. App. Phys.,* 95, 6, 2991
19. Hansen, N. "Flow stress and grain size dependence of non-ferrous metals and alloys", *Yield, Flow and Fracture of Polycrystals,* Ed. By T.N. Baker, Applied Science Publishers
20. Armstrong, R. W. (1961) "On size effects in polycrystalline plasticity", *J. Mech. Phys. Sol.,* 9, 196
21. Miyazaki, S., Fujita, H. and Hiraoka, H. (1979) "Effects of specimen size on the flow stress of rod specimen of polycrystalline Cu-Al alloy" *Scripta Metall.* 13, 447
22. Janssen, P.J.M, Keijser, Th. H., and Geers, M.G.D (2006) "An experimental assessment of grain size effects in uniaxial straining of thin Al sheets with a few grains across the thickness" *Mat. Sci. Eng. A*, 419, 238
23. Kals, R.T.A and Eckstein, R. (2000) "Miniaturization in sheet metal working" *J. Mat. Proc. Tech.* 103, 95
24. ASTM Grain Size Estimation Technique, *ASTM E112*
25. Gertsman, V.Y., Hoffmann, M., Gleiter, H. and Birringer, R. (1994) "The study of grain size dependence of yield stress of copper for a wide grain size range" *Acta Metall. Mater.* 42, 10, 3539
26. Cheng, S., Spencer, J.A., Milligan, W.W. (2003) "Strength and tension/compression asymmetry in nano-structured and ultrafine-grain materials" *Acta Mater.,* 51, 4505

27. Espinosa, H.D., Prorok, B.C. and Fisher, M. (2003) “A methodology for determining mechanical properties of free-standing thin films and MEMS materials”, *Jour. Mech. Phys. Sol.*, 51
28. Espinosa, H.D., Prorok, B.C. and Peng, B. (2004) “Plasticity size effects in free-standing sub-micron polycrystalline FCC thin films subjected to pure tension”, *Jour. Mech. Phys. Sol.*, 52, 667
29. Espinosa, H.D., Panico, M., Berbenni, S., and Schwarz, K.W. (2006) “Discrete dislocation dynamics simulations to interpret size and surface effects in free-standing thin films” *Int. J. Plasticity*, 22, 2091
30. Wenner, F. (1915) “A method of measuring earth resistivity” *Bur. Stand. (U.S.) Bull.*, 12, 469
31. Valdes, L.B. (1954) “Resistivity measurements on germanium for transistors” *Proc. I.R.E.*, 42, 420
32. Smits, F.M. (1958) “Measurements of sheet resistivities with the four point probe” *Bell Syst. Tech. J.*, 37, 711
33. Haque, M.A. and Saif, M.T.A (2003) “Strain gradient effects in nano-scale thin films”, *Acta Mater.*, 51, 3053
34. Kaveh, M. And Wiser, N. (1986) “Deviations from Mathiessen’s rule for the electrical resistivity of dislocations” *J. Phys. F: Met. Phys.*, 16, 795
35. Qian, L.H., Lu, Q.H., Kong, W.J. and Lu, K. (2004) “Electrical resistivity of fully-relaxed grain boundaries in nanocrystalline Cu” *Scripta Mater.* 50, 1407
36. Wollenberger, H.J. (1983) in: *Physical Metallurgy* Eds. Cahn. R.W. and Haasen, P. E, 9, 1189, Elsevier, Amsterdam
37. Chopra, K.L., Suri, R. and Thakoor, A.P. (1977) “Role of structural defect in electron transport properties of Copper films” *J. Appl. Phys.* 48, 2

38. Gangulee, A. (1972) “The structure of electroplated and vapor-deposited Copper films” *J. Appl. Phys.* 43, 3, 867
39. Lu, L, Shen, Y., Chen, X., Qian, L. and Lu, L. (2004) “Ultrahigh strength and high electrical conductivity in Copper” *Science*, 304, 422
40. Schafler, E., Steiner, G., Korznikova, E., Kerber, M. and Zehetbauer, M.J. (2005) “Lattice defect investigation of ECAP Cu by means of X-ray line profile analysis, calorimetry and electrical resistometry” *Mater. Sci. Eng. A* 410-411, 169
41. Kannan, Kh. M. and Karin, Kh. F. (1975) *J Phys. F Metal Phys.*,5, 1687
42. Brandes, E.A. and Brook, G.B. (1998) *Smithells Metal Reference Book* Butterworth-Heinenmann, Oxford
43. Keller, R-M, Baker, S. P. and Arzt, E (1998) “Quantitative analysis of strengthening mechanisms in thin Cu films: Effect of film thickness, grain size and passivation” *J. Mat. Res.*, 13, 5, 1998
44. Lee, Hoo-Jeong, Zhang, P. and Bravman, J. C. (2004) “Study of strength and elongation of free-standing Al beams for microelectromechanical systems applications”, *A P L*, 84 (6), 915
45. Li, J.C. (1963) *Trans. Soc. Petro. Eng. Am. Inst. Min. Metall. Pet. Eng.* , 227, 239
46. Lim, J.W. and Isshiki, M. (2006) “Electrical resistivity of Cu films deposited by ion beam deposition: effects of grain size, impurities and morphological defects” *J Appl. Phys.*, 99, 094909
47. Natter, H. and Hempelmann, R. (1996) “Nanocrystalline Copper by pulsed-electrodeposition: influence of organic additives, bath temperature and pH” *J. Phys. Chem.*, 100, 19525

48. Ungar,T., Schaefler, E., Hanak, P., Bernstorff, S., Zehetbauer, M. (2007) “Vacancy production during plastic deformation in copper determined by in-situ X-ray diffraction” *Mater. Sci. Eng. A*, 462, 398
49. Yamakov, V., Wolf, D., Phillpot, S. R., Mukherjee, A. K., Gleiter, H., (2003) “Deformation mechanism crossover and mechanical behavior in nanocrystalline materials”, *Phil. Mag. Lett.*, 83, 6, 385
50. Yamakov, V., Wolf, D., Phillpot, S. R. and Mukherjee, A. K. (2002) “Dislocation processes in the deformation of nanocrystalline aluminum by molecular dynamics simulations” *Nat. Mater.* 1, 1
51. Taylor, G. F. (1924) “A method of drawing metallic filaments and a discussion of their properties and uses” *Phys. Rev.* 23, 655
52. Andrade, E. N. Da C. (1953) *Inst. Metals. Monograph*, 13, 138
53. Fisher, J. and Hollomon, J. (1947) *Trans. AIME*, 2218
54. Brenner, S. S. (1956) “Tensile strength of whiskers” *J. Appl. Phys.*, 27, 12, 1484
55. Brenner, S. S., Doremus, R. H., Roberts, B. W. and Turnbull, D. (1958) “Growth and perfection of crystals”, John Wiley, NY
56. Greer, J. R., Oliver, W. C. and Nix, W. D. (2005) “Size dependence of mechanical properties of gold at the micron scale in the absence of strain gradients” *Acta Mater.*, 53, 6, 1821
57. Uchic, M. D., Dimiduk, D. M., Florando, J. N. and Nix, W. D. (2004) “Sample dimensions influence strength and plasticity” *Science*, 305, 986
58. Gillman, J. J. (1953) *Applied micromechanics of flow in solids*, McGraw-Hill, New York, 185

CHAPTER 5. EXPERIMENTAL OBSERVATIONS OF THICKNESS EFFECTS ON THE DEFORMATION HETROGENEITIES AND DUCTILITY IN FREESTANDING Cu FILMS

5.1 ABSTRACT

This chapter presents the experimental results for the role of the film thickness on the observed ductility for a wide range of average grain sizes, d_g = 1.8-50μm. The films are loaded in a tensile micro-fixture. The evolution of surface deformation is in situ monitored by non-contact surface profilometer during the history of loading. The acquired surface scans are analyzed via 2D FFT to follow the evolution of different surface wave length as a function of the applied macroscopic strain and the transition from homogeneous to localized deformation field. The results show that the thickness effects are more prominent for larger grain sizes, d_g > 3.5μm in this study. For films with d_g = 1.8μm, the apparent ductility is inherently limited by the loss of strain hardening capability. These films show a limited ductility with maximum uniform strain, ε_u ~2%, irrespective of the thickness. Surface scans showed that plastic deformation evolves into highly localized deformation bands at an early stage of deformation, leading to premature failure. For films with larger grain size, it is found that the film thickness affects the apparent ductility by influencing the deformation heterogeneity. Surface scans showed that plastic deformation remains relatively uniform to higher level of macroscopic plastic deformation. It is speculated that local accommodation of deformation incompatibilities

between neighboring grains are the primary driving mechanism for the observed trends. For thinner films with $\lambda = (d_g / t) \sim 1$, there are no through-thickness compatibility constraints. Thus, such accommodation must occur within the plane of the specimen, leading to unconstrained localized deformation bands and premature failure. For films with $\lambda > 1$, the presence of through-thickness compatibility constraints limits the propensity for localization to a higher macroscopic strain level. The participation of many gains in the accommodation process would lead to near uniform macroscopic strain distribution.

5.2 INTRODUCTION

A number of previous studies have focused on the influence of grain size reduction on ductility (Wang et al, 2002; Koch et al, 2003; Ma et al, 2003; Ma et al, 2004; Zhao et al, 2006). However, there has been little effort to understand the role of thickness reduction on the observed ductility. The current experimental work revealed a clear effect of the thickness as well as grain size on the plastic deformation in miniaturized polycrystalline specimen. It is important to characterize the geometric size effects on the ductility to predict the performance limits of materials at such small length scales. Therefore, the primary objective of this chapter is to highlight the role of thickness on the observed ductility of the specimen. In situ observations of the surface topography evolution are carried out using 3D non-contact surface profilomter. The measured topography is analyzed by 2D FFT to follow the evolution of different surface

wavelength with the deformation, and thereby highlight the active deformation mechanisms leading to the progression of localized plastic deformation. Video images are also acquired to calculate the finite in plane strain distributions.

For the range of film thicknesses and grain sizes, the primary deformation mechanism is the activation and storage of lattice dislocations (Arzt et al, 1998). As a result, in a polycrystalline specimen with a uniform gauge section and under macroscopically uniform deformation, there would be local variations in the strain distribution at the level of individual grains based on the grain size, grain orientation, and proximity to the free surface as well as neighboring grains (Rey et al, 1988). Furthermore, with reducing thickness, the surface grains start to play a prominent role and the overall microstructural constraint on the individual grains is reduced. As a result of their exposure to the free surface and the greatly diminished through-thickness microstructural constraint, miniaturized specimen with $\lambda \rightarrow 1$ are expected to feature rapid evolution of localized deformation bands. In the current context, the ductility was defined as the macroscopic uniform strain before localization, $(\varepsilon_u; d\sigma/d\varepsilon = 0)$ within the gauge section. As a result, the ductility can be understood as the competition between the inherent ability of the material to strain harden and the onset of plastic instability due to deformation heterogeneities. It is expected that following the history of the deformation field and evolution of localizations, would probably elucidate the underlying mechanism of the apparent film thickness effects on its ductility. With these concepts as background, this chapter presents an experimental assessment of the evolution of deformation

heterogeneities, at the micro and macroscopic levels, and relates them to thickness effects on observed macroscopic behavior.

5.3 EXPERIMENTAL PROTOCOL

The ductility data presented in this study was obtained via uniaxial tension tests using INSTRON 8862 machine with a servo-hydraulic controller. The observed ductility of the rolled Cu foil specimens with thickness between 12.5-100µm and grain size 11-50µm (Rolled foil specimen in Chap. 3) as well as the ductility of the electrodeposited Cu films with thickness between 2-50µm and grain size 1.8-5µm is shown (Electrodeposited films in Chap. 4). The experimental protocol is described in detail in Appendix B. For the purpose of elucidating the deformation mechanisms, 4 additional samples were tested using a miniaturized loading stage from Fullam Inc, as shown in Figure 5.1 (a). Two experimental techniques were employed to characterize the initiation and evolution of deformation hetrogeneities: Digital Image Correlation (DIC) to find the surface strain distribution at the level of individual grains and surface roughness measurements. The tensile stage was controlled via a controller (Newport Corp., XPS Universal Controller) using a Labview program. Sample preparation and alignment was similar to the previous methodology (described in Appendix B). The specimens were cut using a stamping technique. The samples were then polished with a 0.05µm Alumina slurry (Buehler Inc.). Following polishing, the samples were cleaned by rinsing sequentially in Acetone,

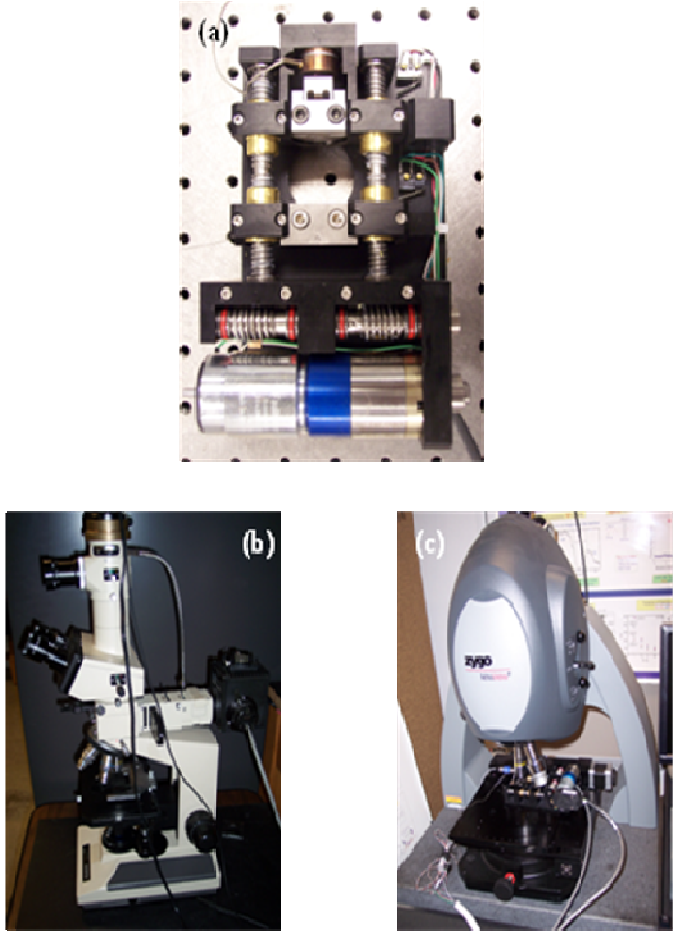

Figure 5.1 Experimental set-up used for the study of deformation heterogeneities.
(a) Miniaturized tensile stage from Fullam Inc.
(b) Optical microscope for obtaining images used for surface strain estimation using DIC.
(c) Zygo profilometer used to monitor surface roughness evolution with strain.

Methanol and DI water. The samples were then slightly etched with a 5% Nitric Acid solution (with DI water). Annealing at 400ºC and 600ºC (for 2 hrs) was performed in a Nitrogen environment prior to testing. Prior to testing, the specimens were aligned in the tensile stage using a low-magnification microscope.

The images used for DIC were taken using an optical microscope with a 10X objective and a digital camera (SPOT Inc.). The images were synchronized with the displacement increments using the 'sequential imaging' option from the camera software. Surface strain was estimated using the DIC technique developed by Wang et al (2008). The surface roughness measurements were performed using a Zygo non-contact profilometer. The tensile stage was alternatively moved from the microscope station to the profilometer in order to obtain corresponding optical images for each surface roughness measurement. Care was taken to retain precise alignment of the tensile stage on the microscope and the profilometer specimen stages. 4 different specimens were tested:

Specimen set	t **(μm)**	d_g **(μm)**
1	100	19.5
1	12.5	20
2	100	47
2	50	48

Table 5.1 Thickness and average grain size of the tested specimens.

5.4 EXPERIMENTAL OBSERVATIONS

5.4.1 Size effects on the experimentally observed ductility

The experimentally obtained stress-strain response of the films was used to ascertain their ductility. The reported 'ductility' here is the maximum uniform strain, ε_u derived from the observed mechanical response of the film, employing the Considere criterion on the engineering stress and strain:

$$\frac{d\sigma}{d\varepsilon}=0 \tag{5.1}$$

A numerical routine was implemented using MATLAB so as to calculate the local slope of the stress-strain curve. Prior to numerical differentiation, a running average was applied to the experimental data, to reduce local fluctuations in the stress strain data that make numerical differentiation difficult.

Figure 5.2 summarizes the experimental results for variation of film ductility with d_g for the examined range of film thicknesses. The observed ductility of the rolled Cu foil specimens with thickness between 12.5-100μm and grain size 11-50μm as well as the ductility of the electrodeposited Cu films with thickness between 2-50μm and grain size 1.8-5μm is shown. The extent of film ductility, ε_u is proportional to both t and d_g, regardless of the processing technique. For a given d_g, ε_u presents strong dependence on t especially for large d_g. specimen. However, for the 1.8μm grain size films virtually no thickness dependence is apparent. The ductility for this group was only about 2%,

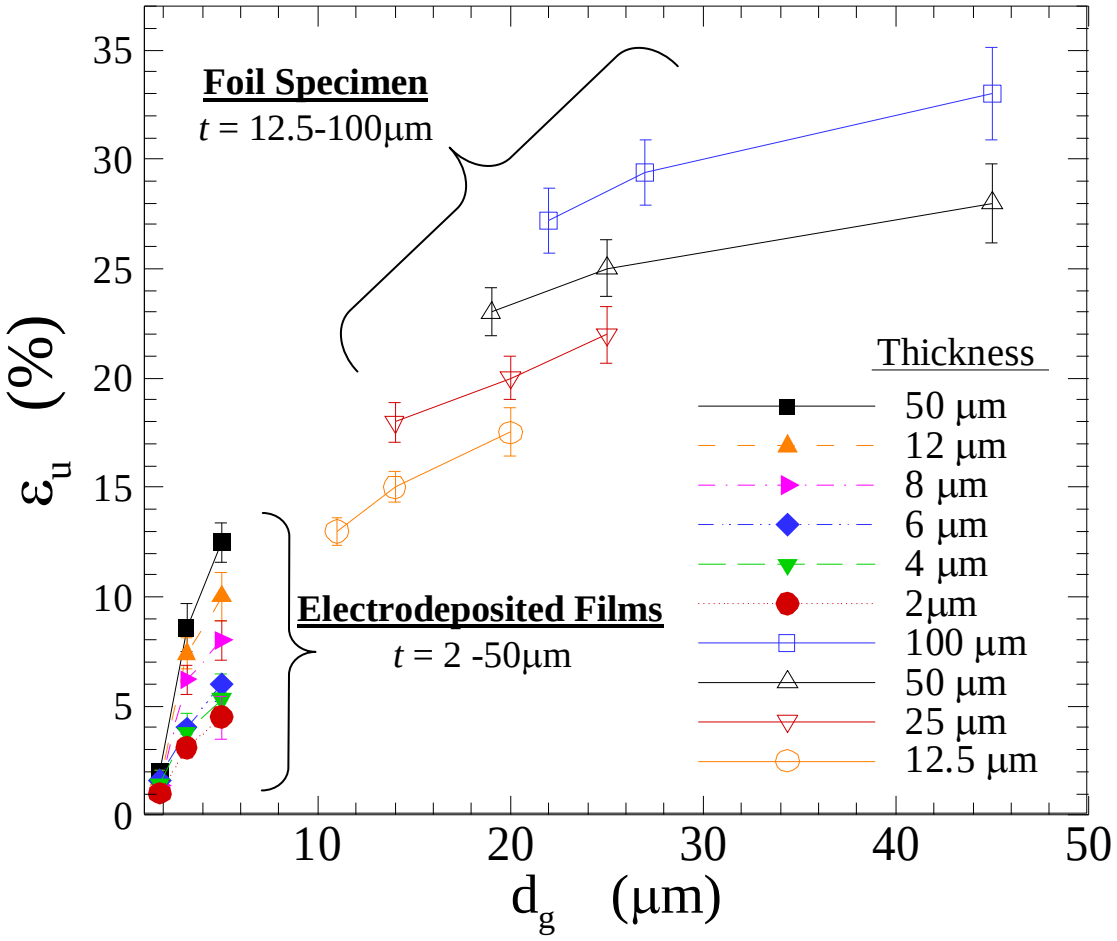

Figure 5.2 Experimentally observed ductility i.e. maximum uniform strain (ε_u), as a function of average grain size (d_g) for all the tested films with varying thickness. While films with larger average grain sizes (d_g = 3.5μm - 47μm) show prominent thickness dependent ductility, electrodeposited specimens with d_g = 1.8μm show virtually no thickness effect on ductility.

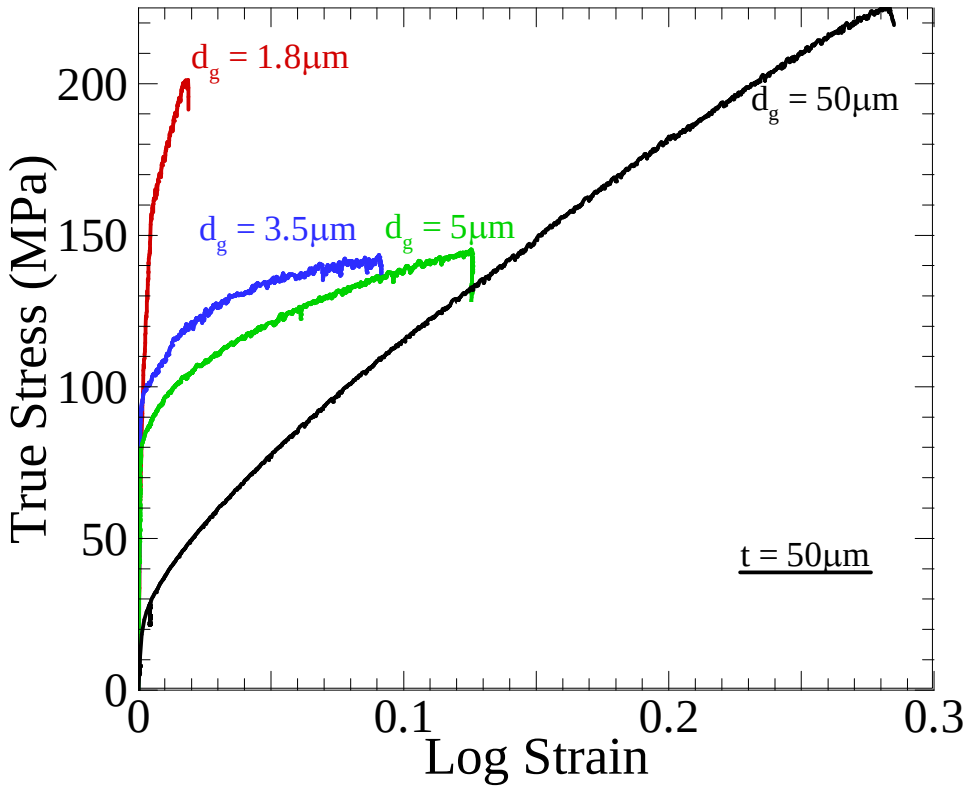

Figure 5.3 Engineering stress-strain curves for specimens with *t=50*µm and varying average grain sizes i.e. d_g=1.8 µm - 50µm. With reducing grain size, increasing yield stress and a reduction in strain hardening ability is observed.

irrespective of the thickness. Thus, these results suggest that at small grain sizes, typically around ~ 1μm or so, thin film ductility may be inherently limited by the microstructural constraint. These results agree with other similar studies in literature. For example, nanocrystalline specimens, even with bulk thickness, have shown limited ductility around ~2% or so (Lu et al, 2004). Therefore, two primary findings emerge with regards to size dependence on ductility in freestanding Cu films. Firstly, ductility is thickness dependent, especially for grain sizes larger than ~ 2μm or so. Secondly, for grain sizes smaller than ~2μm, ductility is inherently limited and no apparent thickness effects are seen.

The role of grain size, as observed here, can be understood in terms of the Considere criterion. In terms of the true stress – log strain, this criterion predicts that the maximum uniform strain is attained when

$$\left(\frac{d\sigma_T}{d\varepsilon}\right)_{\dot{\varepsilon}} = \sigma_T \qquad (5.2)$$

where, σ_T is the true stress and $\left(\frac{d\sigma_T}{d\varepsilon}\right)_{\dot{\varepsilon}}$ is referred to as the 'strain hardening rate'. This equation therefore implies that the specimen loses its load carrying capability i.e. strain instability sets in, when the current strain hardening rate is equal to the current true stress. With reducing average grain size, the right hand side of (RHS) the above equation increases i.e. the yield stress as well as the flow stress at relatively small plastic strains is much higher than that in coarse-grained specimen. Furthermore, small grain sizes also drastically reduce the ability of the material to strain harden. For example, Figure 5.2 shows the observed ductility in specimens with t=50μm and a wide range of average

grain sizes i.e. d_g = 2-50μm. Figure 5.3 shows the stress – strain curves for the two extreme cases for this set i.e. t=50μm, d_g ~2μm and λ~27 specimen, and t=d_g = 50μm with λ~1 specimen.

It can be seen that the yield stress @ 0.2% strain offset, in the d_g ~2μm specimen is about 65% of the fracture stress in the coarse grained specimen @ 27% strain! This is attributed to the fact that such small grains present a formidable microstructural constraint on dislocation nucleation and therefore, dislocations are generated at much higher stress as compared to the coarse grained materials.

It is seen that the specimen with d_g ~2μm loses the ability to strain harden at much lower strains as compared to the specimen with d_g = 50μm. The reason for such limited ability for strain hardening, observed in specimen with reducing average grain sizes, is dynamic recovery (Wang et al, 2004). For substantial strain hardening to occur, the steady state dislocation density should be quite high in a material i.e. the material should have sufficient ability to store dislocations within the microstructure. The steady state dislocation density is an outcome of two competing processes i.e. generation of dislocations with deformation and annihilation of dislocations in recovery processes. For fine microstructures, intragranular dislocation activity is very restricted and the bulk of dislocation nucleation occurs at the grain boundaries. Therefore, with reducing grain sizes, dislocation nucleation occurs in closely spaced sources (i.e. grain boundaries etc.) and the dislocation mean-free path is quite small. Such grain boundary dislocations are

very close to one another and also to dislocation sinks such as grain boundaries; as a result, such small microstructures are not very efficient in storing dislocations (Yamakov et al, 2002; Wang et al, 2004).

The combination of such high stresses required for initial plastic flow as well as greatly diminished ability of the fine-microstructures to store dislocations and strain harden, leads to their susceptibility to plastic instabilities. In addition to these microstructure related effects on the observed ductility, there are also additional thickness effects on both dislocation nucleation as well as dislocation storage (discussed in Ch. 3 and Ch. 4 in detail). However, our data in Figure 5.2 shows that with reducing average grain size, the microstructure related effects dominate and the ductility is inherently limited. As observed in various previous studies (Wang et al, 2004; Lu et al, 2004), even specimen with bulk thicknesses in specimen with ultra-fine microstructures (d_g <1μm), ductility of typically < 5% is seen (Wang et al, 2004). For the purpose of this study, we focus our attention on the foil specimen, which show much greater sensitivity to thickness effects as compared to the electrodeposited films with much smaller grain sizes.

5.4.2 Surface roughness evolution as a tool to characterize deformation heterogeneity

We employed Digital Image Correlation (DIC) to find the surface strain at the level of individual grains. This was accomplished by taking periodic images of the

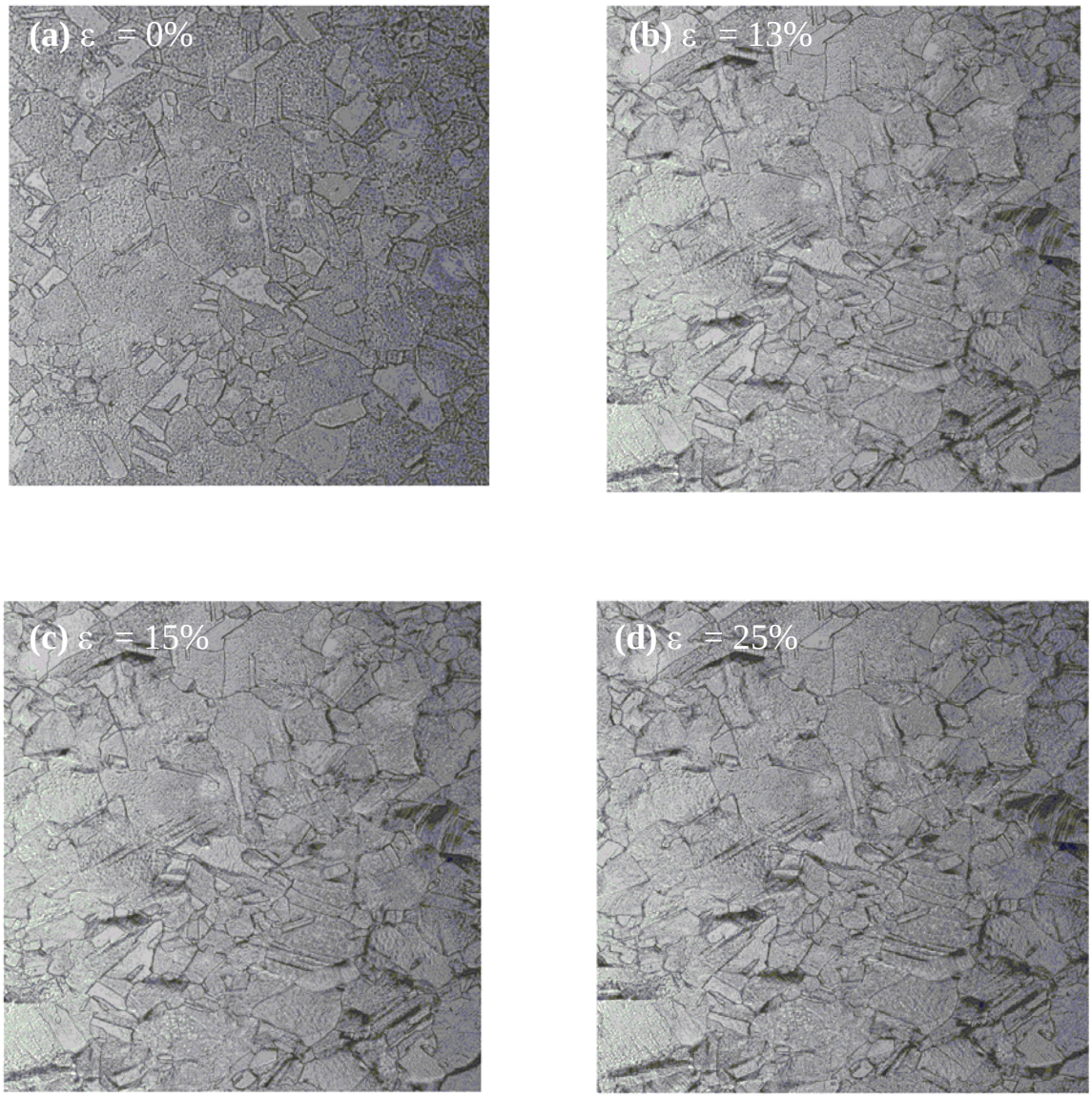

Figure 5.4 Typical optical images showing the evolution of the specimen surface at different levels of macroscopic strains. Progression of slip textures and twining can be observed. (a) ε = 0% (b) ε = 13% (c) ε = 15% (d) ε = 25%. (FOV=500μm).

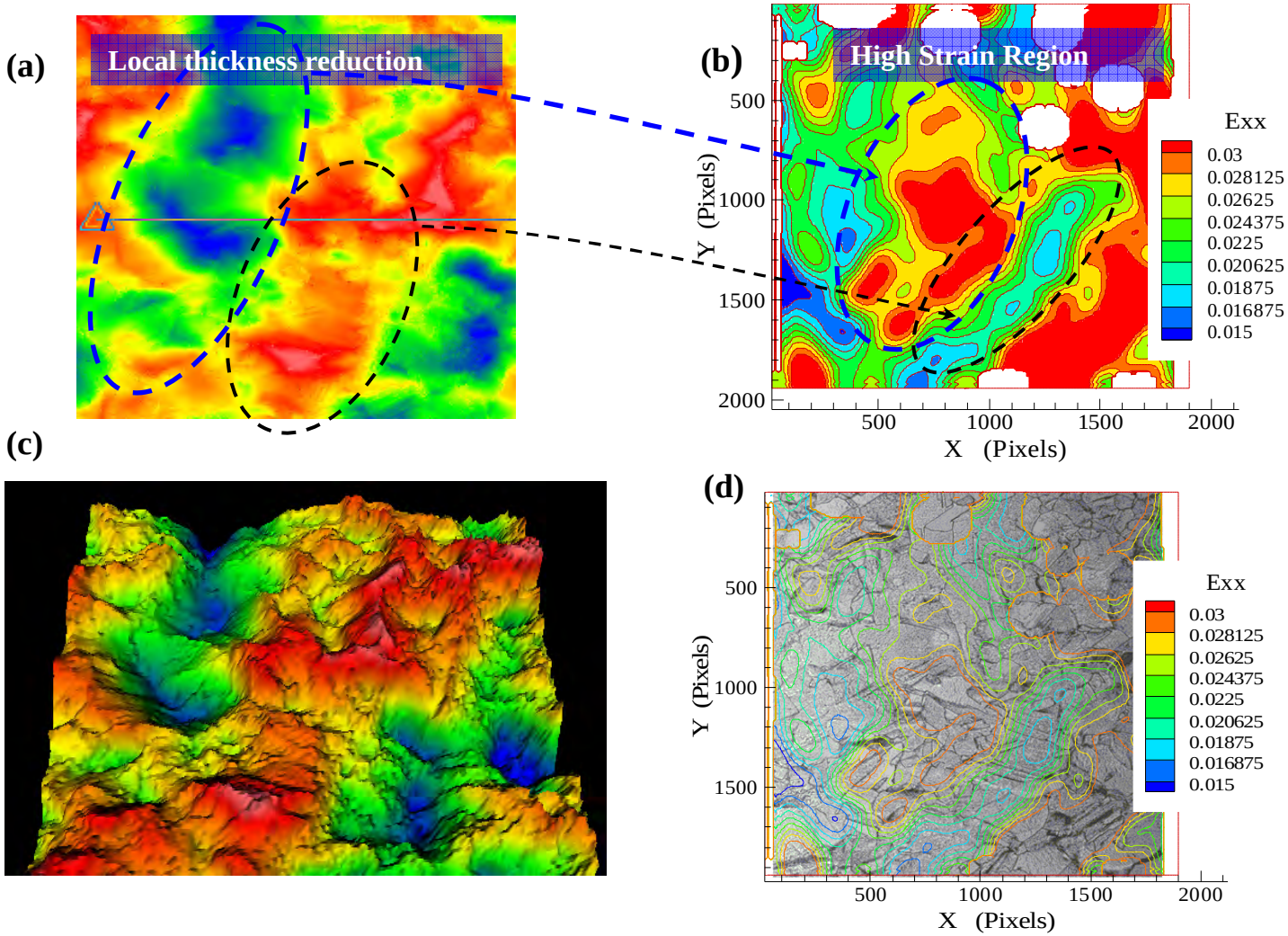

Figure 5.5 The relationship between surface roughness and local strain distribution. **(a)** Surface roughness distribution obtained via surface profilometer **(b)** Surface strain distribution of the same region obtained via DIC. **(c)** 3-D view of the surface roughness distribution shown in (a). **(d)** Optical micrograph of the specimen surface with the surface strain distribution superimposed as a contour plot.

surface of a deforming specimen. The field of view was ~300μm × 300μm. The specimen had a thickness of 50μm and an average grain size of 45μm. The gauge section was 1 mm wide and 5 mm long. The imaging area was in the middle of the gauge section. The DIC method requires local variations in the gray value distributions so as to distinguish different regions of the specimen. The strain resolution of the technique therefore depends on the sharpness of this distribution. For this study, the specimen's surface was lightly etched following annealing. The etching was controlled so as to just highlight the microstructural details like grain boundaries etc as well as produce a sub-grain etch pit distribution that can be a good substitute for a speckle distribution. Images were taken at a strain increment of ~0.1%. Figure 5.5 shows the increment of the surface strain distribution obtained via DIC for the deformation step between 13% and 15% macroscopic strain (Figure 5.5 (b)) along with the surface roughness measured by the 3D non contact surface profilometer at 15% strain (Figure 5.5 (a) in 2-D and Figure 5.5 (c) in 3-D). Figure 5.5 (d) shows the surface strain distribution superimposed over the microscope image of the specimen surface at 15% strain. It should be noted that the surface strain plotted is the strain increment between the two macroscopic loading steps.. The surface strain distribution clearly shows the heterogeneity of the strain field at the aggregate level i.e. some regions are at a higher strain level as compared to other regions. The highest strain in this distribution, of ~ 4%, was found to be about ~5 times the lowest strain of about ~0.8%.

The specimen with the surface strain distribution shown in Figure 5.5 (d) is a multicrystalline specimen i.e. there is just one grain across the thickness on average. As a result, due to the negligible through-thickness microstructural constraint, considerable out of plane deformation at the grain level, as well as the aggregate level, is seen. The 3-D surface roughness representation in Figure 5.5 (c) clearly shows this. This can also be seen in the microscopic images of the deformed specimen's surface in Figure 5.4. We find striking similarities between the surface roughness distributions, shown in Figure 5.5 (a), as well as the surface strain distribution, shown in Fig 5.5 (b). It can be seen that the regions that show larger surface strain also show considerable thickness reduction.

This observation of a direct relationship between the local strain distribution at the microstructural level and the local surface roughness (or thickness) implies that the initiation of plastic instability is a direct consequence of thickness reduction. As in, under a given macroscopic tensile stress, each region of the specimen carries a different strain based on the local thickness. Regions with a smaller local thickness carry a higher local strain. The overall deformation of the specimen can be considered to be stable, or in terms of the Considere criterion as 'uniform', as long as the material being deformed compensates for this thickness reduction (consequently higher local strains) with strain hardening. At some critical local strain however, the material loses its ability to strain harden any further and as a result, plastic instability is initiated. Beyond this point, any further macroscopically imposed deformation results in continued thickness reduction in this local region i.e. strain localization. Therefore, the characterization of thickness

reduction (or surface roughness evolution) with deformation can be employed as a tool to study the mechanisms that limit the ductility of polycrystalline specimens.

Another observation of great significance can be made based on Figure 5.5 (a) and Figure 5.5 (b). It can be seen that the high strain regions as well as the regions that feature thickness reduction span multiple grains. This observation is significant in that it implies that while the heterogeneities quite likely have a microstructural or crystallographic origin, their evolution is a result of aggregate level accommodation of strain in the material (Miyazaki et al, 1979). Such accommodation processes i.e. deformation mechanisms that allow a given grain in a polycrystalline specimen to respond to the ongoing deformation in the neighboring grains, are expected to be dependent on the effective microstructural constraint in the specimens. The following sections of this chapter will further expand on this significant observation.

5.4.3 Surface roughness evolution with deformation

In order to understand the effects of thickness as well as average grain size on the ductility of the tested specimens and to highlight the physical mechanisms that limit the ductility, we characterized the evolution surface roughness with deformation. In particular, we studied the effects of both thickness and average grain size on the roughness evolution with deformation. Figure 5.6 shows the evolution of surface

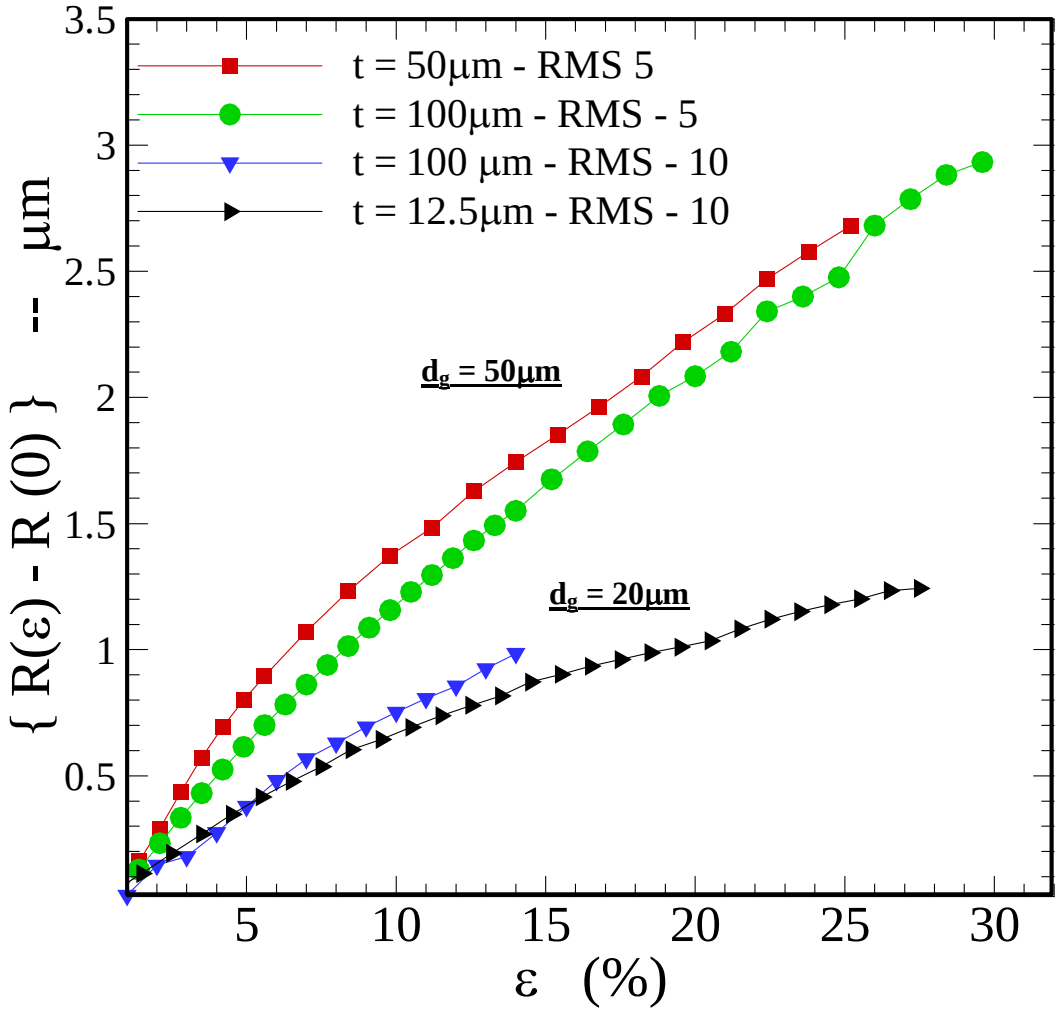

Figure 5.6 Evolution of surface roughness with strain for Set 1 specimens with d_g = ~20μm and Set 2 specimens with d_g = ~50μm. The relative increase in the RMS average of the surface strain with respect to the initial surface roughness of the surface is plotted.

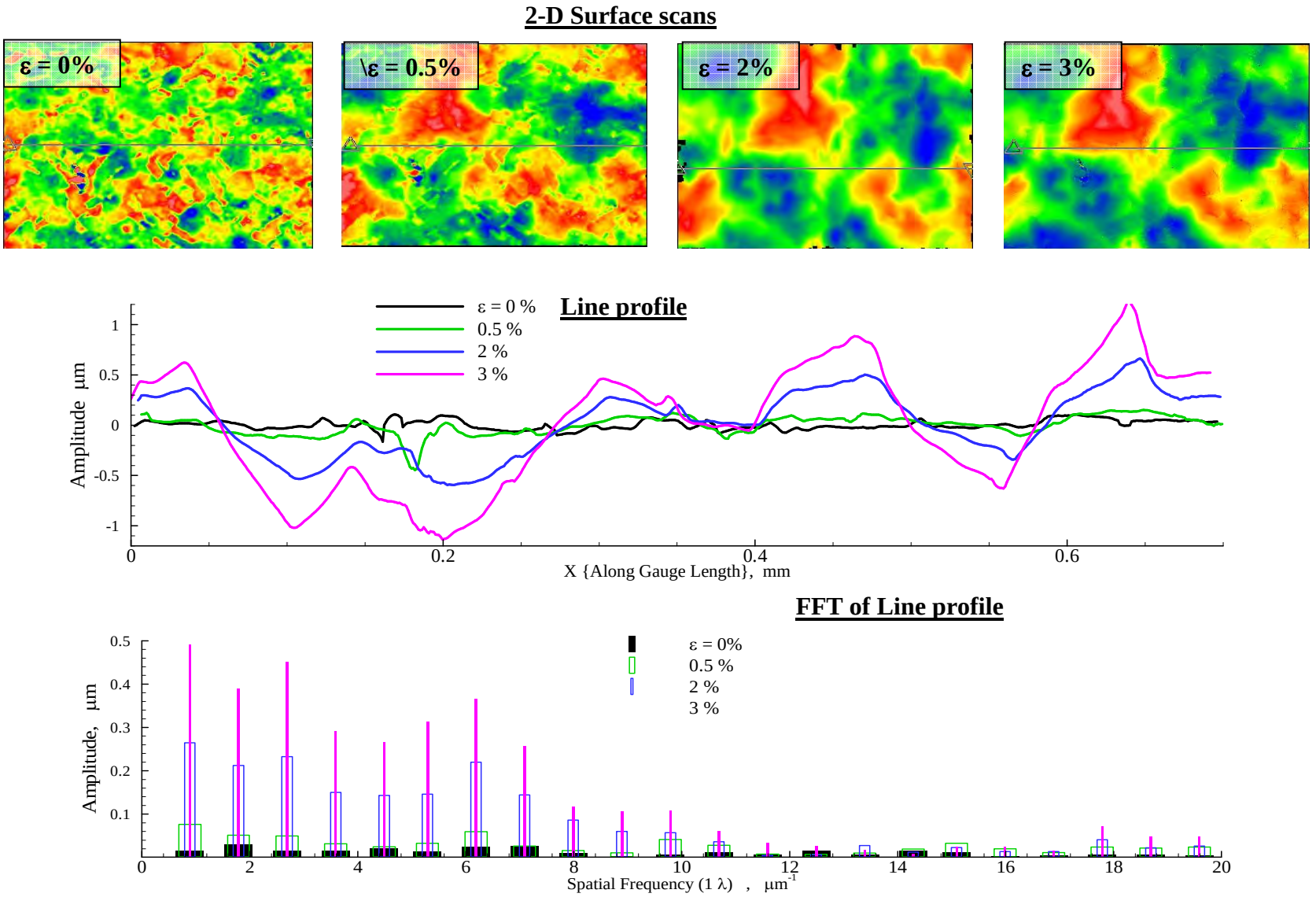

Figure 5.7 Effect of initial imperfections on the surface roughness evolution.

roughness as a function of the macroscopic strain in the specimens. Here, the RMS average of the surface roughness is used. The roughness was measured at 1% strain increments. The Y-axis on Figure 5.6 shows the relative increase in the roughness amplitude i.e. R The RMS average was found over a field of view of 1.2mm × 1.2mm. The results are shown for both Set 1 (d_g = 20μm) as well as Set 2 (d_g = 50μm). Generally, the roughness increases with increasing deformation. It is seen that the roughness amplitude is a strong function of the average grain size i.e. Set 2 specimens with larger average grain size show a larger roughness amplitude as compared to Set 1 specimens. Remarkably, the roughness amplitude does not appear to be very sensitive to the thickness i.e. for d_g = 20μm, the trend for t = 12.5μm is very similar to that for t = 100μm. However, t = 100μm specimen shows much greater ductility as compared to t = 12.5μm. Qualitatively similar trend is seen for Set 2 specimen for 50μm average grain size i.e. roughness amplitude for a given strain is very similar for t = 50μm and t = 100μm. Also, t = 100μm shows greater ductility in both cases. These observations show that the average amplitude of the surface roughness with deformation in polycrystalline freestanding films is dictated by the average grain size.

While the RMS average of the surface roughness shows the strong effect of grain size, it does not reveal the effect of thickness. In order to reveal the effect of the thickness, we study the details of the distribution of the surface roughness. This is accomplished by extracting individual line profiles from the 2-D surface scans of the roughness. Figure 5.7 (a) shows the surface scans obtained for the t = 100μm specimen

from Set 2 at different macroscopic strain levels i.e. 05, 0.5%, 2% and 3%. The individual line profiles extracted from the different surface scans are also shown in Figure 5.7 (b), along with the FFT (Fast Fourier Transform) analysis in Figure 5.7 (c). One key aspect of such an analysis is the effect of initial thickness imperfections i.e. is the final roughness distribution dictated by the pre-existing thickness imperfections in the films? In other words, we showed in Sec. 5.4.2, that the observed thickness reduction in local regions is directly related to the local strain distribution in the films. In order to relate this thickness reduction in the material with deformation to the underlying deformation mechanisms, we first need to show that the thickness reduction is not an outcome of any processing related artifacts.

We address this issue by comparing the surface roughness of an undeformed sample with the surface roughness at different levels of deformation in the same region. These results are shown in Figure 5.7 (b). It can be clearly seen that while there are initial thickness imperfections in the film, the final roughness distributions is very different from these initial imperfections. For example, the line profile as well as the frequency distribution from the FFT analysis for $\varepsilon=0\%$ is quite different from that at $\varepsilon=0.5\%$. Also, it is clear that the distribution of the surface roughness is set quite early in the films and then it simply evolves in a self-similar way with continued deformation. For example, the roughness distribution at 0.5% strain in the film is very different from the roughness distribution at 0% (or undeformed state). However, the roughness distribution observed at 0.5% strain is very similar to that seen at 2% and 3% strain. The dominant frequencies

for 0.5%, 2% and 3% strains are identical. Therefore, the surface roughness distribution is not influenced by initial thickness imperfections. It is set at the very early stages of deformation and evolves in a self-similar way with continued deformation. Thus, the roughness distribution at the microstructural level is independent of strain.

Next, we study the role of thickness, for a given average grain size, on the distribution of the surface roughness with deformation. We first consider the d_g = 50μm specimens with t = 50μm and t = 100μm. Figure 5.8 and Figure 5.9 show the roughness distribution on the specimen surface for Set 2 specimen, at different levels of deformation i.e. 1%, 7%, 14%, 20% and 27% macroscopic strains. Figure 5.8 shows the surface scan (Fig 5.8 (a)), a typical line profile (Figure 5.8 (b)) as well as the FFT of the line profile (Figure 5.8 (c)) for the d_g = 50μm & t = 50μm case. The line profile was extracted along the tensile loading direction. Figure 5.9 shows similar results for the d_g = 50μm & t = 100μm case. It can be clearly seen that the surface roughness evolves in a self-similar way for both these cases i.e. the surface roughness pattern is set fairly early in the deformation process and evolves in a self-similar way thereafter. We also find that while the macroscopic average of the surface roughness (RMS average) did not show any prominent thickness effect, the roughness distribution is different for the two thicknesses. Firstly, the maximum peak-to-valley roughness is seen in the t = 50μm case in Figure 5.8 (b) i.e. +2μm to -10μm. On the other hand, the maximum peak-to-valley roughness in the t = 100μm case is +2μm to -5μm, seen in Figure 5.9 (b). Thus, while the average roughness is the same, the smaller thickness specimen shows a higher peak-to-valley

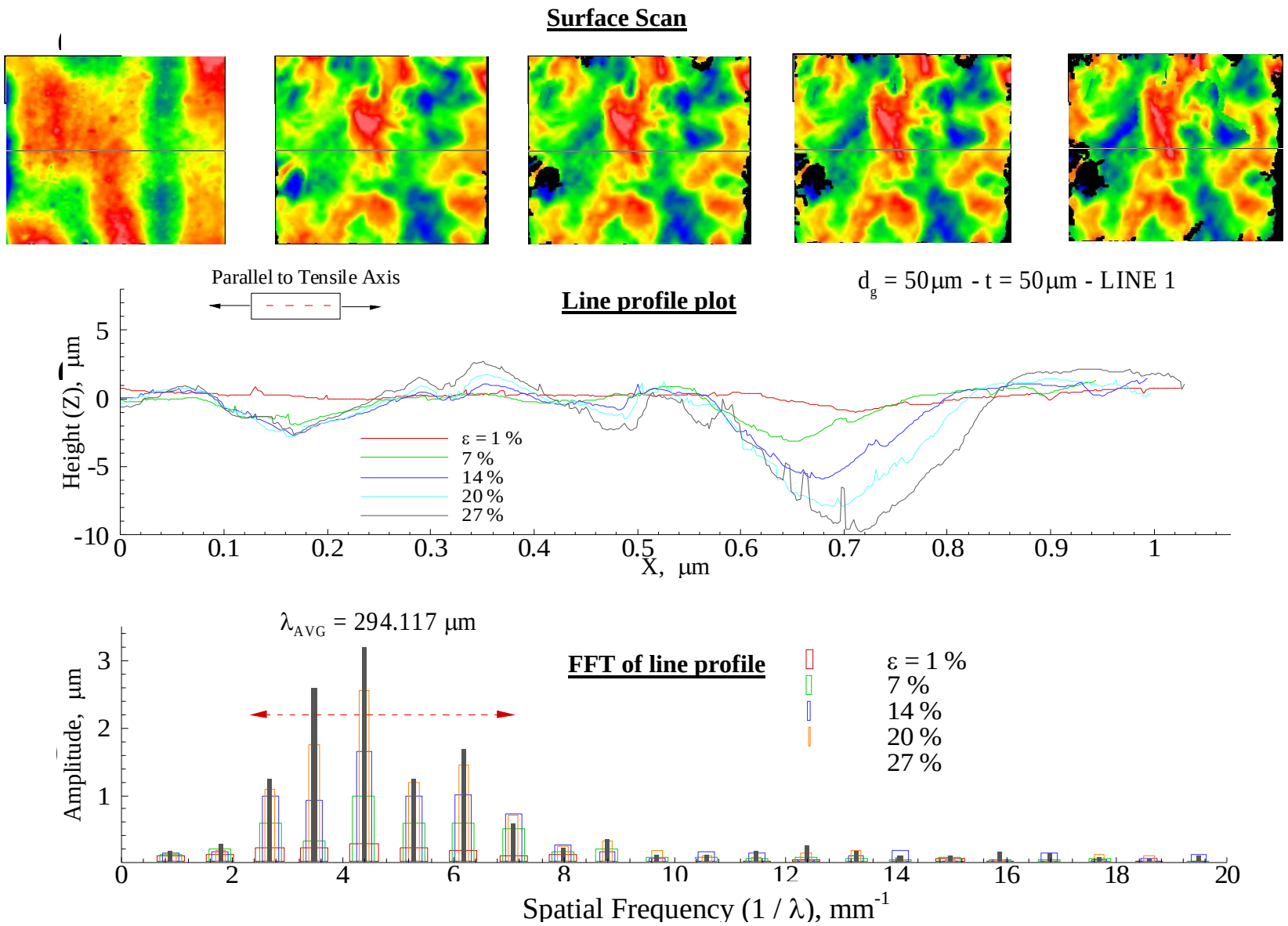

Figure 5.8 Evolution of surface roughness with strain for a specimen with d_a = 50µm & t = 50µm.

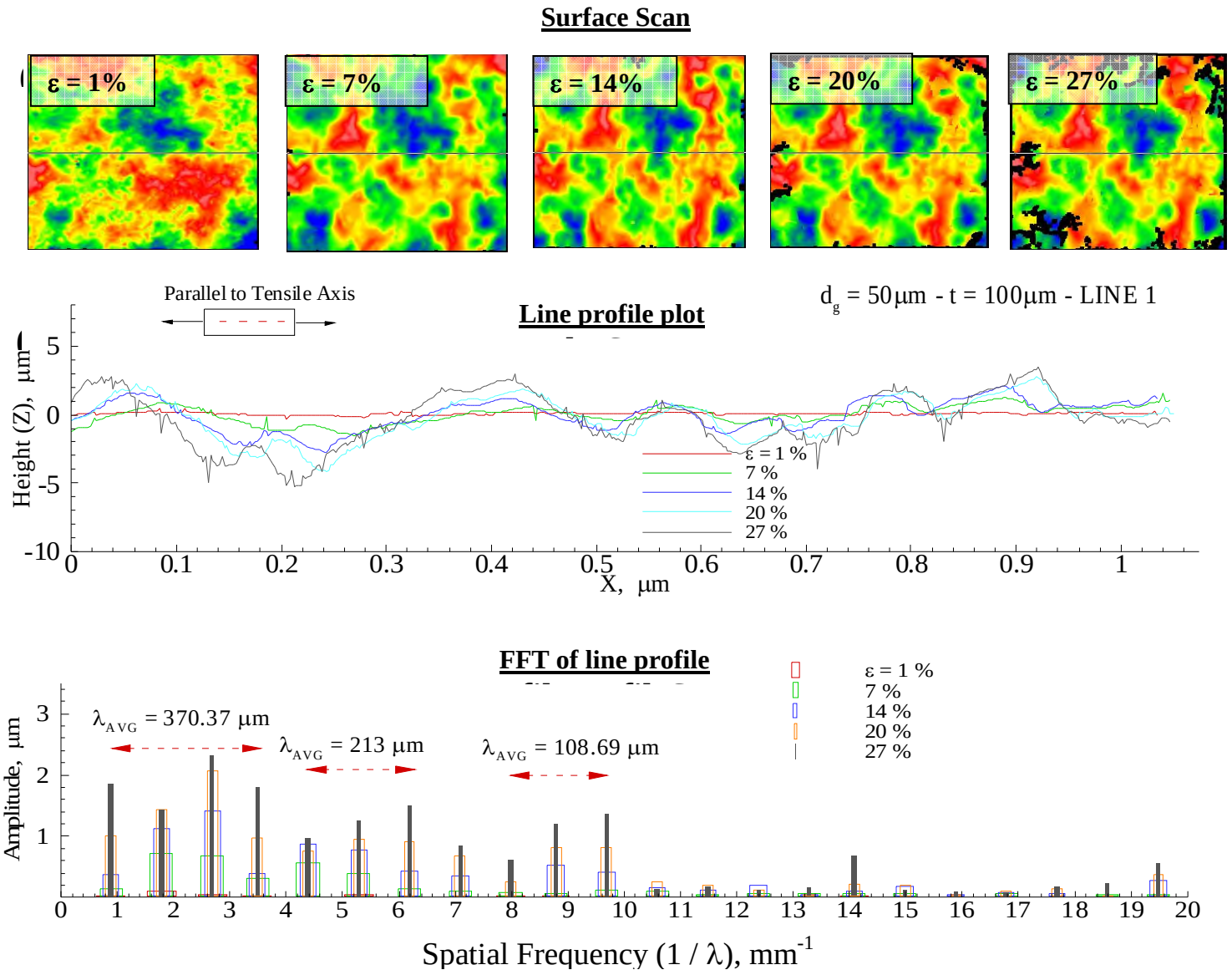

Figure 5.9 Evolution of surface roughness with strain for a specimen with d_g = 50µm & t = 100µm.

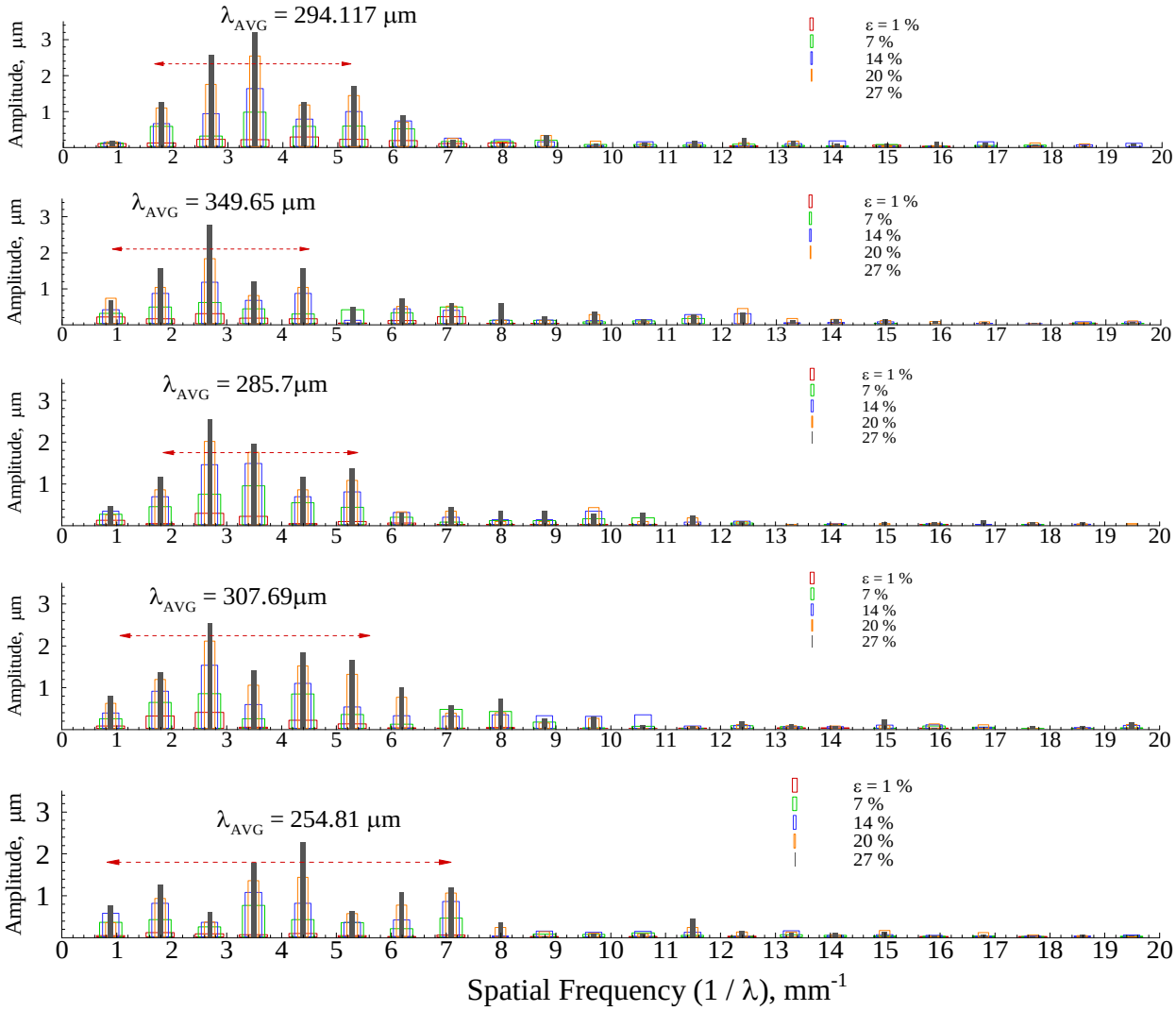

Figure 5.10 (a) Typical FFT analyses of surface roughness line profiles for a specimen with d_g = 50μm and t = 50μm at different levels of strain. In all cases a dominant wavelength of ~ $5d_q$ emerges.

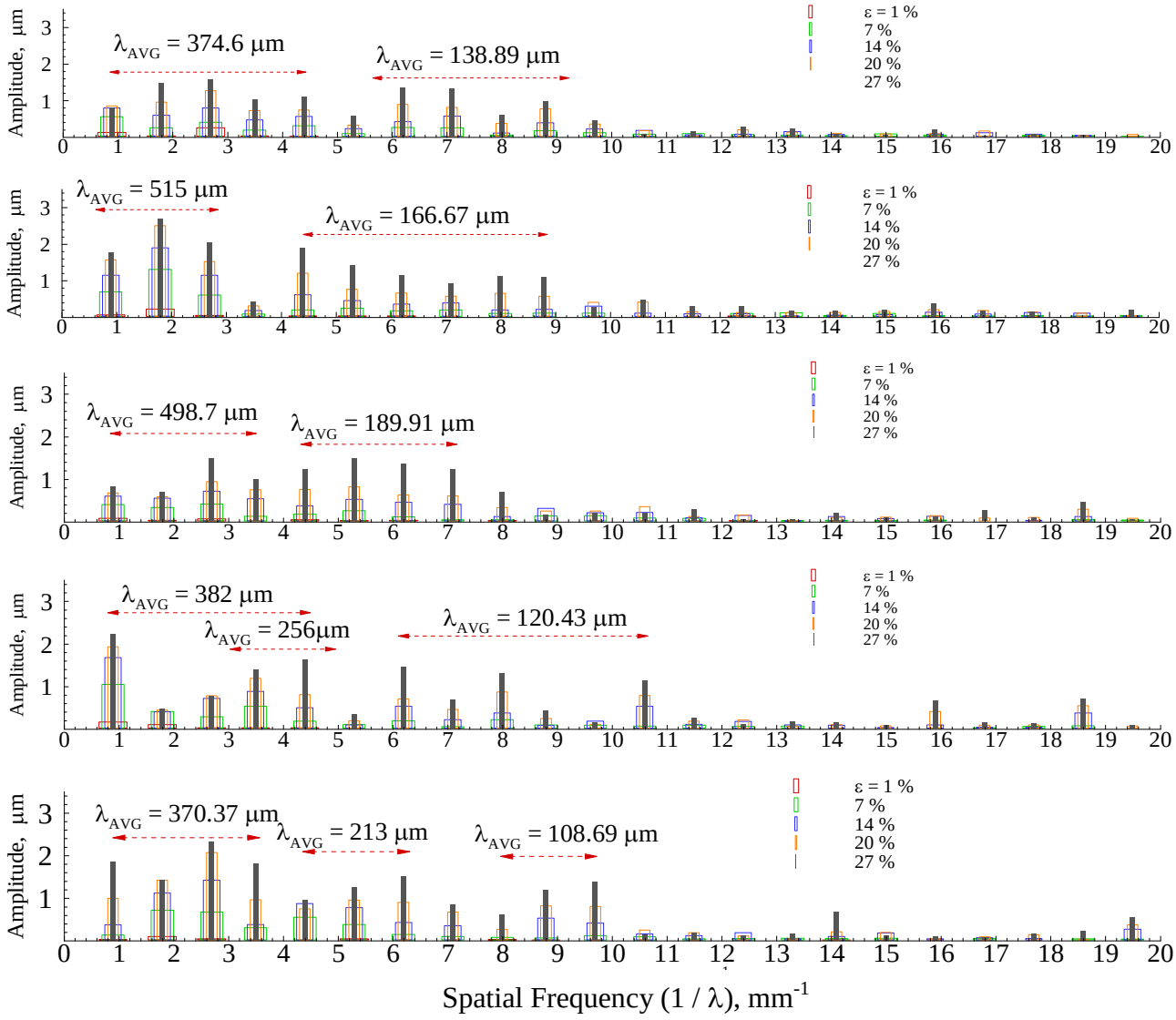

Figure 5.10 (b) Typical FFT analyses of surface roughness line profiles for a specimen with d_g = 50µm and t = 100µm at different levels of strain. A more spread out frequency distribution and a lower roughness amplitude, as compared to the multicrystalline case in Figure 6.9 (a) is seen.

roughness. This implies that the amplitude of the local thickness reduction with deformation is higher in the specimen with smaller thickness as compared to the specimen with the larger thickness, for the same average grain size.

The surface roughness was measured for 5 different scan windows along the specimen gauge length in both these cases. While just one such FFT analysis was shown in Figure 5.8 (c) and Figure 5.9 (c), Figure 5.10 shows the FFT analysis of all the 5 line profiles at different strain levels. Figure 5.10 (a) shows the FFT analysis for the 5 line profiles for t = 50μm case while Figure 5.10 (b) shows the 5 FFT analyses for the t = 100μm case. The dominant frequencies are represented by an average value, λ_{AVG}, calculated by taking the first moment of the individual data points i.e.

$$\lambda_{AVG} = \frac{\sum Amplitude \times \lambda}{\sum Amplitude}$$

Comparing the trends for the t = 50μm and t = 100μm case in Figure 5.10, we make the following salient observations:

1. The specimen with smaller thickness shows higher amplitudes as compared to the specimen with the larger thickness.
2. For a constant average grain size, a dominant frequency emerges for the smaller thickness specimen (with just one grain across the thickness). This dominant frequency is about ~5-6 × d_g for d_g = 50μm and t = 50μm.

3. The specimen with the larger thickness shows a more spread-out distribution where a single dominant frequency cannot always be identified. For d_g = 50μm and t = 50μm case studied here, frequencies of ~7-8 × d_g as well as ~2-3 × d_g are seen to emerge.

Figures 5.11 and 5.12 shows the results for the d_g = 20μm specimens with t = 12.5μm and t = 100μm. Figure 5.13 shows the results of FFT analysis on 4 different line profiles, extracted 4 different locations along the specimen gauge length, at different levels of strain i.e. 1%, 4%, 7% and 14% macroscopic strain. Figure 5.13 (a) shows the results for the d_g = 20μm & t = 12.5μm case while Figure 5.13 (b) shows the results for the t = 100μm case. Similar observations as those made for the d_g = 50μm case can be made: the multicrystalline specimen (t = 12.5μm) shows a single dominant frequency. While this dominant frequency was found to be ~5-6 × d_g for the earlier case, for d_g = 20μm, it is ~10 × d_g. In contrast with the multicrystalline case, the specimen with the larger thickness (t = 100μm) shows lower peak-to-valley roughness and also a more spread-out distribution. In this case, the roughness also develops at the level of individual grains i.e. frequency of ~ d_g also emerges in many cases as seen in Figure 5.13 (b).

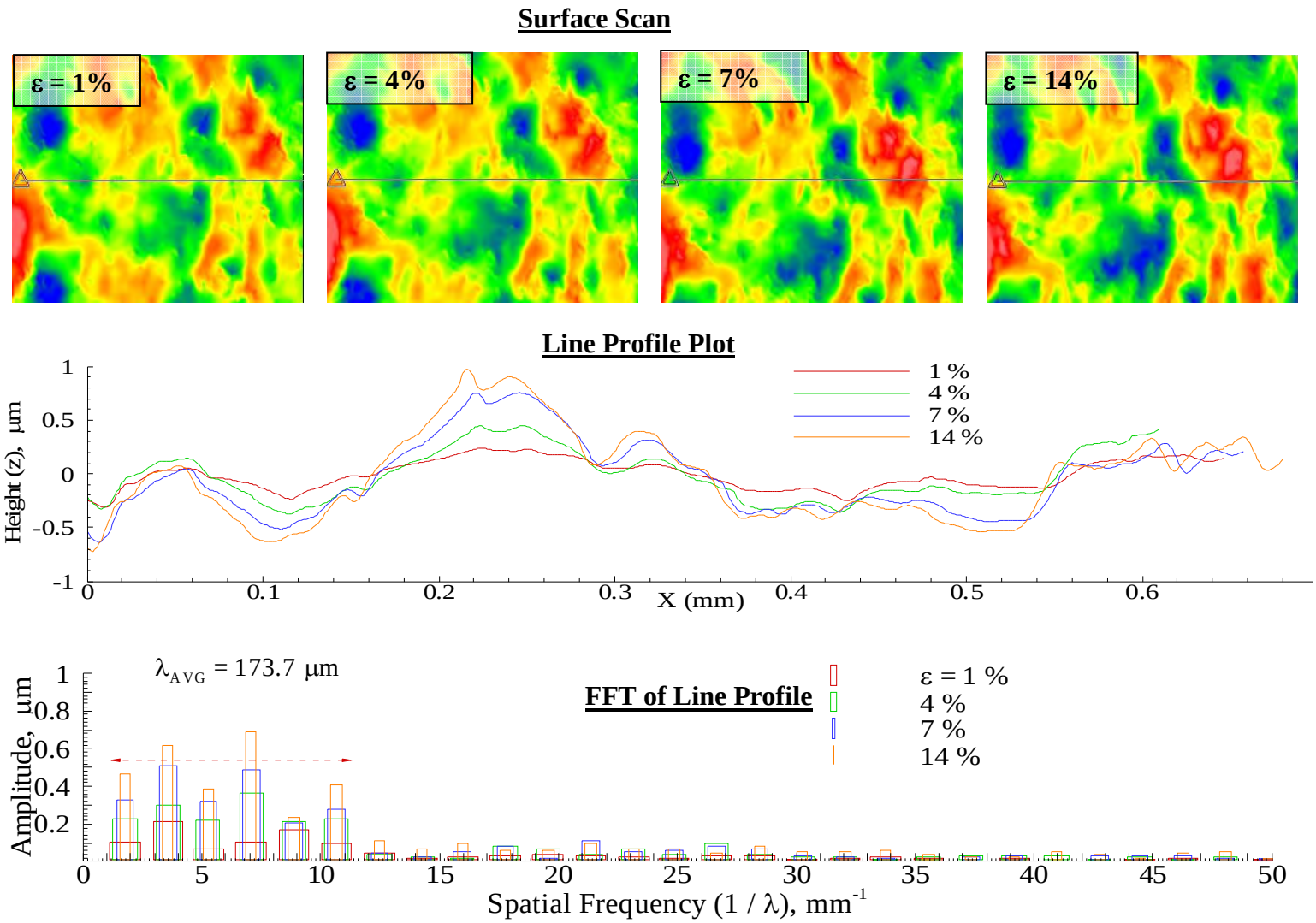

Figure 5.11 Evolution of surface roughness with strain for a specimen with d_g = 19.5µm & t = 12.5µm.

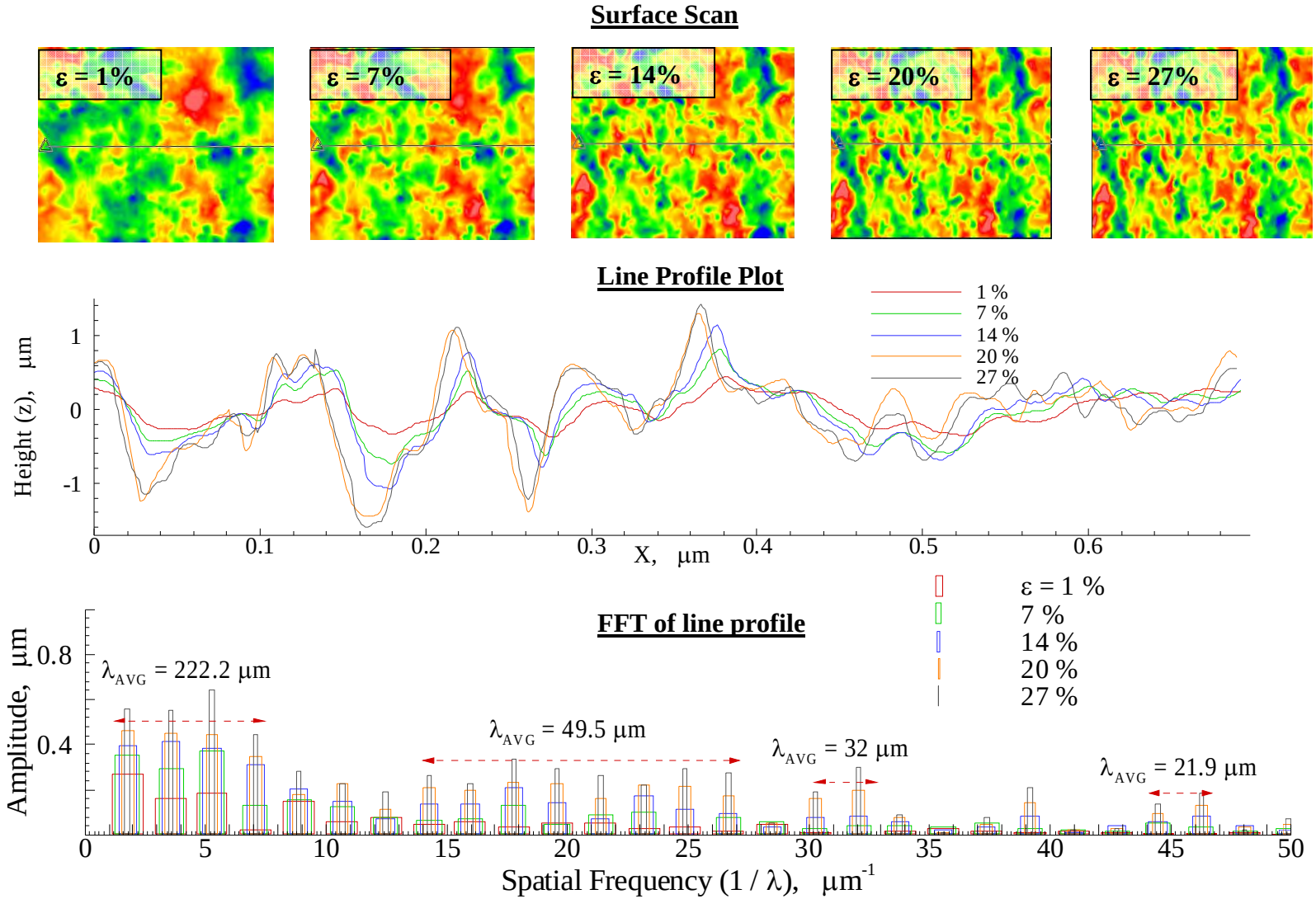

Figure 5.12 Evolution of surface roughness with strain for a specimen with d_g = 19.5µm & t = 100µm.

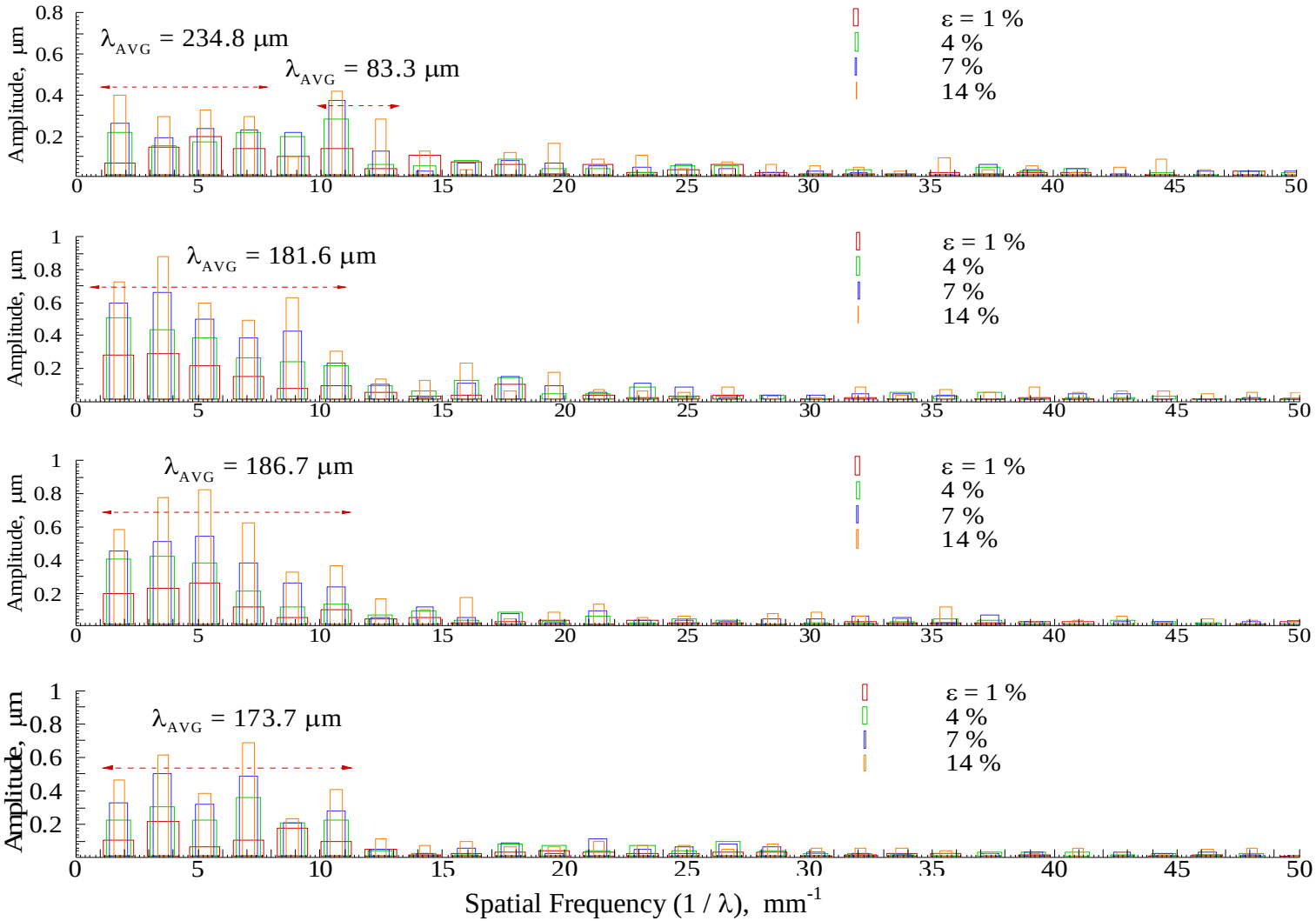

Figure 5.13 (a) Typical FFT analyses of surface roughness line profiles for a specimen with d_g = 19.5μm and t = 12.5μm at different levels of strain. In all cases, a dominant wavelength of ~ 9-11d_g emerges.

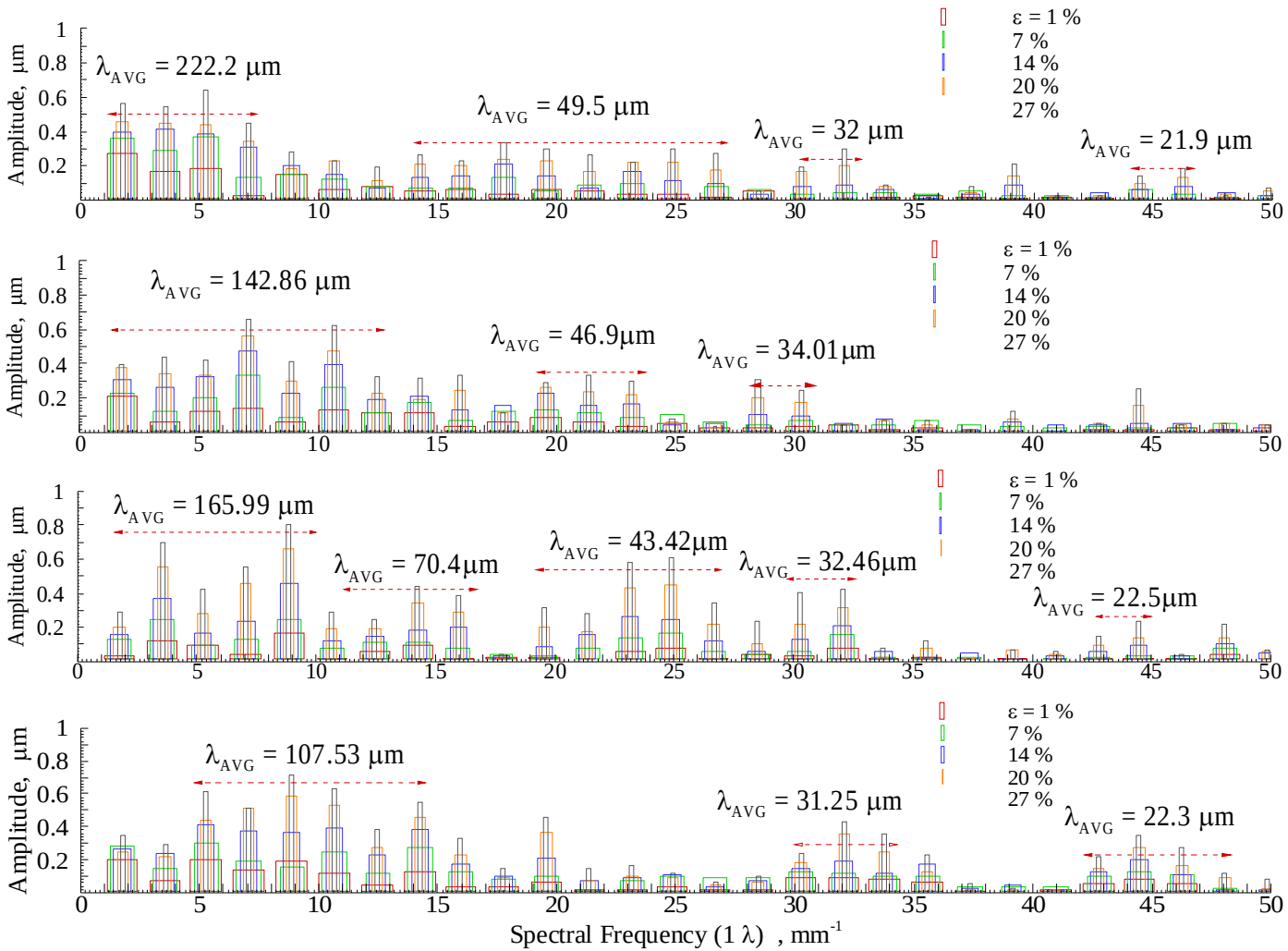

Figure 5.13 (b) Typical FFT analyses of surface roughness line profiles for a specimen with d_g = 20µm and t = 100µm at different levels of strain. In all cases, a more spread out distribution emerges with deformation also occurring at the level of individual grains.

5.5 DISCUSSION

5.5.1 Significance of surface roughness distribution

As discussed in Sec. 5.4.2, the surface roughness evolution is indicative of the local strain distribution at the microstructural level. It was also seen that the local strain distribution in the films is highly heterogeneous i.e. some regions feature much higher strain as compared to adjoining regions with much lower strain. Such heterogeneities in the deformation arise because of a number of factors over varying length scales. In general, heterogeneities arise because different regions of the specimen have different reponse. At the microscopic level, heterogeneities would arise as a result of the very different response from intragranular regions and grain boundary regions (featuring dislocation pile ups). These effects would be even more prominent for surface grains, where given the higher dislocation mobility in the grain interior, significant grain thinning can occur (Lee et al, 2004). As a result, it can be expected that in a polycrystalline specimen, deformation heterogeneities would be initiated in specific surface grains based on the size of the surface grain and its orientation relative to other grains in the vicinity as well as to the macroscopic loading direction.

In a polycrystalline specimen, however, any differences in the deformation at the level of individual grains must be accommodated at the aggregate level i.e. neighboring grains must accommodate the elastic strains that arise at the grain boundaries due to

deformation incompatibilities. While for small deformations i.e. at small strains, such accommodation can take place elastically. However, with continued deformation i.e. at large strains, the accommodation process must involve activation of dislocations in the adjoining grains. It should be noted that this accommodation via activation of dislocations in the adjoining grains would take place within the thickness direction of the specimen as well as within the plane of a typical polycrystalline specimen. This elastic strain due to incompatibility can be accommodated easily if the grain size and the stacking fault energy is large. Thus, while one would expect differences between different materials with respect to the size of the accommodation zone, there would also be differences due to the grain size (Miyazaki et al, 1979; Rey et al, 1988). Furthermore, given the limited number of slip systems available, one would expect that the nearest neighbor grains alone cannot accommodate these incompatibilities. Typically, smaller grains would feature a larger accommodation zone as compared to larger grains. There would also be effects of texture i.e. untextured specimen would have a smaller accommodation zone, all other factors being the same, as compared to textured specimen which would have a much larger accommodation zone.

With this as background, we see that there would be a length scale associated with deformation heterogeneities imposed by the microstructural factors. This length scale can be understood as the size of the accommodation zone required to accommodate the deformation incompatibilities arising from large strains in individual grains due to

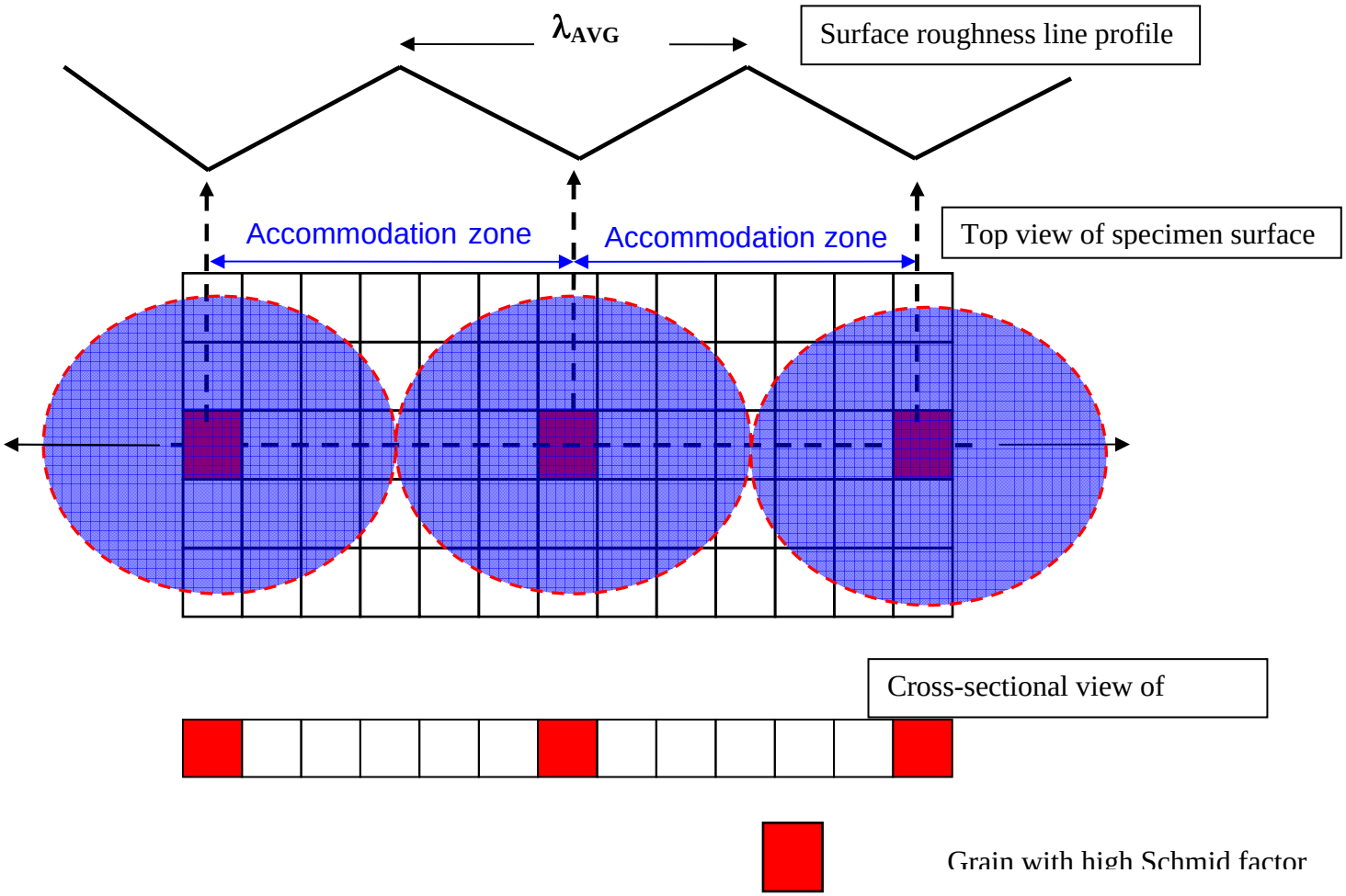

Figure 5.14 The significance of accommodation processes, at the microstructural level, on the development of surface roughness in freestanding polycrystalline films. Top view of the surface of the film, as well as the cross-sectional view is shown to illustrate the relationship between strain distribution due to crystallographic (Schmid factor) and geometric (grain size) factors and the resulting surface roughness.

variations in grain size as well as Schmid factors. Our measurements of the roughness distribution in the multicrystalline specimen for d_g = 20μm (t = 12.5μm) as well as d_g = 50μm (t = 50μm) provides an experimental observation of this accommodation process and the role of grain size on this length scale. Figure 5.14 schematically shows the top view of a polycrystalline specimen with grains approximated as squares. The through-thickness (cross-sectional) view is also shown. A typical roughness line profile with peaks and valleys is also shown adjacent to the schematic representation of the polycrystalline specimen. Let the grains shaded in red be the grains with the highest Schmid factor such that they feature the highest strains at a given stress level. The position of these grains coincides with the valleys in the roughness line profile since high strain regions are associated with thickness reduction, as shown in Sec. 5.3.2. These accommodation zones would separate the individual high strain regions. As a result, the length scale associated with the size of the accommodation zones will be closely related to the wavelength of the surface roughness distribution as found from the FFT analysis, and reported in Figure 5.10 and 5.13 for the two tested average grain sizes. We find that for the multicrystalline cases (Figure 5.10 (a) and Figure 5.13 (a)), a unique dominant wavelength emerges in the FFT analysis of the surface roughness. These dominant wavelengths are a function of the grain size i.e. for d_g = 20μm it is found to be ~ 10 d_g and for d_g = 50μm it is found to be ~ 6 d_g. This implies that the size of the accommodation zone is different for the two tested grain sizes. While it takes a region spanning ~6 grains or so for the d_g = 50μm case, d_g = 20μm requires a region spanning ~10 grains to accommodate the deformation incompatibilities arising from the high strain

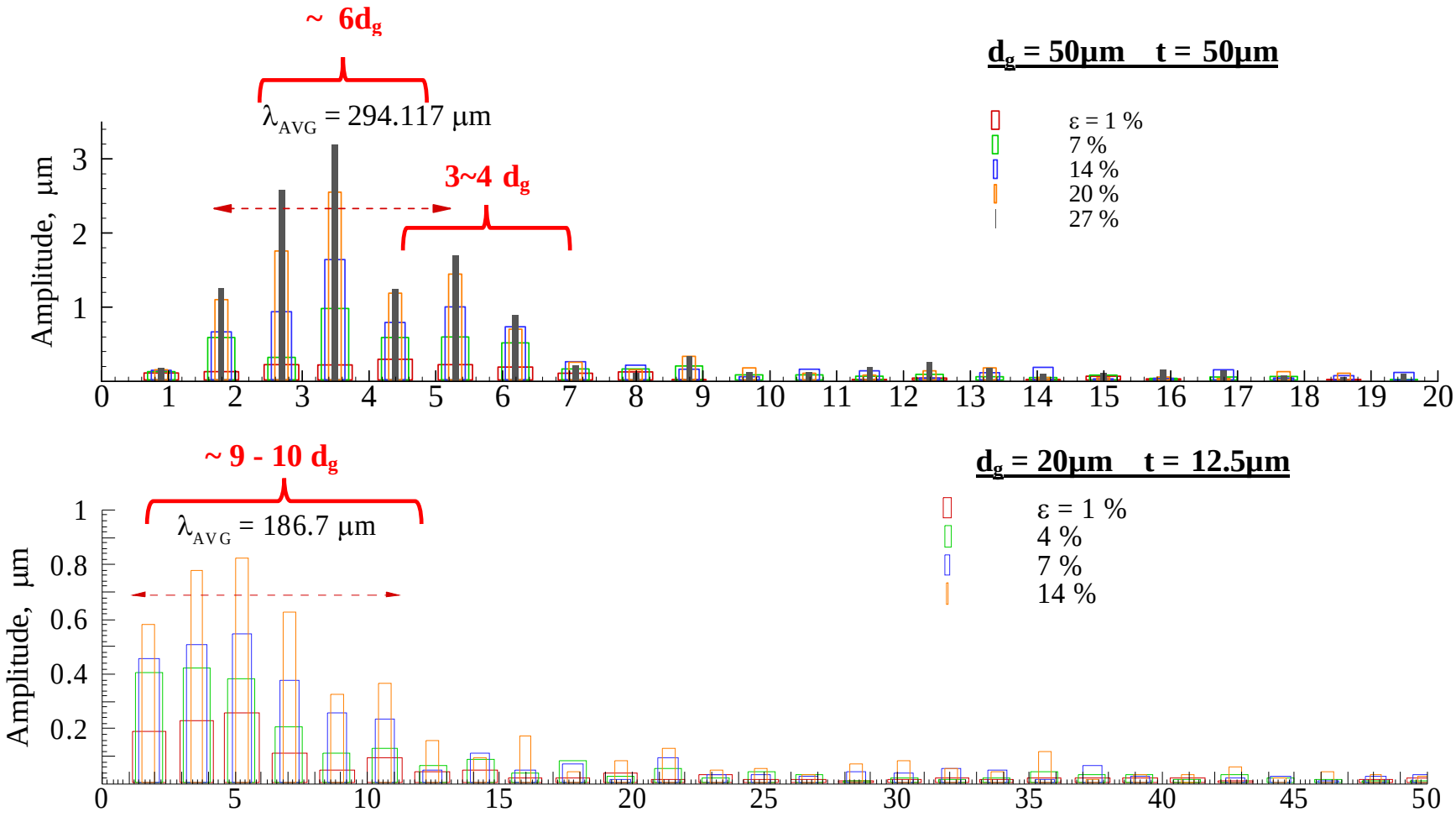

Figure 5.15 Effect of average grain size (d_g) on surface roughness evolution in two multicrystalline specimen i.e. specimen with $\lambda < 1$, with different average grain size **a)** d_g = 50μm **b)** d_g = 19.5μm. In both cases, a dominant frequency emerges. The corresponding wavelength, as a multiple of d_g, is also shown for both cases.

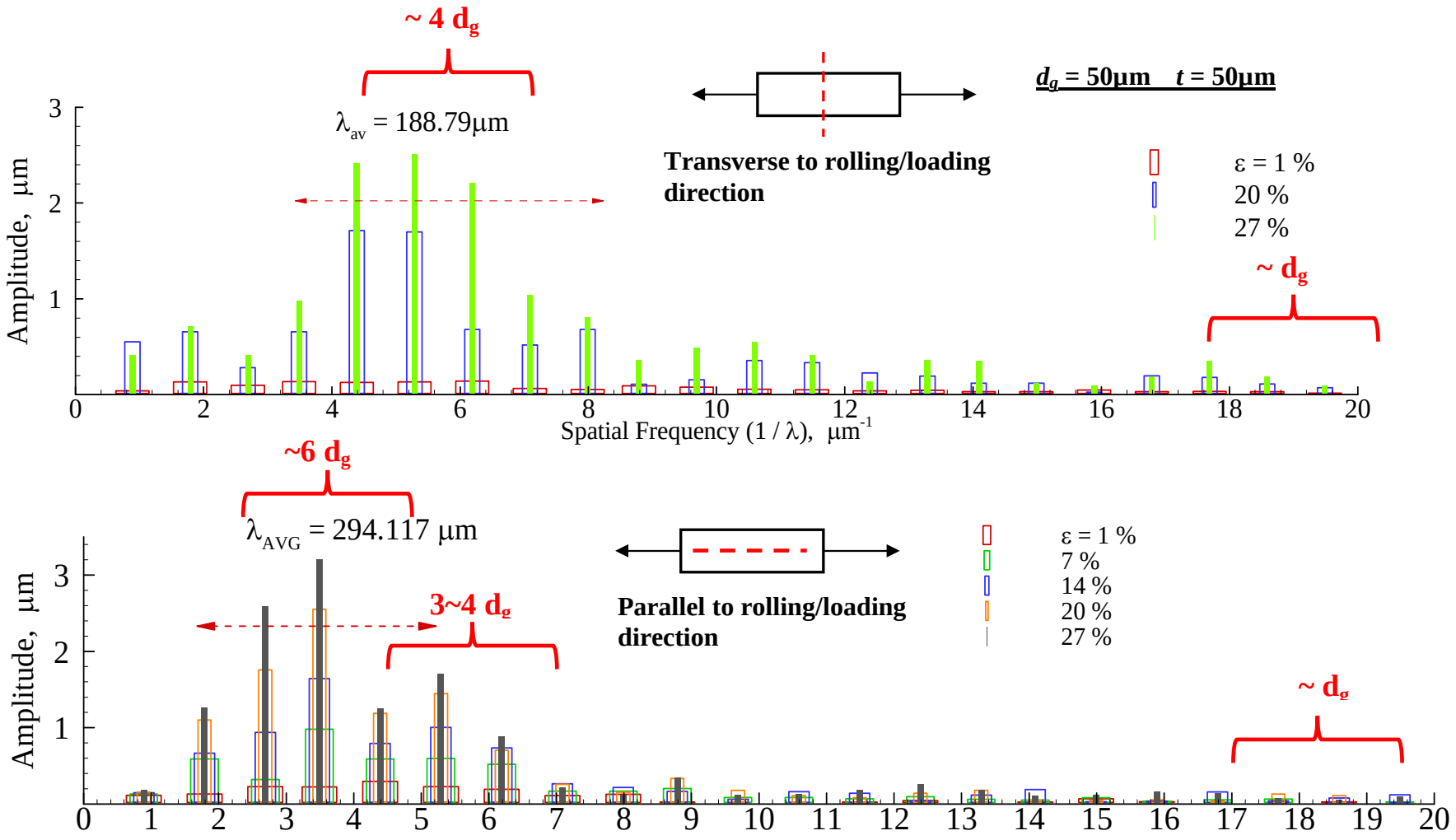

Figure 5.16 Effect of anisotropy on surface roughness evolution in the multicrystalline specimen with d_g = 50ìm and t = 50ìm. The longer wavelength observed in the tensile loading direction, along the rolling direction, as compared to the transverse direction is associated with the rolling texture.

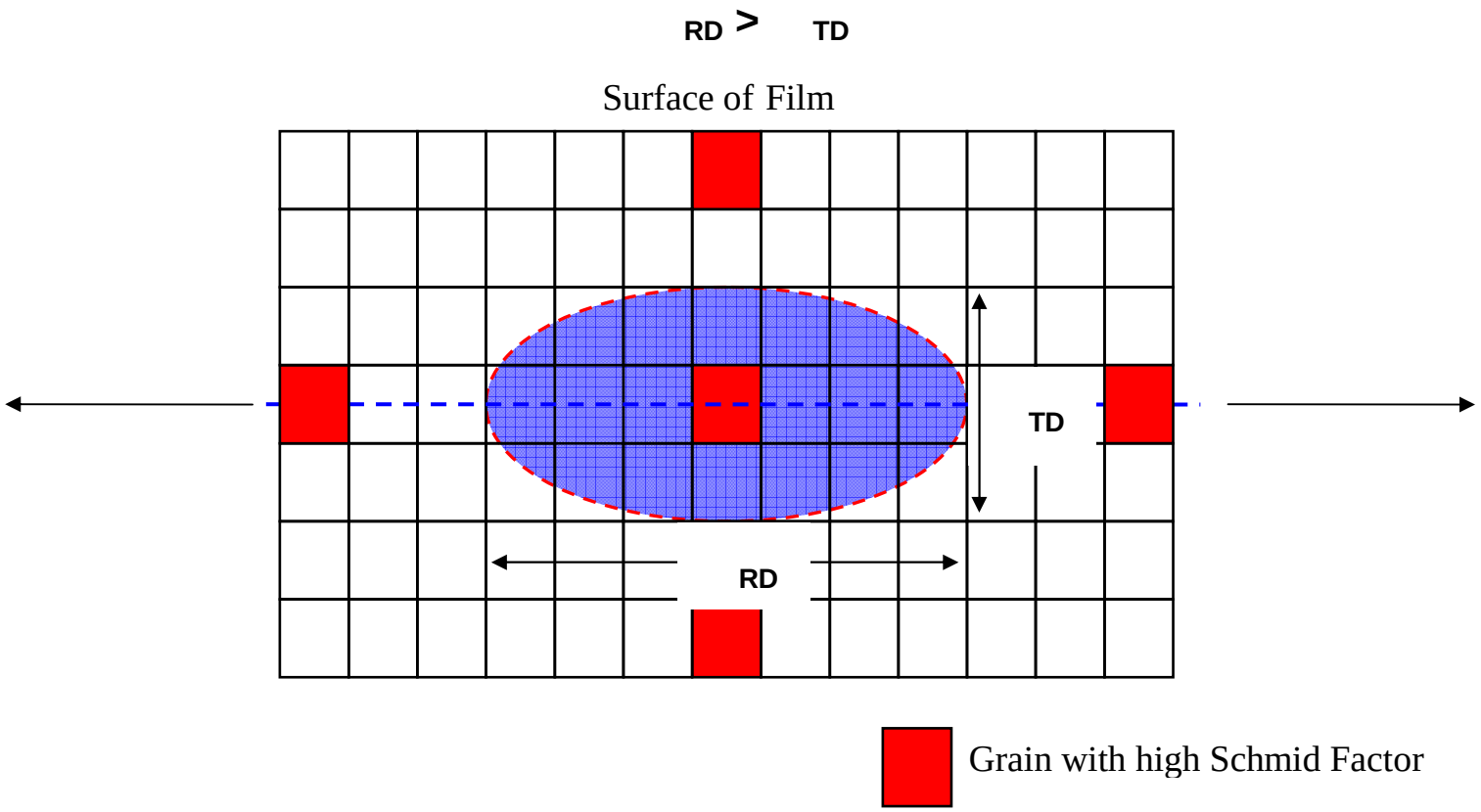

Figure 5.17 Schematic illustration of the effect of anisotropy on the size of accommodation zone. A larger accommodation zone is required along the rolling direction in a specimen with rolling texture.

regions. Figure 5.15 shows typical FFT analysis results for d_g = 20μm, Figure 5.15 (a), and d_g = 50μm, Figure 5.15 (b), to illustrate this point.than that found along the transverse direction. This is however expected since, rolled films are expected to have a prominent rolling texture along the rolling direction. Even though the films used in this study had been annealed, they still show a weak texture along the rolling direction. As a result, it would be easier to accommodate the residual strain in the transverse direction as compared to the rolling direction, where the number of available favorably oriented slip systems would be limited. This concept is illustrated schematically in Figure 5.17.

Another validation for our measurement comes from the analysis of Miyzaki et al (1979) of the critical number of grains across the thickness at which thickness effects first appear in polycrystalline specimen. Based on similar arguments as those here, it was argued that the thickness effects would first appear when the number of grains across the thickness is equal to the critical size of the accommodation zone. This is because, the highly unconstrained deformation of the surface grains influences the microstructural constraint experienced by neighboring grains within the thickness of the specimen. The number of grains across the specimen thickness that are affected by the surface grains is dictated by the size of the accommodation zone. Thickness effects first appear when the thickness of the specimen equals the size of the accommodation zone. At this critical thickness, all the grains across the specimen thickness are affected by the presence of the free surface and as a result the strength of the specimen drops. With further reduction in specimen thickness, the influence of the surface grains increases and prominent

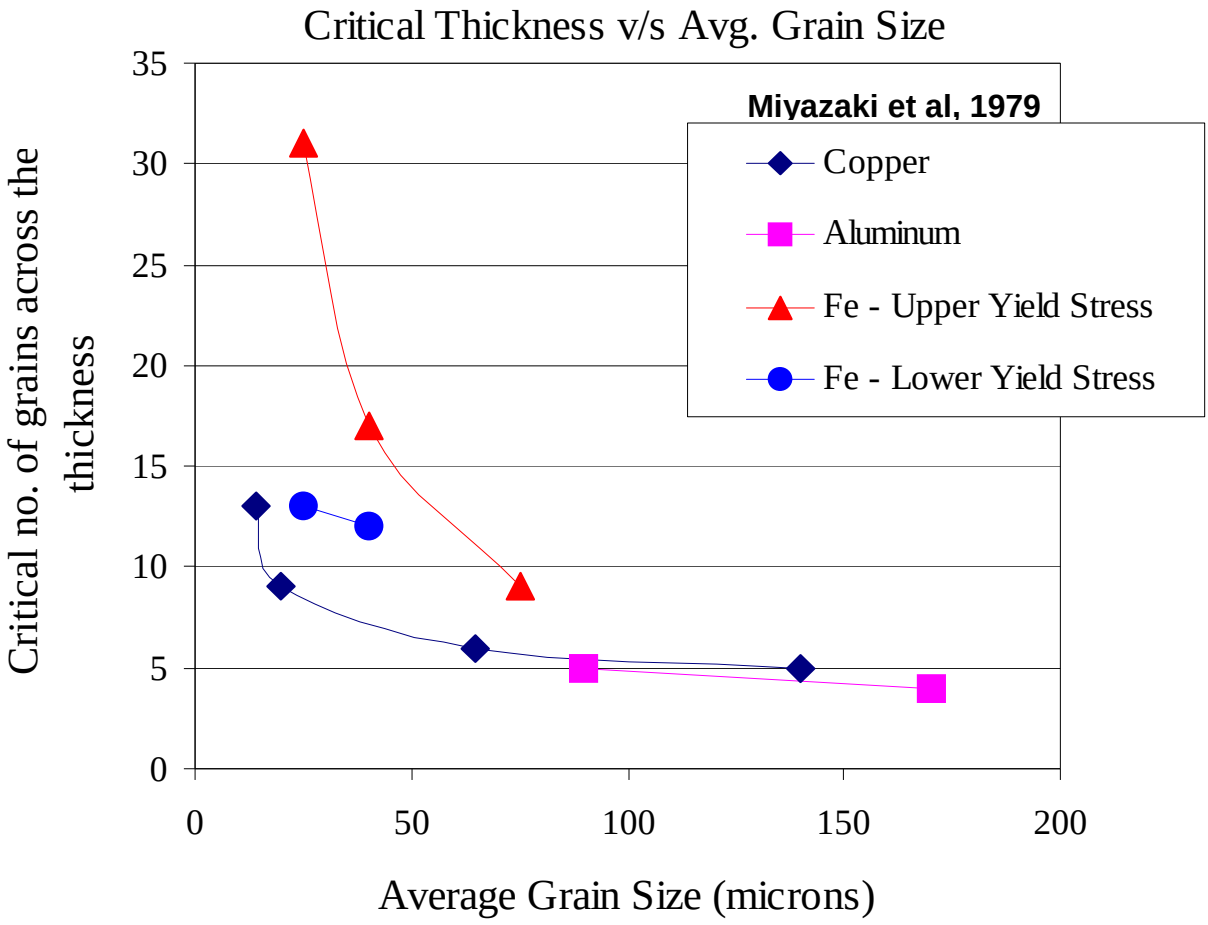

Figure 5.18 The effect of average grain size on the critical no. of grains across the thickness at which thickness effects first appear (Miyazaki et al, 1979).

thickness-related weakening is observed in specimen under uniaxial tension (Miyazaki et al, 1979). Figure 5.18 shows the experimentally observed critical specimen thickness, normalized by the average grain size, seen in Miyazaki et al (1979) for different materials. Based on their trends, in the case of Cu foils, we find that thickness effects would first appear for a critical $t/d_g \sim 7$ and 12 for $d_g = 50\mu m$ and $20\mu m$ respectively. Our interpretation of the size of the accommodation zone as obtained via roughness measurements in our study agrees very well with that obtained in Miyazaki et al (1979) based on the critical thickness at which size effects first appear under uniaxial tension.

Therefore, to conclude, the evolution of the surface roughness is intimately related to the accommodation process through which deformation incompatibilities between adjoining grains are accommodated within a polycrystalline specimen. Based on our roughness measurements, we identified the size of these accommodation zones and their dependence on various microstructural parameters such as grain size and texture distribution.

5.5.2 Effect of specimen thickness: Delocalization of strain

The evolution of surface roughness can also be used to understand the role of thickness on the resulting deformation heterogeneities and the ductility (as seen in Figure 5.3). As seen previously in the FFT analyses of the surface roughness line profiles (Figure 5.10 and Figure 5.13), while a dominant and unique wavelength of the surface

roughness emerges in a multicrystalline specimen, specimens with more than one grain across the thickness (but the same average grain size) show a lower roughness amplitude and a more homogenous roughness distribution (spread out in the frequency space). For example, for d_g = 20μm (shown in Figure 5.13), while the high strain regions were separated by ~10-11 grains or so in a multicrystalline specimen, for a specimen with 4 grains across the thickness i.e. t = 100μm, the high strain regions not only feature a lower strain level (lower peak-to-valley roughness) but were also closer to each other i.e. various smaller wavelengths were found to be active. In this case, wavelengths of the order of ~12-13 d_g, ~2-3 d_g and d_g were also found to be active.

This observation can be understood as follows: in the multicrystalline specimen, the deformation incompatibilities only need to be accommodated within the plane of the specimen i.e. there are no compatibility requirements in the thickness direction. As a result, with continued deformation, only the most favorably oriented grains i.e. grains with the highest Schmid factor (or grains with a relatively larger size) accumulates strain and undergoes local thickness reduction. The surrounding grains within the plane of the specimen only deform so as to accommodate the plastic incompatibilities resulting from the deformation of such high Schmid factor grains. As a result, the dominant wavelength observed from the FFT analysis of the roughness distribution for the multicrystalline specimen is directly related to the accommodation length scale in the multicrystalline specimen. On the other hand, with increasing thickness as the number of grains across the thickness increases, such favorably oriented grains must now also satisfy through-

thickness compatibility constraints (in addition to the in-plane compatibility constraints). As a result, their deformation is more restricted – this accounts for the lower roughness amplitude observed in these cases. In addition to this, the greater overall compatibility constraints on individual grains in these cases also imply that more slip systems are required to satisfy deformation compatibility in all grains (as compared to the multicrystalline case). This leads to a homogenization of strain because more grains get involved in the accommodation processes i.e. even grains with sub-optimal orientation (i.e. lower Schmid factors) feature higher strains than the multicrystalline case. Thus, while the deformation is still heterogeneous and grains featuring high Schmid factors still feature higher strains, the strain distribution is seen to be more spread out.

A direct outcome of this is the delocalization of strain. As seen in Figs. 5.8 and 5.9 for d_g = 50μm and Figs. 5.11 and 5.12 for d_g = 19.5μm, the high strain regions in specimen with larger thickness carry a lower strain as compared to the multicrystalline case. While the strain distribution is still heterogeneous, the strain is distributed more evenly across multiple grains in specimens with $\lambda > 1$ as compared to the multicrystalline specimens. Therefore, unlike in a multicrystalline specimen where the high strain regions were widely separated, a specimen with multiple grains across the thickness features much more closely spaced high strain regions i.e. deformation is more homogeneous. This interpretation can explain the thickness effects seen on the ductility of the foil specimens for varying average grain sizes. As the thickness is reduced, the strain distribution becomes more localized i.e. local regions carry a higher strain as compared to

the surrounding regions and at the same time they are more widely spaced. It is also straightforward to understand that a given local thickness reduction will have a far more serious effect in a specimen with a smaller thickness. As a result, with increasing deformation, the likelihood of the onset of plasticity instability due to such geometric considerations i.e. thickness reductions, is far higher in a small thickness specimen as compared to a specimen with the same average grain size, but a larger thickness.

Besides these considerations of deformation heterogeneities and the consequential localized thickness reduction, specimens with smaller thickness also feature a lower strain hardening capability. This is because with reducing thickness, an increasingly large fraction of the intragranular volume is exposed to the free surface and as a result substantial dislocation annihilation occurs. Such free-surface related effects are particularly evident in the foil specimen with larger grain sizes. With reducing average grain size, in addition to the effect of the free surface with reducing thickness, dynamic recovery due to close proximity of dislocations to dislocation sinks such as grain boundaries also affects the overall dislocation storage. Therefore, while there is increased vulnerability to local thickness reductions, the strain hardening capability is also compromised to a large extent with reducing thickness. These two factors taken together lead to a lower ductility, or uniform strain, with reducing thickness.

While our experimental observations here are limited to the specimen with larger grain sizes, our conclusions agree with similar studies on thin film specimen with grains

sizes around ~1 - 5μm and thickness ~ 2 - 5μm (Lee et al, 2004). Lee et al (2004) investigated the loss of ductility with reducing average grain sizes as well as reducing thickness in thin film specimen with just a few grains across the thickness via TEM observations. Their study showed that thinner specimen showed locally thinned regions due to loss of dislocations to the free surface. They attributed the limited ductility observed in their specimen to the onset of plastic instability due to these local thickness reductions. It was shown that the onset of such plastic instability in the form of diffused necking, closely followed by localized necking, occurs in larger grains that carry a larger strain and greater intragranular dislocation activity susceptible to annihilation at the free surface.

5.6 CONCLUSIONS

This chapter investigated the effects of average grain size and thickness on the experimentally observed ductility, defined here as the maximum uniform strain, for freestanding rolled foils with d_g = 11μm - 50μm and t = 11μm - 50μm as well as freestanding electrodeposited films with d_g = 1.8μm - 5μm and t = 2μm - 50μm, under uniaxial tension. With regards to thickness effects, it was seen that reducing thickness results in reducing ductility. Identifying a direct relationship between the surface roughness and the local strain distribution at the microstructural level highlighted the mechanisms behind these thickness effects. It was shown that high strain regions also feature local thickness reductions that can initiate plastic instabilities. We find that films with just a few grains across the thickness, as in this study, develop substantial

deformation heterogeneities with continued deformation. Such heterogeneities in the strain distribution were shown to be an outcome of the accommodation process at the aggregate level through which grains respond to plastic incompatibilities with surrounding grains. In this context, thickness effects on ductility arise because with reducing thickness, there are no through-thickness compatibility constraints on individual grains within the specimen. As a result, regions with favorably oriented grains accumulate much greater strain as compared to adjoining regions and the resulting thickness reduction can lead to early strain localization. On the other hand, with increasing thickness, through-thickness compatibility constraints result in delocalizing the strain. Consequently, while heterogeneities may still exist, the strain distribution is more spread-out because more grains get involved in the accommodation of plastic incompatibilities. Such thickness effects were quite prominent at larger grain sizes, typically >2μm, however for grain sizes <2μm i.e. approaching ultrafine grained regime, the ductility is inherently limited by the grain size effects and only a marginal ductility of ~2% is seen irrespective of the thickness. This effect was attributed to the limited dislocation activity and the loss of strain hardening capability (due to dynamic recovery) at small grain sizes.

5.7 ACKNOWLEDGEMENTS

I would like to acknowledge the support of NSF under Contract No. CMMI-0134111. The assistance of Pratik Ray and Shallabh Gupta from Dept. of materials

science and engineering and Ames Lab respectively, with annealing is also gratefully acknowledged.

5.8 REFERENCES

1. Ma, E., Wang, Y.M., Lu, Q.H., Sui, M.L, Lu, L. and Lu, K. (2004) "Strain-hardening and large tensile elongation in ultra-high strength nano-twinned copper" *Appl. Phys. Lett.*, 85, No. 21, 4932
2. Yong-Hao Zhao, John F. Bingert, Xiao-Zhou Liao, Bao-Zhi Cui, Ke Han, Alla V. Sergueeva, Amiya K. Mukherjee, Ruslan Z. Valiev, Terence G. Langdon, and Yuntian T. Zhu (2006) "Simultaneously increasing the ductility and strength in ultra-fine grained pure copper" *Adv. Mater.*, 18, 2949
3. Ma, E. (2003) "Instability and ductility in nanocrystalline and ultra-fine grained materials" *Scripta Mater,* 49, 663
4. Wang, Y., Chen, M.m Zhou, F. and Ma, E. (2002) "High tensile ductility in a nano-structured metal" *Nature,* 419, 912
5. Koch, C.C. (2003) "Optimization of strength and ductility in nanocrystalline and ultrafine grained materials" *Scripta Mater,* 49, 657.
6. Lee, H.J., Zhang, P. and Bravman, J.C., (2003) "Tensile failure by grain thinning in micromachined Aluminum thin films" *J Appl. Phys.*, 93 (3), 1443
7. Miyazaki, S., Fujita, H. and Hiraoka, H. (1979) "Effects of specimen size on the flow stress of rod specimen of polycrystalline Cu-Al alloy" *Scripta Metall.* 13, 447
8. Yamakov, V., Wolf, D., Phillpot, S. R. and Mukherjee, A. K. (2002) "Dislocation processes in the deformation of nanocrystalline aluminum by molecular dynamics simulations" *Nat. Mater.* 1, 1
9. Rey, C. (1988) "Effects of grain boundaries on the mechanical behavior of grains in polycrystals", *Revue Phys. Appl.* 23, 491
10. Wang, H. and Bastawros, A.F. (2008) "Modified digital image correlation method to study the full field strain map", *under preparation*

CHAPTER 6. GENERAL CONCLUSIONS

6.1 SUMMARY

In this study we investigated the effects of thickness (t) and average grain size (d_g) on the experimentally observed strength (yield stress and flow stress) and ductility of freestanding Cu films. The films were tested under uniaxial tension, precluding the effects of macroscopic strain gradients. Two sets of specimen were tested in this study: rolled foil specimen with $d_g \approx$ 11μm - 50μm and t ≈ 12.5μm - 100μm and electrodeposited films with $d_g \approx$ 1.8μm - 5μm and t ≈ 2μm - 50μm. In all cases, the effects of thickness and average grain size on the observed strength and ductility were assessed independently of each other.

Our results indicate that for freestanding films under macroscopically homogenous deformation, both thickness and average grain size affect mechanical properties related to plastic deformation. Furthermore, unlike previous results for thickness effects in test configurations featuring strain gradients, film-on-substrate systems and multilayered thin films systems, the results in our study indicate that thickness and grain size effects are coupled i.e. the nature and magnitude of thickness effects depend on the average grain size.

For the foil specimen, with average grain sizes well within the ‘polycrystalline’ regime i.e. $d_g \sim$ O(10μm -100μm), we find that thickness effects arise due to the effect of

the free surface on the overall microstructural constraint experienced by individual grains within the specimen. With reducing thickness for a constant average grain size, thickness affects the overall specimen strength through the volume fraction of surface grains. Grains that are exposed to the free surface experience far lesser microstructural constraint on plastic deformation (propagation of dislocations) as compared to bulk grains. We formulated a Hall-Petch type relationship to describe the experimentally observed limiting strength of a multicrystalline specimen i.e. a specimen with just one grain across the thickness where all the grains are surface grains. The overall specimen strength was shown to be an outcome of the volume average of the surface grain response and the bulk grains' reponse. Our results for this regime of grain sizes show that reducing thickness leads to a reduction in the overall specimen strength.

With reducing average grain size, as in the electrodeposited films in this study i.e. d_g ~ O (1μm), the aforementioned free surface effects, characterized for the foil specimens and associated with thickness dependent weakening, get diminished due to limited intragranular dislocation activity. Residual electrical resistivity measurements performed in this study showed that while there was substantial annihilation of intragranular dislocations with reducing film thickness in films with d_g ~ 5μm – 3.5μm, however, films with d_g = 1.8μm showed only a negligible reduction in dislocation storage with reducing thickness. In such scenarios, where intragranular dislocation activity is quite limited, plastic deformation is essentially an outcome of grain boundary dislocations. Consequently, at such small grain sizes, thickness effects on the overall

specimen strength arise because with reducing thickness, the grain boundary area per unit specimen volume reduces. As a result, reducing specimen thickness results in a statistical reduction of the available grain boundary dislocation sources. This statistical effect of dislocation source reduction with reducing thickness, described as dislocation source starvation was attributed to the observed increasing specimen strength with reducing thickness for these specimens.

Our results here indicate a transition from propagation-limited plasticity in specimens with d_g ~ O (10μm -100μm), to source-controlled plasticity in specimens with d_g ~ O (1μm) or below (typically, thin films). In the former case, thickness effects come about because of the influence of the free surface on the overall microstructural constraint that dictates the required macroscopic flow stress for dislocation propagation within the individual grains. In the latter case, however, the limiting mean free path in such small grain sizes inherently restricts dislocation propagation and multiplication irrespective of the thickness. As a result, thickness effects in these cases arise because of the variation of dislocation source density with thickness. Therefore, with regards to thickness effects on the strength we find that the case of thickness dependent strengthening in freestanding metallic thin films has more in common with metallic whiskers and micro-pillars where similar observations of dislocation starvation strengthening have been made, as compared to strain gradient effects or thickness effects in film-on-substrate and multilayered film systems, where the dimensional constraint on dislocation propagation was held responsible for the thickness effects.

The influence of specimen thickness on the ductility was also investigated. It was found that both, thickness and average grain size affect ductility. It was observed that the thickness dependence of ductility diminishes with reducing grain size. While prominent thickness effects are seen in specimens with larger grain sizes, we find that specimens with d_g = 1.8μm show a limiting ductility of only ~2%, irrespective of the thickness.

Such limiting ductility was explained to be an outcome of the early loss of strain hardening capability in such small grains because of their inability to store dislocations efficiently. It appears from our results that for grain sizes approaching ultrafine grained regime, where intragranular dislocation activity is very restricted and conventional forest hardening is not available, the ductility is inherently limited due to early onset of plastic instabilities.

The study of thickness effects on the observed ductility was carried out on the foil specimens, which show prominent thickness effects. We find that the strain distribution, at the level of individual grains, in specimens with just a few grains across the thickness, is highly heterogeneous. Such strain heterogeneities were directly correlated to local thickness reductions in the specimen cross-section via surface roughness measurements. Such geometric factors are able to trigger a plastic instability when the specimen cannot compensate for local thickness reduction (i.e. higher local strain) via strain hardening. Through surface roughness measurements, we find that while a multicrystalline specimen features widely spaced high-strain regions with a larger local thickness reductions, a

specimen with multiple grains across the thickness shows a relatively more uniform strain distribution and the maximum thickness reduction in high strain regions is much lower. Therefore, higher experimentally observed ductility in specimens with larger thickness is possibly related to such delocalization of strain with increasing thickness. Our analysis here identifies the average spacing between such high strain regions with the intrinsic material length scale related to the accommodation of deformation incompatibilities between neighboring grains.

6.2 FUTURE WORK

This work presented an experimental assessment of the effect of thickness on the plastic deformation and related mechanical properties (yield stress, flow stress & ductility) in freestanding films. It was shown that the nature of thickness effects is very dependent on the underlying deformation mechanisms, dictated by the average grain size (Cheng et al, 2003). At larger grain sizes, ~O (10 - 100μm), the contribution from grain interiors dominates the overall specimen behavior. In this regime, thickness effects appear because with reducing thickness, the proximity of individual grains to the free surface increases. The resulting loss in microstructural constraint was identified as the origin of the thickness effects. On the other hand, for grain sizes approaching ~1μm, grain boundary dislocations start to play an increasingly prominent role and the role of intragranular regions on the overall deformation gets diminished because of the limited intragranular dislocation activity at such small grain sizes. In this regime, thickness

effects appear because reducing thickness results in a reduction in the grain boundary area per unit specimen volume. This statistical reduction in the available grain boundary dislocation source density with reducing thickness leads to source starvation strengthening.

Our results in this study show that both effects i.e. free surface related weakening as well as dislocation source starvation strengthening, are simultaneously present in the specimens with grain sizes between 1 - 10μm. Our work here, as well as previous studies (Lee et al, 2003), suggest that while the free surface effects observed at much larger grain sizes get diminished with reducing grain size, they do persist at grain sizes approaching ~1μm. However, the influence of free surface, and its diminution with reducing grain sizes, has not been categorically characterized for such small grain sizes. Our results clearly show that the surface Hall-Petch parameters obtained for the freestanding foil specimen cannot be translated to these grain sizes i.e. the proposed model overestimates the resultant weakening. In addition to this, the actual contribution from the dislocation source starvation related effects is also uncertain. An important extension of this work could therefore be an effort to distinguish between these two effects in scenarios where both act simultaneously. In this regard, the contribution starvation strengthening should be characterized in specimens with grain size <1μm, where such effects would dominate. Therefore, a study similar to this work where specimens with varying thicknesses but constant average grain size (<1μm) would prove very valuable in understanding the dislocation starvation effects observed here. Such a study could also facilitate the

formulation of a unified phenomenological model that captures both effects and the associated transition.

Another important consideration that emerges from our results is the possible role of dislocation starvation related effects in polycrystalline specimens with larger grain sizes. In this study, we show a reduction in thickness until $\lambda \sim 0.6$ for specimens with $d_g = 20\mu m$. However, with further reduction of specimen thickness beyond the critical mean free path required for intragranular dislocation nucleation and multiplication within the grain interior (~1μm), dislocation starvation effects similar to those observed in micro pillar experiments (Greer et al, 2005) can be expected. As a result, the reported trends relating λ to the specimen strength (yield/flow stress) in Chap. 3 could feature an additional regime showing increasing strength with reducing λ due to dislocation starvation, shown schematically in Fig. 6.1. In this regard, an important extension of this work would be to characterize specimens with grain sizes similar to the foil specimen in this study (10μm - 50μm) but with thickness approaching 1μm.

With regards to the ductility of the specimen, this study fills an important gap in the literature on this topic. Most previous investigations on the size effects on ductility have only focused on the role of the average grain size. Our investigations here present an assessment of the effect of specimen thickness on the observed ductility. We related the observed ductility to the underlying deformation mechanisms at the aggregate level i.e. at

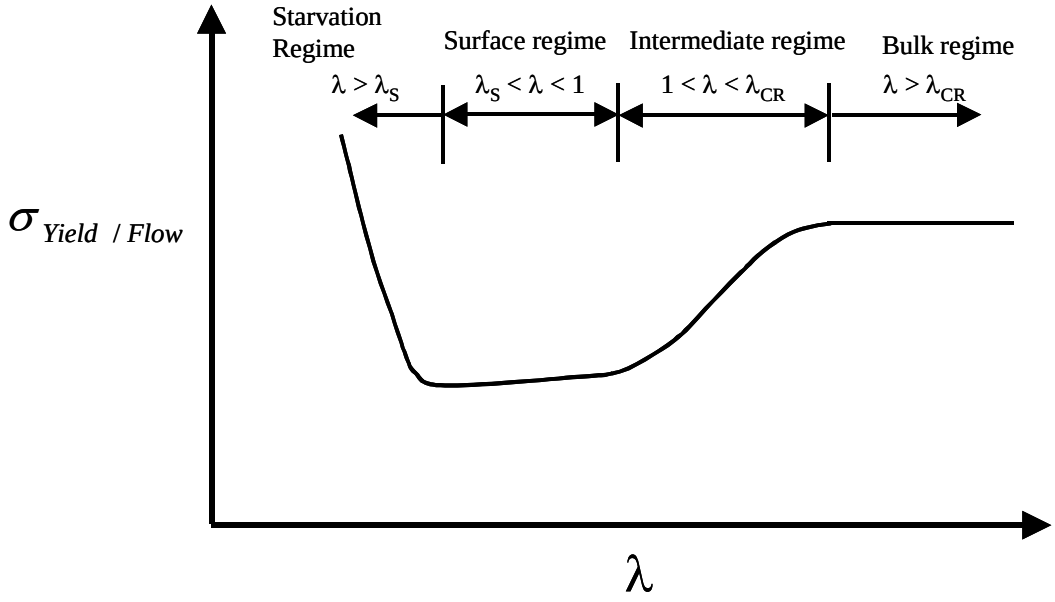

Figure 6.1 The emergence of dislocation starvation effects in freestanding polycrystalline films under uniaxial tension with reducing thickness. With continued thickness reduction, beyond the critical dislocation mean free path for intragranular dislocation nucleation and multiplication, deformation would commence under dislocation-starved conditions. As a result, increasing yield/flow stress would increase with reducing λ.

the level of multiple grains. We show that deformation heterogeneities at the aggregate level play an important role in the onset of plastic instabilities. An important extension of this work could be the investigation of the evolution of deformation texture at the level of individual grains, as opposed to the aggregate level. In this way, the role of average grain sizes, texture distribution and the fundamental mechanisms through which grains accommodate plastic incompatibilities can be understood.

6.3 REFERENCES

1. Cheng, S., Spencer, J.A., Milligan, W.W. (2003) “Strength and tension/compression asymmetry in nano-structured and ultrafine-grain materials” *Acta Mater., 51,* 4505-4518, 2000
2. Lee, H.J., Zhang, P. and Bravman, J.C., (2003) “Tensile failure by grain thinning in micromachined Aluminum thin films” *J Appl. Phys.,* 93 (3), 1443-1451
3. Greer, J. R., Oliver, W. C. and Nix, W. D. (2005) “Size dependence of mechanical properties of gold at the micron scale in the absence of strain gradients” *Acta Mater.* Vol. 53, Issue 6, 1821

APPENDIX A. PULSED ELECTRODEPOSITION AS A MEANS TO FABRICATE FREESTANDING Cu SPECIMEN

A.1 INTRODUCTION

The current study aims at producing freestanding Cu films via a electroplating technique called pulsed electrodeposition (PED). Unlike DC electroplating (DC) which can be performed either under galvanostatic conditions or potentiostatic conditions, PED is performed using square wave pulses of constant peak current. Fig. 1 below compares typical wave forms for DC galvanostatic electrodeposition, with I_{AV} as the constant current amplitude and PED with I_{PEAK} as the peak current value during the 'ON' time (T_{ON}).

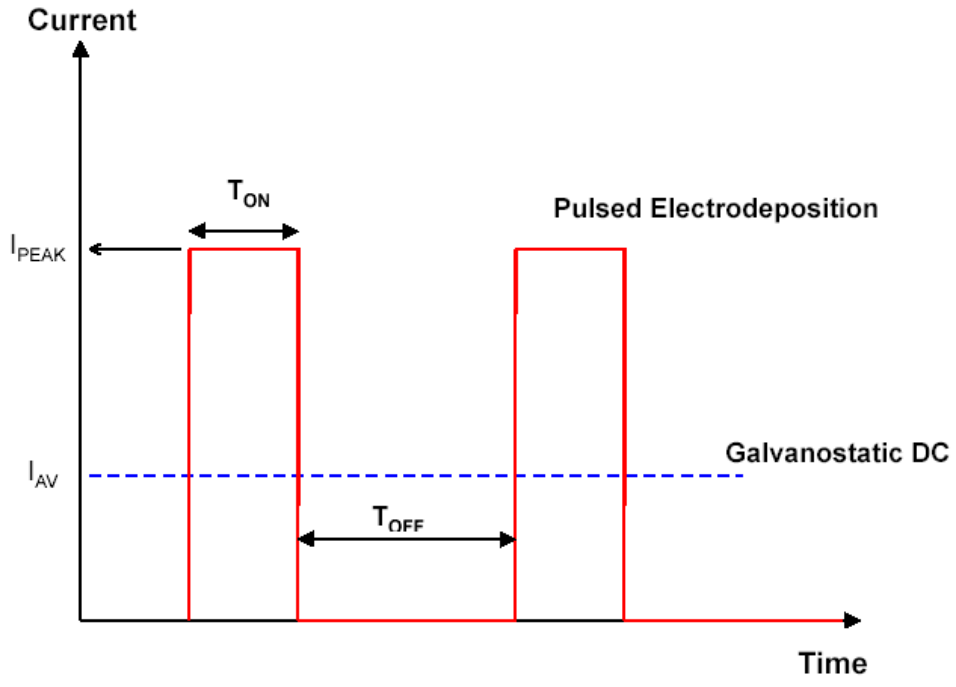

Figure A.1 Typical deposition waveform used in pulsed electrodeposition.

One of the key advantages of PED over DC electroplating is the level of process control afforded by the pulse variables. In DC plating, once the solution chemistry is set, typically there is an optimum DC plating current that yields the most desirable surface morphology (Iwamoto et al, PRL, 1994). Furthermore, any changes in DC plating current do not have an appreciable impact on the avg. grain size (d). On the other hand, in PED, a multitude of grain sizes can be obtained by the appropriate choice of peak current, on time and off times. PED can also favorably influence deposit properties such as morphology (Toth-Kadar et al, 1996; Tsai et al, 2002; Mohan et al, 2005), porosity, hardness (Ebrahimi et al, 1999) as well as crystal orientation (Cui et al, 2007). However, PED has its own share of problems namely, H_2 evolution can be enhanced by higher current densities and also a PED set-up usually requires specialized electronics to facilitate adequate control of the pulse parameters.

With regards to depositing Copper films via PED, the process from Natter et al (1996) (Natter et al, 1998 for Nano-Cu and Ni-Cu alloys) formed the basis for this work**.** The following section provides details of the electrodeposition set-up. Sec. A.2 describes the solution chemistry, the chosen pulse parameters and the deposition set-up. The rationale for the choice of both, the solution chemistry as well as the pulse parameters, is discussed from the point of view of the average grain size of the deposited material. A detailed description of the PED deposition steps is provided along with details such as anode and cathode preparation prior to deposition. Some measurements for the effect of pulse parameters on the observed grain sizes are provided. Sec. A.3 is entirely devoted to

the microfabrication aspects of the process i.e. preparation of glass slides with a seed layer and the eventual lift-off of the deposited films, after patterning, to obtain freestanding tensile specimen.

A.2. SOLUTION CHEMISTRY AND DEPOSITION SET-UP

The choice of solution chemistry is primarily dictated by the desired properties of the electrodeposits. In this regard, the most important property for this study was the attainment of a sufficiently small avg. grain size. The average grain size in PED is dictated by the competition between two phenomenons: i) nucleation of grains and ii) growth of grains. As expected, factors that cause a higher nucleation rate and a slow growth rate of grains lead to fine crystallites (Natter et al, 1996).

A.2.1 NUCLEATION OF GRAINS: 'ON' TIME AND PEAK CURRENT

The nucleation rate is typically a result of both the peak current density and ON time. The solution chemistry was chosen after Natter et al, 1996. Increasing the Peak current increases the nucleation rate i.e. more nuclei are nucleated on the cathode surface (per unit time) when the peak current is high. As a result, a high peak current combined with a small ON time, will result in a larger no. of small crystallites and thus, yield very small grain sizes. For a given ON time, there is also a certain amount of growth of the nucleated grains in the ON time phase. However, the nucleation typically far exceeds the growth. The amount of growth in the ON time phase can be further reduced by adding an inhibitor complex in the solution (Natter et al, 1996), as explained in Sec. 2.2. Therefore,

higher peak currents as well as a smaller ON time are two effective routes to obtain small grain sizes.

It should be noted that the 'ON' time and peak current are actually related to each other (Natter et al, 1996). Generally, smaller ON times are chosen for higher peak currents. The ON time scales with the peak current (I_{PEAK}) in the following way:

$$I_{AVG} = I_{PEAK} \times \frac{t_{ON}}{t_{ON} + t_{OFF}} \qquad \text{(A.1)}$$

The avg. current in this equation is usually obtained from DC plating for a given solution. In this study, different current densities were tried for DC plating for the chosen solution chemistry and based on the appearance of the deposit surface an avg. current density (per unit cathode surface area) of 10mA/cm^2 was chosen. DC plating typically yielded a grain size around ~2µm. The growth rate was estimated to be around ~0.5µm per sec. While a density of only 10mA is appropriate for DC plating, PED allows for much higher current densities provided the ON time is also scaled appropriately. Thus, much higher current can be applied, as long as the ON time is kept sufficiently small. Sec. 2.3 presents the avg. grain size as well as the deposition rates obtained for PED as well as DC plating.

A.2.2 GRAIN GROWTH: 'OFF' TIME AND ORGANIC ADDITIVES (CITRIC ACID)

The other important pulse parameter is the OFF time, which has an important role to play in the grain growth regime of the deposition process. The grain growth is primarily dictated by the cathode overpotential (i.e. potential difference between the cathode surface and the solution). One factor that affects the cathode potential is the substrate (or cathode) material. Different materials, with different reduction potentials, provide different overpotential in the same solution. As a result, the choice of the cathode has a strong bearing on not only the growth of grain but also, perhaps, on other aspects such as grain orientation (Cui et al, Acta Mat, 2007) and surface morphology. The role of the substrate is discussed later in this section when the experimental data is presented. Presently, attention is focused on the pulse parameters (OFF time) as well as the solution chemistry.

The cathode overpotential is also strongly affected by the solution chemistry as well as the OFF time. Once grains are nucleated on the cathode surface during the ON time, grain growth primarily occurs during the OFF time phase of the pulse. Also, regions near the cathode surface usually suffer from depletion of active species (ions required for deposition) after the ON time phase. These ions are usually replenished during the OFF time phase. As a result, the choice of OFF time is dictated by the competition between these two requirements i.e. it should be long enough to allow material transport to the depleted regions but small enough to restrict grain growth if small grain sizes are desired.

With regards to restricting grain growth, besides reducing the 'OFF' time, another factor of importance is the solution chemistry. In particular, the use of an electrolyte which contains organic additives, for instance, Citric acid (used in this study). The additive molecules form complexes in the solution and adsorb in a reversible way on active sites of the electrode surface (e.g., at growth steps on the surface of grains). They block the active sites and reduce the crystallite growth. Furthermore, the surface diffusion of the adatoms is impeded by adsorbed organic molecules. Therefore, less metal-adatoms reach growth sites and the formation of new nuclei is preferred. Therefore, increasing the concentration of the additive (inhibitor) reduces grain growth and therefore reduces avg. grain size.

A detailed study of these parameters can be found in Natter et al, 1996 where the effect of pulse parameters and solution PH, in addition to the effect of additives, on the obtained avg. grain size is studied in detail (Natter et al, 1996). For the purpose of this study, the following solution chemistry was chosen:

$CuSO_4.5H_2O$: 28 g/l

$(NH_4)_2\ SO_4$: 50 g/l

Additive: Sol. 1 - Citric Acid: 21 g/l

Sol. 2 - Citric Acid: 70 g/l

Both solutions yielded a PH of ~1.1. Natter et al used NaOH, in addition to the chemicals mentioned above, to adjust the PH to be closer to 2 instead of 1.1 obtained here. The PH of the solution is quite critical with regards to H_2 evolution. Generally, the tendency for H_2 evolution reduces with increasing acidity. It is primarily for this reason that most

studies relating to pulsed electrodeposition (Lu et al, 2003; Natter et al, 1996; Natter et al, 1997) employed a solution without Sulphuric acid (H_2SO_4), that typically yields a PH ~0.5 or lower. The study of pulse parameters on grain size was primarily carried out using Sol. 1. Sol. 2, with far larger amount of inhibitor forming Citric Acid, yield slightly better surface and smaller grain size (for a 2.5 ms pulse).

A.2.3 PED SET-UP AND METHODOLOGY

A study was conducted to study the effects of pulse parameters on the obtained grain size with the chosen solution. The following salient points are noted about the electrodeposition set-up:

1. A Cu substrate, with thickness ~2mm and surface area of 10mm^2 was used as the cathode. The electrical resistance of the cathode, from the cathode contact wire to the cathode surface to be deposited, was found to be between 2-3Ω.

2. The cathode was first polished with 1µm slurry for about 2 minutes followed by 0.05µm slurry for about 5 minutes to obtain a fairly consistent and scratch-free surface. The cathode surface was washed with DI water, and lightly etched with a 5% (by volume) Nitric acid solution (diluted with water) after polishing using a cotton swab.

3. Following polishing and surface treatment, all but 10mm^2 of area covered with nail polish. Surface area of 10mm^2 was chosen for the initial testing of process parameters so as to reduce the voltage required to obtain a given current density. For cases that

used current of more than 500 Amps, the surface area of deposition was further reduced to 4mm^2.

4. A large copper sheet, with ~3mm thickness, was employed as the cathode. The anode had a surface area of ~20X the size of the cathode. Prior to each run, the anode was washed with DI water, followed by light etching with a 5% Nitric acid + DI water solution using a cotton swab.

5. The nominal separation between the cathode and the anode was 35mm and the cathode was positioned approximately in the middle of the anode. The anode and the cathode were held in place using a Plexiglas holder, machined in-house, so as to allow vertical alignment i.e. they were held securely and parallel to each other.

6. 800 ml of solution was used, in a 1000ml container, for the deposition. The solution was filtered through filter paper before pouring into the container. This is quite important as the impurities can adversely affect the quality, and purity, of the electrodeposits. In cases where multiple deposition runs were performed, the solution was filtered after each deposition run.

7. The solution was also heated upto ~45-55ºC for each run. To achieve a consistent temperature of the solution, the magnetic stirrer temperature knob was set between 3-4 during stirring and the temperature was continuously checked every ~5-10 minutes over the span of 1 hour. The temperature knob was adjusted, if required, so as to keep the temperature approximately constant.

8. N_2 was bubbled through the solution for 1 hour, in the presence of mechanical agitation (set ~ level 7 on a magnetic stirrer). The bubbling pressure was usually quite small and was chosen so that the bubbling would not lead to the spilling of the solution outside the container.

9. After deareation for 1 hr and the attainment of a stable, and relatively constant (with time) temperature profile of the solution, the N_2 flow was cut-off and the lid was lifted. The specimen holder (with the anode and the cathode) was then placed inside the container and the magnetic bead (for stirring) was then placed at the bottom of the container.

10. Electrical contacts were then made with both the anode and the cathode. Care was taken to keep all electrical contacts outside the solution. Exposing metallic connectors to acidic solution (as used in this study) leads to hazardous reactions with the metal, thereby rendering them ineffective as reliable electrical contacts.

11. Care was taken to complete the process of cutting of the N_2, lifting the lid and putting in the holder with anode and cathode as soon as possible. Since a disruption in N_2 bubbling and heating along with stirring can change the solution temperature profile. Once the holder was place and the electrical contacts were made, the lid was closed and the N_2 bubbling and stirring was resumed.

12. After a brief wait of ~2 minutes, the current was applied (with preset pulse parameters and frequency) to start the deposition process. The time was closely monitored during the deposition process to assess the deposition thickness.

13. After the competition of deposition for a given time, N_2 flow was again cut-off, stirring was stopped and the electrical contacts were removed and the lid was lifted to take out the holder with the anode and cathode. The cathode, with the electrodeposited film, was removed first from the holder and washed with DI water immediately and dried with Air (gentle flow rate). Following this, the anode was removed, washed with DI water and dried.

14. As mentioned earlier, following each step the solution was filtered and the process of N_2 flow and temperature stabilization (with mechanical agitation) was repeated.

15. The estimation of the deposit thickness, after deposition, requires a special step. Typically, surface covered with colorless Nail polish (commercially obtained from Walmart – chosen for their quick drying property) do not get deposited. Therefore, a ~1mm diameter circle was coated with nail polish (using the brush that comes with nail polish bottles) in the middle of the cathode. After deposition, the nail polish was dissolved using Acetone. This leads to the creating of a circular region with no deposit surrounded by the electrodeposited film. The thickness can be measured at the edge of this circle i.e. the thickness is the average step height. The average step height was measured at typically 5-10 locations along the circle with Zygo.

A study of H_2 evolution and factors that influence it was also carried out. The temperature of the solution was chosen after Natter el at (1996). Although not mentioned in their paper, a literature survey (see Gabe et al, 1997) revealed that the reason for

deposition at a higher temperature in this PED set-up was to avoid the problem of hydrogen evolution. H_2 evolution leads to the creation of bubbles that can be seen at the cathode surface during deposition. These bubbles are understood to drastically increase the porosity of the deposited material (Tsai et al, 2002) by obstructing small regions and thereby creating a spherical cavity in their place in the electrodeposited material. Furthermore, H_2 incorporation in the electrodeposits can lead to hydrogen embrittlement i.e. abnormally high strength and brittle behavior is seen. As mentioned in Gabe et al (1997), H_2 evolution is very sensitive to the temperature of deposition. Increasing the temperature can drastically reduce the problem of hydrogen evolution.

Fundamentally, the driving force for H_2 evolution at the cathode is the cathode overpotential. Therefore, parameters such as current density, pulse parameters as well as the choice of substrate (or cathode) material have an important bearing on the tendency for H_2 evolution. Generally, the following trends were found from literature (Gabe et al, 1997; Dini et al, 1993, Monev et al, 1998): low temperature, higher current density as well as higher acidity level (low PH) tends to increase the tendency for H_2 evolution. Also the comparison for the reduction potential of the ion of the metal being deposited for a given substrate material and the overpotential for the associated H_2 reaction is an important criterion (See Gabe et al, 1997). Many PED studies, given the high current densities employed, use Iron sheets or Titanium sheets to deposit Copper for this reason. In this study however, Cu substrate was used (Cu seed layer was employed for free-standing film specimens as described in Sec 3). While for the thicker Cu substrates a

current density as high as ~1.5mAmp/cm^2 was used, the optimum current density for thin Cu seed layer was quite limited i.e. 250mAmp/ cm^2. At densities larger than this value, substantial bubble formation was seen at the cathode surface and the deposited film was almost black and powdery in nature. In cases where the deposited film had a lot of voids, the film often cracked and broke at current densities of ~ 30mAmp/cm^2.

A.2.4 EFFECT OF PULSE PARAMETERS ON AVERAGE GRAIN SIZE

All experiments were carried out for 1 hr deposition time i.e. 60 minutes. First, a DC plating experiment was carried out for 1 hr to ascertain the optimum plating current density. This DC current density was used as the Avg. Current density in the PED process to scale the Peak current with the ON time (Sec. 2.1).

The following parameters were defined for the purpose of rationalizing the observed trends:

1. **PEAK**: Peak current density in mAmperes/cm^2. The peak current density can be obtained by divding the current amplitude by the surface area of the cathode.
2. **T**: This is the total length of the pulse in ms.
3. **F:** Defined here as the Frequency of deposition. F is obtained as 1000/T.

4. **Duty Cycle**: The fraction of the total pulse (in %) for which the current is applied on the cathode. It is defined as

$$Duty\,Cycle = \frac{T_{ON}}{T} \times 100$$

5. **RATE**: Rate of deposition i.e. thickness of deposit per unit time. The thickness was obtained as per step 15 in Sec. 2.2 in microns. The deposition time was recorded for each deposition run (fixed at 60 minutes here). The rate was calculated as microns/min.

6. **T EXP**: This is the actual time for which deposition is actually occurring. It was defined as follows: While the total time of the experiment was fixed at 60 minutes, the time for which the current was actually applied was much smaller i.e. only 'On' time for each pulse. Thus, the actual deposition time was actually Duty Cycle * Total Time.

7. **ADJ RATE**: This is the adjusted rate, based on the actual deposition time. It was calculated by diving the total deposit thickness (in microns) by the T EXP term defined in 6 (in minutes). It should be noted that while the 'OFF' time is not explicitly defined here, it is simply T – On Time.

Fig. 3 shows the variation of RATE with Duty Cycle for different pulse lengths. The pulse length here essentially implies the total time of each pulse. It is shown here in terms of the frequency of deposition i.e. F (=1/T). 2.5 Hz therefore implies the longest

pulse duration of 400 ms used and 100 Hz was the shortest pulse with total duration 10ms. Fig. 4 shows the obtained grain sizes v/s duty cycle. The smallest grain size (~200 nm) obtained in this study was not measured rigorously but estimated using the optical microscope. The observed trends can be understood as follows:

1. Higher pulse frequencies, for a given duty cycle, lead to smaller grain size. This is essentially an outcome of smaller On Times for higher frequencies.

2. For a constant pulse frequency, reducing the Duty Cycle leads to smaller grain sizes. This is because reducing Duty Cycle increases the OFF time and reduces the ON time, for constant pulse duration. Because Citric Acid was used as an inhibiting complex, increasing OFF time allows for the inhibition process to be very effective in blocking the active cites to restrict grain growth. Furthermore, smaller ON times allow a higher current density to be used, keeping the AVG density to be the same as the DC case, increasing grain nucleation.

3. The RATE, as defined here, reduces with increasing pulse frequencies. This is because with increasing frequencies, grain nucleation takes precedence over grain growth. Thus this leads to smaller deposition rates and smaller grain sizes.

4. It is also apparent that shorter pulse frequencies are more sensitive to Duty Cycle as compared to greater frequencies with respect to the RATE.

5. We also found that for a given pulse frequency, the deposition rate scales approximately linearly with the duty cycle.

6. PED plating can give larger, as well as smaller, grain sizes as compared to DC plating process for the same solution chemistry. Choice of pulse parameters can be used to obtain grain sizes over approximately 3 orders of magnitude. For example, for a similar solution chemistry, but for deposition on a Titanium coated cathode, the smallest attainable grain size can be just a few nano meters (Natter et al, 1997).

For the purpose of obtained freestanding thin films specimen for tensile testing, a specialized methodology was designed as so to allow the deposition, patterning and release of the freestanding electrodeposited films. The deposition was carried out over microscopic glass slides (1" wide × 3" long). The electrodeposition was performed using a seed layer of Cu, deposited using E-beam evaporation. Following seed layer deposition, electrodeposition was carried out at 100 Hz deposition frequency and 4% duty cycle. A current density of 250 mAmp/cm^2 was employed. The microfabrication steps were primarily chosen so as to allow the successful release of the Cu films as well as their patterning into tensile dog bone specimen.

A.3. MICROFABRICATION

The microfabrication was primarily performed at the Microelectronics Research Center, under the guidance of Dr. Gary Tuttle. What is presented here is a summary for

2.5 HZ

Thickness	G S	AVG	PEAK	On Time	T	F	Duty Cycle	RATE	T EXP	ADJ RATE
microns	microns	mAmp/cm2	mAmp	ms	ms	Hz	%	micron/sec	Minutes	micron/sec
28	13	10	80	50	400	2.5	12.5	0.46666667	7.5	3.73333333
14	6	10	200	20	400	2.5	5	0.23333333	3	4.66666667
6.4	0.8	10	1600	2.5	400	2.5	0.625	0.10666667	0.375	17.0666667

25 HZ

Thickness	G S	AVG	PEAK	On Time	T	F	Duty Cycle	RATE	T EXP	ADJ RATE
microns	microns	mAmp/cm2	mAmp	ms	ms	Hz	%	micron/sec	Deg. C	micron/sec
13	2.3	10	80	5	40	25	12.5	0.21666667	7.5	1.73333333
10	1.1	10	160	2.5	40	25	6.25	0.16666667	3.75	2.66666667
6	0.2	10	1000	0.4	40	25	1	0.1	0.6	10

100 HZ

Thickness	G S	AVG	PEAK	On Time	T	F	Duty Cycle	RATE	T EXP	ADJ RATE
microns	microns	mAmp/cm2	mAmp	ms	ms	Hz	%	micron/sec	Deg. C	micron/sec
17	0.8	10	40	2.5	10	100	25	0.28333333	15	1.13333333
11	0.45	10	100	1	10	100	10	0.18333333	6	1.83333333
7	0.2	10	250	0.4	10	100	4	0.11666667	2.4	2.91666667

SOL. 1 - DC

Thickness	G S	AVG	PEAK	On Time	T	F	Duty Cycle	RATE	T EXP	ADJ RATE
30	2.1	10						0.5	60	0.5

SOL. 2 - DC

Thickness	G S	AVG	PEAK	On Time	T	F	Duty Cycle	RATE	T EXP	ADJ RATE
30	1.1	10						0.5	60	~0.5

Solution 2

Thickness	G S	AVG	PEAK	On Time	T	F	Duty Cycle	RATE	T EXP	ADJ RATE
7.8	~ 0.2	10	250	4 ms	400	2.5	1	0.13	0.6	13

Figure A.2 Pulse plating parameters and their influence on Pulsed Electrodeposition. The obtained parameters for Sc (only for 2.5 Hz pulse frequency) and well as DC plating with Solution 1 and 2 are also shown for comparison. The cl DC plating grain size with increasing Citric Acid concentration (for same current density) was marginal (~2X) while f it reduced the grain size by ~4X for similar plating parameters.

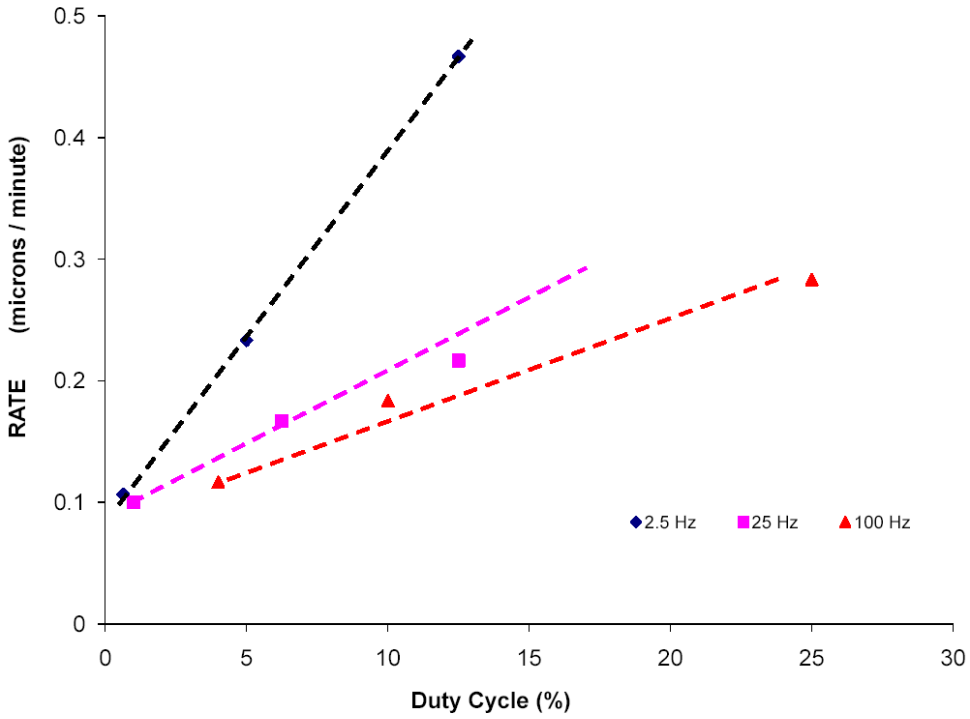

Figure A.3 Effect of duty cycle on deposition rate (microns per minute)

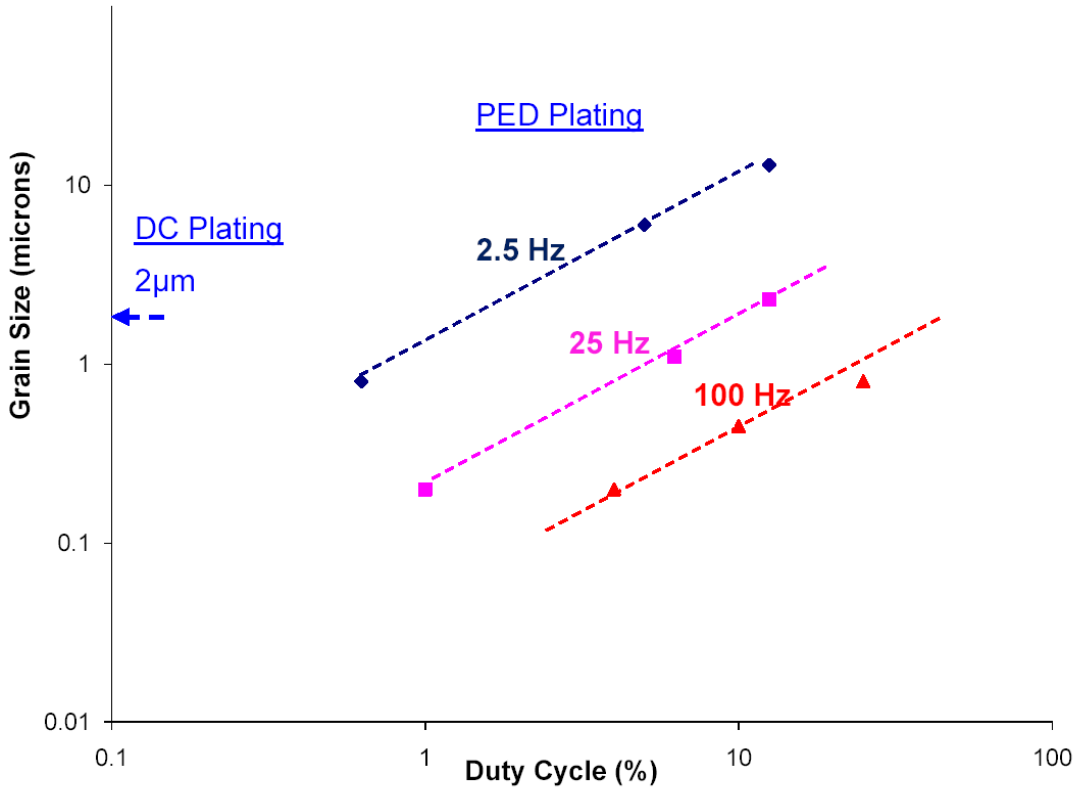

Figure A.4 Effect of duty cycle on average grain size for different pulse frequencies

all the steps. Some individual steps, specially E-beam evaporation as well as Lithography, have their own, detailed Standard Operating procedures (SOP). The specific SOPs must be followed for these steps. The appropriate SOPs are attached with this report for guidance in this regard.

The following is a step-by-step description of the microfabrication process:

1. The glass slides were first cleaned using Acetone for 1 minute. Following this step, they were cleaned in Methanol for 1 minute, followed by DI water for 4 minutes. In each of these steps, N_2 was bubbled through the bath.

2. Following the cleaning step, the slides were heated at 120ºC for 40 minutes in a Fischer Scientific Oven. The temperature control knob was used to set the temperature to 120ºC. The over was pre-heated for 5 minutes before the timer was started.

3. Nitrogen was then sprayed over the slides while keeping the N_2 gun normal to the surface and at a high flow rate. This was done so as to remove any dust particles on the surface.

4. Photoresist (PR), AZ 5214 E, was then deposited over the glass slides. The rotation RPM was set to 1000 rpm. The PR deposite thickness is expected to be around 2µm for the chosen spin rate and known viscosity of the PR.

5. The slides were soft-baked on a hot plate at 125ºC for 2 minutes.

6. A hard bake, at 90ºC for 5 minutes, was then performed.

   A longer than necessary bake time at this stage can make the lift-off at the end of this process difficult and time consuming. Excessive bake can lead to unsuccessful lift-off i.e. the seed layer + Cu electrodeposit assembly will not come off the slide at all as the PR will not dissolve in Acetone.

7. Following the hard bake, the slides were placed in the E-beam evaporator and Cu was sputtered on the surface. A thickness of 50 nm – 100 nm was deposited. Care was taken to obtain a very clean surface of the glass slides (without any dust – spraying with N_2) as well as void-free seed layer (low power setting, ~ 13%, in the evaporator while depositing). The deposition rate was usually chosen to be around ~ 0.25-0.3 nm per sec.

   In the presence of voids the seed layer cracked and broke within 30 seconds of deposition time, with current densities around 30mAmp/cm^2 or higher. This step was found to be critical to successful electrodeposition. The resistance of the cathode in this case, measured between the cathode contact wire and the slide surface, was between 1-2Ω. The resistance can be also play a critical role for the desired current density (depending on the grain size requirement). Generally, as low a resistance as possible should be attained (via sound electrical contact on the slide surface).

8. Electrodeposition was then carried out to deposit the desired thickness of the electrodeposited films.

9. The electrodeposited films were cleaned with DI water and dried with a very gentle air pressure. They were securely stored in a specimen carrier box and left overnight. Care was taken to avoid the air striking the deposited film at an inclined angle near the edges. This usually led to delamination and cracking in the deposited films.

10. After about 24 hrs, the slides were again coated with PR (Step 4).

11. A soft-bake of 3 minutes, at 110^{o}C, was performed on a hot plate.

12. The transparency mask, with the tensile dog bone pattern was then placed over the slides and the edges of the pattern were carefully aligned with the edges of the slides so as to obtain roughly equal grip sections on both sides. Approximately 5 specimens were obtained for each slide. The two specimens at the edges were discarded due to non-uniform electrodeposit thickness at these edges.

13. The exposure system does not feature a mask alignment set-up and feature a much larger separation between the sample and the UV source. However, it has the benefit of a much larger exposure area that allows for multiple slides (~6) to be exposed at the same time. Individual masks were placed and aligned visually for each of the 6 slides under the exposed area (highlighted by a square marker on the base).

14. The specimens were exposed to UV radiation for 70 seconds. A thick (~3 mm) clear glass plate was placed over the sample + mask assembly to ensure the two surfaces (Mask and Slide underneath) would be flush and that alignment would be retained.

15. After exposure, the unexposed PR was dissolved in the developer solution and the slides were rinsed in DI water for 4 minutes with gentle N_2 agitation. Care was taken to only agitate the developer solution gently with the slides in a beaker.

16. Gentle N_2 pressure was further used to dry the glass slide surface. Again, care was taken to avoid delamination and rupturing the films with excessive N_2 pressure.

17. The dried slides were then placed in a sealed oven for a hard-bake. The bake temperature was chosen to be 90ºC for 8 minutes.

    Insufficient bake at this stage can render the PR ineffective as a mask for the etching in Step 8. For thicker electroplated films i.e. thickness > ~12µm or so, the bake time may be increased to 10-12 minutes (depending on the thickness).

18. Following the hard bake, the slides were placed in a dilute (5%) Nitric Acid + DI water solution for etching the exposed Cu. The etching typically took around 5-10 minutes depending on the deposit thickness.

19. Following etching, the patterned Cu film was placed horizontally in a beaker of Acetone so as to release the underlying PR. The PR can be seen slowly dissolving from underneath the specimen and swimming over the specimen upon very gentle agitation. The release process was quite slow and took ~15-20 minutes. Once free

from the substrate, the films slowly move with gentle agitation beneath the released acetone, that swims just over the specimen.

20. The individual films thus released were then carefully lifted out of the beaker with the help of two spatula shaped tweezers and places in another Acetone bath briefly. This clean acetone solution was chosen so as to wash away the film of dissolved PR that gets carried along with the specimen when it is lifted.

EXTREME CARE was taken while lifting the films. Thinner films, specially the 2µm thickness, pose significant challenges in this step. The problem lies in the fact that upon being taken out of the liquid (either Acetone or DI water) the specimen instantly bend and the film surfaces instantly stick to each other. This primarily occurs at the grip sections of the sample i.e. the two grip surfaces tend to stick to each other if they come too close while being taken out of the water. To avoid this, two spatula shaped tweezers were used to gently lift the specimen from both the grip ends simultaneously. In doing so, care should be taken so that the surface tension due to the water does not rupture the specimen, especially as the specimen exits the water.

EXTREME CARE should also be taken while placing the specimen on a clean, dry surface at this point. The tweezers' surface tends to stick to the specimen and do not let go easily. A special, fiber-free cloth was used to gently press on the middle of the specimen, to hold the gauge section down, while the tweezers were being pulled away. Without adequate care, the specimen, especially the thinnest ones, can easily rupture in the gauge section in this step.

21. The released specimen was directly placed into ceramic plate and the acetone was allowed to evaporate. DI water was not used to any further rinse, because it is virtually impossible to dry the specimen once immersed in DI water.

22. The freestanding tensile specimens thus obtained were further annealed in the metal annealing furnace in MRC. The following steps were performed:

    a) Prior to placing the specimen inside, N_2 (at ~1slpm flow rate) was passed for about 2 hrs. The furnace lid was left closed in this step. The N_2 flow rate is a very critical step. In the presence of even minute amounts of Oxygen in the furnace, the specimens can get oxidized. It should be verified that the N_2 is in fact flowing through the furnace by removing the N_2 line going into the furnace and putting a finger against it to feel the flow.

    b) After 2 hrs, the furnace lid was opened and the specimens were loaded in a quartz boat and placed in the middle of the second temperature zone in the furnace. The furnace lid was again closed.

    c) The furnace controller was then set to the appropriate temperature and the furnace was turned on. The N_2 flow was increased to 3 slpm during this step.

    d) The furnace typically heated up at ~ 10^{o}C per minute. After the set point temperature was attained (as seen on the controller temperature gauge), the timer was started to obtain the desired soak time.

e) At the end of the soak time step, the furnace was turned-off and was allowed to cool to 200ºC via radiative cooling. This can take upto ~2 Hrs. The Nitrogen flow was maintained at ~1slpm during this step.

f) Upon cooling, the samples can be gently pulled out of the furnace and stored in a specimen box. The N_2 flow rate is then set to ~0.3 slpm and the lid is closed.

A.4 REFERENCES

1. D. R. Gabe (1997) "The role of hydrogen in metal electrodeposition processes" *J. Appl. Electrochem.*, 27, 908

2. Lu,L., Shen, Y., Chen, X. and Qian, L. and Lu, K. (2003) "Ultrahigh strength and high electrical conductivity in copper", *Supplement material, Science*, 304, 422

3. Natter, H. and Hempelmann, R. (1996) "Nanocrystalline Copper by Pulsed Electrodeposition: The effects of organic additives, bath temperature and PH" *J. Phys. Chem.*, 100, 19525

4. Natter, H. and Hempelmann, R. (1998) "Nanocrystalline Nickel and Nickel-Copper alloys: Synthesis, characterization and thermal stability" *J. Mater. Res.*, 13, 5, 1186

5. Iwamoto, A., Yoshinobu, T. and Iwaski, H. (1994) "Stable growth and kinetic roughening in electrochemical deposition" *Phys. Rev. Lett.*, 72, 25, 4025

6. Toth-Kadar, E., Bakonyi, I., Pogany, L. and Cziraki, A. (1996) "Microstructure and electrical transport properties of pulse-plated nickel electrodeposits" *Surf. Coat. Tech.*, 88, 57

7. Mohan, S. and Raj, V. (2005) "The effect of additives on the pulsed electrodeposition of Copper" *Trans. Inst. Met. F.*, 83, 4, 194

8. Cui, B.Z., Han, K., Xin, Y., Waryoba, D.R., Mbaruku, A.L. (2007) "Highly textured and twinned Cu films fabricated by pulsed electrodeposition" *Acta Mater.* doi:10.1016/j.actamat.2007.04.09

9. Dini, J. (1993) "Electrodeposition: The materials science of coatings and substrates" *Materials Science and Process Technology Series, Noyes Publications*

10. Tsai, W.C., Wan, C.C. and Wang, Y.Y. (2002) "Building on bubbles in metal electrodeposition" *Nature*, 417, 139

11. Bakonyi, I., Toth-Kadar, E., Pogany, L., Cziraki, A., Gerocs, I., Varga-Josepovits, K., Arnold, B. and Wetzig, K. (1996) "Preparation and characterization of D.C.-plated nanocrystalline nickel deposits" *Surf. Coat. Tech.*, 78, 124

APPENDIX B. UNIAXIAL TENSION TESTING

B.1 INTRODUCTION

The experimental characterization of mechanical properties involves three primary issues i.e. specimen preparation, force application (or measurement) and displacement measurement (or application). This section describes the latter two aspects of the experimental methodology. Uniaxial tension test was employed to characterize the mechanical properties of freestanding films in this study. This methodology has the benefit of providing a macroscopically homogenous deformation field. As a result, data analysis is fairly straightforward and can be performed without recourse to any mathematical assumptions. On the other hand, tension tests are very sensitive to misalignment. Therefore, specimen alignment is a critical consideration in tension testing (Sharpe et al, 2003). The tests were performed under displacement control i.e. the specimen were deformed by applying constant displacement increments with time and the force at each displacement increment was measured.

This chapter first describes the experimental set-up. Specifically, the design and utility of a test-fixture as an aid to specimen alignment and handling is discussed. Finally, the methods of displacement measurement and force measurement are discussed. The data analysis methodology to extract stress and strain response from the measured force-displacement response is also described.

B.2 EXPERIMENTAL SET-UP & PROTOCOL

The experiments were performed using an INSTRON 8862 Servo-hydraulic tension test system. The INSTRON machine was operated using a PC with Labview interface. The force was measured using a 30kg (294N) load cell (AM Cells Corp.). The variation (standard deviation) in force data was observed to be ±12.5 mN. The displacement was measured using a non-contact capacitance gauge (Lion Precision Inc). The variation in displacement was observed to be ±0.07 mm. The capacitance gauge was used within its linear range of ~2mm. Figure B.1 shows the calibration data of the capacitance gauge to illustrate this point. The calibration was performed using a standard micrometer with ~1μm least count. The micrometer was used to move an aluminum target that serves as the ground for the capacitance gauge. The capacitance of the circuit is a function of the separation. As a result, a change in capacitance results in a voltage drop that can be sensed. The capacitor was used with a 5 Volts excitation voltage .

Figure B.2 below shows the two Instron platens. It should be noted that the loading axis in the INSTRON machine is vertical. As a result, mounting a miniaturized freestanding specimen, aligning it and gripping it can be a very challenging task. In order to address this challenge, a test-fixture, shown schematically in Figure B.3 was used. Figure B.3 (a) shows the AutoCAD drawing of the test fixture with the specimen. The appropriate dimensions are also shown. Figure B.3 (a) also shows the alignment pins that ensure that the top and bottom halves of the fixture are aligned with each other. The

figure also shows the spring steel ‘arms’ of the fixture. The presence of the steel arms

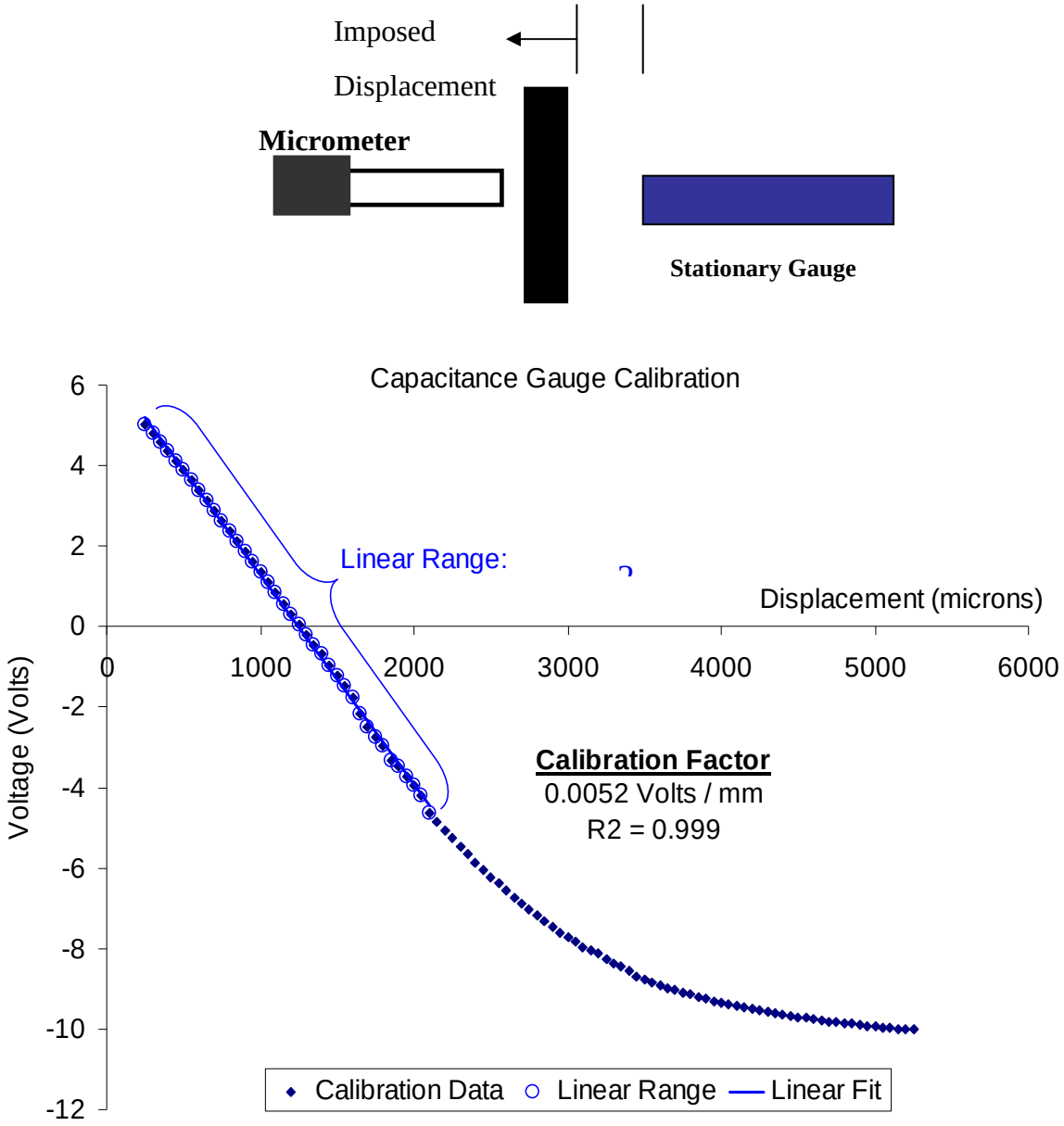

Figure B.1 Calibration data for capacitance gauge. The calibration set-up is also shown schematically.

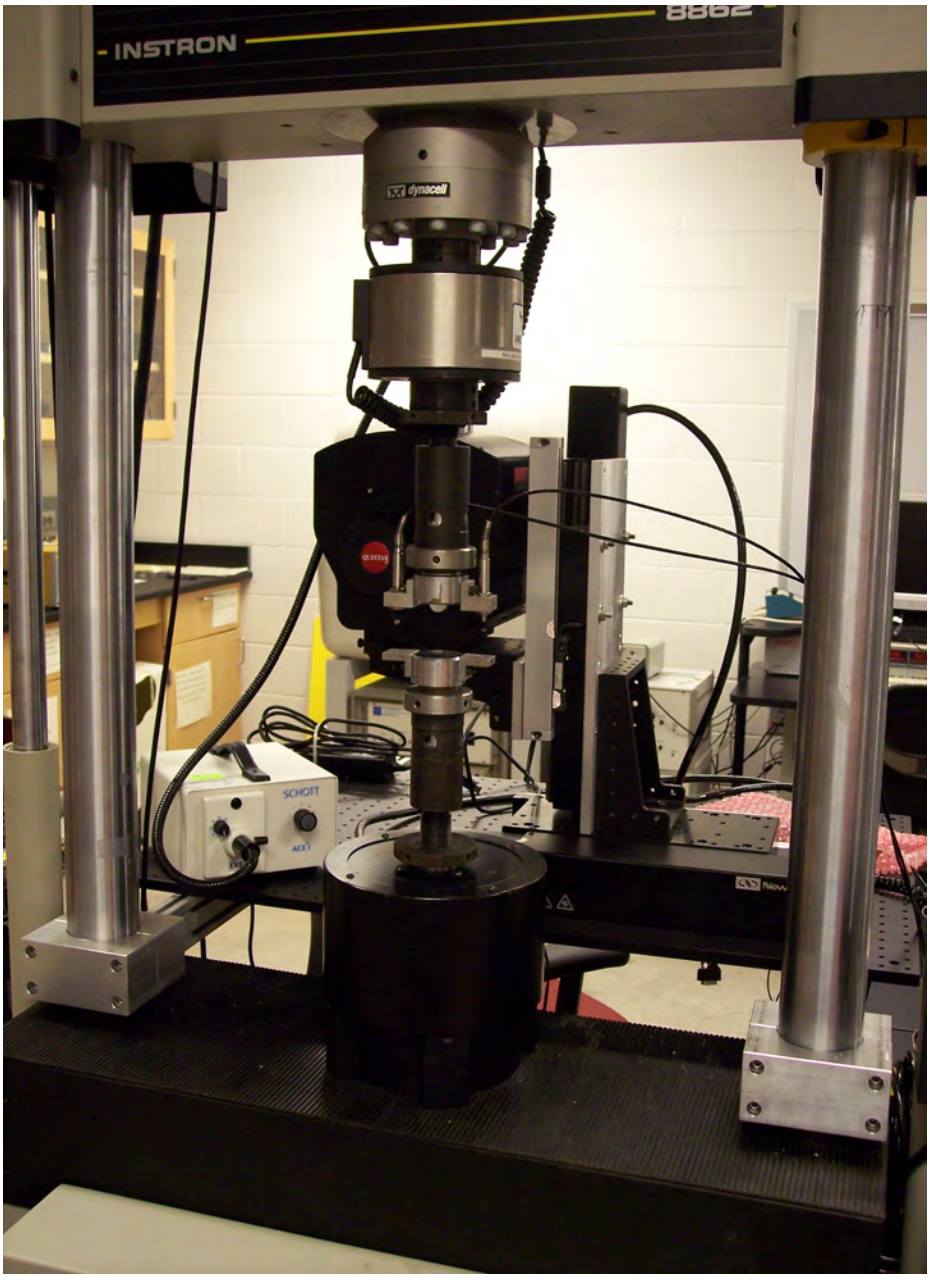

Figure B.2 INSTRON 8862 Servo-hydraulic machine used for the tension tests. The two platens i.e. upper and lower platen, can be clearly seen.

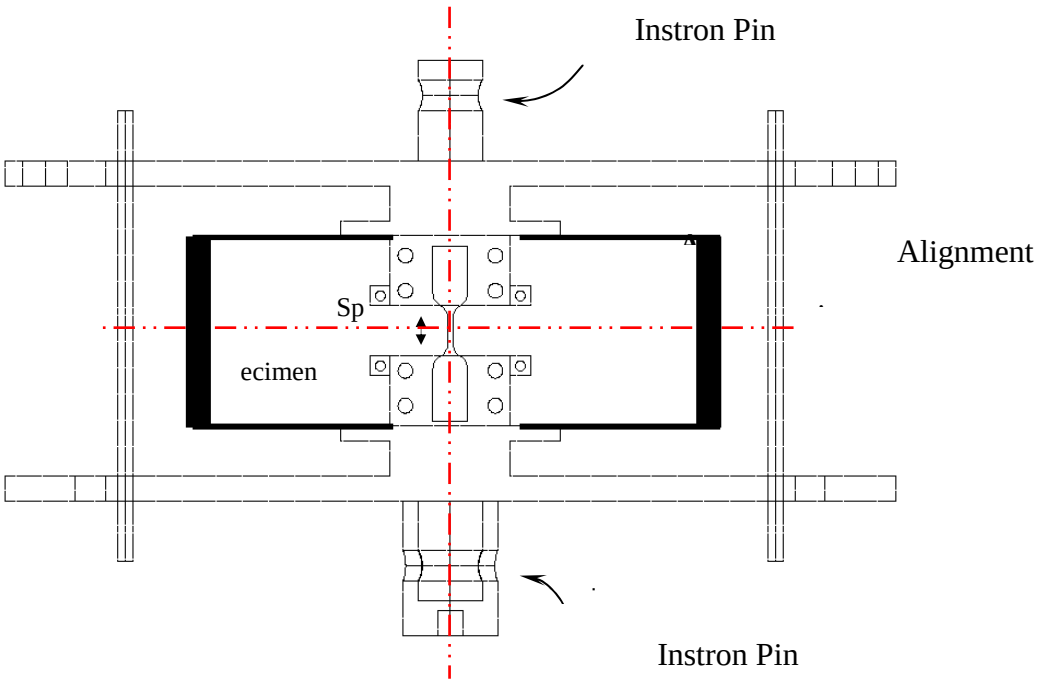

Figure B.3 (a) AutoCAD drawing of the test-fixture.

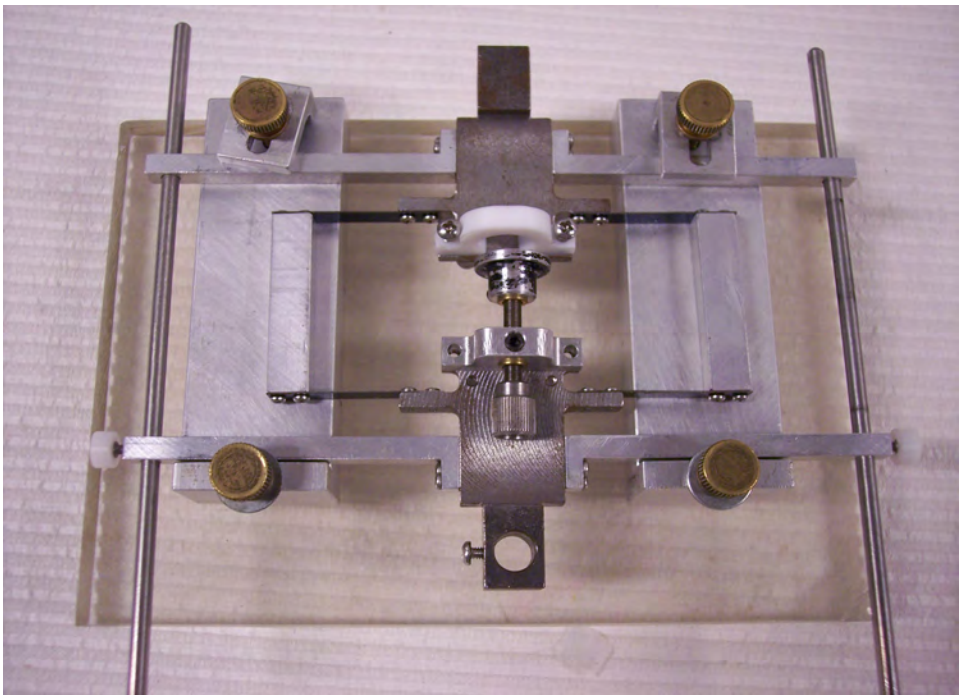

Figure B.3 (b) Test-fixture in holding frame. The capacitance gauge - target assembly side is shown.

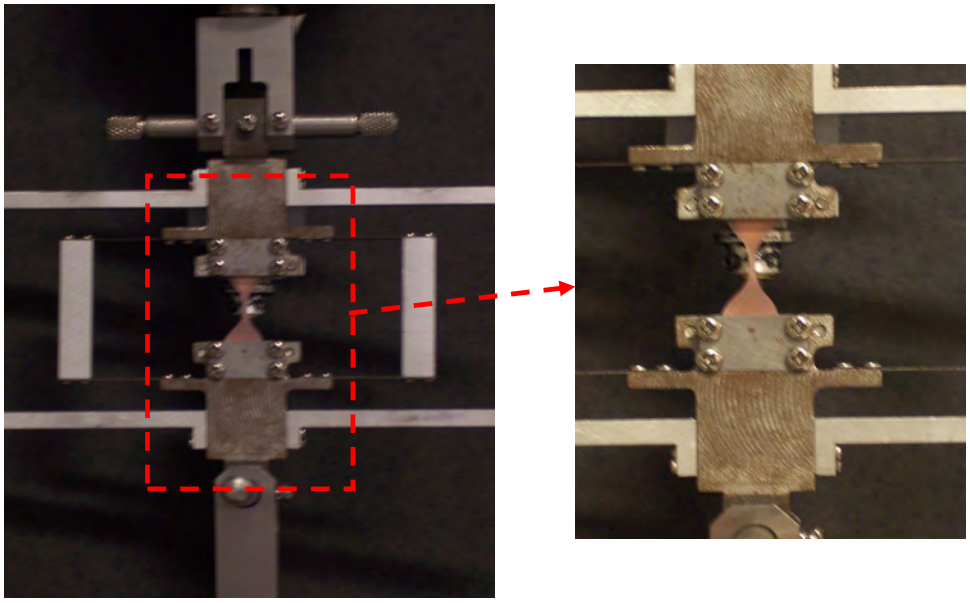

Figure B.3 (c) Images of the test-fixture mounted in the INSTRON machine, after the holding frame is removed. The capacitive displacement gauge can be clearly seen behind the Cu specimen.

aids in alignment and precludes unloading of strain energy from test frame into the deforming specimen. Figure B.3 (b) shows the test fixture, without the specimen, in its holding frame. The holding frame was made out of Plexiglas with brass screws for the purpose of holding the fixture in place. Figure B.3 (c) shows a close-up of the test fixture (with the specimen) mounted in the Instron machine.

The following steps were followed as a part of the experimental methodology:

1. The test-fixture along with the holding frame was placed under a low magnification microscope. The grip sections of the fixture were aligned with the crosshairs of the microscope (horizontal line “H”).
2. Once the test-fixture is aligned with the microscope crosshairs, the tensile specimen is placed between the grip ends. The specimen gauge length is then aligned with the crosshairs of the microscope (vertical line “V”).
3. The gripping screws are then put in place and tightened.
4. The fixture + frame assembly is then moved to the Instron machine and the capacitance gauge is connected. This gauge monitors the displacement between the two grip ends of the fixture. Since the fixture is secured in the holding frame, any further handling should not lead to any relative displacement between the grip ends (or deformation of the specimen).
5. The test-fixture with the gripped specimen along with the holder is then secured in the Instron machine through its pin connections. First, the top pin connection is made. The fixture + holding frame assembly is then aligned vertically so that the

lower pin connection can be made. The lower Instron platen is moved up very slowly, while monitoring the force and displacement. Once the lower pin attachment is done, the top and bottom pins are secured via screws. The screws are provided so that the fixture retains its alignment once the holding frame is removed.

6. Following the attachment of the fixture + holding frame in the Instron machine, the holding frame is slowly removed. Figure B.3 (c) shows the image of the test fixture, after the holding frame is removed, along with the specimen.
7. Once the aligned specimen + test fixture assembly is in place in the Instron machine, the data acquisition system is started and the real time data from the load cell and the displacement is recorded in a file. The data was acquired at a sampling frequency of 1000Hz and saved at a frequency of 20Hz i.e. each saved data point was an average of 50 acquired samples.
8. Finally, the experiment is started using the Instron control computer. The displacement rate and the displacement ramp is defined and the test is starts once the machine starts moving. A displacement rate of 1μm per sec was used for all experiments.

B.3 DATA ANALYSIS

B.3.1 Fixture Calibration

The test fixture used in the experiments has spring steel arms that deform as beams during deformation. The fixture + specimen configuration is such that the specimen and fixture are in parallel. As a result, for a fixed displacement increment (Δ),the total force (F) has a contribution from the fixture ($F_{Fixture}$) and from the specimen ($F_{Specimen}$) i.e.

$$F\big|_{\Delta} = F_{Fixture}\big|_{\Delta} + F_{Specimen}\big|_{\Delta} \qquad \text{(B.1)}$$

The contribution from the fixture was found via experimental calibration i.e. the fixture (without specimen) was deformed and the force – displacement response was recorded. All experiments in this study employed 250μm thick spring steel arms. Figure B.4 shows the force – displacement reponse of the fixture. It is apparent that the loading and unloading response of the fixture is linear. The fixture stiffness ($K_{Fixture}$) is found from the slope of the linear fit through the loading response. As can be seen in Figure B.3, the fixture stiffness is found to be 0.0035 N/μm. Thus the contribution from the fixture to the overall measured force in Eq. (B.1) can be written as

$$F_{Fixture}\big|_{\Delta} = K_{Fixture} \times \Delta \qquad \text{(B.2)}$$

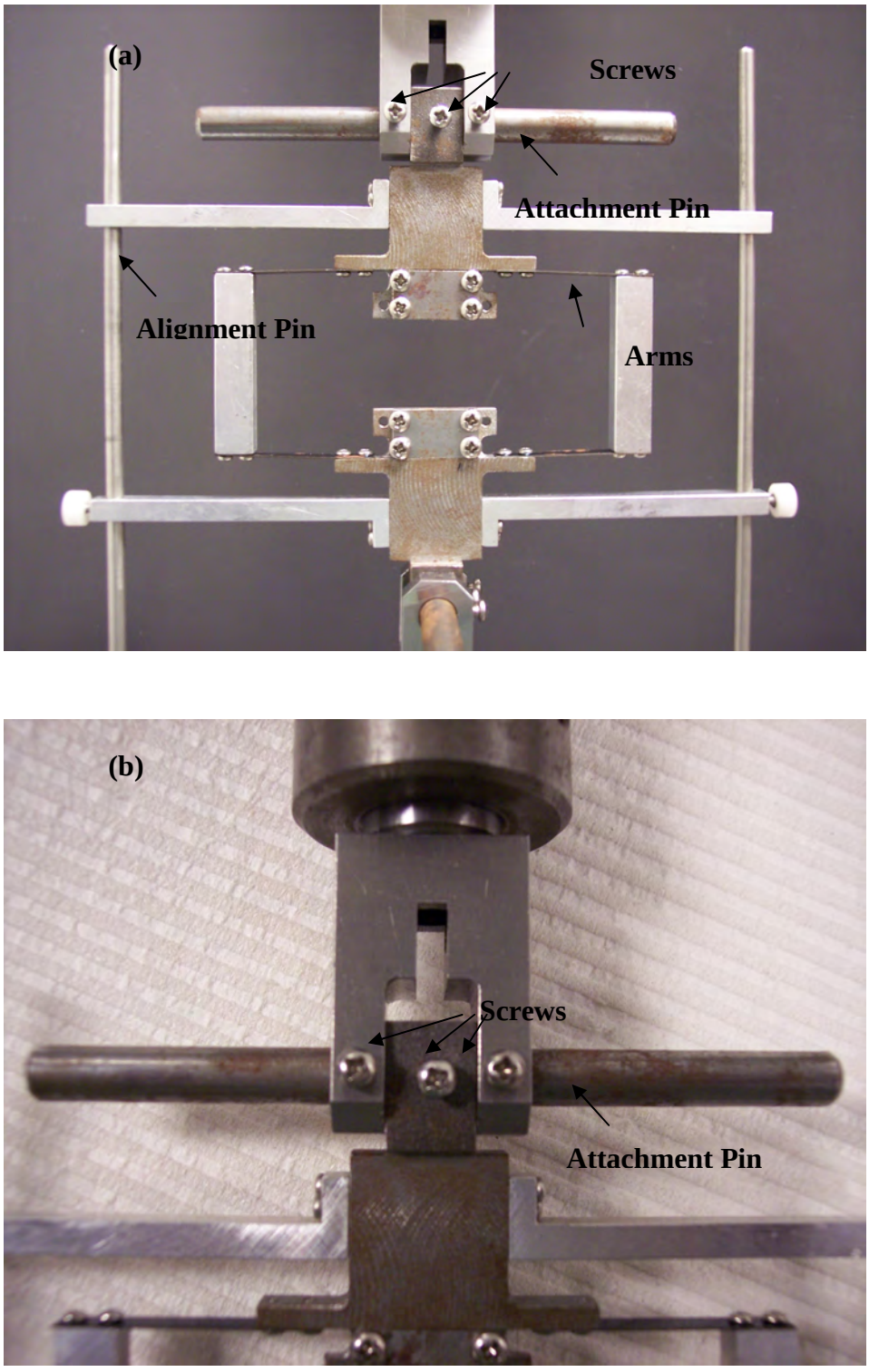

Figure B.4 (a) Image of the fixture alone, without the specimen, held between the two Instron platens using attachments pins. **(b)** The screws for securing the attachment pins.

The fixture was designed such that its loading and unloading response is linear within the range of displacements envisaged in the tests.

B.3.2 Specimen response

Substituting Eq. (B.2) with the experimental fixture stiffness from Figure B.3 into Eq. (B.1), we obtain:

$$F\big|_{\Delta} = K_{Fixture} \times \Delta + F_{Specimen}\big|_{\Delta} \qquad \text{(B.3)}$$

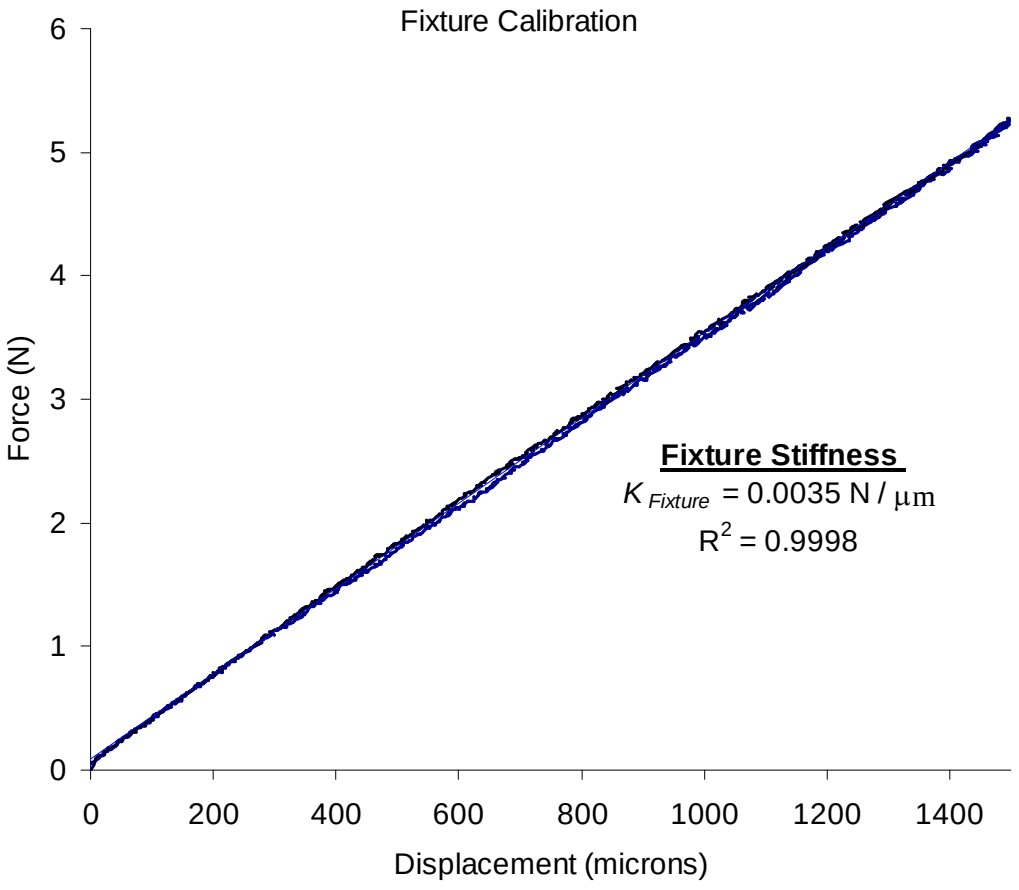

Figure B.5 Typical force – displacement response of the fixture (without specimen).

Upon rearrangement, the force in the specimen, at a given displacement Δ, can be found as:

$$F_{Specimen}\Big|_{\Delta} = F\Big|_{\Delta} - K_{Fixture} \times \Delta \qquad \text{(B.4)}$$

Figure B.5 graphically illustrates this procedure outlined in Eq. (B.3) and (B.4). Figure B.4 (a) shows the total measured force (fixture + specimen) in the loading as well as unloading regime. At the outset, the specimen deforms elastically. Eventually, plastic deformation commences and the overall force displacement response (fixture + specimen) becomes non-linear as seen. Finally, fracture is observed in the specimen and the total force begins to drop as the specimen gradually loses load carrying capacity. Finally, upon complete rupture in the specimen, the loading response coincides with the fixture response alone.

A linear fit to the force – displacement response during the unloading regime is used to find the fixture stiffness for every run. Using Eq. (B.4), the force in the specimen is calculated. Figure B.5 (b) shows the specimen force – displacement response calculated from the data in Figure B.5 (a) using Eq. (B.4).

The next step in the data analysis methodology is to obtain the true stress – log strain response of the specimen from the force- displacement response. Log strain (ε_{th}) can be calculated from the imposed displacement, Δ, as follows

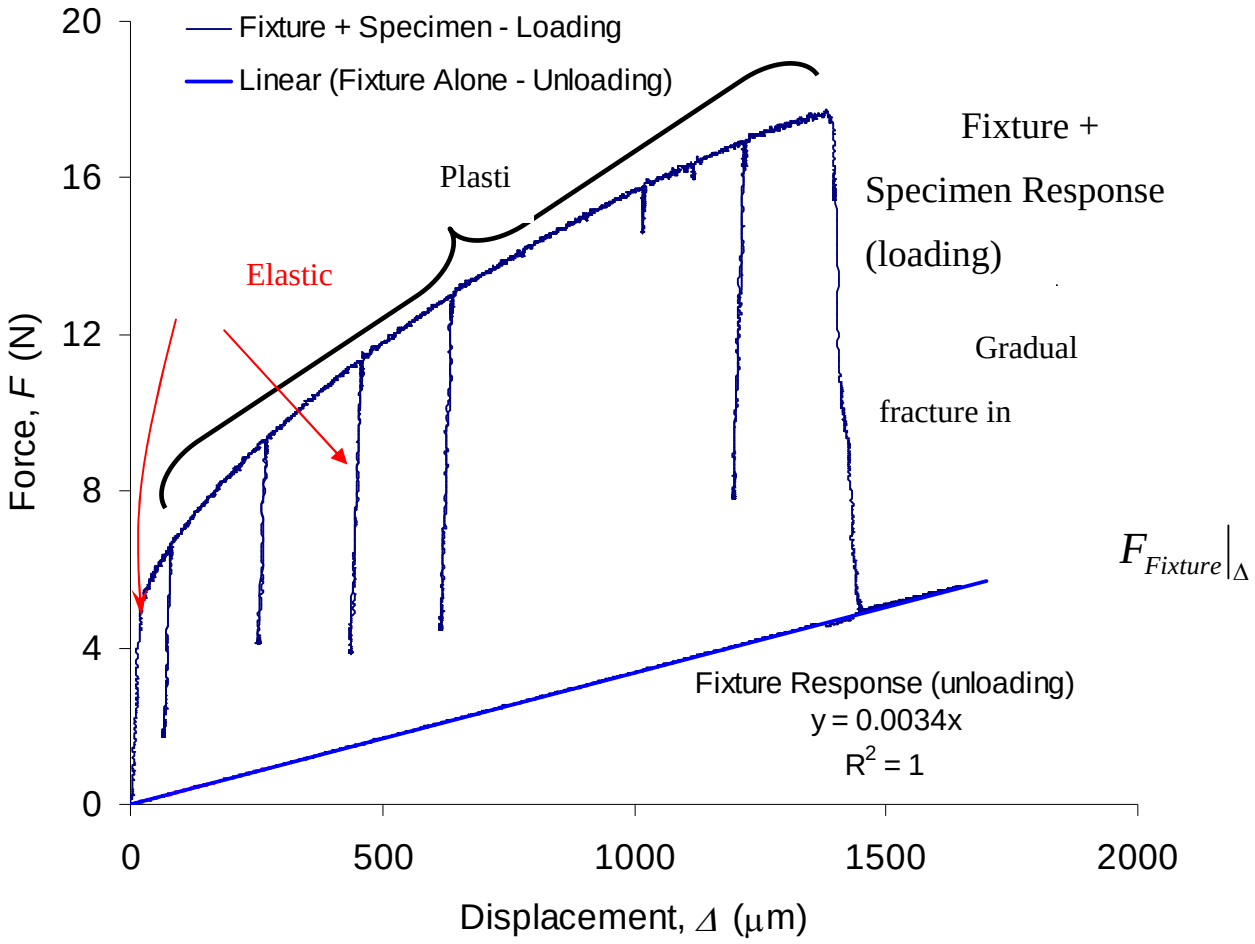

Figure B.6 (a) Typical force – displacement response of fixture + specimen

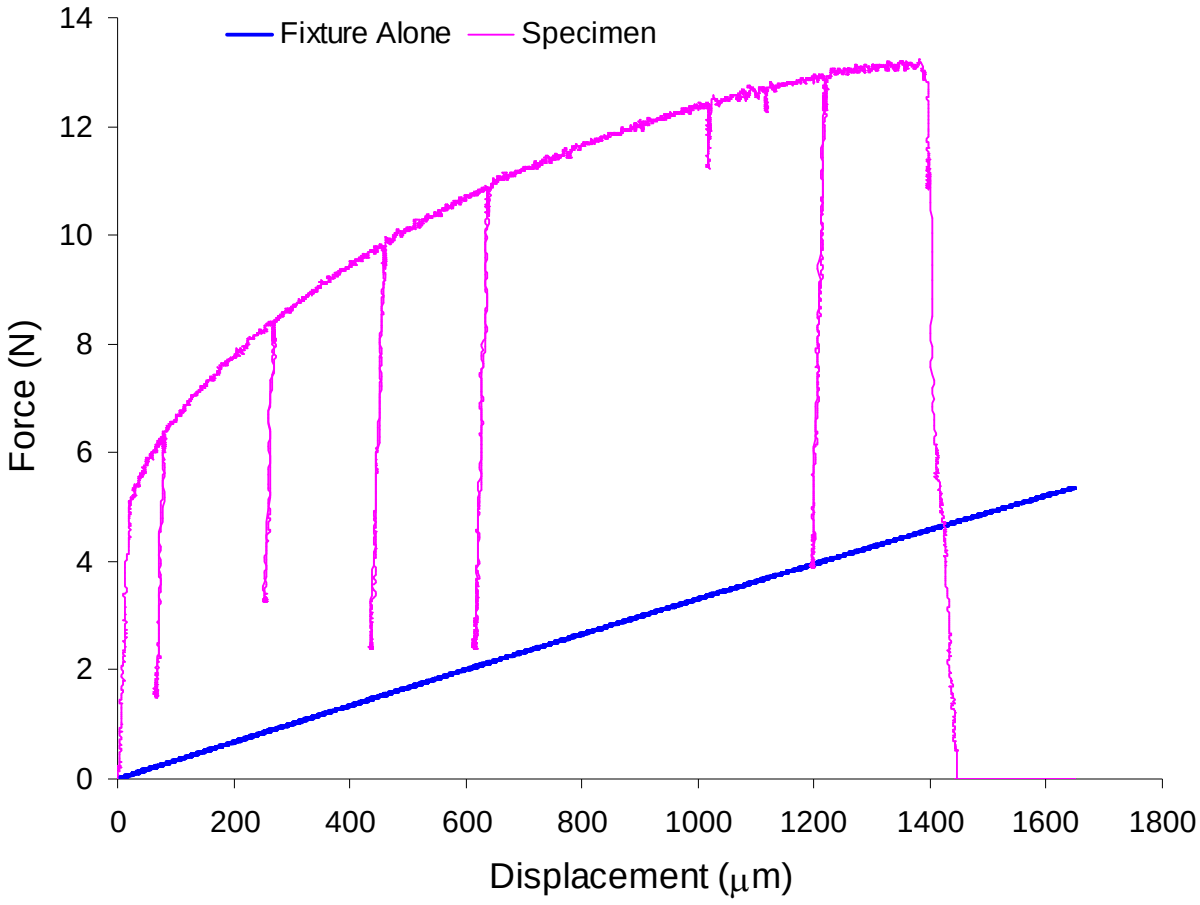

Figure B.6 (b) Specimen force-displacement response calculated from the measured data.

$$\varepsilon_{th} = \ln\left|\frac{\lambda_o + \Delta}{\lambda_o}\right| \qquad \text{(B.5)}$$

Eq. (B.5) assumes that the strain is distributed uniformly over the entire gauge length of the specimen, λ_o. This equation neglects the contribution from the specimen shoulders, as shown in the specimen geometry in Figure B.6. Figure B.6 (a) shows the specimen geometry used in this study. Figure B.6 (b) shows the strain distribution as obtained via FEM analysis. As a result of the strain distribution due to the shoulders, the 'actual' strain in the specimen gauge length is lower than the 'theoretical' strain predicted by Eq. (B.5). Figure B.6 (c) schematically illustrates strain distribution. FEM analysis was employed to calculate a calibration factor after accounting for the shoulder geometry. Copper was modeled using deformation plasticity. The elastic reponse was modeled with E = 120 GPa and ν = 0.3. Figure B.7 shows the FEM strain distribution results for different levels of macroscopic displacement i.e. theoretical strain, ε_{th}. The actual strain, ε_{ac} was obtained by extracting the log strain at specific nodal points along the specimen gauge length. The coordinate system for the specimen is shown in Fig. B.6 (b). Figure B.8 shows the strain calibration equation obtained from the FEM results. It is seen that in until a macroscopic theoretical strain of ~ 0.3% i.e. elastic response, the actual strain is about $1/4^{th}$ the theoretical strain. For theoretical strains beyond 0.3%, the actual strain is about 68% the theoretical strain.

This strain calculation methodology was validated via FEM as follows: the modeled behavior of copper (from deformation plasticity model) was compared with the

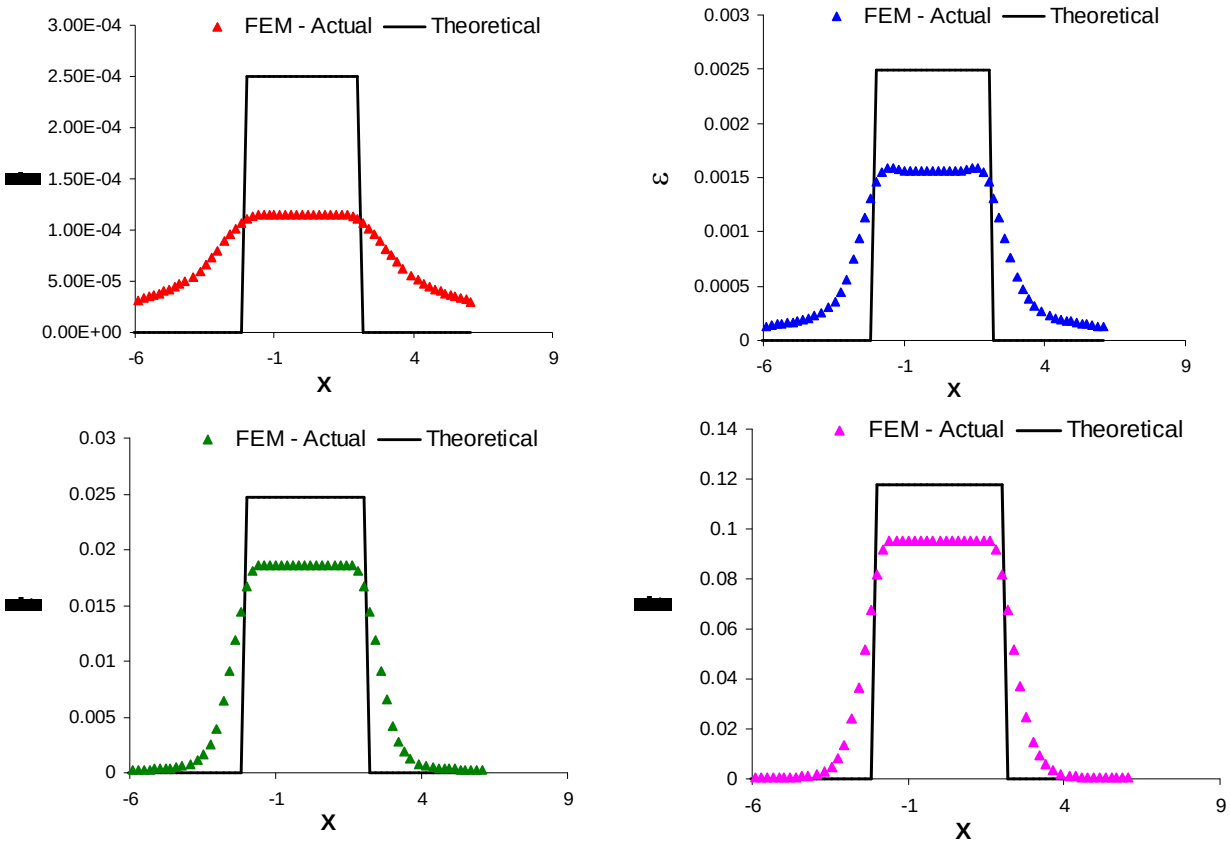

Figure B.7 Typical strain distributions as obtained via FEM. The theoretical distribution (based on Eq. (B.5) is shown as the black line. The actual distribution, based on log strain extracted at different nodes along the specimen gauge length is also shown.

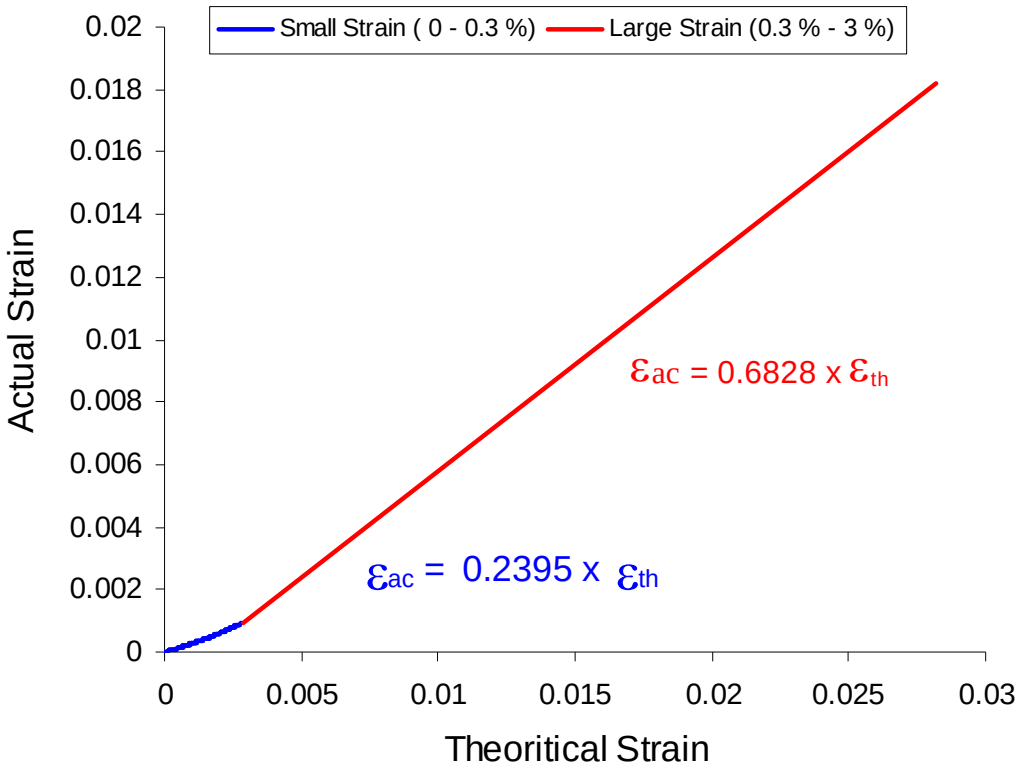

Figure B.8 Results of strain calibration via FEM analysis. A different equation, via linear fit, is obtained in the elastic region (~0.3% strain). In the plastic region, the slope between actual and theoretical strain is found to be 0.68.

stress-strain behavior obtained via data analysis from the force – displacement data obtained from FEM. The tensile specimen was modeled along with the test fixture. The spring steel arms were modeled using typical elastic parameters from spring steel. Firstly, the theoretical strain in the specimen was calculated from the imposed displacement in the FEM model. The actual strain was then calculated from the theoretical strain using the calibration equation given in Figure B.8. Finally, the true stress was calculated from the engineering stress (using FEM force data and the specimen cross-section) and the actual strain. This calibration was performed for fixtures with 250μm thick arms as well as 500μm thick arms. The strain calibration constant for small strains, as shown in Figure B.8 was used in the elastic region, while the large strain constant was used in the plastic region. As can be seen in Figure B.9, the true stress – log strain response of the Cu film extracted from FEM force – displacement data agrees very well with the modeled stress – strain response for Cu in the FE model.

The true stress – log strain response of the specimen was obtained from the force displacement response shown in Figure B.5 (b) using the methodology outlined previously, and validated using FEM. Figure B.10 shows the specimen's stress – strain response. The elastic modulus was calculated as 113.79GPa, which agrees very well with theoretical elastic modulus of Copper.

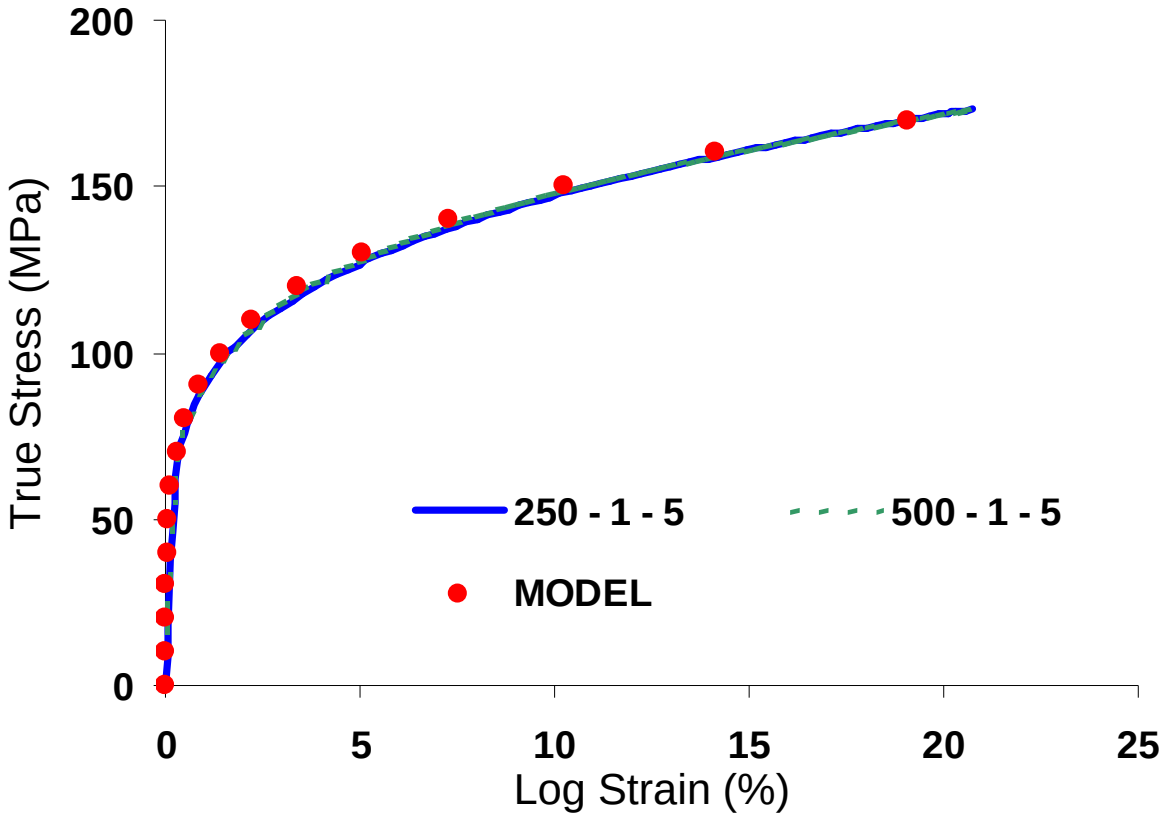

Figure B.9 The true stress-log strain response of the specimen extracted from the FEM force-displacement data is compared with the modeled behavior for Copper. Results for both 250μm arms as well as 500μm arms are shown.